Wave Evolution on Gentle Slopes - Statistical Analysis and Green-Naghdi Modelling

Mohd. Ridza Mohd. Haniffah

St. Edmund Hall

University of Oxford

A thesis submitted for the degree of

Doctor of Philosophy

Trinity 2013

Acknowledgements

First of all, let me express my deepest gratitude to my supervisors, Professor Paul Taylor and Professor Alistair Borthwick for accepting me as their student in the University of Oxford. They have been very patient, tirelessly editing drafts of my report, constantly giving advices and guidance throughout the years. Most importantly, they kept me going until the finishing line with endless words of motivation. Thank you.

I would also like to extend my gratitude to my colleagues in the Coastal and Ocean Engineering Group, in particular towards Myron van Damme for the fruitful discussions with respect to our research and to Jana Orszaghova who has provided me the understanding regarding the numerically solver for a mixed derivative partial differential equations. Outside the department, I should thank all my friends for being a part of my life here. Each and every one of you has helped me throughout my journey. Thanks guys.

Last but definitely not least, my special thanks to my family; supporting both with words of wisdoms, constant prayers and financially from afar. To my wife, Nur Farhana, thank you for your endless love and support during these years. It has been wonderful, and will always be. Thank you for taking care of us, to include our son and daughter, Muhammad Harith and Amna Najiha. Love you all.

Alhamdulillah.

I must greatly acknowledge the financial support provided by the Universiti Teknologi Malaysia (UTM) and also the Ministry of Education Malaysia.

ABSTRACT

An understanding of extreme waves is important in the design and analysis of offshore structures, such as oil and gas platforms. With the increase of interest in the shipping of LNG, the design of import and export terminals in coastal water of slowly varying intermediate depth requires accurate analysis of steep wave shoaling. In this thesis, data from laboratory experiments involving random wave simulations on very gentle slopes have been analysed in terms of a model of large wave events, and the results interpreted by observation of the shape and magnitude of the large wave events. The auto-correlation function of the free surface elevation time histories, called NewWave, has been calculated from the wave spectrum and shown to fit very well up to the point where waves start to break (when compared to the 'linear' surface elevation time history). It has been shown that NewWave is an appropriate model for the shape of the 'linear' part of large waves provided $kd \geq 0.5$. A Stokes-like expansion for NewWave analysis has been demonstrated to match the average shape of the largest waves, accounting for the dominant vertical asymmetry. Furthermore, an appropriate local wave period derived from NewWave has been inserted into a Miche-based limiting criterion, using the linear dispersion equation, to obtain estimates for the limiting wave height. Overall, the analysis confirms the Miche-type criterion applies to limiting wave height for waves passing over very mild bed slopes.

A derivation of general Green-Naghdi (GN) theory, which incorporates non-linear terms in its formulation, is also presented. This approach satisfies the boundary conditions exactly and approximates the field equations. The derived 2-dimensional vertical GN Level 1 model, capable of simulating steep waves on varying water depth, is validated against solitary waves and their interactions, and solitary waves on varying water depth and gives good qualitative agreement against the KdV equation. The developed and validated numerical model is used to simulate focussed wave groups on both constant depth and gentle slope. In general, the behaviour of waves simulated by the numerical model is very similar to that observed in the experimental data. There is evidence of vertical asymmetry as the water depth is reduced, owing to the non-linearity. Although the main physics is still controlled by linear dispersion, the higher order harmonics become increasingly important for shoaling waves. The numerical results also show a slope-induced wave set-up that keeps on increasing in amplitude as the wave group travels on the gentle slope.

Table of Contents

Acknowledgements i

Abstract ii

Nomenclature vii

1 Introduction and Literature Review

1.1 Background 1

1.2 Linear Wave Theory 3

1.3 Wave Spectrum 3

1.4 Extreme Waves 4

1.5 NewWave 5

1.6 Green-Naghdi Numerical Model 6

1.7 Motivation of Research 8

1.8 Aim and Objectives 10

1.9 Synopsis 10

2 Physics of Random Waves on Gentle Slopes

2.1 Introduction 12

2.2 Laboratory Flume 13

2.3 Wave Input Conditions and Tank Geometry 14

2.4 Surface Elevation Time History 18

2.5 Detailed Analysis 20

2.5.1 ‘Crest’ and ‘Trough’ Surface Elevation 20

2.5.2 Linear and Second Order Term Surface Elevation 25

2.6 General Overview of the Results for the Largest Waves 29

2.7 Post-breaker Line ($kd < 0.5$) 39

2.7.1 Waves in Shallow Limit as a Succession of Uncorrelated Solitary Waves 42

2.7.2 Waves in Shallow Limit as a Succession of Uncorrelated Hydraulic Jumps 46

2.8 Conclusion 47

3 NewWave Analysis of Experimental Data

3.1 Introduction 49

3.2 NewWave Comparison with ‘Linear’ Surface Elevation 50

3.3 Extraction and Detailed Analysis of the Bound Sum Harmonics 52

3.3.1 Odd Harmonics 52

3.3.2 Even Harmonics 57

3.4 Spectral Modification due to Shoaling 62

3.5 Effect of Friction 64

3.6 Comparison with other Test Cases 68

3.6.1 Influence of Offshore Significant Wave Height (H_{so}) 68

3.6.2 Effect of Bed Slope 70

3.7 Conclusion 72

4 Mathematical Formulation of the Green-Naghdi Equations

4.1 Introduction 73

4.2 3-D Mass and Momentum Equations and Kinematic Boundary Conditions for Free Surface Flow of Inviscid, Incompressible Liquid 73

4.3 3-D Green-Naghdi Continuity Equation for Free Surface Flow of Inviscid, Incompressible Liquid 75

4.4 2-D Green-Naghdi Momentum Equations for Free Surface Flow of Inviscid, Incompressible Liquid 76

4.4.1 x-direction Green-Naghdi Momentum Equation 76

4.4.2 z-direction Green-Naghdi Momentum Equation 79

4.5 Green-Naghdi (GN) Level 1 Equation for Shallow Water Flow over a Non-uniform Bed 83

4.6 Analytic Structure of Harmonic Solutions to GN Level 1 Equations 92

4.6.1 GN Linear Wave Dispersion 92

4.6.2 2nd Order Perturbation Analysis 94

4.7 Numerical Solver 102
4.7.1 Finite Difference Scheme 103
4.7.2 Time Integration 104
4.7.3 Boundary Conditions 106
4.8 Conclusion 107

5 GN Numerical Simulation of Solitary Waves

5.1 Introduction 109
5.1.1 Solitary Wave Profile 110
5.2 Simulation Setup 111
5.3 GN Simulation of Solitary Wave Separation 113
5.3.1 Integrability of GN Equations 117
5.4 GN Simulation of Solitary Wave Interaction 121
5.5 GN Simulation of Solitary Wave on a Sloping Bed 127
5.6 Conclusion 134

6 GN Numerical Simulation of Focussed Wave Groups

6.1 Introduction 137
6.2 Simulation Setup 138
6.3 Focussed Wave Groups on Water of Constant Depths 139
6.3.1 Accuracy Test 141
6.3.2 Effect of Water Depth on Linear Wave Groups 147
6.3.3 Effect of Water Depth on Weakly Non-linear Wave Groups 151
6.3.4 Separation of Second Order Bound and Free Wave Components 155
6.3.5 The Shape of the Second Order Sum and Difference Bound Waves Components 158
6.3.6 Wave Steepness Effects for Intermediate Water Depth 160
6.3.7 Most Non-linear Case in Terms of Amplitude and Water Depth 163
6.3.8 Most Non-Linear Case in Amplitude but in Deep Water 163
6.3.9 Non-linear Defocussing 166
6.4 Focussed Wave Groups on Sloping Bed 169

6.4.1 Accuracy Test 171
6.4.2 Wave Steepness Effects 173
6.4.3 Comparison with Lowish data 180
6.5 Conclusion 190

7 Conclusions and Recommendations 193

8 References 202

Nomenclature

a @ A	wave amplitude
a_{tj}	amplitude of the *j*th transmitted wave
A_i	coefficients of the linear, second and third order terms for surface elevation using the orthogonality principle (Section 3.3)
A_{ij}	Stokes coefficient for velocity
b	inverse width of the solitary wave
B_{ij}	Stokes standard coefficient (using water depth, *d* explicitly)
c	wave speed
c_{hj}	speed of a hydraulic jump
c_{sol}	solitary wave speed
c'	effective wave speed
d	water depth
d_1	water depth at the shallow water region
e_2	second order sum term coefficient of the GN equations (surface elevation)
E	error for the *i*th numerical grid point
$\|E\|$	total error contribution
EH_2	second order sum term obtained from the numerical data
f	wave frequency
f_p	spectrum @ wave peak frequency
g	gravity
G	Gauge
H	wave height
H_{max}	maximum wave height
H_{so}	offshore @ deep water significant wave height
k	wave number

k_{NW}	wave number based on zero down-crossing period of local NewWave
k_p	peak wave number
k_W	width of the transition region at both ends of the sloping bed
L	distance
m	bed slope
M	multiplication factor for surface elevation and velocity
M_i	initial wave mass
M_s	steady-state solitary wave mass
$\boldsymbol{M}$	coefficient matrix for the numerical solver
n_r	ratio of the group velocity to phase speed
NW	NewWave (the auto-correlation function of surface elevation time history)
$\mathrm{NW_H}$	Hilbert transformation of NW
NW2	second order sum term in Stokes wave expansion
NW2Δ	second order difference term in Stokes wave expansion
NW3	third order term in Stokes wave expansion
OH	odd harmonics obtained from the numerical data
$\mathrm{OH_H}$	Hilbert transformation of OH
$\bar{p}$	pressure on bottom surface
$\hat{p}$	pressure on top surface
P	pressure
S	wave spectrum @ spectrum energy
S_{ij}	Stokes coefficient for surface elevation defined by Walker et al. (2004)
S_j	JONSWAP spectrum
S_n	coefficient of the *n*th order harmonics for the Stokes wave expansion
S_p	Pierson-Moskowitz (PM) spectrum
t	time
t_c	time at crest
T	wave period

T_p	spectrum @ wave peak period
T_{NW}	local NewWave-wave period
$\vec{u}$	velocity vector (u, v, w)
u_c	local current velocity
v_2	second order sum term coefficient of the GN equations (velocity)
$\overrightarrow{W}_n$	time-dependent vectors (u_n, v_n, w_n)
x	horizontal x-coordinate
y	horizontal y-coordinate
z @ ζ	vertical coordinate
α	bottom surface boundary
β	top surface boundary
Δx	spatial resolution
Δt	time step interval
Φ	TMA factor
γ	JONSWAP peak enhancement factor
η	surface elevation
η_{c}	surface elevation centred at crest
η_{t}	surface elevation centred at trough
κ	scalar multiplier for the magnitude of a solitary wave
λ	wave length
λ_{n}	assumed shape functions
θ	wave phase
ρ	density
σ	standard deviation
ω	angular frequency
ω_{p}	peak frequency

1 Introduction and Literature Review

1.1 Background

The offshore oil and gas industry produces much of the energy required for industry, commerce, transport, and domestic consumption, worldwide. Offshore structures are designed to withstand the loadings from extreme waves and resist fatigue from typical operating wave conditions. Accurate prediction of ocean waves is very important in the design and safe operation of offshore structures, and can be a major factor in determining the economic viability of an offshore project.

Most ocean waves are wind-generated waves. These result from wind blowing over a stretch of open water surface for a long period of time. The developed waves can travel large distances over the sea from their area of origin. As a wave travels, its properties (for example amplitude, period and spectrum) change due to a range of physical processes such as shoaling, diffraction, breaking and refraction. During a storm, irregular short-crested waves propagate away from the generation area with a range of different speeds and directions (Holthuijsen, 2006). Low frequency long waves travel faster than the higher frequency shorter ones. This process is known as frequency-dispersion. The linear dispersion equation used to describe this is shown below:

$$\omega^2 = gk\tanh(kd) \tag{1.1}$$

where ω is angular frequency, g is the acceleration due to gravity, k is wave number and d is water depth.

Ocean waves are both essentially random in time and can be highly non-linear (e.g. large amplitude, with tall narrow crests and shallow troughs). Shoaling steepens the waves, increases their amplitudes due to non-linear interactions between wave components and ultimately leads to breaking. Wave breaking occurs when an individual wave crest is so steep that it can no longer hold its shape. Dissipation of wave energy through breaking produces turbulent motion within the water and also changes the behaviour of waves. A useful but empirical criterion in estimating the maximum wave height achievable by waves is given by Miche (1944);

$$H_{max} = 0.142\, \lambda \tanh kd \tag{1.2}$$

where H is wave height, λ is wavelength, k is wave number and d is water depth.

In deep water, the equation reduces to a maximum wave steepness $H_{max}/\lambda = 0.142$, and in shallow water, it reduces to a maximum height-to-depth ratio $H_{max}/d = 0.89$. This result is based on the structure of limiting regular waves on deep water and the highest possible solitary wave on very shallow water.

Recently, there has been a growth in interest in the installation of large offshore structures for oil and gas recovery from sites where the water depth is relatively shallow. The design of these structures is particularly challenging, as they are subjected to waves that steepen non-linearly as the water depth decreases. Moreover, there is a growing consensus among researchers that ocean waves occasionally occur with heights well in the excess of what is expected (Haver et al., 2004). Extreme wave events are highly non-linear and ongoing research is being undertaken to quantify high order wave harmonics and non-linearity. An example of an extreme or 'freak' wave event is the Draupner wave which occurred in the central North Sea at the Statoil's Draupner platform in 1995. A single wave crest of 18.5 m was recorded in a 70 m water depth in a sea-state with a significant wave height, H_s of approximately 12 m (Walker et al., 2004 and Adcock et al., 2011).

Improved understanding of the processes and behaviour of extreme waves is needed in order to have a good and sound design methodology for offshore structures in deep, intermediate and shallow water. Much physical experimentation and numerical modelling has been undertaken to study the behaviour of these extreme ocean waves. Advances in computer technology, such as fast computational speed, low cost and sophisticated symbolic and mathematical manipulations, have made numerical modelling an appealing approach by which to study the behaviour of ocean waves.

1.2 Linear Wave Theory

Linear Wave Theory (also known as Airy Theory and small amplitude wave theory) (Sarpkaya and Isaacson, 1981; Dean and Dalrymple, 1984; and Billingham and King, 2000) is the simplest theory for surface gravity waves. Besides the assumption that the fluid is irrotational, inviscid and also incompressible, the non-linear terms in the free surface boundary conditions are also neglected. This theory gives a reasonably approximation of wave characteristics over a wide range of wave parameters. This linearization means that each wave component will not interact with any other, and each wave component will always maintain its sinusoidal form, as shown in Figure 1.1. But, care has to be taken as this wave theory is not suitable for the real open sea surface which includes random waves because of the local occurrence of much taller and steeper waves.

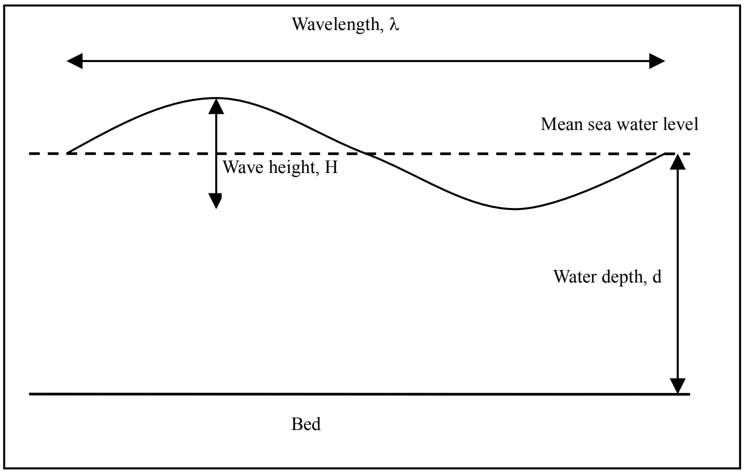

Figure 1.1: 2-Dimensional linear wave characteristics

1.3 Wave Spectrum

In offshore engineering generally, knowledge of the wave spectrum is assumed to describe adequately the random nature of waves in the open sea, where the sea-state is assumed to be a mixture of components with different frequencies, phases and amplitudes (Holthuijsen, 2006). The wave spectrum gives the mean distribution of wave energy at different frequencies on the sea surface with the sea surface represented by an infinite series of sine and cosine functions of different wave-lengths moving in many directions (Stewart, 1997). The Pierson-Moskowitz (PM) spectrum (e.g. Sarpkaya and Isaacson, 1981) is a standard model for a fully developed sea (a sea produced by winds blowing steadily over hundreds of miles for several days). But observations from the Joint North Sea Wave Project (JONSWAP) found that the ocean waves are not necessarily fully developed (Tucker and Pitt, 2001), and instead continue to develop in time and space. In practice, most engineers use the JONSWAP spectrum, which represents the wave spectral energy $S_j(f)$ empirically from:

$$S_j(f) = \frac{\alpha g^2}{(2\pi)^4 f^5} \exp\left[-\frac{5}{4}\left(\frac{f_p}{f}\right)^4 \right] \gamma^r \tag{1.3}$$

where

$$r = -\frac{(f - f_p)^2}{2\sigma^2 f_p{}^2}, \quad \sigma = \begin{cases} 0.07; f \le f_p \\ 0.09; f > f_p \end{cases}$$

where α is an empirical constant, g is the acceleration due to gravity, f is wave frequency, f_p is peak frequency, σ is the standard deviation and γ is peak enhancement factor. Figure 1.2 compares the PM and JONSWAP spectra.

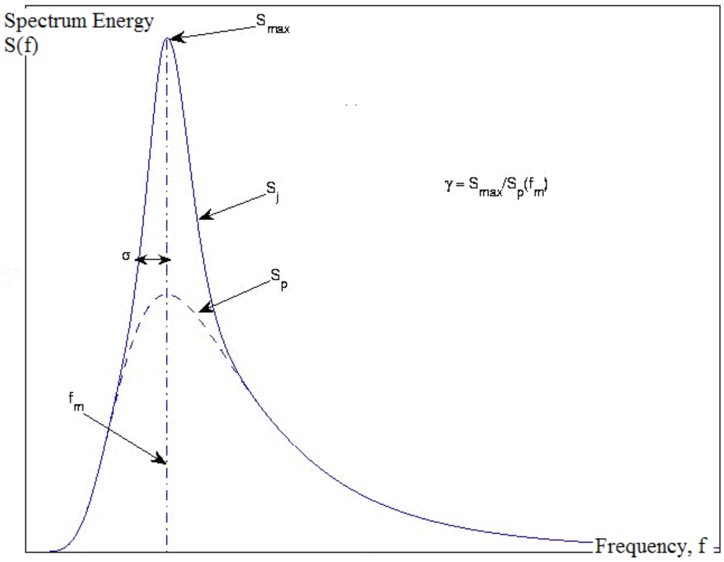

Figure 1.2: Relationship between the PM (S_p) and JONSWAP (S_j) Spectrum.

1.4 Extreme Waves

There have been many sightings of very large waves by mariners, and evidence of damage on ships and offshore structures that can only be caused by high waves. The terms ‘white wall’ and ‘freak waves’ have been used to describe these large waves and have been cited as one of the factors for missing ships. Prior to the now famous and reliably measured Draupner wave event in 1995, it was unclear whether such waves were real. Findings by The European Space Agency reported by BBC in 2004[1] have proved the occurrence of these ‘freak waves’, which exist in higher numbers than anyone expected. Unlike idealised linear waves, real large ocean waves are vertically asymmetric and non-linear, due to the crests being larger and steeper compared to the troughs. A lot of research studies have been undertaken to understand aspects of these large, extreme waves. Here, the term ‘extreme waves’ is used to describe waves which are at least twice higher than the significant wave height, defined as the average height of the highest one-third of the surrounding waves. The occurrence of extreme waves can be due to many different processes, such as refraction of waves in varying bottom topography, wave-current interaction of opposite directions (e.g. the Agulhas current, (Smith, 1976)) and two wave groups crossing at sea (Adcock et al., 2011). The latter explains the unusual underlying wave set-up in the 1995 Draupner wave event discovered by Walker et al. (2004).

One reason for the occurrence of locally higher waves is the dispersive focussing of waves; random waves combining at a point in time and space where the height of the resulting crest is higher than the linear combination of all crests. The act of waves coming together linearly to generate a large wave triggers the non-linearity. Non-linear interactions consist of quadruple and triad interactions. The former dominates the evolution of the spectrum in deep water by transferring energy from the spectral peak to lower frequencies (thus lowering the peak frequency) and to higher frequencies (where white capping dissipates the energy), whilst the latter occur in shallow water by transfer of energy from lower to higher frequencies resulting often in higher harmonics (Beji and Battjes, 1993). Research on this non-linear focussing phenomenon has been done by Baldock et al. (1996), Slunyaev et al. (2002), Gibson and Swan (2007), and many others with the objective of understanding large wave events.

1.5 NewWave

For design purposes, instead of random ocean waves, a focused wave group known as NewWave can be used as the design input wave condition in order to predict wave forces acting on a structure in the ocean. NewWave is the average shape of extreme events in a linear random Gaussian process (Tromans et al., 1991). Lindgren (1970) and Boccotti (1983) showed that the average shape of very large events in time is proportional to the auto-correlation function of the time history, but only took into account the linear behaviour of the

---

[1] Freak Waves Spotted from Space, 2004, *BBC News*; http://news.bbc.co.uk/1/hi/3917539.stm

moving surface waves. Boccotti (1983) introduced the use of the auto-correlation function into offshore engineering using linear wave motion, which can be applied to a broad banded energy spectrum such as obtained for wind waves. Tromans et al. (1991) then used the NewWave model in the context of structural reliability analysis. One major advantage is that it can replace the computer-time demanding random wave analysis and, as stated before, can model broad banded sea-states. The theory provides a good basis for deriving models of extreme waves.

Jonathan and Taylor (1997) investigated the expected form of a wave in time using the linear order theory by Lindgren (1970), which accurately gives the result for large sized crests when compared with measured field data. Taylor and Williams (2004) and Walker et al. (2004) have shown that NewWave fits well to the linear part of average shape of large waves of both the WACSIS and Draupner datasets for field data from the North Sea. Thus, NewWave can be used to predict the local wave structure of large events given a frequency spectrum at any spatial point. However, real ocean waves are random and non-linear. By adding non-linear components; correct to second order in Stokes theory, to the obtained linear profile, it is clear from observation that the crest slope steepens and height increases while the trough broadens. This result provides a further step in understanding the behaviour of extreme waves.

1.6 Green-Naghdi Numerical Model

The overall aim of the proposed DPhil research is to develop a numerical wave model to simulate the behaviour of free surface flow and to analyse the physics involved in extreme waves. The Navier-Stokes equations describe the motion of Newtonian fluid flow (Munson et al., 2006). If viscosity is neglected, the Navier-Stokes equations reduce to the Euler equations for inviscid, incompressible, and irrotational flow (Li and Lam, 1964). In turn, this leads to the governing Laplace equation normally used for free surface water flow, whereby a potential can represent the velocity vectors (Longuet-Higgins and Cokelet, 1976). Fully non-linear potential theory (FNPT) is particularly useful for representing the interaction of water with large structures, where viscous effects can be ignored. In solving the governing equations, non-linearity exists explicitly in the boundary conditions of the free surface; involving fluid velocity, surface displacement, velocity potential and its normal derivative on the free surface. There are many numerical methods for solving the non-linear free surface motions of ocean waves such as the Finite Element Method (Ma and Yan, 2006; Yan and Ma,

2007) and the Spectral Method (Fenton and Rienecker, 1982; Craig and Sulem, 1993; Bateman et al., 2001 and 2003). Although these numerical schemes can model a wide range of water wave problems, there is still need for more accurate models of extreme wave interactions with structures.

Various other alternative approaches are available to simulate free surface flows. A standard perturbation method such as Stokes' wave theory assumes that the solution is a perturbation in a small parameter, the wave steepness, to describe weakly non-linear and dispersive waves. It is successful in deep water with relatively short wave lengths as compared to the water depth but is limited use for shallow water, because it needs many terms before convergence towards the solution. The Boussinesq equations are preferred in shallow water, where Taylor expansions are used for the flow field and applied to the boundary conditions. It is valid for weakly non-linear wave and incorporates frequency dispersion, unlike the shallow water equations. Both the derivations of Stokes perturbation method and the Boussinesq equations are given respectively in Part 1 and Part 2 of Dingemans (1997).

The theory of fluid sheets, introduced by Green, Laws and Naghdi (1974), has been used in a variety of fluid flow problems; for example waves in shallow and deep water (Green and Naghdi, 1986; Shields and Webster, 1988), waves due to a moving pressure disturbance (Ertekin et al., 1986) and water wave evolution at a wave-absorbing beach (Xu et al., 1997). Green-Naghdi (GN) theory is a relatively recent invention which appears to be very effective as the kinematics become increasingly violent (steep waves). GN theory satisfies the boundary conditions exactly while approximating the field equation, incorporating the momentum equation. This is the opposite way around to the standard Stokes-type perturbation method. Prescribing the dependency of the kinematic structure in the vertical direction results in a two-dimensional equation that represents the three-dimensional problem. Demirbilek and Webster (1992) derived the general GN equations for inviscid and incompressible fluid, with GN Level I and Level II formulated to solve two-dimensional steady and unsteady flows over flat and uneven bottom topography.

Shields and Webster (1988) demonstrated that there are advantages to this approach, by comparing predictions for steady, two-dimensional waves over a horizontal bed. Numerical solutions indicate that the GN theory converges more rapidly than the more standard perturbation theories. Other works using GN are by Kim and Ertekin (2002), Chan and Swan (2003) and Zhao et al. (2009 and 2010). The latter have applied Level II and III GN theory to simulate earthquake induced tsunami and underwater landslides by varying the bottom topography with time, and also compare the dispersive relations between Level VII GN theory and linear Stokes theory. In contrast to the derivation of GN theory by a direct method, which uses fundamental principles of continuum mechanics, Kim et al. (2001 and 2003) derived the GN equations for irrotational flow using the principle of virtual work and performed numerical tests to show convergence of the theory as the level increases.

1.7 Motivation of Research

Industrial Motivation

New sources of energy are always in demand. The increase of interest in the shipping of Liquefied Natural Gas (LNG) since the year 2000 has been dramatic. For countries such as Japan and Korea, without large energy resources, the importation of LNG has been essential in supplying energy. For the energy companies, LNG provides a method of producing from gas fields and then transporting the product to market. In the case of exporting countries like Australia and Brunei, the shipping of LNG allows them to benefit from their gas resources which otherwise would have no market.

As LNG production plants and tankers are enormous, it has become increasingly desirable to establish LNG export and import terminals in intermediate water depth, particularly in areas where the slope of the continental shelf is very gradual. There is lack of research going on regarding this transition zone; where the waves are slowly affected by the water depth, as compared to both the deep and shallow water. Offshore engineers are mostly concerned with deep water waves which are little affected by the water depth while coastal engineers are mostly concerned with waves in the surf zone i.e. between the point of incipient wave breaking and the still water shoreline.

Shell initiated a Joint Industry Project (JIP) under the Limits of Waves in Shallow Water (Lowish, Imperial College et al., 2007)[2] project to address the uncertainties of waves propagating on these slowly varying water depths, particularly regarding the limiting wave

---

[2] The Lowish material was covered by confidentiality agreement but the material has been made available for this thesis.

heights. The Gulf of Mexico provides a very good example for this intermediate water depth on the continental shelf where the bathymetry includes slowly varying water depth from deep to shallow water. There is some evidence that the limiting wave height may be as low as 0.55 times the water depth, much lower than that is used in engineering practice of 0.78 (Nelson, 1994). This lower limit will have a huge impact in reducing the cost of design and construction of structures and ships. But before any new implementation, concrete evidence is needed. That is the aim of the project, to provide sound evidence of a better limiting wave height of waves propagating on gentle slopes through the analysis of experiments on a purpose-built wave flume, field measurements and also numerical modelling.

Scientific Motivation

Questions that can be answered through this research include determining the shape of the large wave events as the waves shoal on the continental shelf and also the local maximum wave height. The Miche limiting criteria is put to the test on waves interacting with the slowly varying water depth, as any strong evidence of a lower limiting criterion would be important in saving the cost by way of designing structures and ships using a lower and better approximation of the wave force. The analysis is done by statistical modelling using NewWave, a representation of the linear large wave event and can be applied at any spatial point (where the physics are dominated by linear dispersion), given the local input spectrum. In the absence of local spectral information, it is likely that deep water spectral information will be available even if this is simply the assumption of a standard JONSWAP form. In the absence of a computer package such as SWAN (a third-generation wave model that computes the spectra associated with random, short-crested wind-generated waves), a simple spectral modification method to account for shoaling is used as the waves advance into shallower water. The deep water spectrum can be modified to be a function of water depth by using the linear dispersion equation, resulting in the TMA (Texel, Marsen and Arsloe) spectrum. It should be stressed here that SWAN is not phase resolving, so the output is a local wave spectrum even if such a sophisticated code is available.

Through the developed and validated GN model, which is able to simulate steep waves on varying water depth, the behaviour of focussed wave groups on gentle slopes can be examined and compared to the limited records from the Lowish experiments at Imperial College. Records of wave kinematics for any time and space can be extracted numerically, which could be essential as the Lowish experiments have wave gauges which are 5 m (several wavelengths) apart from one another. NewWave-focussed wave groups from the experimental data of random waves are used as the initial conditions. The focussed wave groups are simulated from their dispersed conditions and made to focus at a particular point rather than by interpreting random waves as has been done in the Lowish experiments. Together with the data analysis work, this research aims to provide greater understanding of wave groups shoaling on continental shelf.

1.8 Aim and Objectives

The aim of the research being reported in this thesis is to develop a validated numerical wave model which is accurate, robust, and efficient for simulating propagating waves from deep to shallow water, taking into account steep slopes and extreme waves. What is new to this research is the combination of the GN model with the physical structure of the wave field gained from the data analysis work. Then, the behaviour of extreme waves which are highly non-linear can be modelled using the experimentally derived results as the initial conditions. This will then feed into the planning and design of offshore structures.

The objectives are as follows:

a) Interpretation of the physical structure of the wave field from measured data of waves propagating on a very mild bed slope representative of the continental shelf.
b) Applying NewWave (NW) analysis to estimate the local properties of a large wave event.
c) Extending NW from being a linear representation of large wave events to represent higher order harmonics.
d) Validating the developed 2D GN Level 1 theory by simulations of solitary waves and comparing against the well-known KdV equation.
e) Simulating NewWave-type focussed wave groups’ propagation on gentle slope, representing the behaviour of extreme waves to understand the physics of focussed wave groups’ interaction with varying water depth.

1.9 Synopsis

Chapters 2 and 3 deal with the interpretation of experimental data on the propagation of waves from deep to shallow water and the application of NewWave method and its Hilbert transformation-based method to represent large wave events on the experimental data. Details of the experimental setup by Imperial College London are also described in Chapter 2. Chapter 4 deals with the mathematical derivation of the Green-Naghdi Level 1 equations, which include investigation of the derived GN equations' dispersion and non-linearity properties and the numerical method for solving them. Chapter 5 proceeds with the validation of the developed GN model and also improvement in understanding the nature of the GN equations by simulation of solitary waves (which are inherently non-linear). These are then compared against solutions of the solitary waves for the KdV equation. Chapter 6 investigates the behaviour of focussed wave groups as representations of extreme waves; in particular the interaction of an extreme wave group with the mild sloping bed is studied in detail. Together with the data analysis in Chapter 2 and Chapter 3, the numerical results give insight on the behaviour of extreme waves. The final chapter summarises the main conclusions of this work, and makes several recommendations as to how the work could be extended.

2 Physics of Random Waves on Gentle Slopes

2.1 Introduction

Wind blowing on the surface of the ocean will create a random sea state composed of waves with variable heights, periods and wavelengths, depending on the fetch length, duration and also the wind speed. As the random waves propagate away from their source, their behaviour changes and they start to shoal on the continental shelf and enter progressively shallow water before reaching the coast line. A physical scale model of these processes can be established using a laboratory wave flume; with controlled conditions (use of input wave paddle signal and known bed topography) and precise measurements (see e.g. Hughes, 1993).

This chapter describes the interpretation of laboratory data in order to understand better the mechanics of waves propagating from deep water to shallow water on a very mild bed slope representative of the continental shelf. The laboratory experiments were undertaken using a wave flume at Imperial College London in the first phase of the Limits on Waves in Shallow Water project (Lowish Report, Imperial College et al., 2007 and Katsardi et al., 2013), where the data obtained are of very high quality. Lowish was a joint project under the Joint Industry Project initiated by Shell International Exploration and Production aimed at addressing more precisely the uncertainties in waves propagating from deep water to shallow water, in particular for intermediate water depths where waves slowly evolve as the water depth reduces. In the present work, the wave profiles along the flume are examined by studying the change of shape, crest, trough and wave heights as the waves shoal. The effects of non-linearity are also investigated by separating the harmonics of the surface elevation time history, using Stokes water wave expansion theory to reveal the physical processes involved in the propagation of random waves from deep into shallow water.

2.2 Laboratory Flume

Figure 2.1 shows the wave flume at Imperial College, which is 0.6 m wide and 60 m long. In the Lowish study, the water depth varied (based on bed slope) from 0.7 m at the wave paddle to 0 m at the beach.

Figure 2.1: The wave flume (without the sloping bed).

Up to eleven wave gauges were installed along the length of the wave flume. Each wave gauge consisted of two thin wires piercing the water surface. The wires were of diameter 1 mm and spaced 10 mm apart so that they were hydrodynamically transparent and did not alter the water streamlines (Lowish Report, Imperial College et al., 2007). The wave gauges were used to measure the water surface elevation by producing a voltage output which depended on the length of the thin wires being immersed in water. An accuracy of better than ± 1 mm was expected after calibration. Figure 2.2 shows the position of the wave gauges.

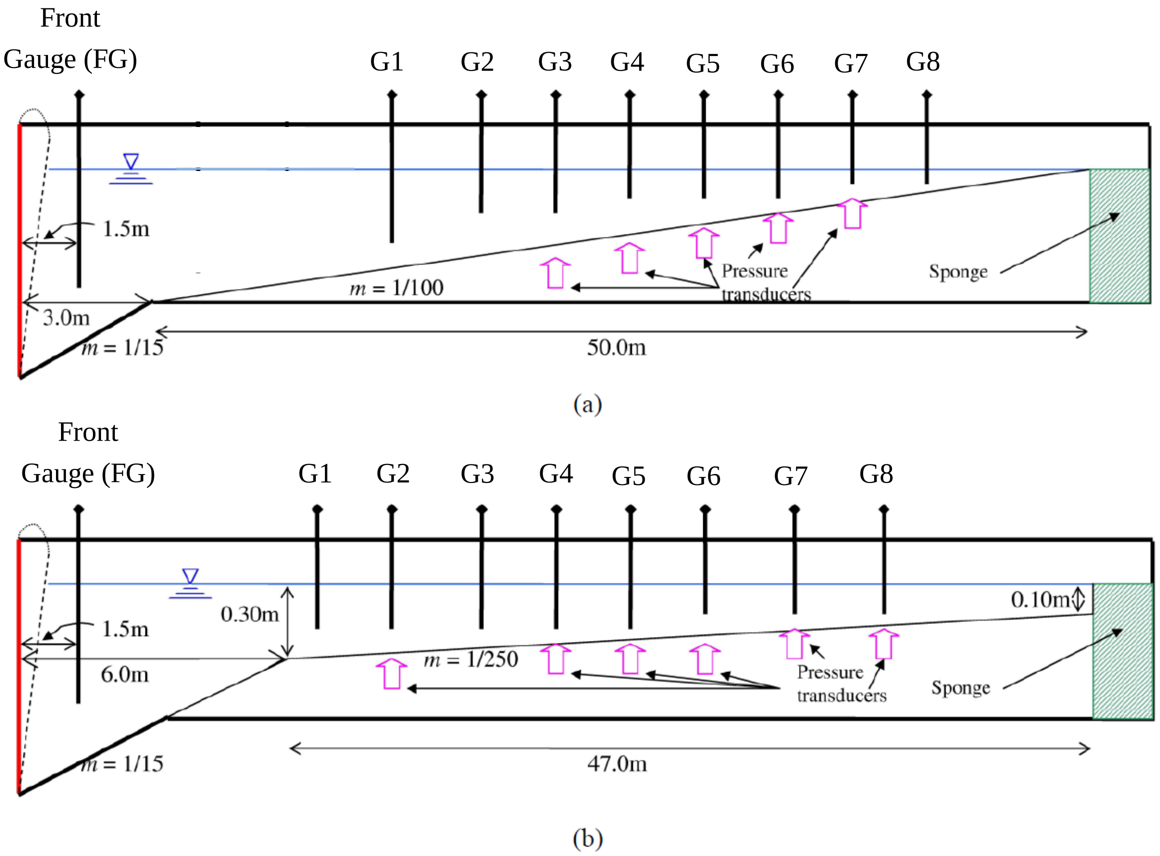

Figure 2.2: Longitudinal layout of the wave flume with a) 1:100 and b) 1:250 bed slope, showing the position of the wave gauges.

2.3 Wave Input Conditions and Tank Geometry

The depth of water in the wave flume varied according to the bed slope. Three bed slopes were considered; namely 1:100, 1:250 and constant depth of 0.3 m. The wave spectrum input was chosen to simulate a realistic deep water ocean spectrum bearing in mind that wave breaking would be likely to occur throughout the wave flume. For the present analysis, there are three parameters of the spectrum input which are important;

i) Peak period, T_p

ii) JONSWAP peak enhancement factor, γ

iii) Deep water significant wave height, H_{so}, recorded at the Front Gauge (1.5 m from the wave paddle)

26 test cases with different values of the input parameters were configured to produce the different wave conditions. In each test case, 8 separate runs were undertaken with 256 s of data acquired during each run. The data sampling frequency was 128 Hz. This gave a total data series of 2048 s duration, containing between 1200 to 1700 wave cycles. The test cases were used to examine the effects on the wave field of varying water depth, peak period, spectral bandwidth (peak enhancement factor), wave steepness and bed slope. Tables 2.1 to 2.7 summarise the test cases and the values of non-dimensional water depth (using wavenumber, *k*) with corresponding bed slopes and spectral periods.

Table 2.1: Input wave conditions for cases involving a bed slope of 1:100

Sea State	Spectral Shape	T_p (s)	γ	H_{so} (mm)
1a 1b	JONSWAP	1.2	2.5	96.0 120.2
2a 2b	JONSWAP	1.5	1.0	88.5 126.8
3a 3b 3c 3d 3e	JONSWAP	1.5	2.5	11.2 29.2 83.3 102.9 121.3
4a 4b	JONSWAP	1.5	5.5	106.7 120.8
5	JONSWAP	1.8	2.5	174.7
6a 6b	LOG-NORMAL	1.5	-	74.2 101.3

Table 2.2: Input wave conditions for cases involving a bed slope of 1:250

Sea State	Spectral Shape	T_p (s)	γ	H_{so} (mm)
1b	JONSWAP	1.2	2.5	119.1
2b	JONSWAP	1.5	1.0	125.5
3e	JONSWAP	1.5	2.5	122.2
4b	JONSWAP	1.5	5.5	119.5
5	JONSWAP	1.8	2.5	175.6
6b	LOG-NORMAL	1.5	-	100.0

Table 2.3: Input wave conditions for cases involving a constant depth, d = 0.30m

Sea State	Spectral Shape	T_p (s)	γ	H_{so} (mm)
1b	JONSWAP	1.2	2.5	120.0
2b	JONSWAP	1.5	1.0	111.7
3e	JONSWAP	1.5	2.5	128.9
4b	JONSWAP	1.5	5.5	128.2
5	JONSWAP	1.8	1.8	111.0
6b	LOG-NORMAL	1.5	-	101.8

Table 2.4: Non-dimensional still water depths at wave gauges for random waves with spectral peak period of 1.2 s over 1:100 bed slope

Gauge	FG	1	2	3	4	5	6	7	8
d(m)	0.60	0.40	0.35	0.30	0.25	0.20	0.15	0.10	0.05
k(m^{-1})	2.96	3.24	3.38	3.56	3.77	4.10	4.67	5.47	7.65
kd	1.78	1.30	1.18	1.06	0.95	0.83	0.69	0.56	0.38

Table 2.5: Non-dimensional still water depths at wave gauges for random waves with spectral peak period of 1.5 s over 1:100 bed slope

Gauge	FG	1	2	3	4	5	6	7	8
d(m)	0.60	0.40	0.35	0.30	0.25	0.20	0.15	0.10	0.05
k(m^{-1})	2.10	2.40	2.53	2.69	2.88	3.16	3.64	4.29	6.07
kd	1.26	0.96	0.88	0.80	0.73	0.64	0.54	0.44	0.30

Table 2.6: Non-dimensional still water depths at wave gauges for random waves with spectral peak period of 1.2 s over 1:250 bed slope

Gauge	FG	1	2	3	4	5	6	7	8
d(m)	0.60	0.29	0.27	0.25	0.23	0.21	0.19	0.17	0.15
k(m^{-1})	2.96	3.58	3.67	3.77	3.90	4.02	4.18	4.39	4.60
kd	1.78	1.05	1.00	0.95	0.90	0.86	0.81	0.75	0.71

Table 2.7: Non-dimensional still water depths at wave gauges for random waves with spectral peak period of 1.5 s over 1:100 bed slope

Gauge	FG	1	2	3	4	5	6	7	8
d(m)	0.60	0.29	0.27	0.25	0.23	0.21	0.19	0.17	0.15
k(m^{-1})	2.10	2.71	2.79	2.88	2.99	3.09	3.23	3.41	3.58
kd	1.26	0.79	0.76	0.73	0.69	0.66	0.62	0.58	0.55

2.4 Surface Elevation Time History

Figure 2.3 shows a typical series of time histories at different gauge locations. It can be seen that, as the wave shoals from deep water to shallow water, there is a reduction in crest height and trough height. Vertical wave asymmetry becomes more evident with the sharpening of crests and broadening of troughs as the waves shoal. In shallow water (Gauge 8 with *kd* of 0.38), the number of crests decreases and each appears to behave more like a solitary or bore-like wave. From now on, examples will be shown for Case 1a1100 (Case 1a with 1:100 slope), unless stated otherwise.

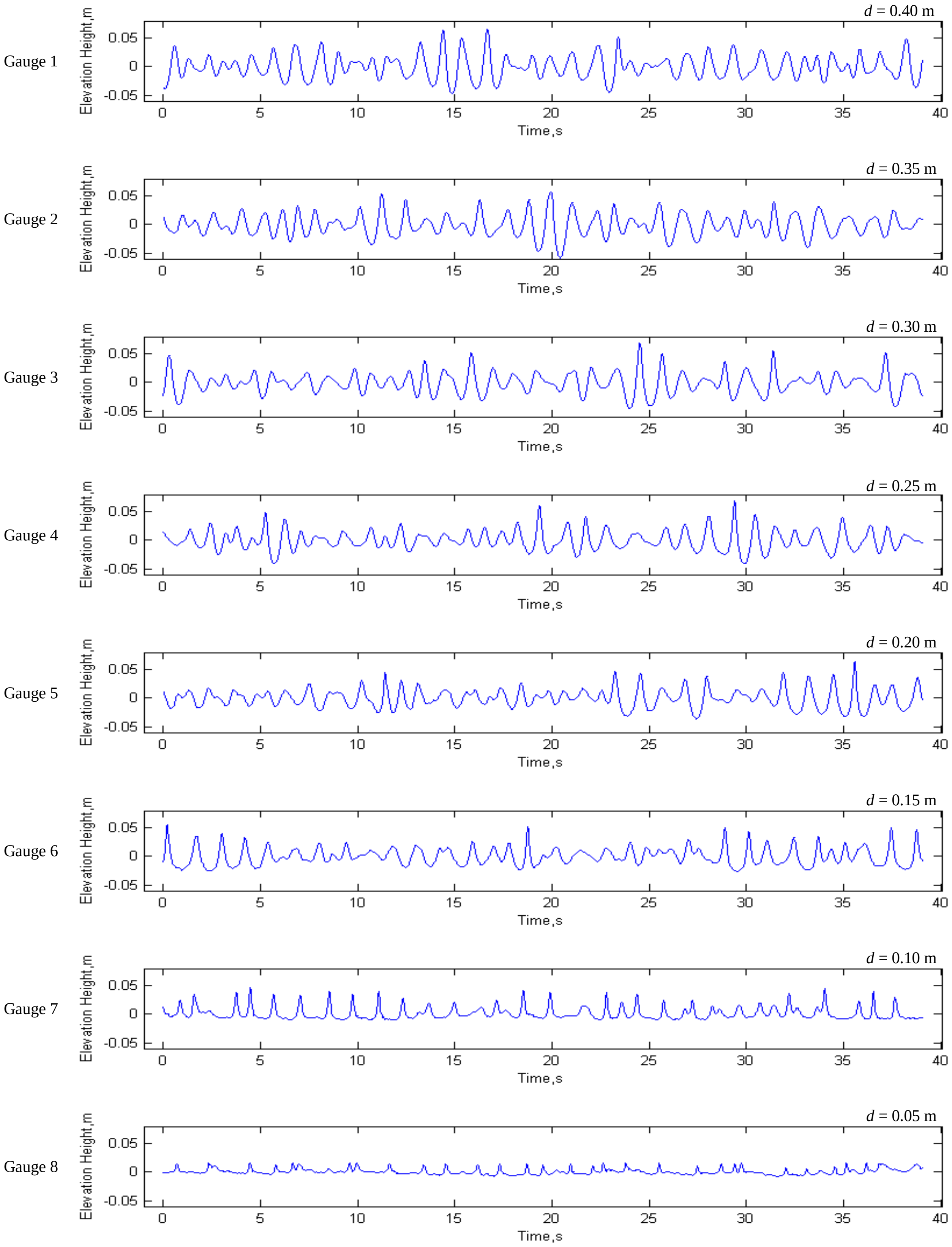

Figure 2.3: Surface elevation time history of Case 1a with 1:100 bed slope at different wave gauges (in progressively shallow depth from Gauge 1 to Gauge 8).

2.5 Detailed Analysis

The averaged top 10 %, averaged top 2 % and the maximum of ‘crest’ surface elevation and ‘trough’ surface elevation are now considered for further analysis. Only the top 10 % of Case 1a1100 is examined in detail here, but all the different classifications will be discussed later in Section 2.6.

2.5.1 ‘Crest’ and ‘Trough’ Surface Elevation

The largest 10 % crest elevations are identified in the record, and in each case the portion of wave history 5 s before and after the peak is extracted in order to examine the average shape near the large crest. The time is then re-set for every case such that each large crest occurs at zero relative time (t-tc). All the crests are then aligned together and the profile averaged over the total number of cases. The same procedure is then repeated for the deepest troughs.

Figure 2.4 shows that the shapes of all of the waves considered are almost the same during the time from 1 s before to 1 s after the crest. Further from the crest, the individual shapes are distributed randomly. Sharpening of crest and broadening of troughs can also be seen as the waves propagate into shallow water. At Gauge 8, there is a definite crest height limiting criterion and also a loss of symmetry in the horizontal direction. Figure 2.5 shows the averaged ‘crest’ surface elevation over time which also includes the time-reversed data series (used to examine temporal asymmetry). As the waves propagate from deep into shallow water, the horizontal asymmetries increase due to non-linear effects. Note the reduced troughs at Gauge 7 and the saw-tooth shaped crest with troughs virtually having disappeared at Gauge 8. The same processes are evident in the trough elevations shown in Figure 2.6 and Figure 2.7.

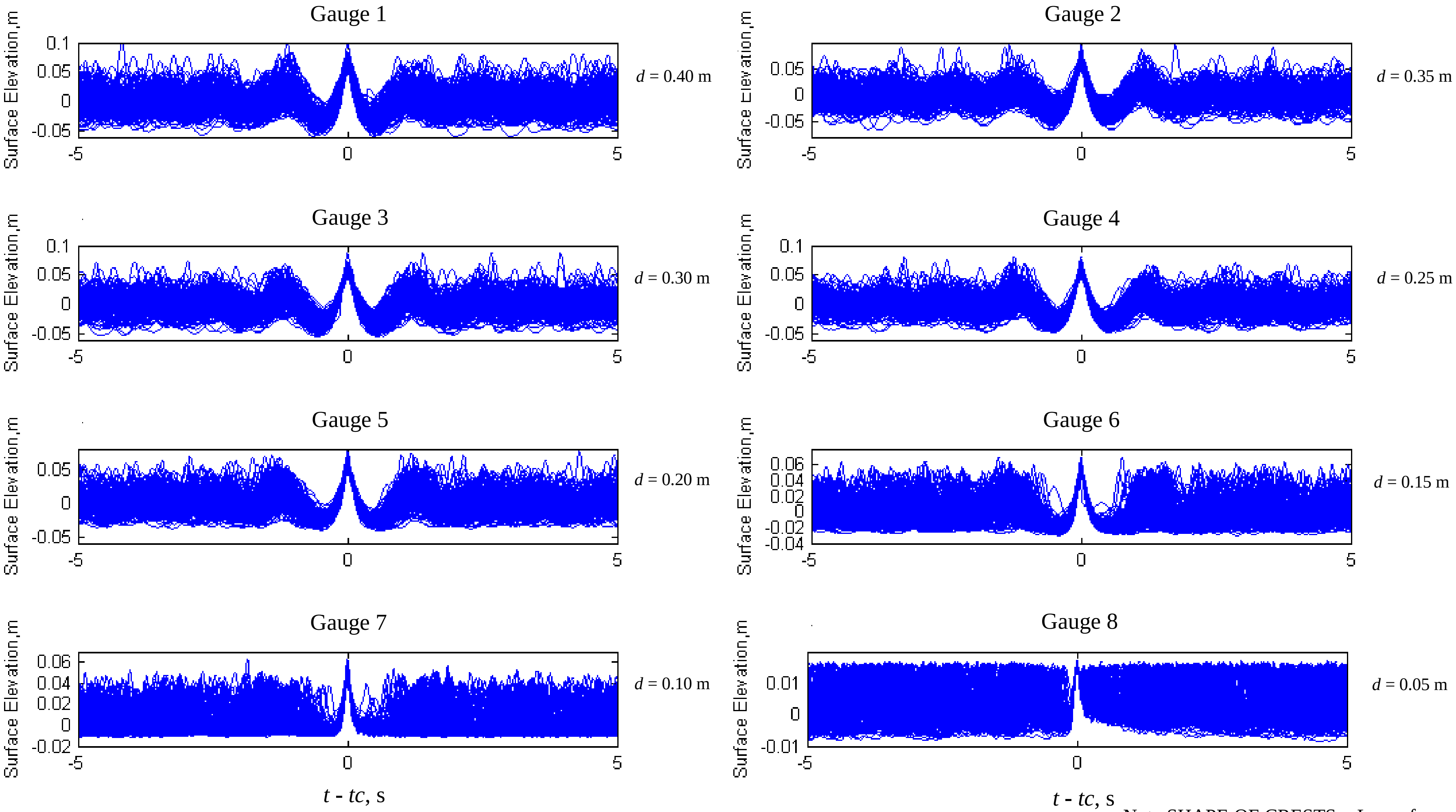

Note SHAPE OF CRESTS – Loss of symmetry
and saturation of peak crest elevation

Figure 2.4: Top 10 % **'crest'** surface elevation vs time (t - tc) for Case 1a1100

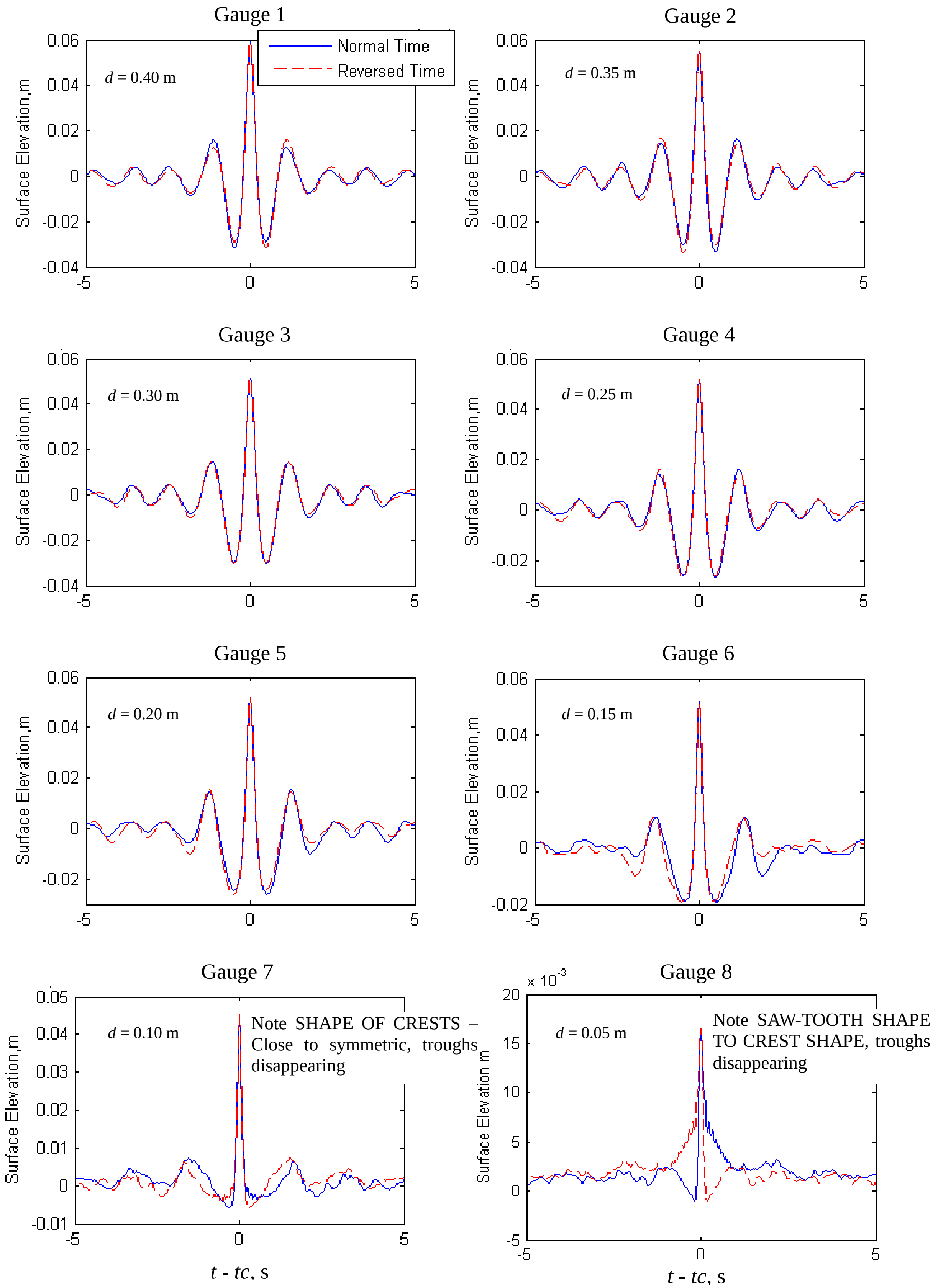

Note SHAPE OF CRESTS – Close to symmetric, troughs disappearing

Note SAW-TOOTH SHAPE TO CREST SHAPE, troughs disappearing

Figure 2.5: Top 10 % **‘crest’** averaged surface elevation vs time (*t* - *tc*) for Case 1a1100 overlapped with reversed time

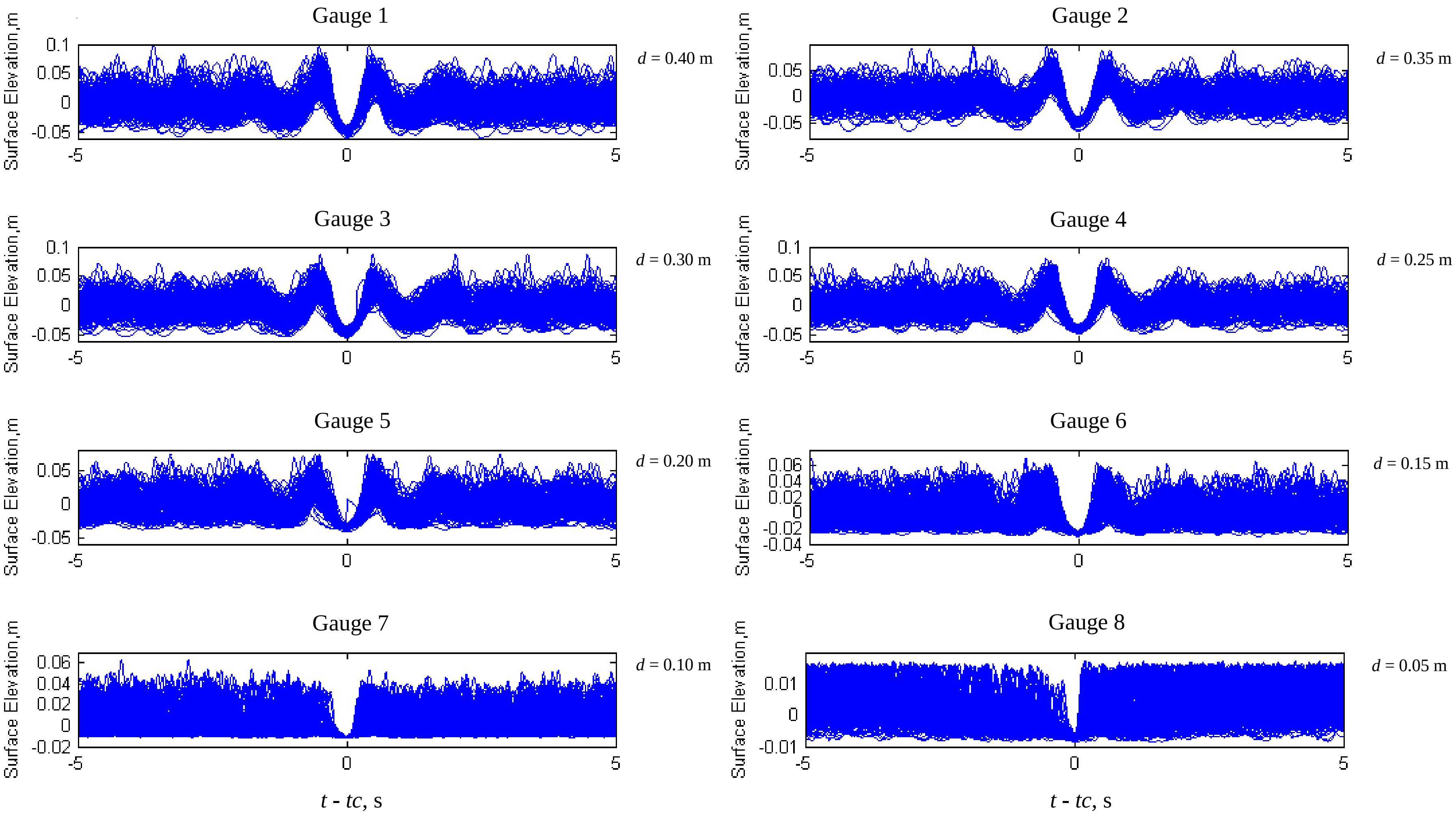

Note saturation of crest elevation, troughs disappearing

Figure 2.6: Top 10 % ‘**trough**’ surface elevation vs time (*t* - *tc*) for Case 1a1100

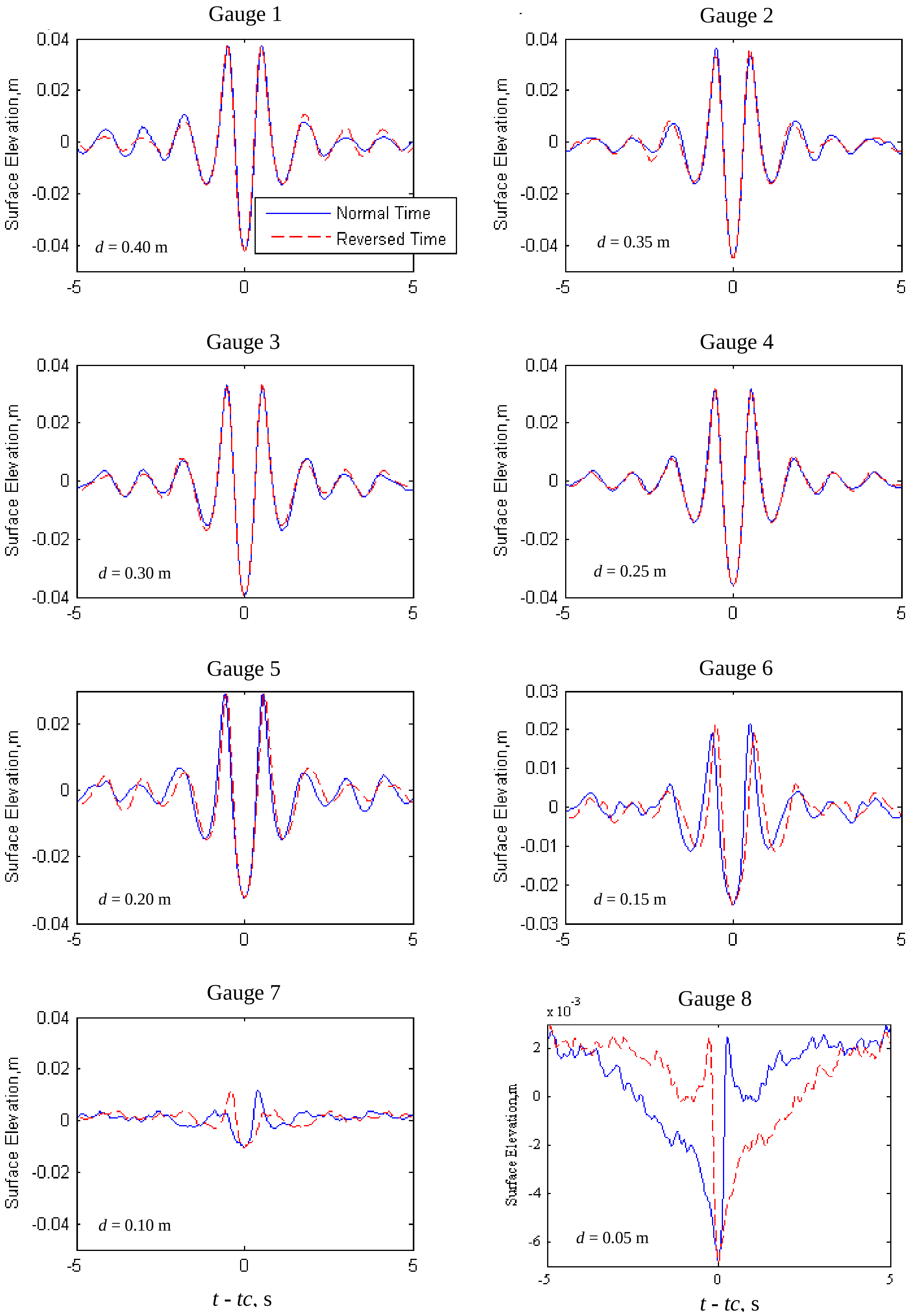

Figure 2.7: Top 10 % **‘trough’** averaged surface elevation vs time (*t* - *tc*) for Case 1a1100 overlapped with reversed time

2.5.2 Linear and Second Order Term Surface Elevation

Applying Stokes water wave expansion theory to the combination of expansions centred at a crest and at a trough, the combination [η_c - η_t]/2 leaves only the odd harmonics (dominated by the linear term) whereas [η_c + η_t]/2 contains the even harmonics (dominated by the second order terms), as shown in Equations (2.1) to (2.4).

$$\eta_c = S_0A^2\cos(0) + A\cos(\omega t) + S_2A^2\cos(2\omega t) + S_3A^3\cos(3\omega t) + ... + S_nA^n\cos(n\omega t) \tag{2.1}$$

$$\eta_t = S_0A^2\cos(0) - A\cos(\omega t) + S_2A^2\cos(2\omega t) - S_3A^3\cos(3\omega t) + ... + S_nA^n\cos(n\omega t) \tag{2.2}$$

$$\frac{\eta_c - \eta_t}{2} = A\cos(\omega t) + S_3A^3\cos(3\omega t) + ... + S_{n-1}A^{n-1}\cos((n-1)\omega t) \tag{2.3}$$

$$\frac{\eta_c + \eta_t}{2} = S_0A^2\cos(0) + S_2A^2\cos(2\omega t) + ... + S_nA^n\cos(n\omega t) \tag{2.4}$$

where A is the wave amplitude, ω is the wave angular frequency, n + 1 is the number of terms (counting from the difference term which for a regular wave has zero frequency) and the coefficients S_n determine the magnitude of the components. Notice that a zero frequency term (mean shift) is included, as this idea of combining crest and trough centred signals is in practice here applied to the broad banded signals i.e. random waves rather than regular waves.

η_c is taken to be the average surface elevation time series for the largest crests (i.e. largest 10 %) while η_t is the average surface elevation time history for the largest troughs, as explained in Section 2.5.1. The first combination of the average large crest and trough profile is shown in Figure 2.8. It can be seen that the odd harmonics separation (‘linear term’) works well up to Gauge 6 where the asymmetry starts to become apparent and increases in shallower water. It is important to look at the effect of the contribution from the even harmonics; dominated by second order terms. It can be seen in Figure 2.9 that the period taken from trough to trough along the crest is halved compared to the odd harmonics. Also seen is a set-down term in deeper water (the troughs either side of the crest are larger than the crest itself); a wave group rides in a hole of its own making (see Figure 3.4a of Section 3.3.2). Note also the loss of symmetry when breaking starts.

Further examination of Figure 2.9 shows that there is an increase in the peak values for the even harmonics from Gauge 2 to Gauge 7 (the gauge just before the waves are finally broken). The increment of the even harmonics between gauges demonstrates the increasing non-linearity as the wave group propagates to shallow water. The rate of increment of the even harmonics is the largest between Gauge 6 to Gauge 7 (about 5 x 10^{-3} m per gauge when compared to an average of 2 x 10^{-3} m per gauge for the previous gauges) as near-breaking waves are highly non-linear. Likewise, the ratio of second order terms to linear order terms increases when the waves propagate from deep water to shallow water, due to increasing non-linearity.

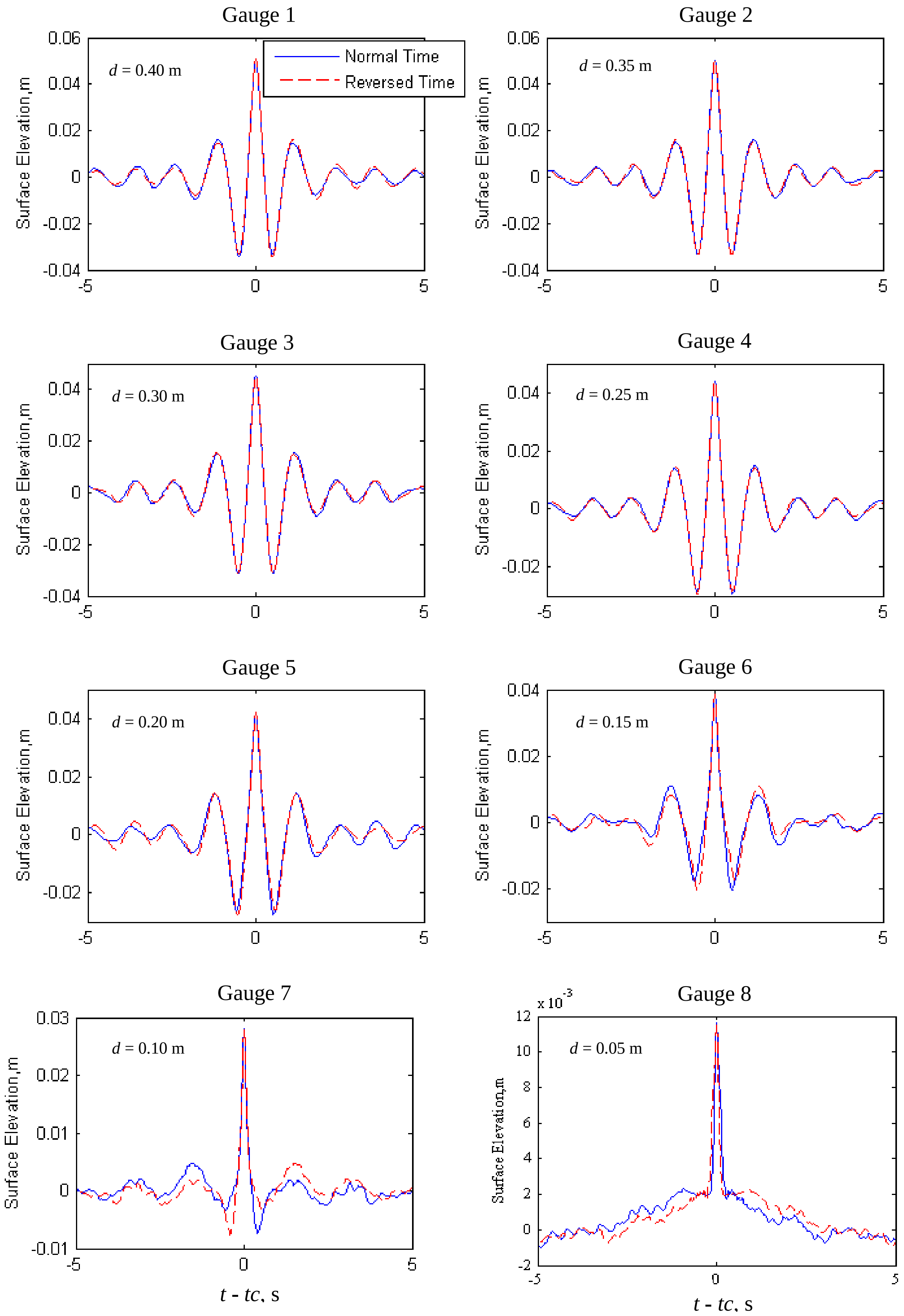

Figure 2.8: Top 10 % averaged [η_c - η_t]/2 surface elevation vs time (t - tc) for

Case 1a1100

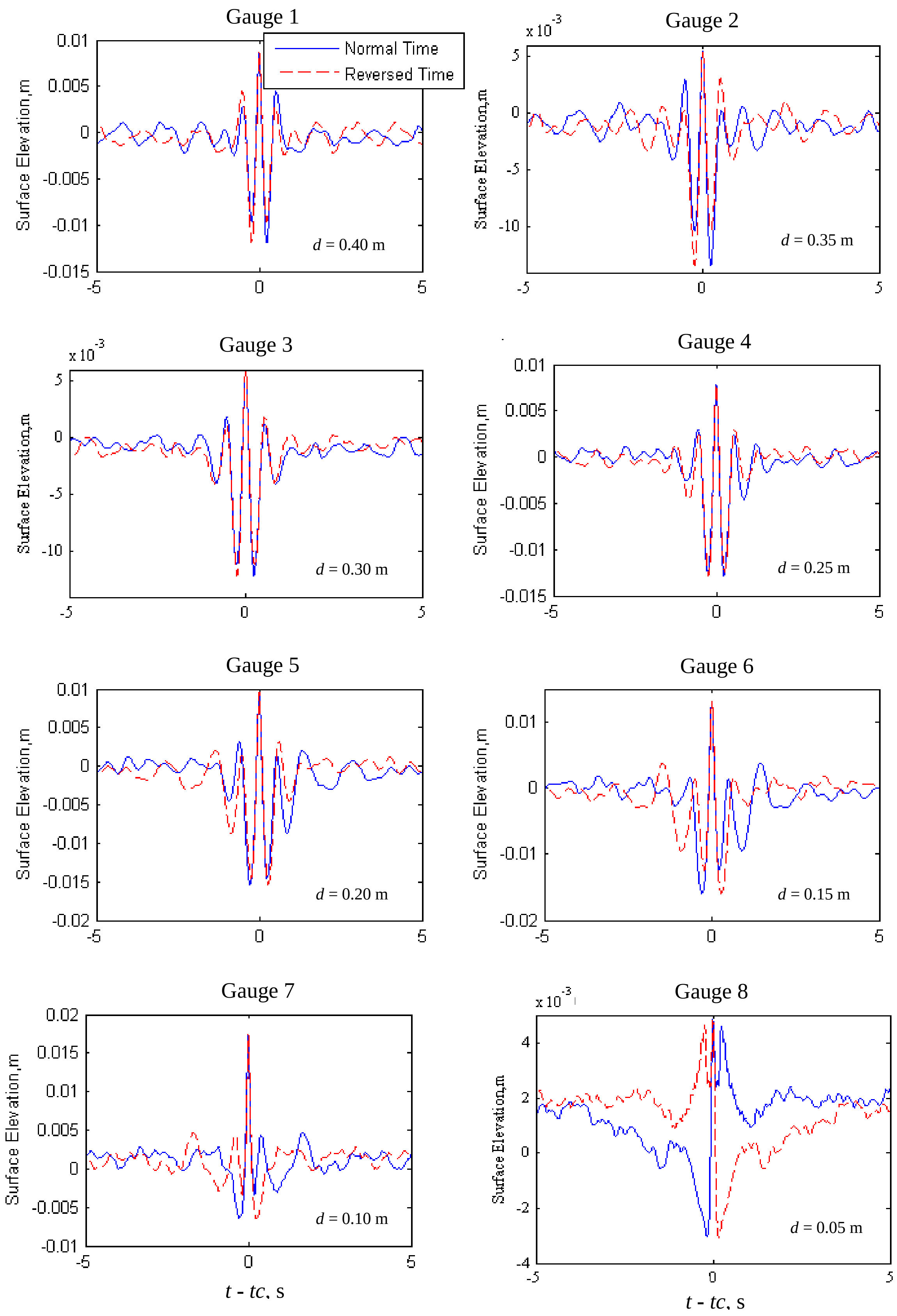

Figure 2.9: Top 10 % averaged [$\eta_c + \eta_t$]/2 surface elevation vs time (t - tc) for

Case 1a1100

2.6 General Overview of the Results for the Largest Waves

The maximum crests, troughs and wave heights have been extracted from all the test cases and plotted against the water depth, as have their non-dimensional counterparts. The results are compared for a few cases so that the overall behaviour of the waves can be seen clearly. Results for the largest individual crest anywhere in the record at each gauge, and the averages of the top 2 % largest (30 - 40 waves) and top 10 % largest (150 - 200 waves) will be presented.

Figure 2.10 shows the variation of maximum crest elevations for Case 3a1100-3e1100 over water depth on the slope. Here, the variation in elevation with water depth remains small down to a water depth of 0.1 m. A sudden drop in values for Cases 3b and 3c from about 0.05 m crest elevation to 0.017 m indicates that there is a limiting crest elevation criterion at a water depth of about 0.05 m. Furthermore, for all cases the values of the crest height at that water depth of about 0.05 m almost converge to a single value. This condition can be partly seen at Gauge 8 in Figure 2.4 where the wave height starts to saturate. Analysis from Section 3.5 for Case 1bflat (constant water depth) provides evidence that friction does not play an important role in the limiting criteria of crest height.

The reduction in crest elevation is also clear for the middle (top 2%) and bottom (top 10%) plots of Figure 2.10. As would be expected, the averaging reduces the point to point variability, making the overall downward trend of wave elevation with reducing water depth more evident.

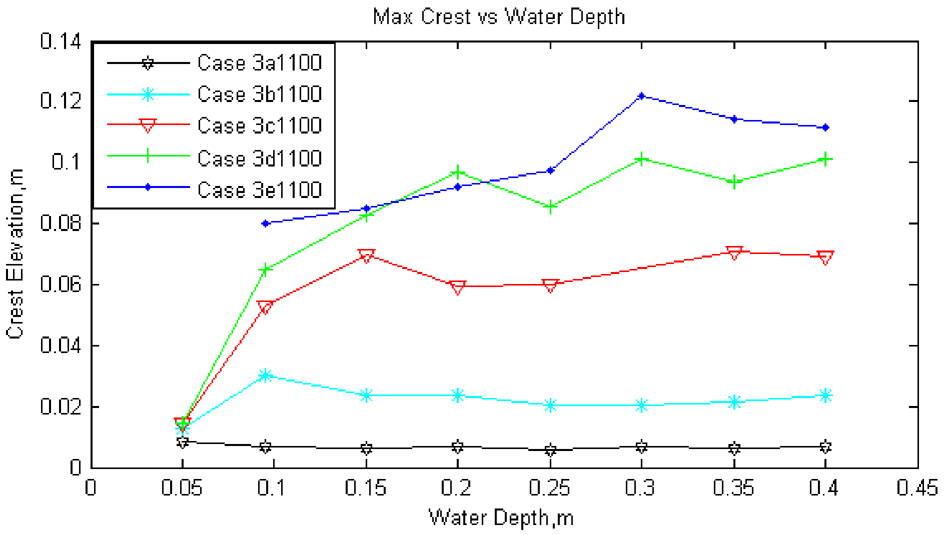

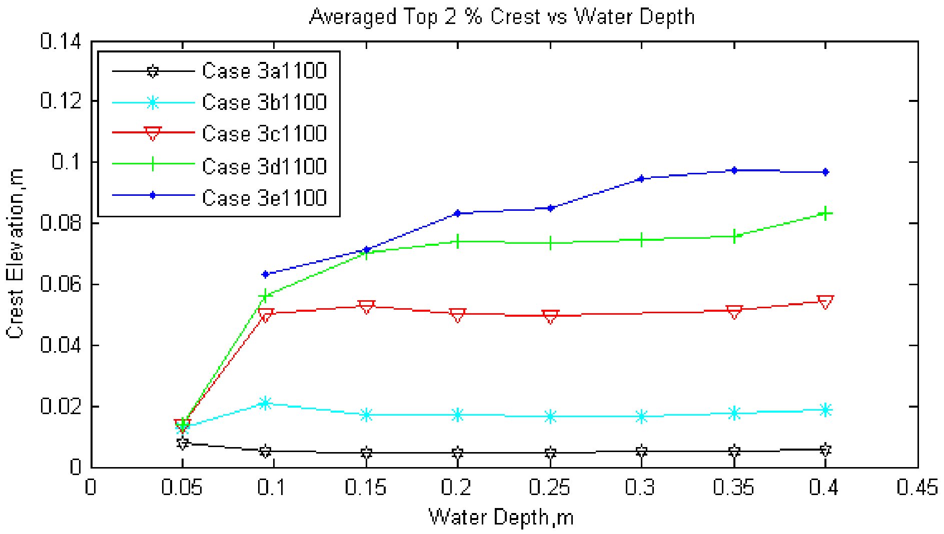

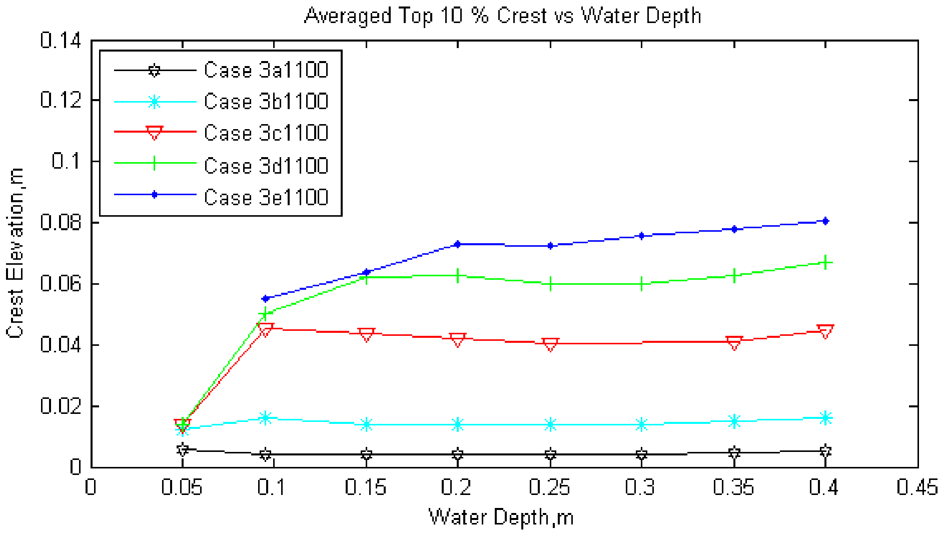

Figure 2.10: Maximum crest elevations along the wave flume

Figure 2.11 shows the variation of the maximum magnitudes of trough elevations against water depth on the slope (and the averaged top 2 % and 10 %) where the trough elevation reduces linearly from deep water to shallow water. This suggests that the troughs reduce more smoothly than the crests in deeper water. This holds true as the wave moves from deep water to shallow water, owing to non-linearity which makes the wave asymmetric, with steeper crests and broader and smaller troughs. The same global behaviour is noted for the shallowest water depths, with the maximum elevation of the troughs approaching a common value in all cases.

Figure 2.12 of maximum wave height against water depth shows that the trend in wave height is similar to that in crest elevation. This is because the troughs reduce over a wider range of depths compared to the crests as the waves shoal. Note that the maximum wave height here is the maximum height between the trough and corresponding following crest in a surface elevation time history (not by pairing the maximum crest in the record with the maximum trough at an entirely different time in the time series).

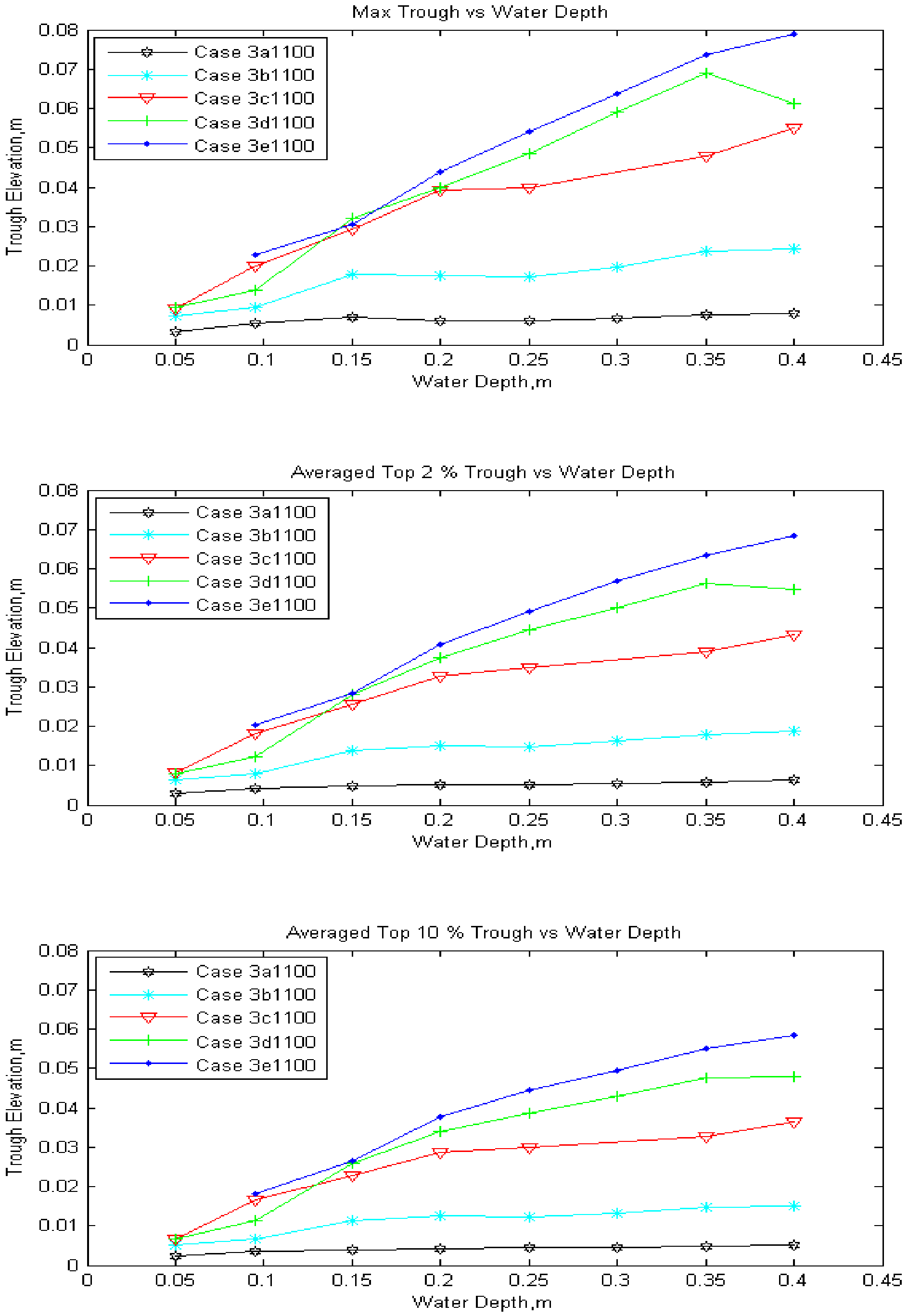

Figure 2.11: Maximum magnitudes of trough elevations along the wave flume

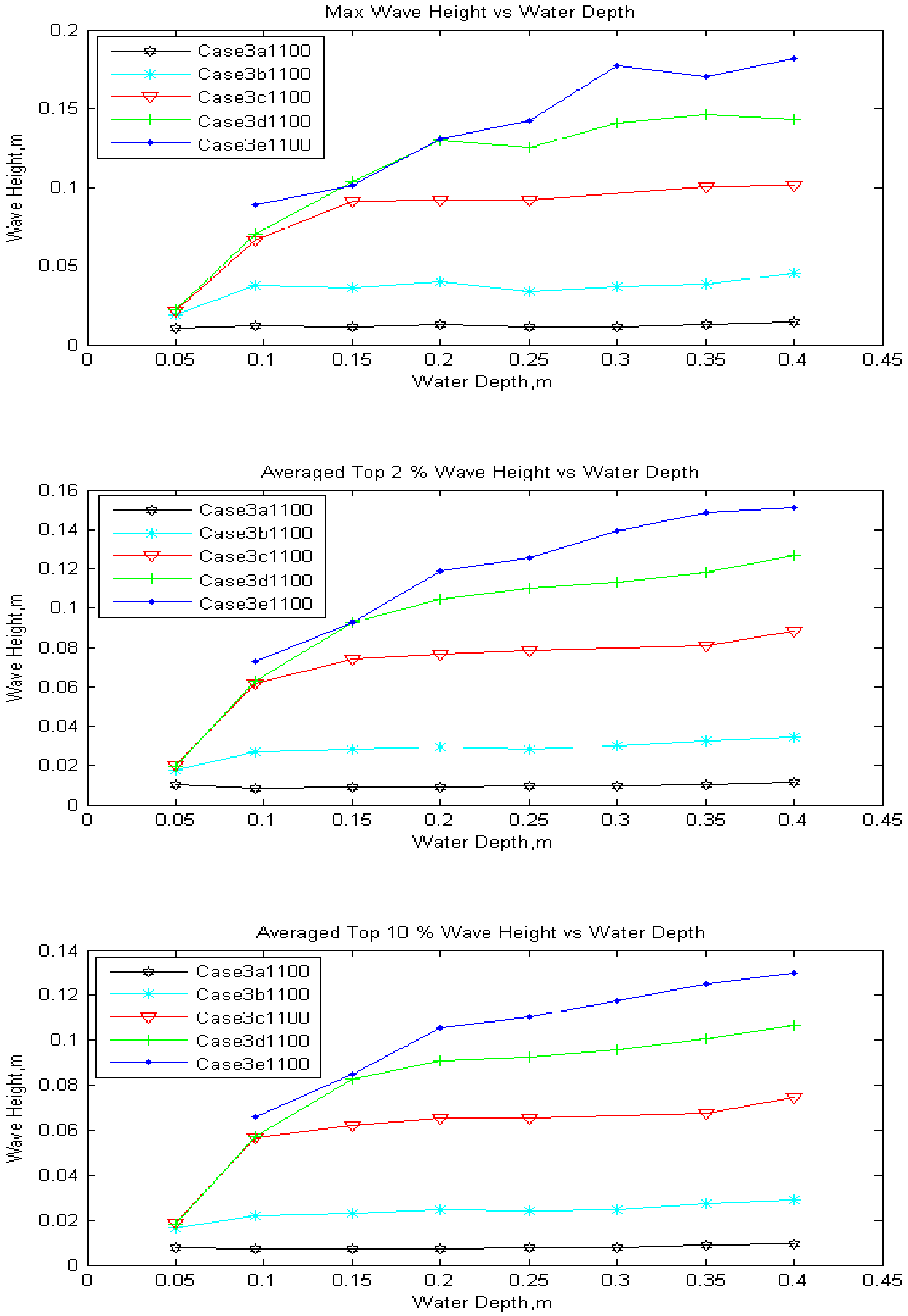

Figure 2.12: Maximum wave heights along the wave flume

Figure 2.14 and Figures 2.15a show plots of the non-dimensional maximum crest elevations ($\eta_c k_p$), and wave heights (Hk_p) against non-dimensional water depth ($k_p d$). Here, the values for both the non-dimensional maximum crest elevations ($\eta_c k_p$), and wave heights (Hk_p) at each cases tend to approach one another as compared to the dimensional crest elevations and wave heights in the previous figures. This should hold true as most of the important factors (for example the water depths, wave numbers and wave periods) have been considered for a wave propagating from deep water to shallow water. However, the significant wave height (H_{so}) and the immediate change of slope were not taken into account in the non-dimensional form. This is the reason why the smallest amplitude Case 3a1100 has values far below that of the other cases. This sea-state simply is not energetic enough to produce depth limited individual waves.

The sudden change in value for the peak crests in both Case 1b1250 (at $k_p d \approx 1$) and Case 3e1250 (at $k_p d \approx 0.8$) at the second gauge signals that the sudden change from a 1:15 slope to the 1:250 slope (as shown in Figure 2.2b) affects the surface elevation values locally as a local overshoot in wave height. The effect is not visible in cases of 1:100 slope because the deepest water gauge used in the data analysis is 10 m inshore of the step change, so the wave field has apparently become adapted to the uniform shallow slope. Gauge 1 and Gauge 2 for case 1:250 slope are only 2.5 and 7.5 m away from the step change. This suggests that there might be an overshoot also for case 1:100 bed slope before Gauge 1, but there are no data available to confirm this.

In the field, waves are irregular and there is a distribution of wave heights and wave periods (Smith, 1999), instead of regular waves which form the basis for the Miche limiting criterion. Equation (2.5) gives a modified Miche limiting criterion as proposed in the Lowish study (see Katsardi et al., 2013 for further information on the Lowish experiment). A constant of 0.12 is applied instead of 0.142 for the Miche limiting criterion because it gives a better result when applied to the experimental data. As has been shown in Gauge 7 and Gauge 8 of Figure 2.4, there is a limiting wave height at these two spatial points and Figure 2.15 shows that the modified limiting criteria gives a better representation of the wave height limit for these waves. In deep water, the equation reduces to a maximum wave steepness $H_{max}/\lambda = 0.12$, and in shallow water, it reduces to a maximum height-to-depth ratio $H_{max}/d = 0.76$.

$$H_{max} = 0.12\,\lambda \tanh kd \tag{2.5}$$

where H is wave height, λ is wavelength, k is wave number and d is water depth.

Figure 2.15a is plotted by non-dimensionalising the maximum wave height and water depth using the wavenumber (k_p) based on deep water spectral peak period T_p. Figure 2.15b is plotted by non-dimensionalising the maximum wave height and water depth using the wavenumber (k_{NW}) based on zero down-crossing period of the local NewWave group (T_{NW}), where NewWave (NW) is an analytical model which describes the profile of large wave events near a crest in a specified sea-state. NW is obtained by scaled auto-correlation function of the original time history. It has to be stressed that the local NewWave is based on the local spectrum at each water depth. The change in wavenumber from deep water spectral peak period to zero down-crossing period of NewWave stretches the lines upward and to the right, with no significant effect on the modified Miche limit. All results are within the limit except for the case where the bed slope is 1:250 (where the wave height overshoots for reasons which have been explained previously) and also for a single point at the shallowest water depth Case 3e1100.

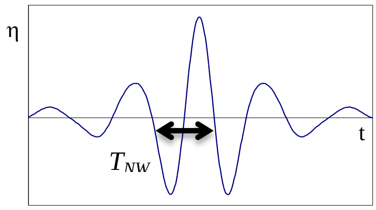

Figure 2.13: NewWave profile and the zero down-crossing period

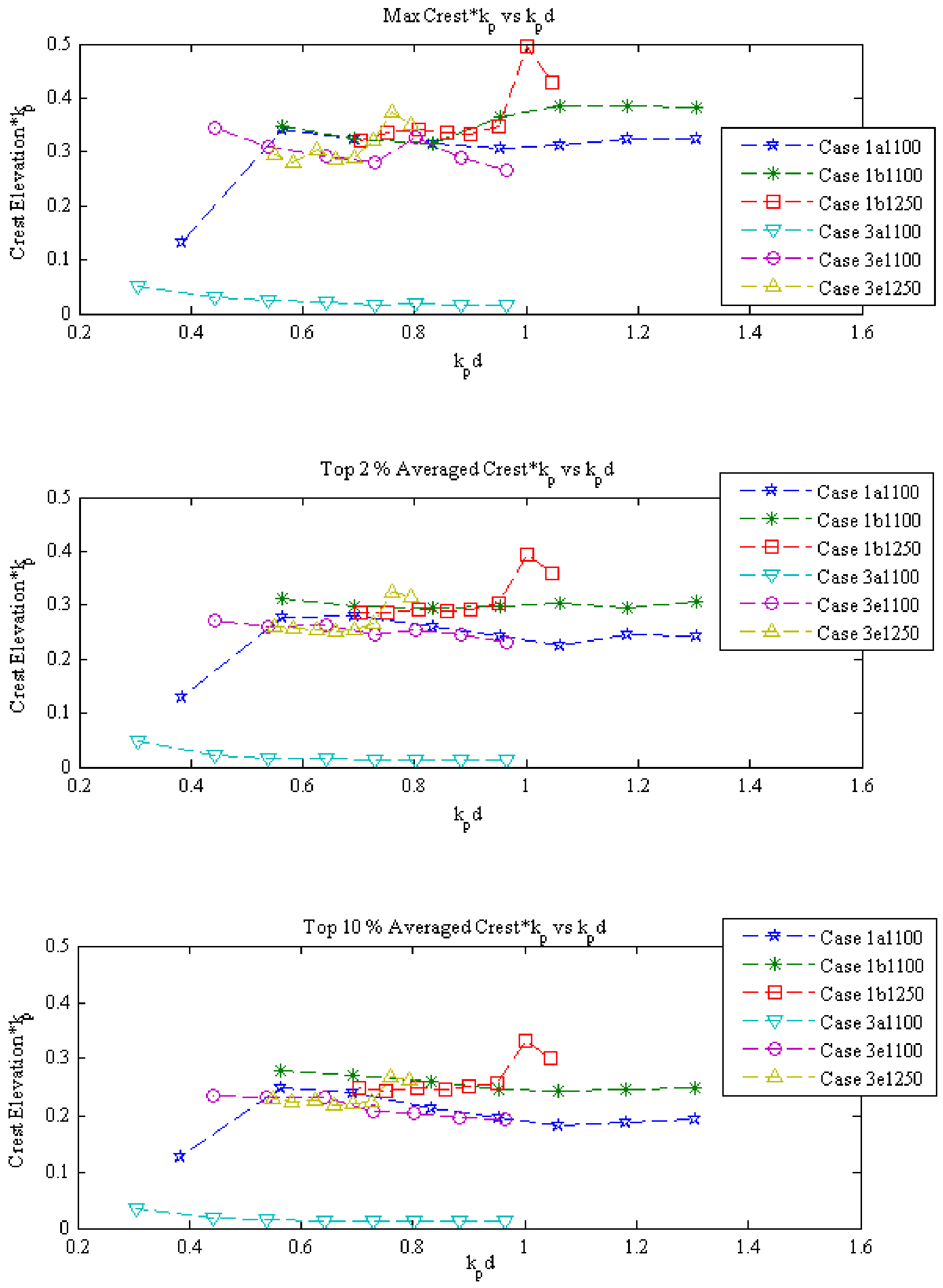

Figure 2.14: Non-dimensional maximum crest elevation against non-dimensional water depth

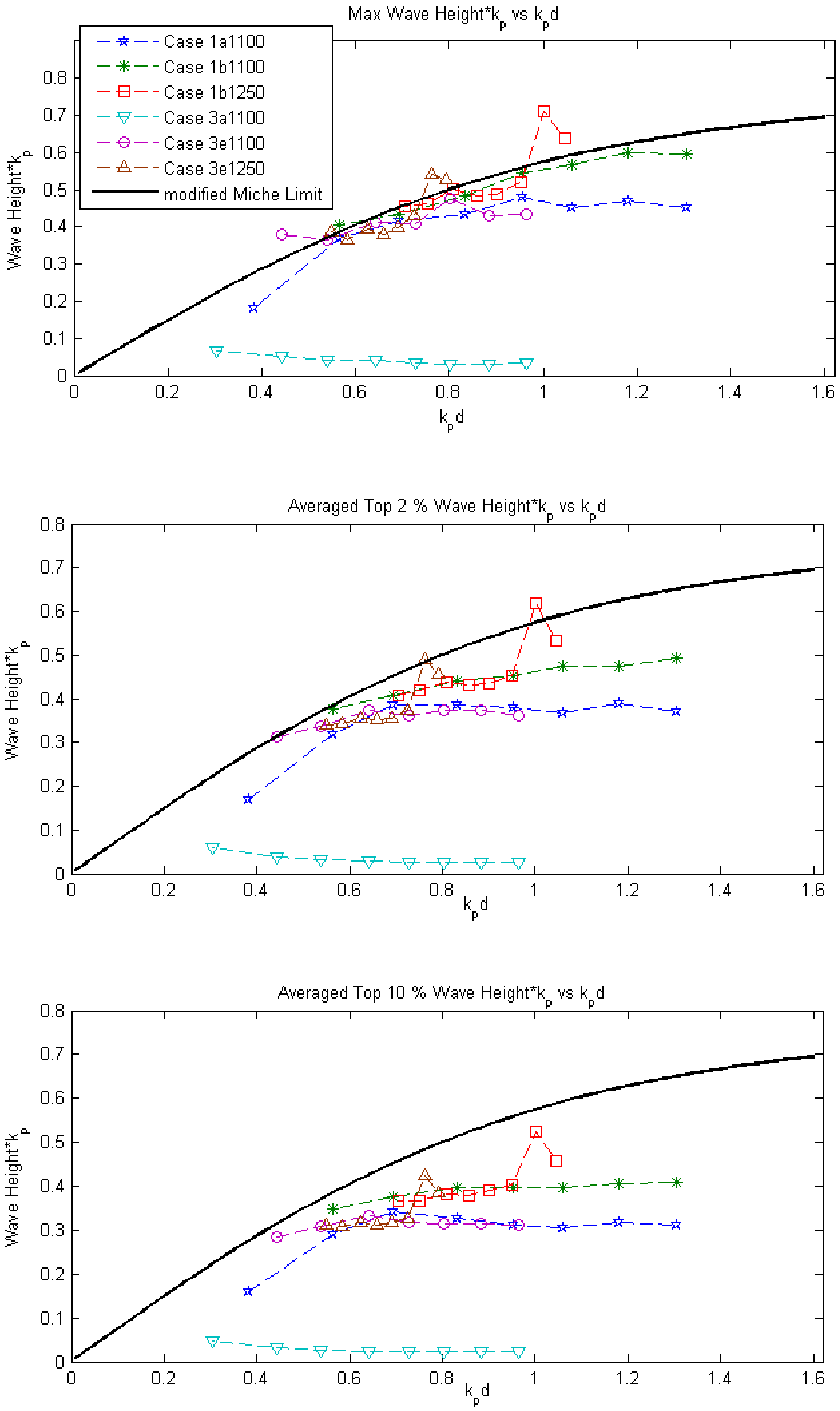

Figure 2.15a: Non-dimensional maximum wave heights (using k_p) against k_pd

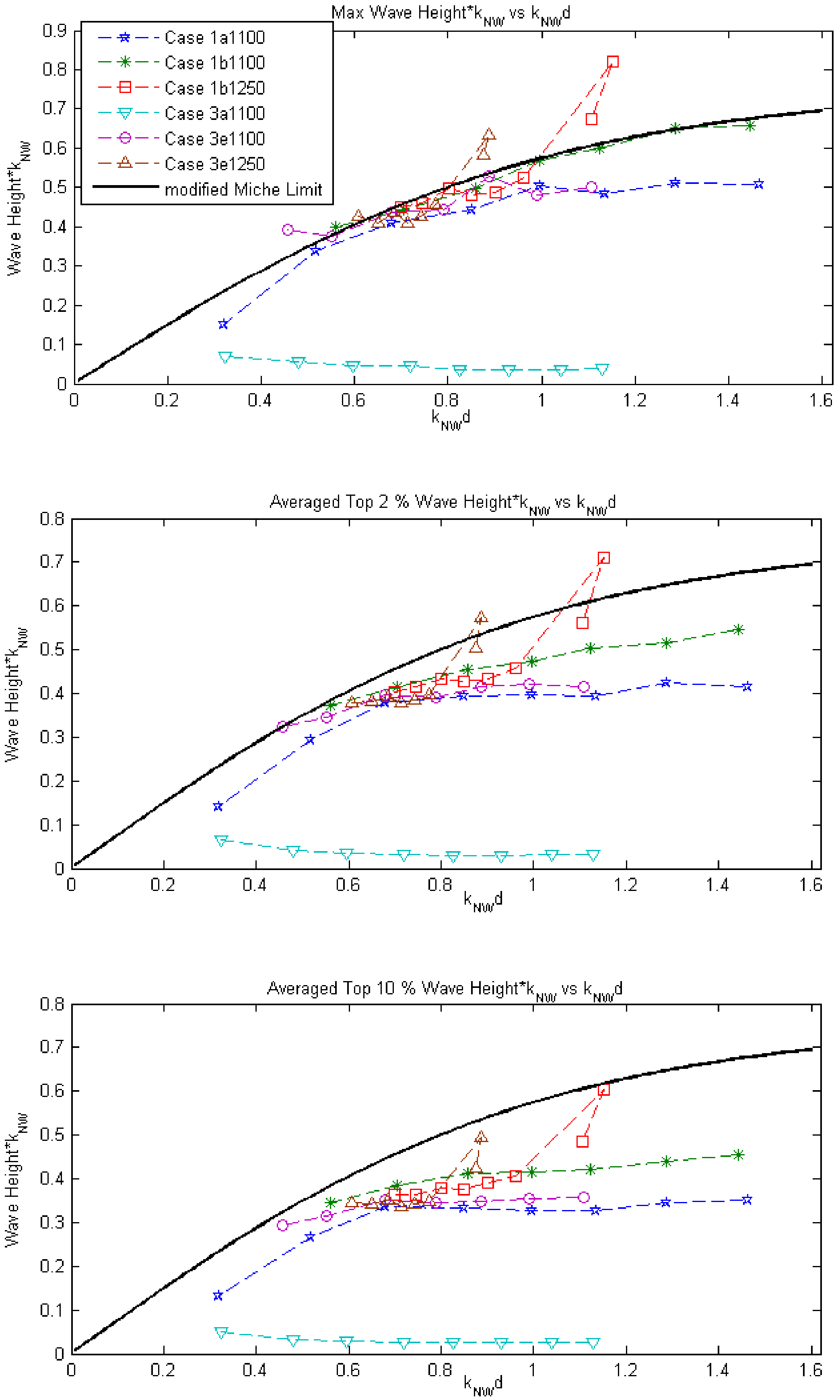

Figure 2.15b: Non-dimensional maximum wave heights (using k_{NW}) against $k_{NW}d$

2.7 Post-breaker Line (*kd* < 0.5)

Waves before breaking are frequency dispersive, with complications arising from wave group non-linearity, quadruplet wave-wave interactions and triad interactions in shallow water. Post-breaking, the frequency dispersion changes to amplitude dispersion and involves mostly triad interactions between waves. Crests become dominant (cnoidal theory for regular waves) and involve close to solitary wave interactions (which may be modelled with Boussinesq or Korteweg-de Vries (KdV) type equations). The energy dissipation through the wave breaking process is considerable and the breaking itself can have various forms from spilling through to violent plunging. Overall, for positions inshore of the main-breaker line, it seems likely that the non-linear shallow water equations (NLSWE) may be valid, and, with a shock-capturing NLSWE solver, this zone might be amenable to detailed analysis.

Figure 2.16 shows the surface elevation time history at 3 locations in the shallow water regime. There is a fast decay of wave height as the waves move inshore. Note also for the smallest depth the saw-tooth nature of the waves and how few crests there are.

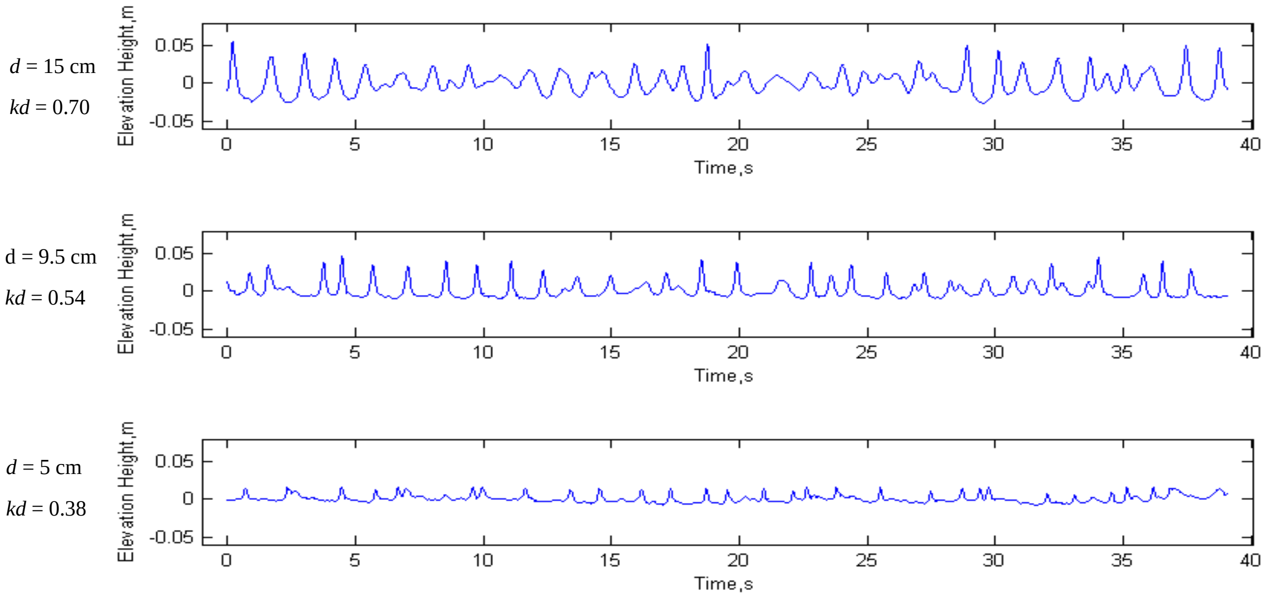

Figure 2.16: Surface elevation time history of Case 1a with 1:100 bed slope at shallow water.

The 20 largest crests and troughs (which is the top 10 % of the first run, as explained in Section 2.3) are superimposed at the midpoint of the time histories, as shown in Figure 2.17 and Figure 2.18. From Figure 2.17, there is clearly a saturation of maximum crest height for all three depths, particularly for the smallest depth (the last one). The data indicate that there is a fixed upper limit on elevation. Note the time asymmetry of the data for Gauges 7 and 8 (*kd* = 0.54 and 0.38) and also the vanishing of coherent wave troughs, which is shown clearly in Figure 2.18.

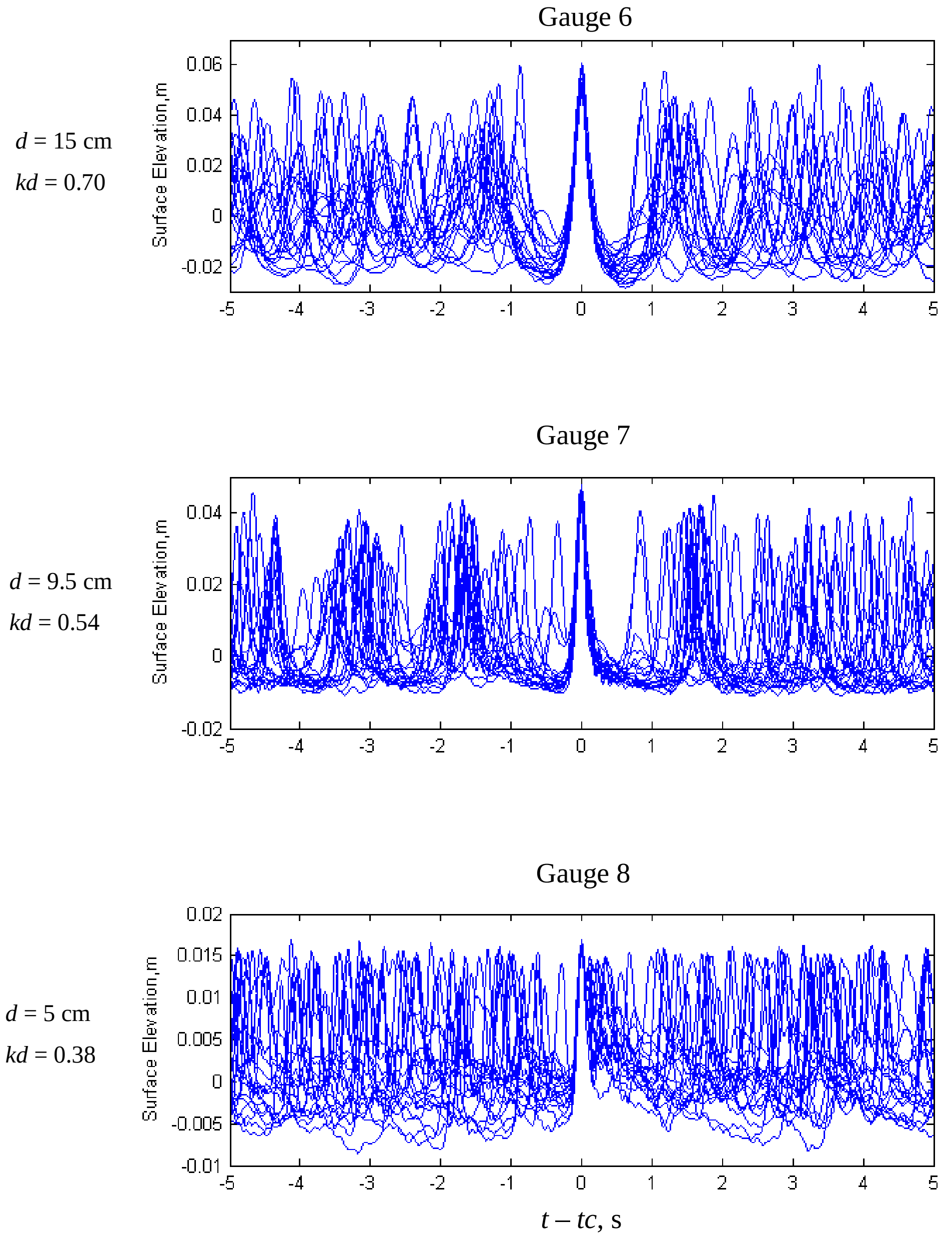

Figure 2.17: Top 20 ‘**crest**’ surface elevation vs time (t - tc) for Case 1a1100

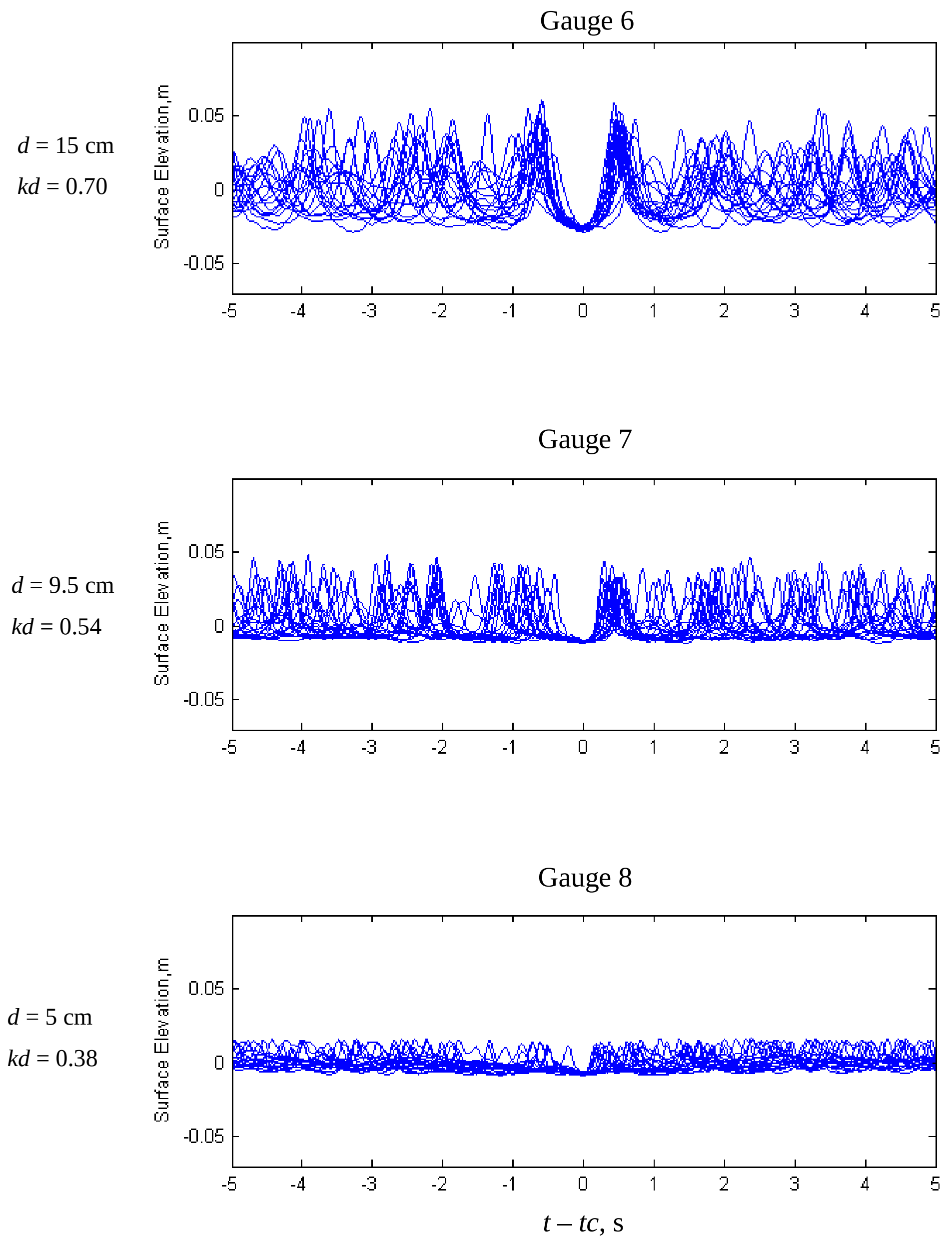

Figure 2.18: Top 20 **'trough'** surface elevation vs time (*t-tc*) for Case 1a1100

It should be noted that for $kd < 0.5$, the wave period becomes much less important as indicated by the shallow water limit of the modified Miche, $H/d = 0.754$ (independent of period). Note in passing that the shallow depth asymptotic form of the modified Miche criterion is:

$$\frac{H}{d} = 0.754\left(1 - \frac{(kd)^2}{3}\right) + \dots, \tag{2.6}$$

so for *kd* sufficiently small, the criterion is independent of the local depth.

2.7.1 Waves in Shallow Limit as a Succession of Uncorrelated Solitary Waves

Waves in the shallowest depths are fitted to individual solitary waves riding on a current. The simplest Korteweg-de Vries equation form for a solitary wave is

$$\eta = H * \mathrm{sech}^2\left[\frac{\sqrt{3}}{2}\left(\frac{H}{d^3}\right)^{1/2}(x - c't)\right] \tag{2.7}$$

$$c' = c_{sol} + u_c \tag{2.8}$$

$$c_{sol} = \sqrt{gd\left(1 + \frac{H}{d}\right)} \tag{2.9}$$

where H is the wave height, d is the water depth, c_{sol} is the solitary wave speed, and u_c is the assumed local current. Given the height of peak and the shape, the idea is to match the effective speed of assumed solitary wave, c'. Data from Case 3c1100 are considered here as an example. Figure 2.19 shows the solitary wave fit for the averaged shape of the top 20 ‘crest’ surface elevation while Figure 2.20 fits the largest individual wave elevation at each depth. It can be seen that the speed of the wave is larger than the solitary wave speed, and that this value varies. For *kd* below 0.3, the wave profiles take on a saw-toothed shape, and so the solitary wave model does not fit well in very shallow water situations.

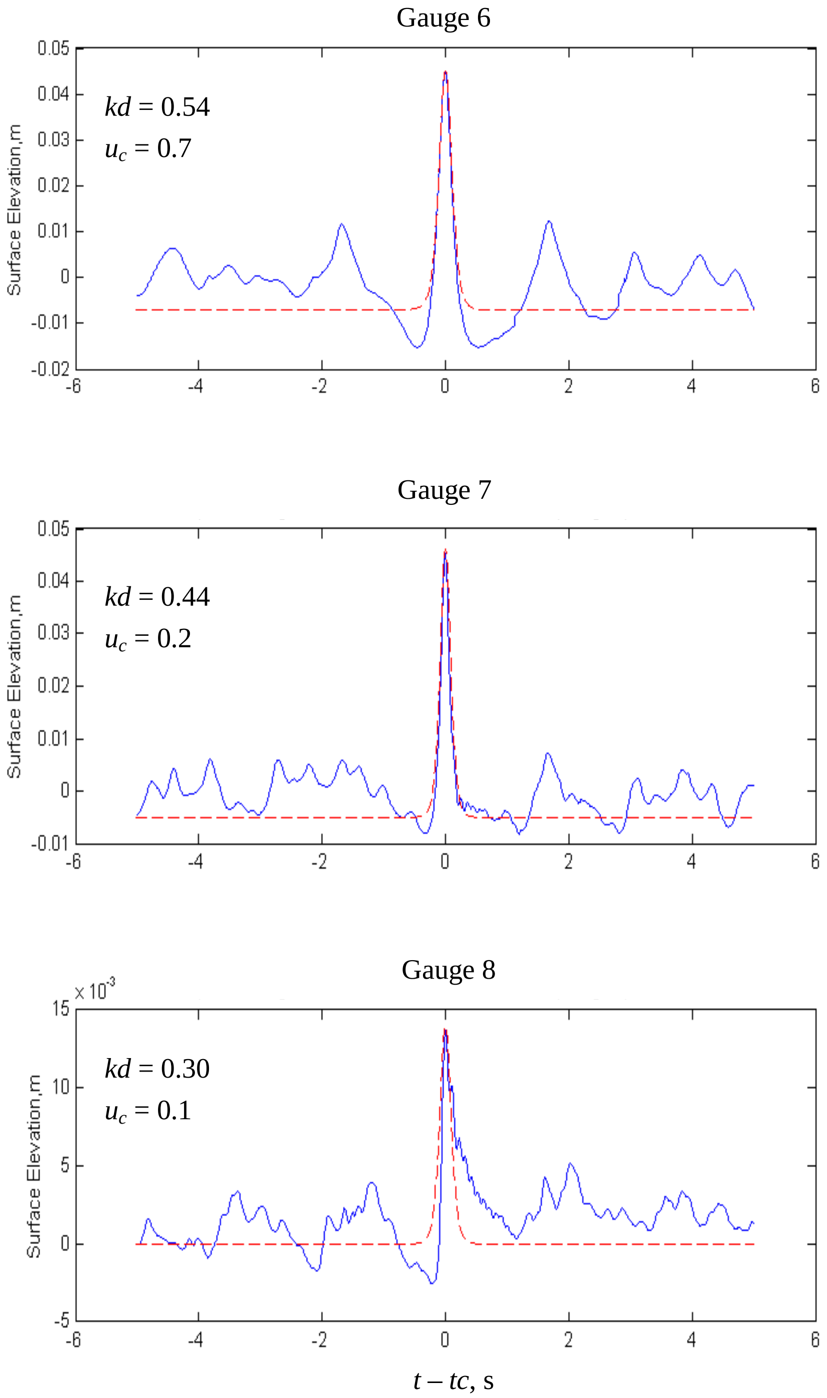

Figure 2.19: Solitary wave fit to averaged top 20 of ‘crest’ surface elevation for Case 3c1100

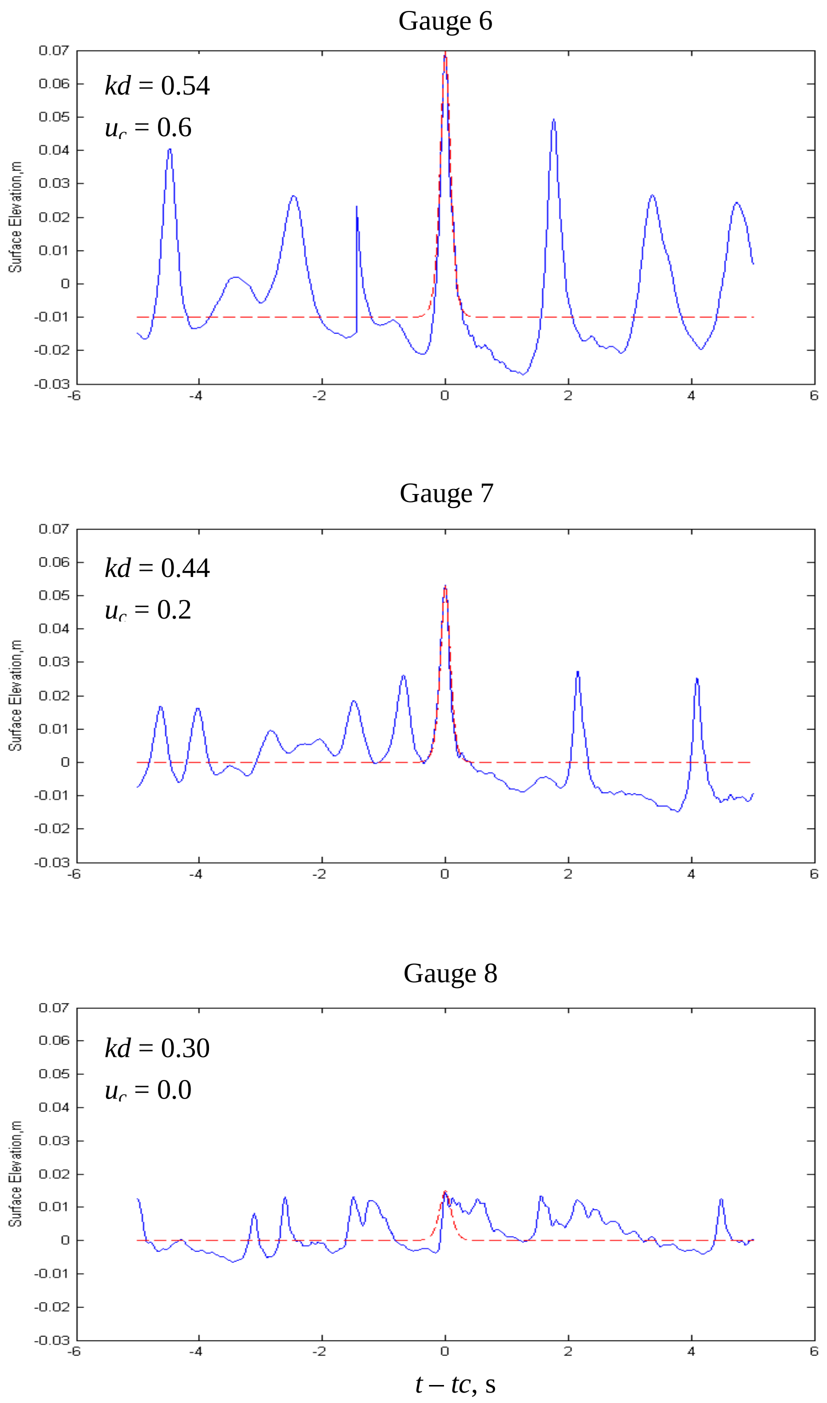

Figure 2.20: Solitary wave fits to largest ‘crest’ surface elevation for Case 3c1100

Figure 2.21 shows the ratio of effective wave speed relative (c') to the solitary wave speed (c_{sol}) for Case 1 and Case 3 of both 1:100 and 1:250 slopes (Table 2.1 and Table 2.2). Only the gauges with a clear saturation of maximum crest surface elevations are chosen. The flat bed cases and Case 3a1100 are not included as the waves are still not broken when they reached Gauge 8. Only a few of the waves move at the undisturbed solitary wave speed, i.e. the relative speed of 1. All the other crests move faster by a factor up to 1.5. This result holds whether the analysis is based on the averaged time history of the top 10 % of all the waves (Figure 2.21a), or only the largest individual waves (Figure 2.21b). The mismatch in speed appears independent of water depth (kd), defined in terms of the deep water peak of the wave spectrum.

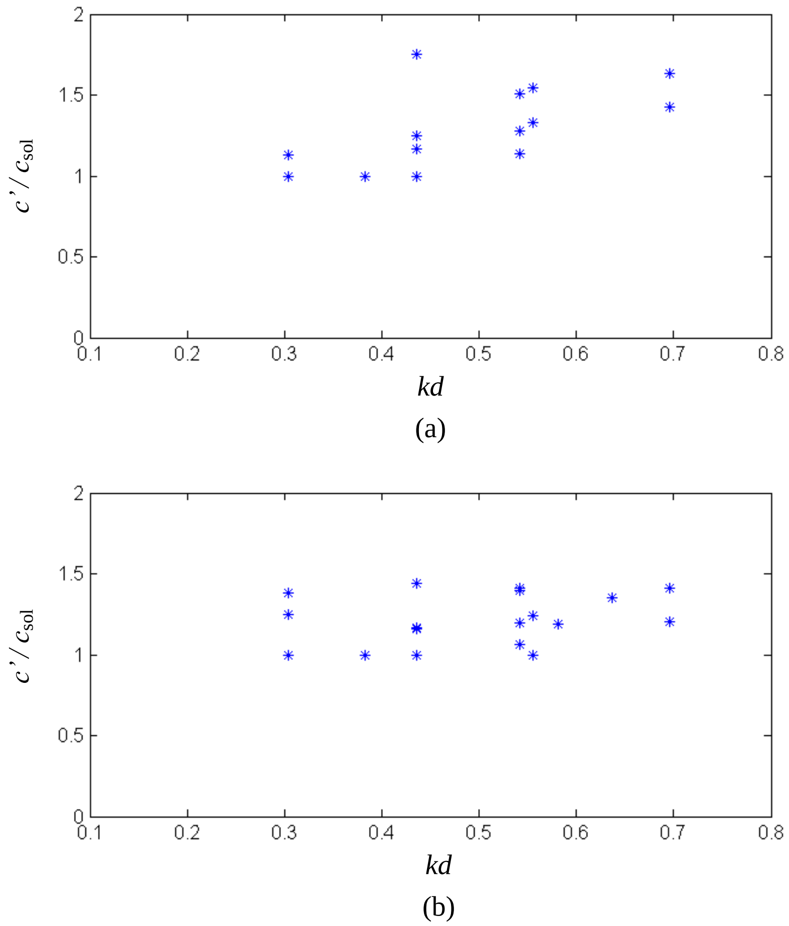

(a)

(b)

Figure 2.21: Non-dimensional effective wave speed for a) top 10 % and b) largest individual waves assuming each wave crest can be modelled as a solitary wave

There are several possibilities for the poor fit of the solitary waves. Are the waves moving faster than solitary waves?

If there is no active breaking, it is more plausible that the width of the assumed sech^2 form is not appropriate. This would be compatible with the individual waves being convected past the wave gauge by a locally strong mean flows (current). On a wave-by-wave basis this current may be highly variable. The assumed shape fits well although with the wrong apparent width for $kd > 0.3$.

If there is active breaking, the horizontal velocity is larger than the celerity. A hydraulic jump might be a better model.

2.7.2 Waves in Shallow Limit as a Succession of Uncorrelated Hydraulic Jumps

Waves in the shallowest depths are fitted to individual hydraulic jumps riding on a current. It is assumed that the height of the wave crest above still water is H and the undisturbed depth is d. Then,

$$c' = c_{hj} + u_c$$

$$c_{hj} = \sqrt{g(d+H)\left(1+\frac{H}{2d}\right)} \tag{2.10}$$

For realistic hump heights, $0 < H/d < 0.75$, the effective speed can be larger than the solitary wave speed by up to 20%. Figure 2.22 plots the effective wave speed relative to the hydraulic jump speed as the moving jump advances on still water for the same cases used for fitting the solitary wave. The present model then appears to work slightly better. However, there are insufficient wave data to proceed further (with wave information only available at two kd values). 1-D shock theory assumes a jump in depth across the front, whereas the available experimental data comprise signals in time at a point.

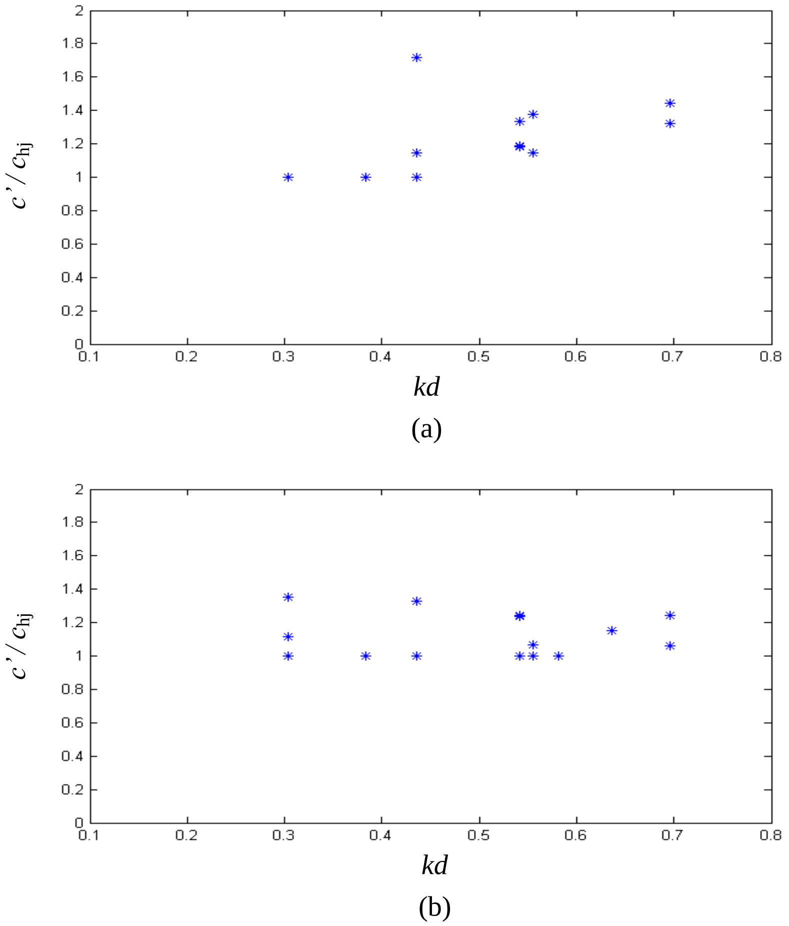

(a)

(b)

Figure 2.22: Non-dimensional effective wave speed for a) top 10 % and b) largest individual waves assuming each wave can be modelled as a hydraulic jump.

2.8 Conclusion

- Sharpening of crests and broadening of troughs can be seen as the waves propagate into shallow water.
- The shapes of all the waves considered are almost the same during the time from 1 s before to 1 s after the maximum crest occurs, for random waves data with T_p of 1.2 s. Further from the crest, the individual shapes are distributed randomly. In shallow water, there is a definite crest height limiting criterion and also a loss of symmetry in the horizontal direction.
- The odd harmonics separation (‘linear term’) works well up to the gauge where the

asymmetry in shape with time starts to become apparent and increases in shallower water.

- For even harmonics; dominated by second order terms, the period taken from trough to trough along the crest is halved compared to the odd harmonics.
- Also seen is a set-down term in deeper water (the troughs either side of the crest are larger than the crest itself); a wave group rides in a depression of its own making.
- Attempts have been made to model waves after the main breaker line, which appears to be at around $kd \approx 0.5$ for sufficiently energetic wave fields. Two models have been used; a simple solitary wave form riding on an unknown local current, and a hydraulic jump. In both cases, the wave crests move faster than the assumed wave forms on shallow water, requiring that they ride on a significant and highly variable onshore current. Given the limited data available for the shallowest depths, the analysis cannot be taken further.
- In terms of the modified Miche criterion, use of either the wavenumber ($k = k_p$) based on the deep water wave spectral peak or a local NewWave type model with a zero-crossing based wavenumber ($k = k_{NW}$) is appropriate, with the NewWave based model appearing to be a closer limit to the data.

3 NewWave Analysis of Experimental Data

3.1 Introduction

NewWave (NW) is an analytical model which describes the profile of large wave events near a crest in a specified sea-state. It has the same shape as the auto-correlation function of the original time history, and has been shown to be proportional to the average shape of the largest wave event in a linear random Gaussian process (Bocotti, 1983). The analysis is first applied to the experimental data as a validation process by comparing NewWave with large wave events identified in the surface elevation time history. Then, NewWave analysis is applied to the experimental data to understand further the mechanics of waves propagating from deep water to shallow water. In keeping with the aim of the present research to investigate the behaviour of very large waves which are highly non-linear, NewWave analysis is extended from being a model solely of the largest wave event to being able to determine the shape and magnitude of second and third order harmonics.

NewWave can also be used to predict the wave forces acting on a structure in the ocean. This could greatly reduce the processing time of a simulation compared to running random waves in a laboratory to produce large waves. It is an appropriate approach by which to estimate the local properties of a large wave event in water where the dynamics are controlled by linear dispersion; different wavelength components travelling at different speeds. The global properties of the whole set of time histories can be transformed to the local properties of individual NewWaves using Fast Fourier Transforms (FFT). Thus, local properties of a large event wave (such as a local wave period) can be estimated and then used as to provide design criteria. A NewWave-based approach using spectral information is developed here, where the idea is to use the local wavenumber extracted from NewWave, without knowledge of the measured time histories.

3.2 NewWave Comparison with 'Linear' Surface Elevation

Restated in Section 3.3, $[\eta_c - \eta_t]/2$ of the Stokes water wave expansion is the odd harmonics of the surface elevation time history, which is dominated by the linear order term. 'Linear' surface elevation will be used as shorthand. It has to be stressed that η_c is taken to be the average surface elevation time series for the largest crests (i.e. largest 10%) while η_t is the average surface elevation time history for the largest troughs, as explained in Section 2.5.1. This 'linear' surface elevation is compared with NewWave which can be obtained by a simple Fourier transform of the power spectrum $S(\omega)$, Mathematically, NewWave is defined as;

$$\eta_{NW}(t) = A\frac{\int S(\omega)\cos\omega t\, d\omega}{\int S(\omega)\, d\omega} \tag{3.1}$$

where A is the wave amplitude of the 'linear' surface elevation used to scale NewWave, so the crest values match. The shape of NewWave is shown in Figure 3.1.

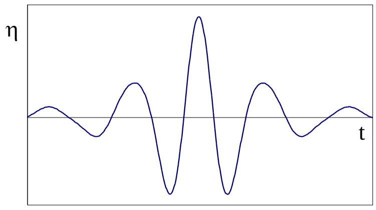

Figure 3.1: Shape of NewWave

Figure 3.2 compares the spectrally derived NewWave profile to the 'linear' surface elevations $[\eta_c-\eta_t]/2$. NewWave ($\eta_{NW}(t)$) fits very well to the linear contribution of the surface elevation in deep water. However, the match is less good for Gauges 7 and 8; for these the horizontal asymmetry increases and NewWave fails to match the averaged profile in the shallower depths. When compared with the 'linear' surface elevation, it can be seen that NewWave is broader at the crest and deeper at the following troughs. This is due to the contribution of third order effects (triple frequency term) on the 'linear' surface elevation, as can be seen in the combination of Stokes expansions for $[\eta_c-\eta_t]/2$, restated in Section 3.3.

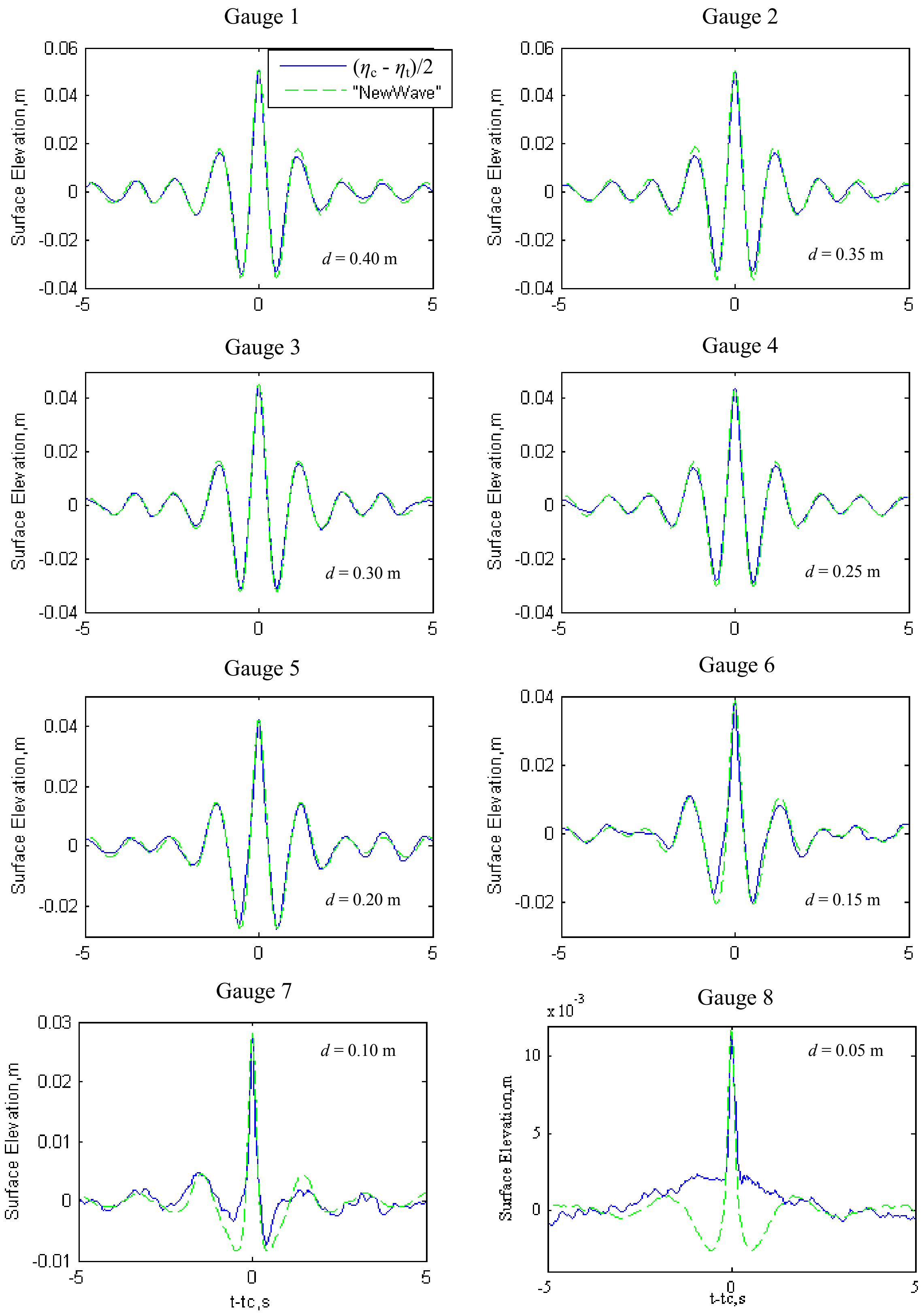

Figure 3.2: NewWave compared with top 10 % averaged [η_c-η_t]/2 for Case 1a1100

3.3 Extraction and Detailed Analysis of the Bound Sum Harmonics

Large deep ocean waves are vertically asymmetric and non-linear, due to the crests being larger and steeper compared to the troughs. Thus, it is important to quantify the magnitude of the harmonics. From the Stokes water wave expansion, the magnitude of the linear and third order contribution for the odd harmonics, $[\eta_c - \eta_t]/2$ and second order contributions for the even harmonics, $[\eta_c + \eta_t]/2$ are now estimated. Stokes water wave expansion and its combinations are restated here.

$$\eta_c = S_0 A^2 \cos(0) + A\cos(\omega t) + S_2 A^2 \cos(2\omega t) + S_3 A^3 \cos(3\omega t) + ... + S_n A^n \cos(n\omega t) \qquad (2.1)$$

$$\eta_t = S_0 A^2 \cos(0) - A\cos(\omega t) + S_2 A^2 \cos(2\omega t) - S_3 A^3 \cos(3\omega t) + ... + S_n A^n \cos(n\omega t) \qquad (2.2)$$

$$\frac{\eta_c - \eta_t}{2} = A\cos(\omega t) + S_3 A^3 \cos(3\omega t) + ... + S_{n-1} A^{n-1} \cos((n-1)\omega t) \qquad (2.3)$$

$$\frac{\eta_c + \eta_t}{2} = S_0 A^2 \cos(0) + S_2 A^2 \cos(2\omega t) + ... + S_n A^n \cos(n\omega t) \qquad (2.4)$$

where A is the wave amplitude, ω is the wave angular frequency, $n + 1$ is the number of terms and the coefficients S_n determine the magnitude of the components. Note a zero frequency term (mean shift) is included, as this idea of combining crest- and trough- centered signals is in practice here applied to the broad-banded signals rather than regular waves.

Case 3e1100 with peak period, T_p of 1.5 s and deep water significant wave height, H_{so} of 121.3 mm is considered here, being the most extreme case of all (See Table 2.1 of Section 2.3).

3.3.1 Odd Harmonics

The $[\eta_c - \eta_t]/2$ data have been averaged with the time reversed waveform (centred at the time when the maximum crest occurs) to reduce noise. Based on Equation (2.3), the linear term is simply NewWave (NW), the auto-correlation function of the overall time series whilst the third order term (NW3) can be approximated by using the Hilbert Transformation of NewWave (Walker et al. 2004). The approximation for the shape of the third order contribution to NewWave is based on the identity;

$$\cos(3\theta) = \cos^3\theta - 3\sin^2\theta.\cos\theta \tag{3.2}$$

giving an approximation for the local third harmonics as

$$\mathrm{NW3} = \mathrm{NW}^3 - 3\mathrm{NW_H}^2.\mathrm{NW} \tag{3.3}$$

where $\mathrm{NW_H}$ is the Hilbert transform of the NewWave signal, requiring simply the replacement of the cosine function in Equation (3.1) by the sine function.

The magnitude of NW and NW3 contributions can be sought by fitting an equation of the form

$$\frac{\eta_c - \eta_t}{2} = A_1{*}\mathrm{NW} + A_3{*}\mathrm{NW3} \tag{3.4}$$

The coefficients A_1 and A_3 are determined using the equations below, with the assumption that the linear and third order terms are orthogonal to each other (which is very close to being exactly correct).

$$A_1 = \frac{\int \left(\frac{\eta_c - \eta_t}{2}\right) \times (NW)\,dt}{\int NW^2\,dt} \tag{3.5}$$

$$A_3 = \frac{\int \left(\frac{\eta_c - \eta_t}{2}\right) \times (NW3)\,dt}{\int (NW3)^2\,dt} \tag{3.6}$$

Figure 3.3 shows the odd harmonics: $[\eta_c - \eta_t]/2$ from the data and the sum of linear and third order fitted terms using NewWave, based on Equation (3.4). The sum contribution fits very well up to Gauge 6 where waves start to break. The $[\eta_c - \eta_t]/2 - A_1{*}\mathrm{NW} - A_3{*}\mathrm{NW3}$ is the difference between the data and sum of the linear and third order contributions and represents an error component, arising from the lack of perfect fit. Fortunately, this error is usually small. It can be clearly seen there is an increment in value for this difference (error) from Gauge 5 to Gauge 6, and it is a significant contribution to the odd harmonics at Gauge 7. The difference could represent the higher order odd harmonics terms (5th and etc.), or could simply be noise;

a break-down of NewWave formulation. The magnitude of the coefficients A_1 and A_3 (in m) for every gauge are given in Table 3.1.

Table 3.1: Values of coefficients A_1 and A_3 for Case 3e1100

Case 3e1100		
Based on unit amplitude NewWave		
Gauge	A_1 (m)	A_3 (m)
1	0.0606	0.0044
2	0.0573	0.0051
3	0.0546	0.0066
4	0.0503	0.0077
5	0.0449	0.0109
6	0.0320	0.0116
7	0.0223	0.0113

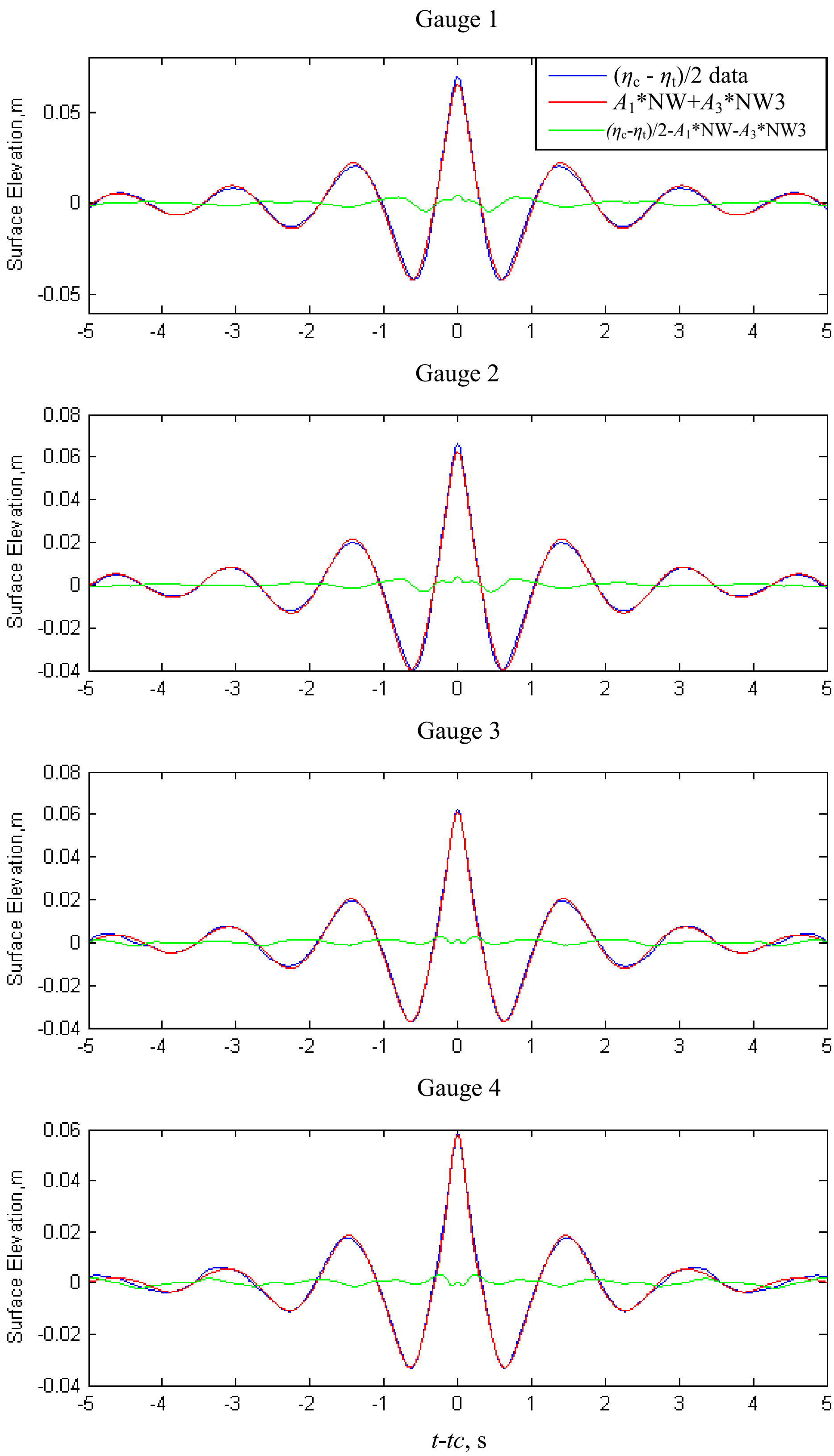
Gauge 1
$(\eta_c - \eta_t)/2$ data
A_1*NW+A_3*NW3
$(\eta_c-\eta_t)/2-A_1$*NW-A_3*NW3
Surface Elevation,m
0.05
0
-0.05
-5
-4
-3
-2
-1
0
1
2
3
4
5
Gauge 2
Surface Elevation,m
0.08
0.06
0.04
0.02
0
-0.02
-0.04
-5
-4
-3
-2
-1
0
1
2
3
4
5
Gauge 3
Surface Elevation,m
0.08
0.06
0.04
0.02
0
-0.02
-0.04
-5
-4
-3
-2
-1
0
1
2
3
4
5
Gauge 4
Surface Elevation,m
0.06
0.04
0.02
0
-0.02
-0.04
-5
-4
-3
-2
-1
0
1
2
3
4
5
t-tc, s

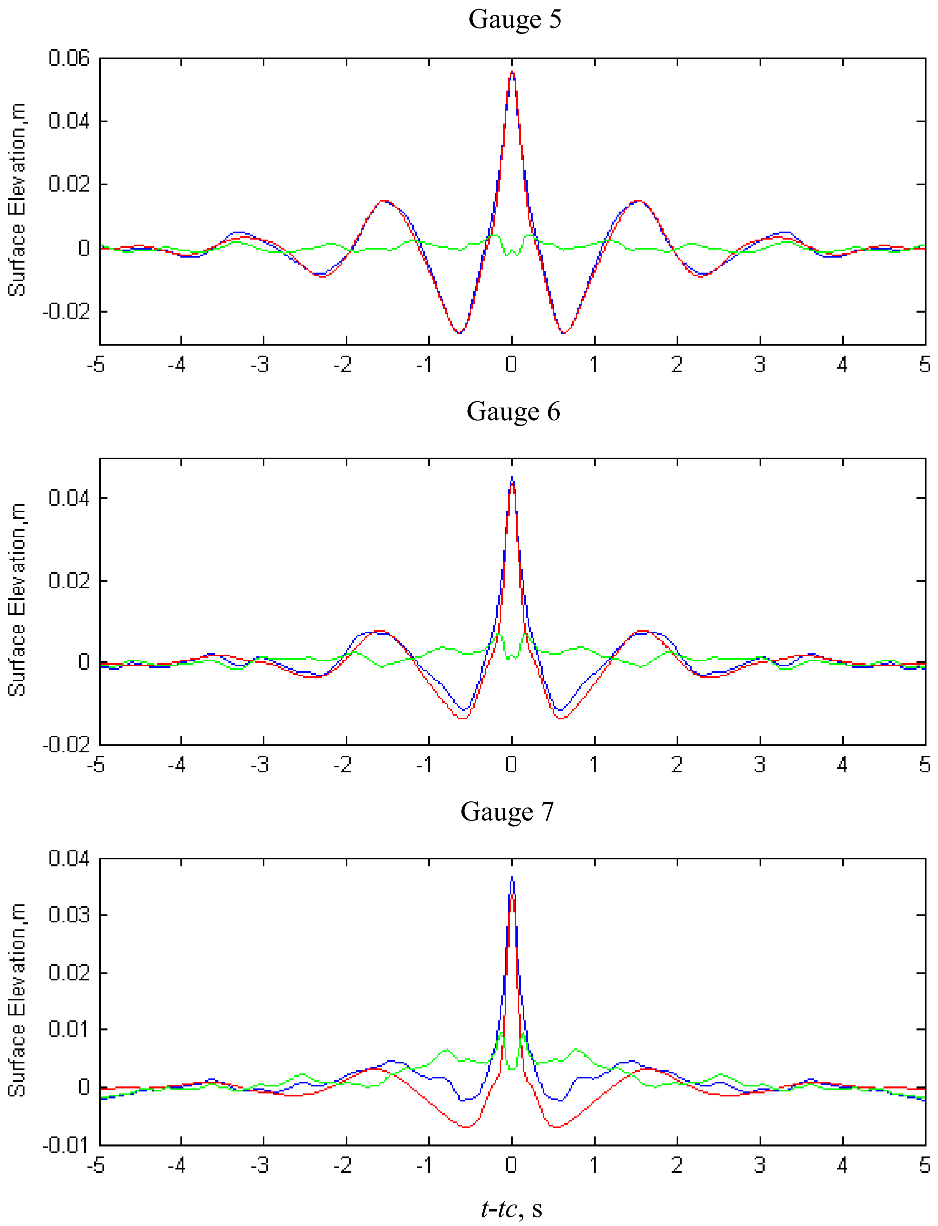

Figure 3.3: Top 10 % averaged odd harmonics vs time for Case 3e1100

3.3.2 Even Harmonics

The $[\eta_c + \eta_t]/2$ data have also been averaged with the time reversed waveform to reduce noise. Then, the spectrum is obtained using FFT with peak frequency (f_p) of 0.667 Hz (for the same case as in Section 3.3.1). The spectrum is filtered to obtain estimates for the second order sum and second order difference terms of the Stokes wave expansion. The cut off point for lower frequency (second order difference) is around $0.5\,f_p$ and the cut off point for higher frequency (second order sum) is around $1.5\,f_p$. The filtered second order sum term is then compared with its equivalent Hilbert Transform based approximations of NewWave (NW2) using the identity;

$$\cos 2\theta = \cos^2\theta - \sin^2\theta \tag{3.7}$$

giving an approximation for the second harmonics as

$$\mathrm{NW2} = \mathrm{NW}^2 - \mathrm{NW_H}^2 \tag{3.8}$$

The upper plots of Figure 3.4a and Figure 3.4b show the even harmonics, $[\eta_c + \eta_t]/2$ from Case 3e1100 and its second order sum and second order difference contribution by spectral filtering for Gauge 1 and Gauge 7 respectively. Generally for all gauges, the second order sum contribution of NewWave (NW2) fits well with the filtered data as shown in the middle plot of both figures, with Gauge 7 being at the shallowest depth with broken waves. In these plots, the magnitude of NW2 is normalised with the crest height of the filtered data so that direct comparison of the shape can be observed. The reconstruction of the overall $[\eta_c + \eta_t]/2$ are shown in the third plots where the filtered second order difference is used. The reason for the use of a filtered spectrum is that there is no way to determine accurately the magnitude of the second order difference using the orthogonality principle, as applied in Section 3.3.1 for the magnitude of A_1 and A_3. It should be noted that the crest value of the reconstruction data should have the same value as $[\eta_c + \eta_t]/2$ because the same second order difference signal is used for the reconstruction. This discrepancy is due to information loss during the spectrum filtering to obtain the filtered second order difference signal.

The magnitude of the second order sum, A_2 is then calculated using the same principle as for the odd harmonics before, with the assumption that the linear and second order sum terms are orthogonal to each other. Table 3.2 below shows the magnitude of the second order sum term for every gauge of Case 3e1100.

$$A_2 = \frac{\int \left(\frac{\eta_c + \eta_t}{2} \right) \times (NW2)\, dt}{\int (NW2)^2 \, dt} \tag{3.9}$$

Table 3.2: Values of coefficients A_2 for Case 3e1100 and crest height of the filtered second order sum

Gauge	A_2 (m)	Crest height of the filtered 2nd order sum	Percentage difference (%)
1	0.0142	0.0170	16
2	0.0159	0.0186	15
3	0.0186	0.0200	7
4	0.0192	0.0203	5
5	0.0218	0.0230	5
6	0.0184	0.0193	5
7	0.0153	0.0161	5

Table 3.2 also shows the difference in magnitude between the filtered second order sum and the calculated value, A_2, with the filtered spectrum giving higher magnitude. Presumably the small differences may be due to fourth order contributions embedded in the filtered spectrum. The small difference in shape (middle plot of Figure 3.4) may also be a result of the fourth order contributions as well as statistical noise. Together with Table 3.1, the contribution of both second and third order sum harmonics increases in magnitude as the waves shoal.

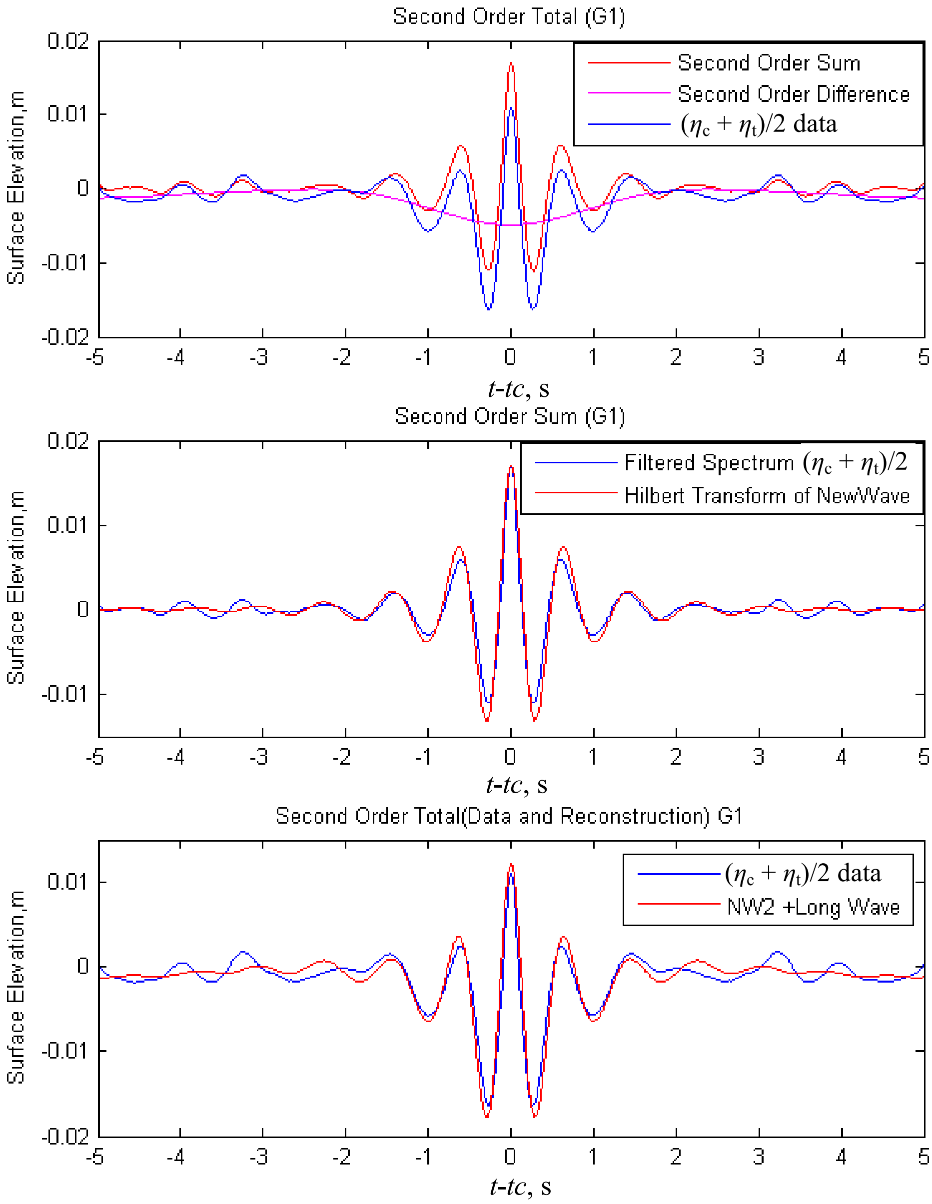
Second Order Total (G1)

Second Order Sum (G1)

Second Order Total(Data and Reconstruction) G1

Figure 3.4a: Top 10 % averaged even harmonics vs time for Case 3e1100 at Gauge 1

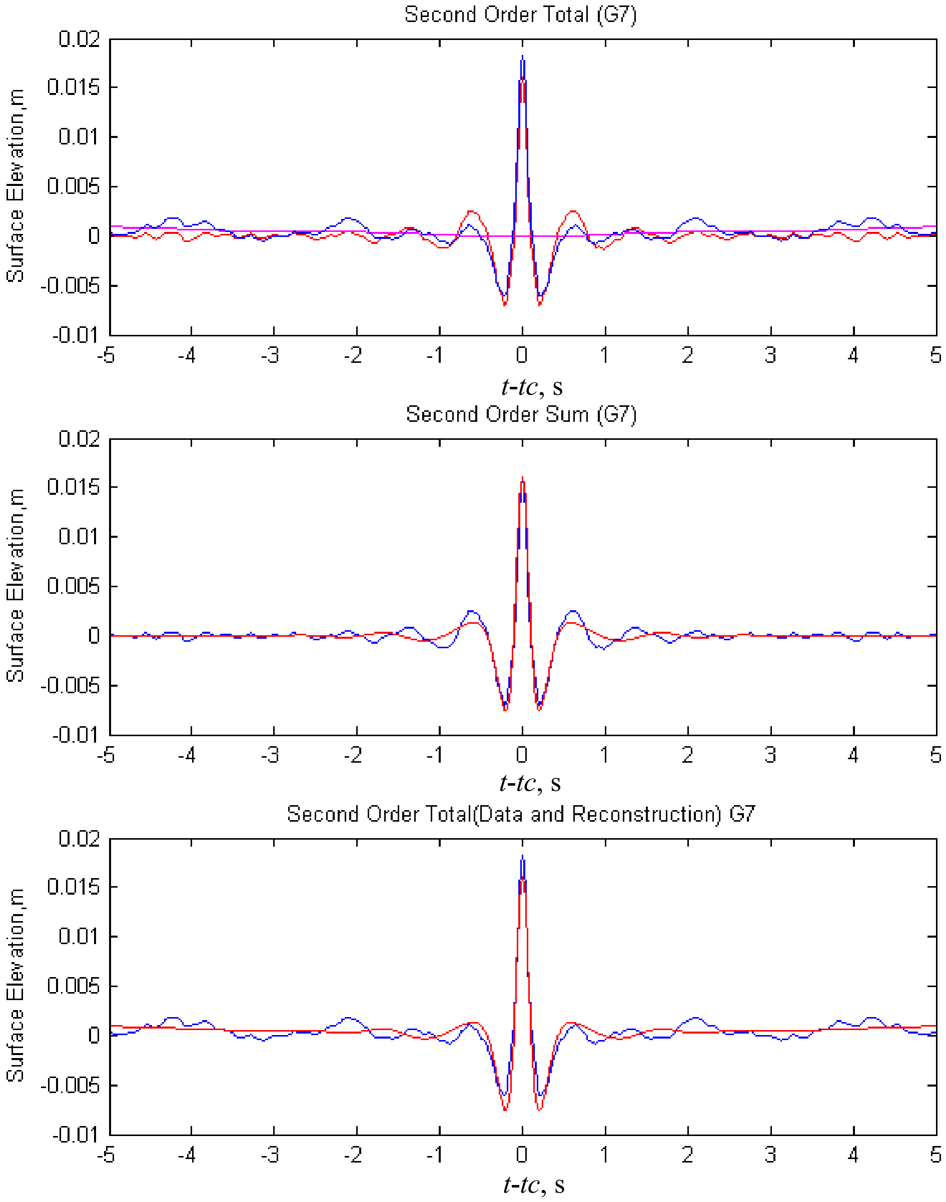

Figure 3.4b: Top 10 % averaged even harmonics vs time for Case 3e1100 at Gauge 7

Based on the Stokes water wave expansion (Section 3.3), the S_2 and S_3 terms are related to the Stokes coefficient defined by Walker et al. (2004) as $S_2 = S_{22}/d$ and $S_3 = S_{33}/d^2$. The coefficients S_{22}, S_{33} etc. are simply those given in a standard Stokes expansion rearranged to use the depth (d) explicitly rather than the wavenumber (k) i.e. the standard form

$$\eta = A\cos\theta + B_{22}kA^2\cos 2\theta + B_{33}k^2A^3\cos 3\theta + ... \tag{3.10}$$

is replaced by

$$\eta = A\cos\theta + \frac{S_{22}}{d}A^2\cos 2\theta + \frac{S_{33}}{d^2}A^3\cos 3\theta \tag{3.11}$$

The standard coefficients B_{ij} are related to the Walker-type ones by

$$B_{22}.k = \frac{S_{22}}{d} \text{ etc.} \tag{3.12}$$

The aim in doing this is to remove the requirement of estimating the local wavenumber, k. By comparing Equation (3.4) with Equation (3.11) and applying it to the double frequency term (A_2*NW2), the Stokes coefficient for the experimental result can be given by

$$\begin{aligned} S_{22_{NW}} &= \frac{A_2 d}{A^2} \\ S_{33_{NW}} &= \frac{A_3 d^2}{A^3} \end{aligned} \tag{3.13}$$

Figure 3.5 plots the variation of both the theoretical (Walker et al., 2004) and experimentally derived Stokes coefficient with kd. The experimental data show the same trend as the theory, with the rate of change of the coefficients decreasing with increasing kd. The rather large discrepancy especially for S_{33} at high kd could due to the fact that the amplitude, A in Equation (2.3) is the average of the cubes of amplitude for every large wave event considered and not the cube of the averaged amplitude, as used here. Given that double and triple frequency contributions to the wave are small, the level of agreement between the approximate NewWave coefficients and the exact (regular wave) Stokes values is satisfactory.

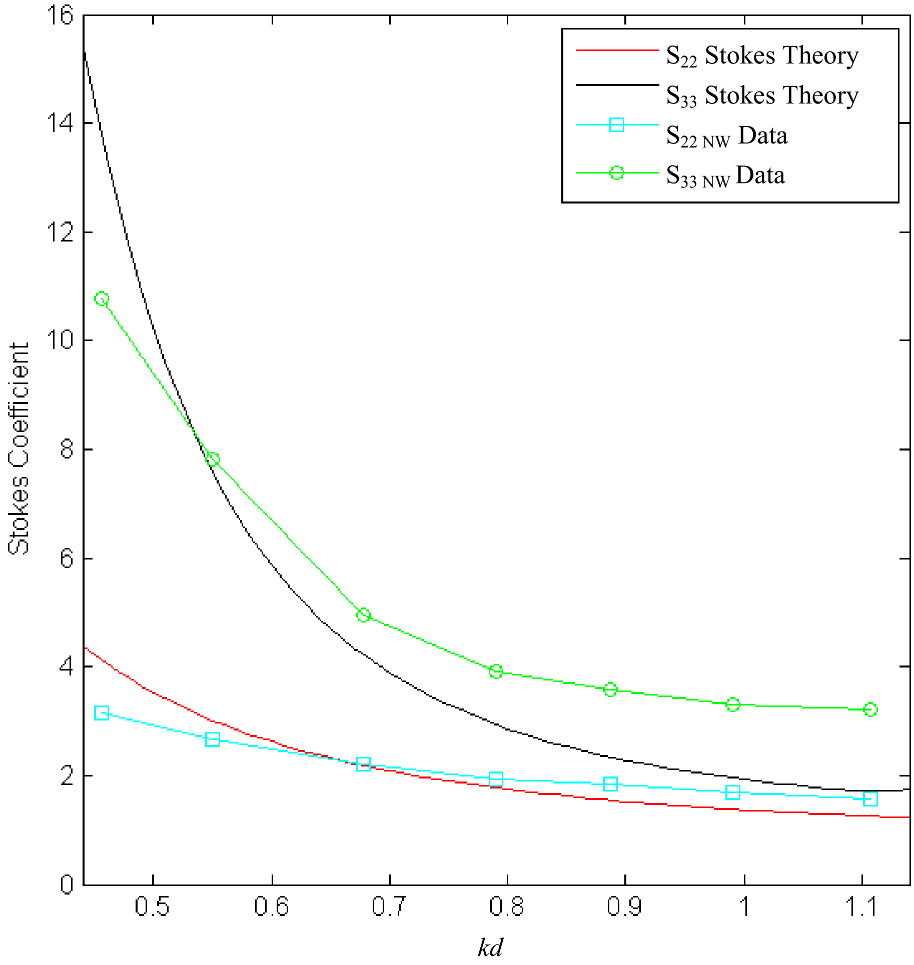

Figure 3.5: Stokes second and third order sum coefficients, S_{22} and S_{33} against *kd*

In conclusion, the NewWave analysis can be extended from being solely a model of the average large wave event to being able to provide estimates of the shape and magnitude of second and third order sum contributions with reasonably good results by using a Hilbert Transformation-based method (Walker et al., 2004).

3.4 Spectral Modification due to Shoaling

NewWave can be used to predict the local wave structure of large events given a frequency spectrum at any spatial point. Unfortunately, spectral data at all points up a gentle slope may not be readily available, so the construction of the appropriate NewWave requires some more assumptions. In the absence of local spectral information, it is likely that deep water spectral information will be available even if this is simply the assumption of a standard JONSWAP form. In the absence of a computer package such as SWAN (a third-generation wave model that computes random, short-crested wind-generated waves), a simple spectral modification method to account for shoaling is used as the waves advance into shallower water. The deep water spectrum, $S(f;d)$ can be modified to be a function of water depth by using the linear dispersion equation, resulting in the TMA (Texel, Marsen and Arsloe) spectrum (Bouws et.al., 1985);

$$S(f;d_1)=\frac{\Phi(f;d_1)}{\Phi(f;d)}S(f;d) \tag{3.14}$$

with the TMA factor, $\Phi(f,d) = 1/(2n_r)\ (\tanh\ (kd))^2$ and n_r is the ratio of the group velocity to phase speed. This gives an estimation of the conservative and non-breaking wave spectrum at different locations as the waves slowly adapt to varying water depth.

Figure 3.6a shows the wave spectrum based on gauge to gauge transformation for Case 1a1100. The wave spectrum at Gauge 1 is multiplied by the TMA factor for Gauge 2 to produce a TMA spectrum at Gauge 2 and this is then compared with the measured wave spectrum of Gauge 2. Next, the measured wave spectrum at Gauge 2 is then multiplied by the TMA factor for Gauge 3 to produce a TMA spectrum at Gauge 3 and this is then compared with the measured spectrum of Gauge 3. This procedure is then continued for the other gauges. From Figure 3.6a, it is shown that the TMA spectra fit very well up to Gauge 6. Beyond that, vigorous wave breaking starts to take place and the TMA model starts to fail, as does NewWave representation for large waves (as evident in Figure 3.2).

Also, the TMA spectrum at all gauges has been produced based on one single wave spectrum at Gauge 1. This is to assess the cumulative changes of the spectrum at different locations based on only one wave spectrum in deep water. This can be seen in Figure 3.6b. It shows similar results as the gauge to gauge transformation, failing to fit well with the measured spectrum at Gauge 7 and Gauge 8. However, there is some net loss of energy starting at Gauge 5 and Gauge 6 at a frequency range of 0.5 to 0.8 Hz compared to the gauge to gauge transformation spectrum. Overall, the TMA model for the spectral changes in a shoaling wave field appears to work quite well until the onset of strong breaking.

As well as the simple TMA model, the computationally intensive SWAN model (Booij et al., 1999) could be used as an approach to spectral modifications in shallow water. The evolution of spectral action in SWAN includes shoaling and refraction, approximating diffraction, wind input, dissipation by white capping, bed friction, surf-breaking, four-wave and three-wave interactions, wave induced set up, etc. But, it should be stressed here that SWAN is not phase resolving, so the output is a local wave spectrum. Thus, it is also possible to use NewWave to convert SWAN spectral information into local wave structure.

3.5 Effect of Friction

Bouws et.al. (1985) stated that friction plays almost no part in the balance of energy in deep water. Figure 3.7 relates to Case 1bflat (constant water depth of 30 cm) and shows that at different gauges a distance of 10 m apart, the NewWave shape does not change but there is slow dissipation of amplitude through viscous damping by the side walls due to the narrow width of the wave flume. The reduction of wave height per wavelength for regular wave trains is less than 1 %, as stated in the Lowish Report (2007). This suggests that friction is not significant in the channel and that the wave heights are limited by non-linear dynamics as the waves shoal; more energy dissipation in breaking. This is presumably the reason for the same limiting values in crest amplitude of waves, as stated in Section 2.6. Comparing Figure 3.7 and Figure 2.5 (of Section 2.5.1) for the case with sloping bed, note the difference between breaking as energy dissipation, a localised and violent process, compared to slow but cumulative dissipation due to bed and sidewall friction.

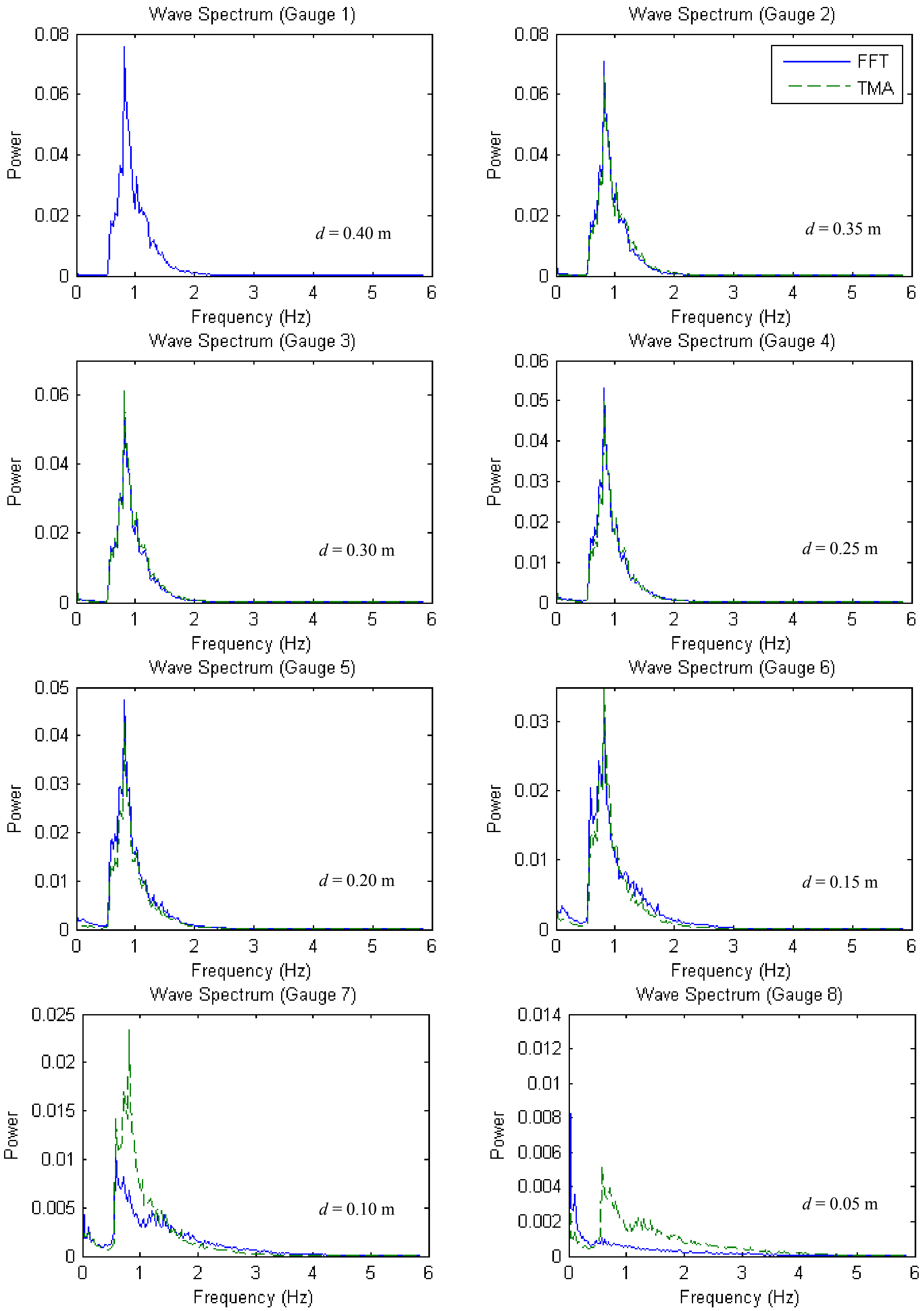

Figure 3.6a: Wave spectra based on gauge to gauge TMA transformation for Case 1a1100

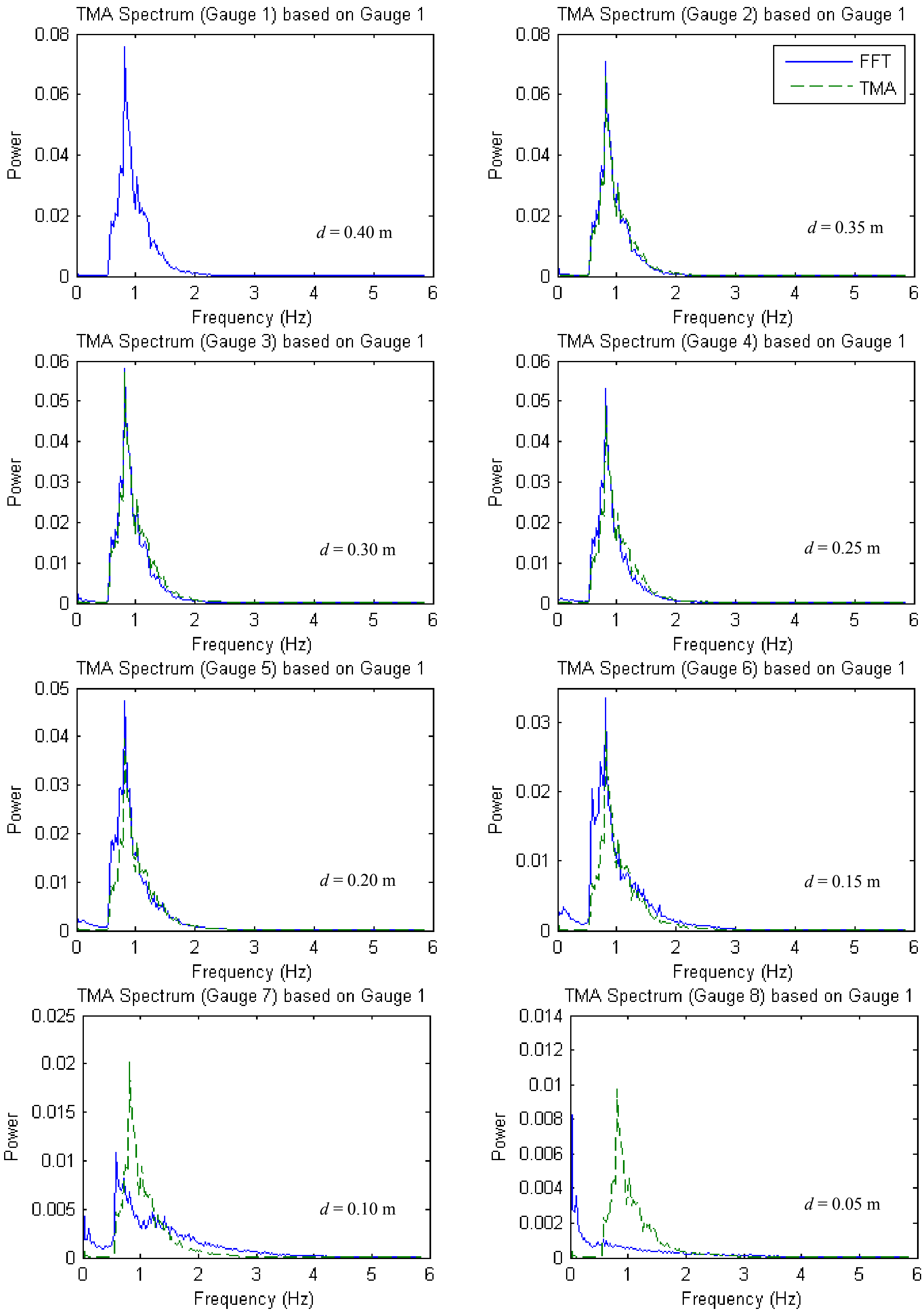

Figure 3.6b: Wave spectra based on gauge 1 TMA transformation for Case 1a1100

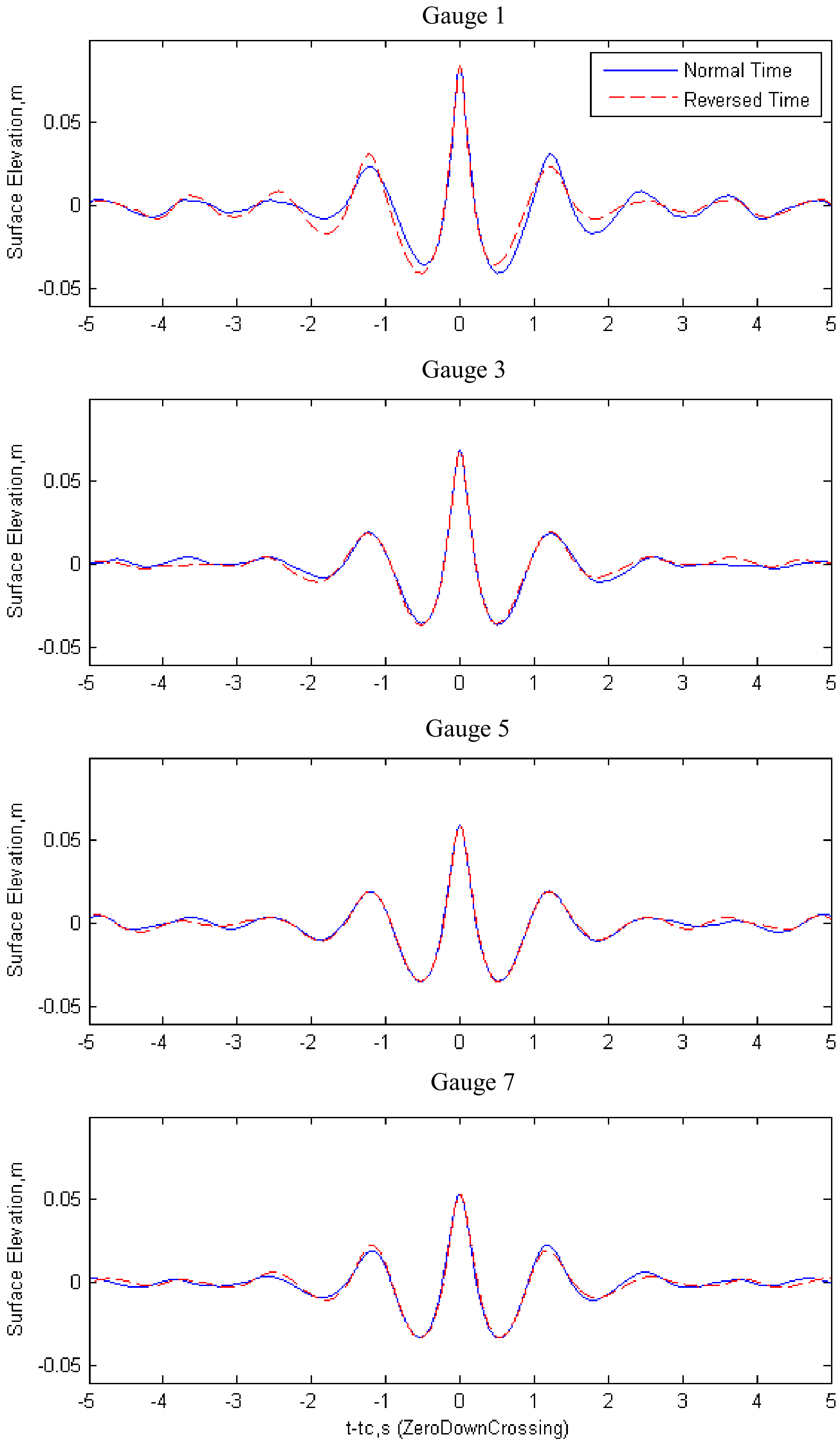

Figure 3.7: Top 10 % **crest** averaged surface elevation vs time (*t-tc*) for Case 1bflat (d = 0.3 m) overlapped with reversed time

3.6 Comparison with other Test Cases

Based on the configuration of the test case undertaken, comparisons have been made to further characterise and understand the behaviour of waves; the influence of offshore significant wave height (H_{so}) and the effect of bed slope.

3.6.1 Influence of Offshore Significant Wave Height (H_{so})

The wave field is influenced by the total energy content of the wave spectrum. Figure 3.8 shows five cases of varying offshore significant wave height (H_{so}) at the same water depth (Gauge 7 in 10 cm depth). The wave height of linear response scales with the significant wave height. NewWave works well up to the point where the wave height starts to saturate in relatively shallow water depth, due to the Miche limiting criterion which is based on the height to depth ratio (H/d) for shallow water.

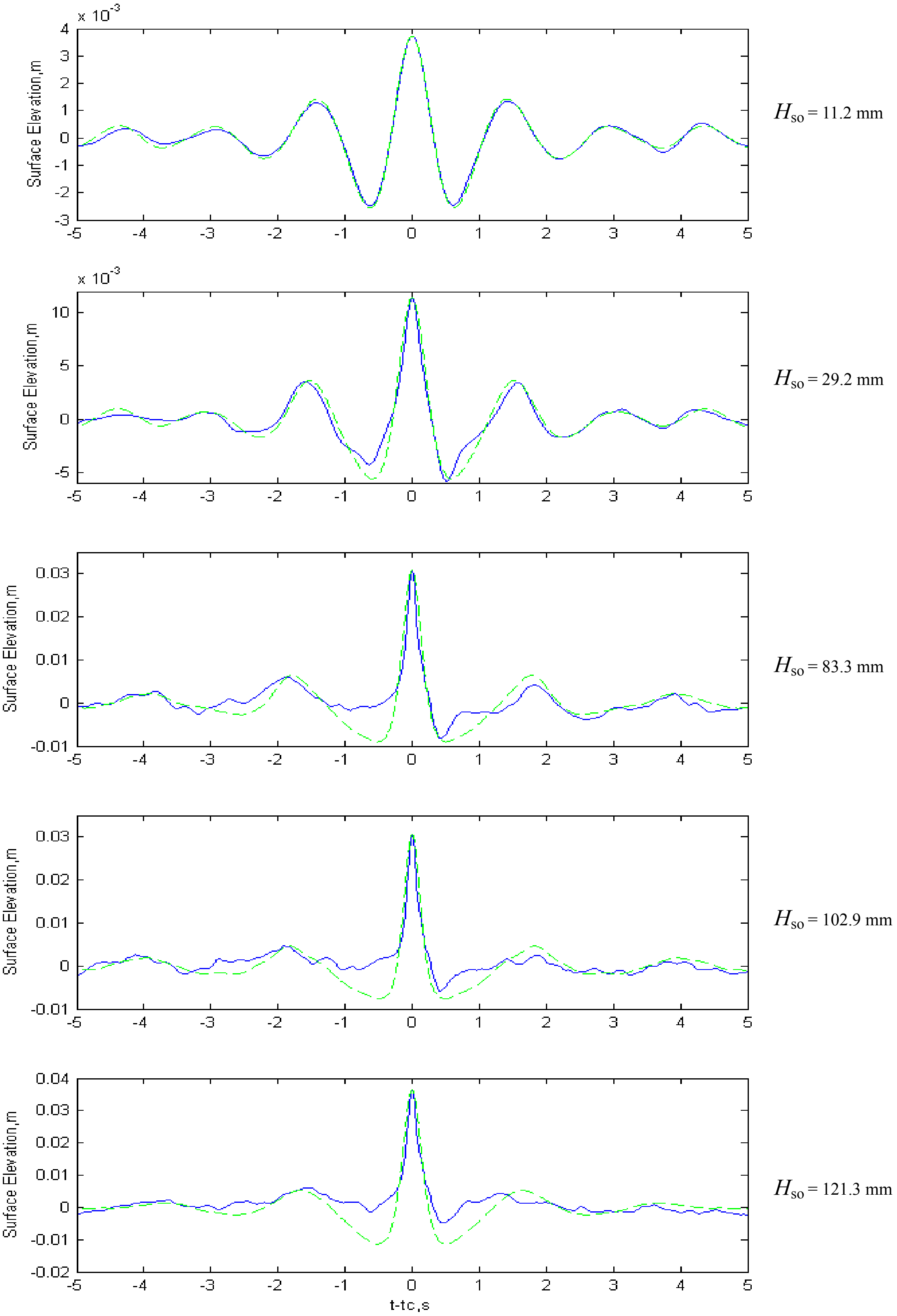

Figure 3.8: NewWave (dashed line) compared to top 10 % averaged [η_c - η_t]/2 (solid line) of Case 3a1100-3e1100 with the same water depth (d = 10 cm)

3.6.2 Effect of Bed Slope

Tests with bed slopes of both 1:100 and 1:250 have been carried out to look at the effect on the propagation of deep water waves into shallow water. Figure 3.9 shows the NewWave and top 10% averaged profiles for Case 3e1100 and 3e1250 side by side for the same water depths. The behaviour of crests is similar except for the water depth, d = 30 cm where there is a slight overshoot (higher crest) due to sudden change of steep (1:15) slope to gentle (1:250) slope compared to the 1:100 case. It should be noted that water depth of 30 cm for case 1:100 is 20 m away from the step change.

Overall, the pairs of figures are sufficiently similar to imply that the local shapes of the largest values at various points on the slope are affected by the depth via the local kd value but hardly at all by the value of the bed slope.

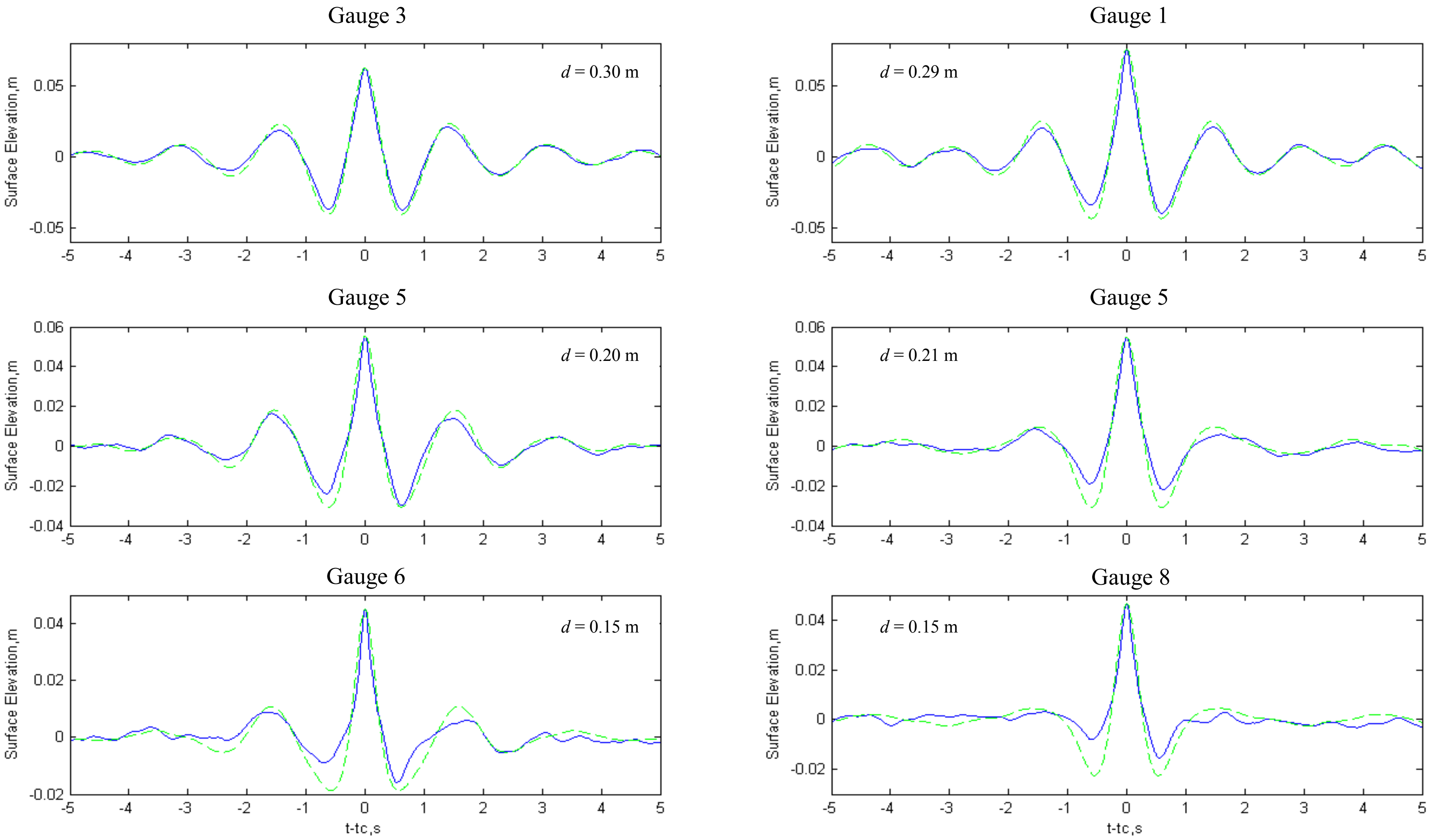

(a) (b)

Figure 3.9: NewWave (dashed line) compared with top 10 % averaged $[\eta_c - \eta_t]/2$ (solid line) of a) Case 3e1100 and b) Case 3e1250

3.7 Conclusion

- The main finding of the NewWave analysis is that for non-breaking waves, both the TMA transformation and NewWave methodologies give very satisfactory representations of average large wave events. Once large-scale breaking occurs, both methods fail to match the measured data. NewWave appears to be a reasonable model for waves in deep and intermediate water depth.
- In deeper water with $kd > 0.5$,
    - frequency dispersion is still significant and NewWave remains a reasonable model.
    - Detailed non-linear analysis has been performed and a Stokes-like expansion for NewWave shown to match the average shape of the largest waves.
    - Based on a given input spectrum (e.g. the TMA spectrum), NewWave can be used to find the local wave period of averaged large event waves from the random surface elevation time history.

      This value is then inserted in the modified Miche limiting wave height criterion by using the dispersion equation.
- For $kd < 0.5$ and with strong breaking,
    - NewWave fails to work because shoreward of the breaker line, virtually all large crests are breaking. Possibly a solitary wave theory or a bore wave model ought to be applicable and a limiting wave height of $H_{\max}/d = 0.76$ appears to be appropriate.
- NewWave analysis can be extended from being a model of the average large wave event only to being able to provide estimates for the shape and magnitude of second and third order sum contributions by using a Hilbert Transformation-based method.
    - The contribution of both second and third order sum harmonics increases in magnitude as the waves shoal.

4 Mathematical Formulation of the Green-Naghdi Equations

4.1 Introduction

The Green-Naghdi (GN) theory is a relatively new method in the field of ocean engineering when compared with other standard water wave theories, e.g. equations derived using perturbation methods such as Boussinesq and Stokes higher order equations. The GN approach assumes that the water is inviscid and incompressible, but not necessarily irrotational and satisfies the boundary conditions exactly and approximates the field equations. The velocity field is approximated by a finite sum of fundamental kinematic profiles. GN theory incorporates non-linear terms in its formulation, even at the lowest order. High level GN theory is capable of solving both shallow and deep water problems. Demirbilek and Webster (1992) derived the general GN equations for inviscid and incompressible fluid, with GN Level I and Level II formulated to solve two-dimensional steady and unsteady flows over flat and uneven bottom topography.

The derivation starts from the 3-dimensional conservation equations before reducing to the 2-dimensional vertical Green-Naghdi equations, using notation which is different from that used by Demirbilek and Webster (1992). Then, the derived 2-dimensional GN equations are investigated through their dispersion and non-linearity properties before a numerical method for solving them is presented.

4.2 3-D Mass and Momentum Equations and Kinematic Boundary Conditions for Free Surface Flow of Inviscid, Incompressible Liquid

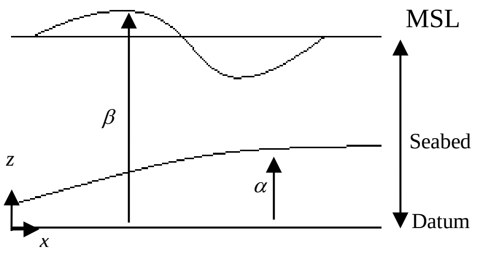

Figure 4.1: 2-D Definition sketch of the physical domain

It is assumed that the liquid (water) is inviscid and incompressible. With respect to the definition sketch in Figure 4.1, the dependent variables comprise the flow velocity vector, $\vec{u}=(u,v,w)$; the vector of gravitational acceleration, $\vec{g}=(g_x,g_y,g_z)$; the elevation of the bottom surface boundary above a fixed datum, $\alpha(x,y,t)$; and the elevation of the top surface boundary above a fixed datum, $\beta(x,y,t)$. In vector notation, the 3-dimensional mass and momentum equations for inviscid, incompressible flow are

(continuity) $$\nabla\cdot\vec{u}=0 \quad , \tag{4.1}$$

(momentum) $$\left(\frac{\partial}{\partial t}+\vec{u}.\nabla\right)\rho\vec{u}=-\nabla\left(P\right)-\rho\vec{g} \quad , \tag{4.2}$$

where *P* is pressure, ρ is density, and *t* is time. Writing these out in long hand, the continuity and conservative momentum component equations are as follows:

(continuity) $$\frac{\partial u}{\partial x}+\frac{\partial v}{\partial y}+\frac{\partial w}{\partial z}=0 \quad , \tag{4.3}$$

(*x*-direction momentum) $$\frac{\partial\rho u}{\partial t}+\frac{\partial\rho uu}{\partial x}+\frac{\partial\rho uv}{\partial y}+\frac{\partial\rho uw}{\partial z}=-\frac{\partial P}{\partial x} \quad , \tag{4.4a}$$

(*y*-direction momentum) $$\frac{\partial\rho v}{\partial t}+\frac{\partial\rho vu}{\partial x}+\frac{\partial\rho vv}{\partial y}+\frac{\partial\rho vw}{\partial z}=-\frac{\partial P}{\partial y} \quad , \tag{4.4b}$$

and

(*z*-direction momentum) $$\frac{\partial\rho w}{\partial t}+\frac{\partial\rho wu}{\partial x}+\frac{\partial\rho wv}{\partial y}+\frac{\partial\rho ww}{\partial z}=-\frac{\partial P}{\partial z}-\rho g_z \quad . \tag{4.4c}$$

The kinematic boundary conditions at the bed and free surface are

(bottom surface) $$\frac{D(z-\alpha)}{Dt}=0 \quad \text{or} \quad w=\frac{\partial\alpha}{\partial t}+u\frac{\partial\alpha}{\partial x}+v\frac{\partial\alpha}{\partial y} \quad , \tag{4.5a}$$

and

(free surface) $$\frac{D(z-\beta)}{Dt}=0 \quad \text{or} \quad w=\frac{\partial\beta}{\partial t}+u\frac{\partial\beta}{\partial x}+v\frac{\partial\beta}{\partial y} \quad . \tag{4.5b}$$

4.3 3-D Green-Naghdi Continuity Equation for Free Surface Flow of Inviscid, Incompressible Liquid

To derive the Green-Naghdi equations, the velocity field is first approximated using the following fundamental kinematic assumption,

$$\vec{u}(x,y,z,t)=\sum_{n=0}^{K}\vec{W}_n(x,y,t)\lambda_n(z) \quad , \tag{4.6}$$

where $\vec{W}_n=(u_n,v_n,w_n)$ and λ_n are assumed shape functions, which depend only on *z*, and *K* is the level of approximation of the GN theory.

Insertion of Equation (4.6) into the continuity equation [Equation (4.3)] gives

$$\sum_{n=0}^{K}\left[\frac{\partial u_n}{\partial x}+\frac{\partial v_n}{\partial y}\right]\lambda_n(z)+\sum_{m=0}^{K}w_n\frac{\partial\lambda_n(z)}{\partial z}=0 \quad . \tag{4.7}$$

Similarly, insertion of Equation (4.6) into the kinematic boundary conditions [Equation (4.5)], leads to

(bottom surface) $$\sum_{n=0}^{K}w_n\lambda_n(\alpha)=\frac{\partial\alpha}{\partial t}+\sum_{n=0}^{K}u_n\lambda_n\frac{\partial\alpha}{\partial x}+\sum_{n=0}^{K}v_n\lambda_n\frac{\partial\alpha}{\partial y}, \tag{4.8a}$$

and

(free surface) $$\sum_{n=0}^{K}w_n\lambda_n(\beta)=\frac{\partial\beta}{\partial t}+\sum_{n=0}^{K}u_n\lambda_n\frac{\partial\beta}{\partial x}+\sum_{n=0}^{K}v_n\lambda_n\frac{\partial\beta}{\partial y} \quad . \tag{4.8b}$$

4.4 2-D Green-Naghdi Momentum Equations for Free Surface Flow of Inviscid, Incompressible Liquid

From now on, the derivation is given for 2-dimensional (*x* and *z*) vertical plane flow. Restating the momentum equations [Equation (4.4)] in conservation form gives,

x-direction
$$\frac{\partial \rho u}{\partial t}+\frac{\partial \rho uu}{\partial x}+\frac{\partial \rho uw}{\partial z}=-\frac{\partial P}{\partial x}, \tag{4.9a}$$

and

z-direction
$$\frac{\partial \rho w}{\partial t}+\frac{\partial \rho wu}{\partial x}+\frac{\partial \rho ww}{\partial z}=-\frac{\partial P}{\partial z}-\rho g_z \quad . \tag{4.9b}$$

To satisfy the momentum equation in a depth-averaged form for each fluid sheet, Equation (4.9) is multiplied by λ_n and depth-integrated from the bottom surface, $\alpha(x,t)$ to the free surface, $\beta(x,t)$ (Krylov-Kantorovich method [Demirbilek and Webster, 1992]). The *x*-direction momentum equation is considered first, before the *z*-direction momentum equation.

4.4.1 *x*-direction Green-Naghdi Momentum Equation

After integration, Equation (4.9a) becomes

$$\int_{z=\alpha}^{\beta}\left(\frac{\partial \rho u}{\partial t}+\frac{\partial \rho uu}{\partial x}+\frac{\partial \rho uw}{\partial z}\right)\lambda_n dz=-\int_{\alpha}^{\beta}\left(\frac{\partial P}{\partial x}\right)\lambda_n dz \quad . \tag{4.10}$$

Rewriting the left hand side (LHS) of Equation (4.10),

$$\int_{z=\alpha}^{\beta}\left(\lambda_n\frac{\partial \rho u}{\partial t}+\frac{\partial \rho uu}{\partial x}\lambda_n+\frac{\partial \rho uw}{\partial z}\lambda_n\right)dz \quad ,$$

and using the chain rule for the third term, gives

$$\int_{z=\alpha}^{\beta}\left(\frac{\partial \rho u\lambda_n}{\partial t}\right)dz+\int_{z=\alpha}^{\beta}\left(\frac{\partial \rho uu\lambda_n}{\partial x}\right)dz+\rho\left(uw\lambda_n\right)\Big|_{\alpha}^{\beta}-\int_{z=\alpha}^{\beta}\left(\rho uw\lambda_n{}'\right)dz \quad , \tag{4.11}$$

where $\lambda_n{}' = \dfrac{d\lambda_n}{dz}$. Next, applying Leibnitz' Rule to the RHS of Equation (4.10), gives

$$
\begin{aligned}
&-\int_{z=\alpha}^{\beta}\left(\frac{\partial P\lambda_n}{\partial x}\right)dz \\
&= -\frac{\partial\left(\displaystyle\int_{z=\alpha}^{\beta}\left(P\lambda_n\right)dz\right)}{\partial x} + \left[P\lambda_n\right]\Big|_{z=\beta}\frac{\partial\beta}{\partial x} - \left[P\lambda_n\right]\Big|_{z=\alpha}\frac{\partial\alpha}{\partial x}.
\end{aligned}
\tag{4.12}
$$

Combining Equation (4.11) and Equation (4.12) gives,

$$
\begin{aligned}
&\int_{z=\alpha}^{\beta}\left(\frac{\partial\rho u\lambda_n}{\partial t}\right)dz + \int_{z=\alpha}^{\beta}\left(\frac{\partial\rho uu\lambda_n}{\partial x}\right)dz + \rho\left(uw\lambda_n\right)\Big|_{z=\alpha}^{\beta} - \int_{z=\alpha}^{\beta}\left(\rho uw\lambda_n{}'\right)dz = \\
&-\frac{\partial P_n}{\partial x} + \hat{p}\,\lambda_n\Big|_{z=\beta}\frac{\partial\beta}{\partial x} - \overline{p}\,\lambda_n\Big|_{z=\alpha}\frac{\partial\alpha}{\partial x},
\end{aligned}
\tag{4.13}
$$

where

$P_n = \left(\displaystyle\int_{z=\alpha}^{\beta}\left(P\lambda_n\right)dz\right)$, $\hat{p}$ is pressure at the free surface and $\overline{p}$ is pressure at the bottom surface.

Inserting the kinematic assumptions [Equation (4.6)] into the LHS of Equation (4.13), gives

$$
\begin{aligned}
&\int_{z=\alpha}^{\beta}\left(\frac{\partial\rho\displaystyle\sum_{m=0}^{K}u_m\lambda_m\lambda_n}{\partial t}\right)dz + \int_{z=\alpha}^{\beta}\left(\frac{\partial\rho\displaystyle\sum_{m=0}^{K}u_m\lambda_m\sum_{r=0}^{K}u_r\lambda_r\lambda_n}{\partial x}\right)dz + \rho\sum_{m=0}^{K}u_m\lambda_m\sum_{r=0}^{K}w_r\lambda_r\lambda_n\Bigg|_{z=\alpha}^{\beta} \\
&-\int_{z=\alpha}^{\beta}\left(\rho\sum_{m=0}^{K}u_m\lambda_m\sum_{r=0}^{K}w_r\lambda_r\lambda_n{}'\right)dz \\
&= \sum_{m=0}^{K}\rho\frac{\partial u_m}{\partial t}\int_{z=\alpha}^{\beta}\left(\lambda_m\lambda_n\right)dz + \sum_{m=0}^{K}\sum_{r=0}^{K}\rho\frac{\partial u_m u_r}{\partial x}\int_{z=\alpha}^{\beta}\left(\lambda_m\lambda_r\lambda_n\right)dz + \sum_{m=0}^{K}\sum_{r=0}^{K}\rho u_m w_r\left(\lambda_m\lambda_r\lambda_n\right)\Bigg|_{z=\alpha}^{\beta} \\
&-\sum_{m=0}^{K}\sum_{r=0}^{K}\rho u_m w_r\int_{z=\alpha}^{\beta}\left(\lambda_m\lambda_r\lambda_n{}'\right)dz \\
&= \sum_{m=0}^{K}\rho\frac{\partial u_m}{\partial t}y_{mn} + \sum_{m=0}^{K}\sum_{r=0}^{K}\rho\frac{\partial u_m u_r}{\partial x}y_{mrn} + \sum_{m=0}^{K}\sum_{r=0}^{K}\rho u_m w_r\left(\lambda_m\lambda_r\lambda_n\right)\Bigg|_{z=\alpha}^{\beta} - \sum_{m=0}^{K}\sum_{r=0}^{K}\rho u_m w_r y_{mr}^{n},
\end{aligned}
\tag{4.14}
$$

where

$$y_{mn} = \int_{z=\alpha}^{\beta} (\lambda_m \lambda_n) dz \, , \, y_{mrn} = \int_{z=\alpha}^{\beta} (\lambda_m \lambda_r \lambda_n) dz \, , \, y_{mr}^{n} = \int_{z=\alpha}^{\beta} \left(\lambda_m \lambda_r \lambda_n{}'\right) dz \quad .$$

Equation (4.13) can now be written as,

$$\begin{gathered}\sum_{m=0}^{K} \rho \frac{\partial u_m}{\partial t} y_{mn} + \sum_{m=0}^{K} \sum_{r=0}^{K} \rho \frac{\partial u_m u_r}{\partial x} y_{mrn} + \sum_{m=0}^{K} \sum_{r=0}^{K} \rho u_m w_r \left(\lambda_m \lambda_r \lambda_n\right)\Big|_{z=\alpha}^{\beta} - \sum_{m=0}^{K} \sum_{r=0}^{K} \rho u_m w_r y_{mr}^{n} = \\ -\frac{\partial P_n}{\partial x} + \hat{p}\, \lambda_n\big|_{z=\beta} \frac{\partial \beta}{\partial x} - \bar{p}\, \lambda_n\big|_{z=\alpha} \frac{\partial \alpha}{\partial x} .\end{gathered} \qquad (4.14)$$

Equation (4.14) can be reduced further by applying the Krylov-Kantorovich method to the continuity equation [Equation (4.7)]. Changing the index *m* to *r*, Equation (4.7) becomes

$$\sum_{r=0}^{K} \frac{\partial u_r}{\partial x} \lambda_r + \sum_{r=0}^{K} w_r \lambda_r{}' = 0 \quad . \qquad (4.15)$$

Next, Equation (4.15) is multiplied with λ_m and λ_n (and summed over m). It is then depth integrated, giving

$$\int_{z=\alpha}^{\beta} \sum_{m=0}^{K} \sum_{r=0}^{K} \frac{\partial u_r}{\partial x} \lambda_r \lambda_m \lambda_n dz + \int_{z=\alpha}^{\beta} \sum_{m=0}^{K} \sum_{r=0}^{K} w_r \lambda_r{}' \lambda_m \lambda_n dz = 0 \quad . \qquad (4.16)$$

Interchanging the order of summation and integration,

$$\begin{gathered}\sum_{m=0}^{K} \sum_{r=0}^{K} \frac{\partial u_r}{\partial x} y_{mrn} + \sum_{m=0}^{K} \sum_{r=0}^{K} w_r y_{mn}^{r} = 0 \\ \sum_{m=0}^{K} \sum_{r=0}^{K} \frac{\partial u_r}{\partial x} y_{mrn} = -\sum_{m=0}^{K} \sum_{r=0}^{K} w_r y_{mn}^{r} ,\end{gathered} \qquad (4.17)$$

where $y_{mn}^{r} = \int_{z=\alpha}^{\beta} \left(\lambda_m \lambda_n \lambda_r{}'\right) dz$.

From the LHS of Equation (4.14), the second term can be expanded using the chain rule and then replaced by Equation (4.17),

$$\begin{aligned}
&\sum_{m=0}^{K}\rho\frac{\partial u_m}{\partial t}y_{mn}+\sum_{m=0}^{K}\sum_{r=0}^{K}\rho\frac{\partial u_m}{\partial x}u_r y_{mrn}+\sum_{m=0}^{K}\sum_{r=0}^{K}\rho\frac{\partial u_r}{\partial x}u_m y_{mrn}+\sum_{m=0}^{K}\sum_{r=0}^{K}\rho u_m w_r\left(\lambda_m\lambda_r\lambda_n\right)\Big|_{z=\alpha}^{\beta}-\sum_{m=0}^{K}\sum_{r=0}^{K}\rho u_m w_r y_{mr}^{n}\\
&=\sum_{m=0}^{K}\rho\frac{\partial u_m}{\partial t}y_{mn}+\sum_{m=0}^{K}\sum_{r=0}^{K}\rho\frac{\partial u_m}{\partial x}u_r y_{mrn}-\sum_{m=0}^{K}\sum_{r=0}^{K}\rho u_m w_r y_{mn}^{r}+\sum_{m=0}^{K}\sum_{r=0}^{K}\rho u_m w_r\left(\lambda_m\lambda_r\lambda_n\right)\Big|_{z=\alpha}^{\beta}-\sum_{m=0}^{K}\sum_{r=0}^{K}\rho u_m w_r y_{mr}^{n}\\
&=\sum_{m=0}^{K}\rho\frac{\partial u_m}{\partial t}y_{mn}+\sum_{m=0}^{K}\sum_{r=0}^{K}\rho\frac{\partial u_m}{\partial x}u_r y_{mrn}-\sum_{m=0}^{K}\sum_{r=0}^{K}\rho u_m w_r\left(y_{mn}^{r}+y_{mr}^{n}\right)+\sum_{m=0}^{K}\sum_{r=0}^{K}\rho u_m w_r\left(\lambda_m\lambda_r\lambda_n\right)\Big|_{z=\alpha}^{\beta},
\end{aligned}\tag{4.18}$$

where $\left(y_{mn}^{r}+y_{mr}^{n}\right)$ can be determined using integration by parts as follows

$$\begin{aligned}
\left(y_{mn}^{r}+y_{mr}^{n}\right)&=\int_{z=\alpha}^{\beta}\left(\lambda_m\lambda_n\lambda_r'\right)dz+\int_{z=\alpha}^{\beta}\left(\lambda_m\lambda_r\lambda_n'\right)dz\\
&=\int_{z=\alpha}^{\beta}\left(\lambda_m\left(\lambda_n\lambda_r\right)'\right)dz\\
&=\lambda_m\lambda_n\lambda_r\big|_{z=\alpha}^{\beta}-\int_{z=\alpha}^{\beta}\left(\lambda_n\lambda_r\lambda_m'\right)dz\\
&=\lambda_m\lambda_n\lambda_r\big|_{z=\alpha}^{\beta}-y_{rn}^{m}.
\end{aligned}\tag{4.19}$$

Inserting this into Equation (4.18) to cancel the last term and combining with the RHS as in Equation (4.14), the *x*-direction momentum equation becomes,

$$\sum_{m=0}^{K}\rho\frac{\partial u_m}{\partial t}y_{mn}+\sum_{m=0}^{K}\sum_{r=0}^{K}\rho\frac{\partial u_m}{\partial x}u_r y_{mrn}+\sum_{m=0}^{K}\sum_{r=0}^{K}\rho u_m w_r y_{rn}^{m}=-\frac{\partial P_n}{\partial x}+\hat{p}\,\lambda_n\big|_{z=\beta}\frac{\partial\beta}{\partial x}-\bar{p}\,\lambda_n\big|_{z=\alpha}\frac{\partial\alpha}{\partial x}\quad .\tag{4.20}$$

4.4.2 *z*-direction Green-Naghdi Momentum Equation

To obtain the *z*-momentum equation in a depth-averaged form for each fluid sheet, Equation (4.9b) is multiplied by λ_n and depth-integrated from the bottom surface, $\alpha(x,t)$ to the free surface, $\beta(x,t)$ following the Krylov-Kantorovich method.

$$\int_{z=\alpha}^{\beta}\left(\frac{\partial\rho w}{\partial t}+\frac{\partial\rho wu}{\partial x}+\frac{\partial\rho ww}{\partial z}\right)\lambda_n dz=\int_{z=\alpha}^{\beta}\left(-\frac{\partial P}{\partial z}-\rho g_z\right)\lambda_n dz\quad .\tag{4.21}$$

Taking the left hand side (LHS) of Equation (4.21),

$$\int_{z=\alpha}^{\beta}\left(\lambda_n\frac{\partial\rho w}{\partial t}+\frac{\partial\rho wu}{\partial x}\lambda_n+\frac{\partial\rho ww}{\partial z}\lambda_n\right)dz \quad . \tag{4.22}$$

Using the chain rule for the third term,

$$\int_{z=\alpha}^{\beta}\left(\frac{\partial\rho w\lambda_n}{\partial t}\right)dz+\int_{z=\alpha}^{\beta}\left(\frac{\partial\rho wu\lambda_n}{\partial x}\right)dz+\rho\left(ww\lambda_n\right)\Big|_{\alpha}^{\beta}-\int_{z=\alpha}^{\beta}\left(\rho ww\lambda_n{}'\right)dz \quad . \tag{4.23}$$

Taking the right hand side (RHS) of Equation (4.22) and again using the chain rule,

$$\begin{aligned}&\int_{z=\alpha}^{\beta}\left(-\frac{\partial P}{\partial z}\lambda_n-\rho g_z\lambda_n\right)dz\\&=-\left[P\lambda_n\right]\Big|_{z=\alpha}^{\beta}+\int_{z=\alpha}^{\beta}P\lambda_n{}'dz-\rho g_z\int_{z=\alpha}^{\beta}\lambda_n dz.\end{aligned} \tag{4.24}$$

Combining Equation (4.23) and Equation (4.24),

$$\begin{aligned}&\int_{z=\alpha}^{\beta}\left(\frac{\partial\rho w\lambda_n}{\partial t}\right)dz+\int_{z=\alpha}^{\beta}\left(\frac{\partial\rho wu\lambda_n}{\partial x}\right)dz+\rho\left(ww\lambda_n\right)\Big|_{z=\alpha}^{\beta}-\int_{z=\alpha}^{\beta}\left(\rho ww\lambda_n{}'\right)dz=-\hat{p}\,\lambda_n\big|_{z=\beta}+\overline{p}\,\lambda_n\big|_{z=\alpha}\\&+P_n{}'-\rho g_z\int_{z=\alpha}^{\beta}\lambda_n dz,\end{aligned} \tag{4.25}$$

where $P_n{}'=\int_{z=\alpha}^{\beta}P\lambda_n{}'dz$.

After inserting the kinematic approximation, Equation (4.6), into the LHS of Equation (4.25),

$$
\begin{aligned}
&\int_{z=\alpha}^{\beta}\left(\frac{\partial \rho \sum_{m=0}^{K} w_m \lambda_m \lambda_n}{\partial t}\right) dz+\int_{z=\alpha}^{\beta}\left(\frac{\partial \rho \sum_{m=0}^{K} w_m \lambda_m \sum_{r=0}^{K} u_r \lambda_r \lambda_n}{\partial x}\right) dz+\rho \sum_{m=0}^{K} w_m \lambda_m \sum_{r=0}^{K} w_r \lambda_r \lambda_n \bigg|_{z=\alpha}^{\beta} \\
&-\int_{z=\alpha}^{\beta}\left(\rho \sum_{m=0}^{K} w_m \lambda_m \sum_{r=0}^{K} w_r \lambda_r \lambda_n{}'\right) dz \\
&=\sum_{m=0}^{K} \rho \frac{\partial w_m}{\partial t} \int_{z=\alpha}^{\beta}\left(\lambda_m \lambda_n\right) dz+\sum_{m=0}^{K} \sum_{r=0}^{K} \rho \frac{\partial w_m u_r}{\partial x} \int_{z=\alpha}^{\beta}\left(\lambda_m \lambda_r \lambda_n\right) dz+\sum_{m=0}^{K} \sum_{r=0}^{K} \rho w_m w_r\left(\lambda_m \lambda_r \lambda_n\right)\bigg|_{z=\alpha}^{\beta} \\
&-\sum_{m=0}^{K} \sum_{r=0}^{K} \rho w_m w_r \int_{z=\alpha}^{\beta}\left(\lambda_m \lambda_r \lambda_n{}'\right) dz \\
&=\sum_{m=0}^{K} \rho \frac{\partial w_m}{\partial t} y_{mn}+\sum_{m=0}^{K} \sum_{r=0}^{K} \rho \frac{\partial w_m u_r}{\partial x} y_{mrn}+\sum_{m=0}^{K} \sum_{r=0}^{K} \rho w_m w_r\left(\lambda_m \lambda_r \lambda_n\right)\bigg|_{z=\alpha}^{\beta}-\sum_{m=0}^{K} \sum_{r=0}^{K} \rho w_m w_r y_{mr}^{n} .
\end{aligned}
\tag{4.26}
$$

The equation now can be written as,

$$
\begin{aligned}
&\sum_{m=0}^{K} \rho \frac{\partial w_m}{\partial t} y_{mn}+\sum_{m=0}^{K} \sum_{r=0}^{K} \rho \frac{\partial w_m u_r}{\partial x} y_{mrn}+\sum_{m=0}^{K} \sum_{r=0}^{K} \rho w_m w_r\left(\lambda_m \lambda_r \lambda_n\right)\bigg|_{z=\alpha}^{\beta}-\sum_{m=0}^{K} \sum_{r=0}^{K} \rho w_m w_r y_{mr}^{n} \\
&=-\hat{p} \lambda_n\big|_{z=\beta}+\bar{p} \lambda_n\big|_{z=\alpha}+P_n'-\rho g_z y_n,
\end{aligned}
\tag{4.27}
$$

where $y_n=\int_{z=\alpha}^{\beta} \lambda_n dz$. Equation (4.27) can be reduced further by expanding the second term on the LHS of Equation (4.27) using the chain rule and replacing it by Equation (4.17) to give

$$
\begin{aligned}
&=\sum_{m=0}^{K} \rho \frac{\partial w_m}{\partial t} y_{mn}+\sum_{m=0}^{K} \sum_{r=0}^{K} \rho \frac{\partial w_m}{\partial x} u_r y_{mrn}+\sum_{m=0}^{K} \sum_{r=0}^{K} \rho \frac{\partial u_r}{\partial x} w_m y_{mrn}+\sum_{m=0}^{K} \sum_{r=0}^{K} \rho w_m w_r\left(\lambda_m \lambda_r \lambda_n\right)\bigg|_{z=\alpha}^{\beta} \\
&-\sum_{m=0}^{K} \sum_{r=0}^{K} \rho w_m w_r y_{mr}^{n} \\
&=\sum_{m=0}^{K} \rho \frac{\partial w_m}{\partial t} y_{mn}+\sum_{m=0}^{K} \sum_{r=0}^{K} \rho \frac{\partial w_m}{\partial x} u_r y_{mrn}-\sum_{m=0}^{K} \sum_{r=0}^{K} \rho w_m w_r y_{mn}^{r}+\sum_{m=0}^{K} \sum_{r=0}^{K} \rho w_m w_r\left(\lambda_m \lambda_r \lambda_n\right)\bigg|_{z=\alpha}^{\beta} \\
&-\sum_{m=0}^{K} \sum_{r=0}^{K} \rho w_m w_r y_{mr}^{n} \\
&=\sum_{m=0}^{K} \rho \frac{\partial w_m}{\partial t} y_{mn}+\sum_{m=0}^{K} \sum_{r=0}^{K} \rho \frac{\partial w_m}{\partial x} u_r y_{mrn}-\sum_{m=0}^{K} \sum_{r=0}^{K} \rho w_m w_r\left(y_{mn}^{r}+y_{mr}^{n}\right)+\sum_{m=0}^{K} \sum_{r=0}^{K} \rho w_m w_r\left(\lambda_m \lambda_r \lambda_n\right)\bigg|_{z=\alpha}^{\beta} .
\end{aligned}
\tag{4.28}
$$

Inserting Equation (4.19) into Equation (4.28) to cancel the last term and combining with the RHS as in Equation (4.27), the *z*-direction momentum equation is,

$$\sum_{m=0}^{K}\rho\frac{\partial w_m}{\partial t}y_{mn}+\sum_{m=0}^{K}\sum_{r=0}^{K}\rho\frac{\partial w_m}{\partial x}u_r y_{mrn}+\sum_{m=0}^{K}\sum_{r=0}^{K}\rho w_m w_r y_{rn}^{m}=-\hat{p}\,\lambda_n\big|_{z=\beta}+\bar{p}\,\lambda_n\big|_{z=\alpha}+P_n'-\rho g_z y_n \quad \cdot \tag{4.29}$$

The governing equations, which comprise the kinematic assumption, continuity equation, top and bottom kinematic boundary conditions and momentum equations in 2-D are listed below.

Kinematic assumption:

$$\vec{u}(x,y,z,t)=\sum_{n=0}^{K}\vec{W}_n(x,y,t)\lambda_n(z)\,. \tag{4.6}$$

Continuity equation:

$$\sum_{n=0}^{K}\frac{\partial u_n}{\partial x}\lambda_n(z)+\sum_{n=0}^{K}w_n\frac{\partial\lambda_n(z)}{\partial z}=0\,. \tag{4.7}$$

Bottom kinematic boundary condition

$$\sum_{n=0}^{K}w_n\lambda_n(\alpha)=\frac{\partial\alpha}{\partial t}+\sum_{n=0}^{K}u_n\lambda_n\frac{\partial\alpha}{\partial x}\,. \tag{4.8a}$$

Free surface kinematic boundary condition

$$\sum_{n=0}^{K}w_n\lambda_n(\beta)=\frac{\partial\beta}{\partial t}+\sum_{n=0}^{K}u_n\lambda_n\frac{\partial\beta}{\partial x}\,. \tag{4.8b}$$

x-direction momentum equation:

$$\sum_{m=0}^{K}\rho\frac{\partial u_m}{\partial t}y_{mn}+\sum_{m=0}^{K}\sum_{r=0}^{K}\rho\frac{\partial u_m}{\partial x}u_r y_{mrn}+\sum_{m=0}^{K}\sum_{r=0}^{K}\rho u_m w_r y_{rn}^{m}=-\frac{\partial P_n}{\partial x}+\hat{p}\,\lambda_n\big|_{z=\beta}\frac{\partial\beta}{\partial x}-\bar{p}\,\lambda_n\big|_{z=\alpha}\frac{\partial\alpha}{\partial x}\,, \tag{4.20}$$

for *n* = 0, 1, 2 … *K*.

z-direction momentum equation:

$$\sum_{m=0}^{K}\rho\frac{\partial w_m}{\partial t}y_{mn}+\sum_{m=0}^{K}\sum_{r=0}^{K}\rho\frac{\partial w_m}{\partial x}u_r y_{mrn}+\sum_{m=0}^{K}\sum_{r=0}^{K}\rho w_m w_r y_{rn}^{m}=-\hat{p}\,\lambda_n\Big|_{z=\beta}+\bar{p}\,\lambda_n\Big|_{z=\alpha}+P_n{}'-\rho g_z y_n\,, \tag{4.29}$$

for n = 0, 1, 2 … K, where $\hat{p}$ and $\bar{p}$ are pressures on the top and bottom surfaces respectively and;

$$y_{mn}=\int_{z=\alpha}^{\beta}\lambda_m\lambda_n dz \quad,\quad y_{mrn}=\int_{z=\alpha}^{\beta}\lambda_m\lambda_r\lambda_n dz \quad,\quad y_{mr}^{n}=\int_{z=\alpha}^{\beta}\lambda_m\lambda_r\frac{d\lambda_n}{dz}dz \quad,\quad y_n=\int_{z=\alpha}^{\beta}\lambda_n dz\,,$$

$$P_n=\int_{z=\alpha}^{\beta}P\lambda_n dz \quad,\quad P_n^{'}=\int_{z=\alpha}^{\beta}P\frac{d\lambda_n}{dz}dz \quad .$$

4.5 Green-Naghdi (GN) Level 1 Equation for Shallow Water Flow over a Non-uniform Bed

This section describes the derivation of the Green-Naghdi equations for a single sheet fluid model of shallow water flow over variable bed topography. It is assumed that the flow velocity profile over the water depth at any section is such that the horizontal component is uniform whereas the vertical velocity component varies linearly from zero at the bed to a maximum at the free surface. Thus, the number of sheets, $K = 1$, the second component of the horizontal velocity, $u_1 = 0$, and the shape functions are $\lambda_0 = 1$ and $\lambda_1 = z$.

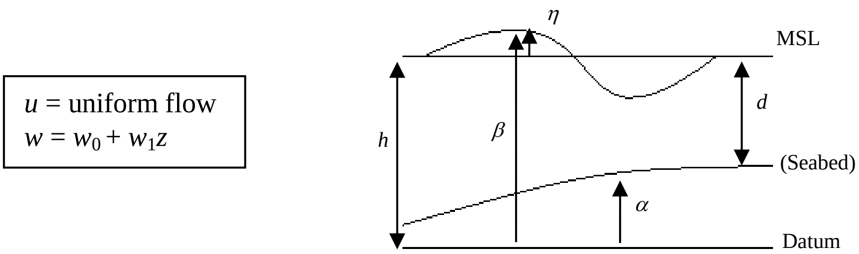

Figure 4.2: Definition sketch of flow in the vertical plane over a non-uniform bed

Figure 4.2 provides a definition sketch of the flow geometry. Here, the free surface elevation above a prescribed constant horizontal datum is defined as $\beta(x,t)=\eta(x,t)+d(x)+\alpha(x)$, where $\eta(x,t)$ is the free surface elevation above mean sea level (MSL), $d(x)$ is the vertical elevation of MSL above the seabed, and $\alpha(x)$ is the bed elevation which does not change in time. *h* is the vertical elevation of the MSL above the datum. From Equation (4.6), Equation (4.7) and Equation (4.8), the Green-Naghdi kinematic assumption gives

$$u(x,z,t)=u_0(x,t) \quad , \tag{4.30a}$$

$$w(x,z,t)=w_0(x,t)+w_1(x,t)z \, , \tag{4.30b}$$

where the free surface kinematic boundary condition (FSKBC) gives

$$w_0+w_1\beta=\frac{\partial\beta}{\partial t}+u_0\frac{\partial\beta}{\partial x} \quad , \tag{4.31a}$$

the bottom kinematic boundary condition (BKBC) gives

$$w_0+w_1\alpha=u_0\frac{\partial\alpha}{\partial x} \quad , \tag{4.31b}$$

and the continuity equation gives

$$\frac{\partial u_0}{\partial x}+\frac{\partial(w_0+w_1z)}{\partial z}=0 \tag{4.32a}$$

$$\frac{\partial u_0}{\partial x}+w_1=0 \tag{4.32b}$$

$$w_1=-\frac{\partial u_0}{\partial x} \, . \tag{4.32c}$$

Insertion of Equation (4.32c) into Equation (4.31b) at the bottom surface presents,

$$\begin{aligned} w_0 &= u_0 \frac{\partial \alpha}{\partial x} + \frac{\partial u_0}{\partial x} \alpha \\ w_0 &= \frac{\partial \left(\alpha u_0 \right)}{\partial x}. \end{aligned} \tag{4.33}$$

Then, inserting both Equation (4.32c) and Equation (4.33) into Equation (4.31a), the first GN equation is obtained as follows

$$\begin{aligned} &\frac{\partial \left(\alpha u_0 \right)}{\partial x} - \frac{\partial u_0}{\partial x} \beta = \frac{\partial \beta}{\partial t} + u_0 \frac{\partial \beta}{\partial x} \\ &\frac{\partial \beta}{\partial t} = \frac{\partial \left(\alpha u_0 \right)}{\partial x} - \frac{\partial \left(u_0 \beta \right)}{\partial x} \\ &\frac{\partial \beta}{\partial t} = \frac{\partial \left(\left(\alpha - \beta \right) u_0 \right)}{\partial x}, \end{aligned} \tag{4.34}$$

and noting that $\beta\left(x,t\right) = \eta\left(x,t\right) + d\left(x\right) + \alpha\left(x\right)$,

$$\frac{\partial \eta}{\partial t} = -\frac{\partial \left(\left(\eta + d \right) u_0 \right)}{\partial x} \quad . \tag{4.35}$$

The previously derived general GN *x*-momentum and *z*-momentum equations [Equation (4.20) and Equation (4.29)] are restated as

x-direction

$$\sum_{m=0}^{K} \rho \frac{\partial u_m}{\partial t} y_{mn} + \sum_{m=0}^{K} \sum_{r=0}^{K} \rho \frac{\partial u_m}{\partial x} u_r y_{mrn} + \sum_{m=0}^{K} \sum_{r=0}^{K} \rho u_m w_r y_{rn}^{m} = -\frac{\partial P_n}{\partial x} + \hat{p}\, \lambda_n \Big|_{z=\beta} \frac{\partial \beta}{\partial x} - \overline{p}\, \lambda_n \Big|_{z=\alpha} \frac{\partial \alpha}{\partial x}, \tag{4.36a}$$

for *n* = 0, 1, 2 … *K*.

z-direction

$$\sum_{m=0}^{K} \rho \frac{\partial w_m}{\partial t} y_{mn} + \sum_{m=0}^{K} \sum_{r=0}^{K} \rho \frac{\partial w_m}{\partial x} u_r y_{mrn} + \sum_{m=0}^{K} \sum_{r=0}^{K} \rho w_m w_r y_{rn}^{m} = -\hat{p}\, \lambda_n \Big|_{z=\beta} + \overline{p}\, \lambda_n \Big|_{z=\alpha} + P_n{}' - \rho g_z y_n, \tag{4.36b}$$

for n = 0, 1, 2 … K, where $\hat{p}$ and $\overline{p}$ are pressures on the top and bottom surfaces respectively and;

$$y_{mn} = \int_{\alpha}^{\beta} \lambda_m \lambda_n dz \quad , \quad y_{mrn} = \int_{\alpha}^{\beta} \lambda_m \lambda_r \lambda_n dz \quad , \quad y_{mr}^{n} = \int_{\alpha}^{\beta} \lambda_m \lambda_r \frac{\partial \lambda_n}{\partial z} dz \quad , \quad y_n = \int_{\alpha}^{\beta} \lambda_n dz \, ,$$

$$P_n = \int_{z=\alpha}^{\beta} P \lambda_n dz \quad , \quad P'_n = \int_{z=\alpha}^{\beta} P \frac{d\lambda_n}{dz} dz \, .$$

Inserting the given shape functions of $\lambda_0 = 1$ and $\lambda_1 = z$, the above give

$$\begin{aligned}
&y_{000} = y_{00} = y_0 = \int_{z=\alpha}^{\beta} 1 \, dz = \beta - \alpha, \\
&y_{100} = y_{001} = y_{10} = y_1 = \int_{z=\alpha}^{\beta} z \, dz = \frac{\beta^2 - \alpha^2}{2}, \\
&y_{110} = y_{101} = y_{011} = y_{11} = \int_{z=\alpha}^{\beta} z^2 dz = \frac{\beta^3 - \alpha^3}{3}, \\
&y_{mr}^{0} = \int_{z=\alpha}^{\beta} \lambda_m \lambda_r \frac{d1}{dz} dz = 0, \\
&y_{00}^{1} = \int_{z=\alpha}^{\beta} 1 \frac{dz}{dz} dz = \beta - \alpha, \\
&y_{10}^{1} = y_{01}^{1} = \int_{z=\alpha}^{\beta} z \frac{dz}{dz} dz = \frac{\beta^2 - \alpha^2}{2}, \\
&y_{11}^{1} = \int_{z=\alpha}^{\beta} z^2 \frac{dz}{dz} dz = \frac{\beta^3 - \alpha^3}{3}, \\
&P_0 = \int_{z=\alpha}^{\beta} P \, dz, P_1 = \int_{z=\alpha}^{\beta} Pz \, dz, \\
&P'_1 = \int_{z=\alpha}^{\beta} P \frac{dz}{dz} dz = \int_{z=\alpha}^{\beta} P \, dz = P_0.
\end{aligned} \tag{4.37}$$

Expanding Equation (4.36) based on the given kinematic assumptions (for n = 0 and 1), gives the following. In the x-direction:

n = 0

$$\rho \frac{\partial u_0}{\partial t} y_{00} + \rho \frac{\partial u_0}{\partial x} u_0 y_{000} + \rho u_0 w_0 y_{00}^{0} + \rho u_0 w_1 y_{10}^{0} = -\frac{\partial P_0}{\partial x} + \hat{p} \, \lambda_0 \big|_{z=\beta} \frac{\partial \beta}{\partial x} - \overline{p} \, \lambda_0 \big|_{z=\alpha} \frac{\partial \alpha}{\partial x} \quad , \tag{4.38a}$$

$$n = 1 \qquad \rho\frac{\partial u_0}{\partial t}y_{01} + \rho\frac{\partial u_0}{\partial x}u_0 y_{001} + \rho u_0 w_0 y_{01}^0 + \rho u_0 w_1 y_{11}^0 = -\frac{\partial P_1}{\partial x} + \hat{p}\,\lambda_1\big|_{z=\beta}\frac{\partial\beta}{\partial x} - \overline{p}\,\lambda_1\big|_{z=\alpha}\frac{\partial\alpha}{\partial x}\ , \tag{4.38b}$$

And in the *z*-direction:

$$n = 0 \qquad \begin{bmatrix} \rho\frac{\partial w_0}{\partial t}y_{00} + \rho\frac{\partial w_1}{\partial t}y_{10} + \rho\frac{\partial w_0}{\partial x}u_0 y_{000} + \rho\frac{\partial w_1}{\partial x}u_0 y_{100} \\ +\rho w_0 w_0 y_{00}^0 + \rho w_0 w_1 y_{10}^0 + \rho w_1 w_0 y_{00}^1 + \rho w_1 w_1 y_{10}^1 \end{bmatrix} = -\hat{p}\,\lambda_0\big|_{z=\beta} + \overline{p}\,\lambda_0\big|_{z=\alpha} + P_0' - \rho g y_0, \tag{4.39a}$$

$$n = 1 \qquad \begin{bmatrix} \rho\frac{\partial w_0}{\partial t}y_{01} + \rho\frac{\partial w_1}{\partial t}y_{11} + \rho\frac{\partial w_0}{\partial x}u_0 y_{001} + \rho\frac{\partial w_1}{\partial x}u_0 y_{101} \\ +\rho w_0 w_0 y_{01}^0 + \rho w_0 w_1 y_{11}^0 + \rho w_1 w_0 y_{01}^1 + \rho w_1 w_1 y_{11}^1 \end{bmatrix} = -\hat{p}\,\lambda_1\big|_{z=\beta} + \overline{p}\,\lambda_1\big|_{z=\alpha} + P_1' - \rho g y_1, \tag{4.39b}$$

Insertion of Equation (4.37) into Equation (4.38) and Equation (4.39) gives the following. In the *x*-direction:

$$n = 0 \qquad \rho\frac{\partial u_0}{\partial t}(\beta-\alpha) + \rho\frac{\partial u_0}{\partial x}u_0(\beta-\alpha) = -\frac{\partial P_{0_x}}{\partial x} + \hat{p}\frac{\partial\beta}{\partial x} - \overline{p}\frac{\partial\alpha}{\partial x}\,, \tag{4.40a}$$

$$n = 1 \qquad \rho\frac{\partial u_0}{\partial t}\left(\frac{\beta^2-\alpha^2}{2}\right) + \rho\frac{\partial u_0}{\partial x}u_0\left(\frac{\beta^2-\alpha^2}{2}\right) = -\frac{\partial P_{1_x}}{\partial x} + \hat{p}\beta\frac{\partial\beta}{\partial x} - \overline{p}\alpha\frac{\partial\alpha}{\partial x}\,, \tag{4.40b}$$

And in the *z*-direction

$$n = 0 \qquad \begin{bmatrix} \rho\frac{\partial w_0}{\partial t}(\beta-\alpha) + \rho\frac{\partial w_1}{\partial t}\left(\frac{\beta^2-\alpha^2}{2}\right) + \rho\frac{\partial w_0}{\partial x}u_0(\beta-\alpha) + \\ \rho\frac{\partial w_1}{\partial x}u_0\left(\frac{\beta^2-\alpha^2}{2}\right) + \rho w_1 w_0(\beta-\alpha) + \rho w_1{}^2\left(\frac{\beta^2-\alpha^2}{2}\right) \end{bmatrix} = -\hat{p} + \overline{p} - \rho g(\beta-\alpha), \tag{4.40c}$$

$$n = 1 \quad \begin{bmatrix} \rho\frac{\partial w_0}{\partial t}\left(\frac{\beta^2-\alpha^2}{2}\right) + \rho\frac{\partial w_1}{\partial t}\left(\frac{\beta^3-\alpha^3}{3}\right) + \rho\frac{\partial w_0}{\partial x}u_0\left(\frac{\beta^2-\alpha^2}{2}\right) + \\ \rho\frac{\partial w_1}{\partial x}u_0\left(\frac{\beta^3-\alpha^3}{3}\right) + \rho w_1 w_0\left(\frac{\beta^2-\alpha^2}{2}\right) + \rho w_1{}^2\left(\frac{\beta^3-\alpha^3}{3}\right) \end{bmatrix} = -\hat{p}\beta + \overline{p}\alpha + P_{1_z}{}' - \rho g\left(\frac{\beta^2-\alpha^2}{2}\right). \tag{4.40d}$$

Eliminating w_0 and w_1 from z-direction momentum equations [Equation (4.40c) and Equation (4.40d)] using Equation (4.32c) and Equation (4.33), gives the following:

$n = 0$

$$\begin{bmatrix} \rho\left(\beta-\alpha\right)\left(\alpha\frac{\partial^2 u_0}{\partial x\partial t}+\frac{\partial u_0}{\partial t}\frac{\partial \alpha}{\partial x}\right)-\rho\frac{\partial^2 u_0}{\partial x\partial t}\left(\frac{\beta^2-\alpha^2}{2}\right)+ \\ \rho u_0\left(\beta-\alpha\right)\left(\alpha\frac{\partial^2 u_0}{\partial x^2}+2\frac{\partial u_0}{\partial x}\frac{\partial \alpha}{\partial x}+u_0\frac{\partial^2 \alpha}{\partial x^2}\right)-\rho\frac{\partial^2 u_0}{\partial x^2}u_0\left(\frac{\beta^2-\alpha^2}{2}\right) \\ -\rho\frac{\partial u_0}{\partial x}\left(\beta-\alpha\right)\left(\alpha\frac{\partial u_0}{\partial x}+u_0\frac{\partial \alpha}{\partial x}\right)+\rho\left(\frac{\partial u_0}{\partial x}\right)^2\left(\frac{\beta^2-\alpha^2}{2}\right) \end{bmatrix}=-\hat{p}+\overline{p}-\rho g\left(\beta-\alpha\right), \tag{4.41a}$$

$n = 1$

$$\begin{bmatrix} \rho\left(\frac{\beta^2-\alpha^2}{2}\right)\left(\alpha\frac{\partial^2 u_0}{\partial x\partial t}+\frac{\partial u_0}{\partial t}\frac{\partial \alpha}{\partial x}\right)-\rho\frac{\partial^2 u_0}{\partial x\partial t}\left(\frac{\beta^3-\alpha^3}{3}\right)+ \\ \rho u_0\left(\frac{\beta^2-\alpha^2}{2}\right)\left(\alpha\frac{\partial^2 u_0}{\partial x^2}+2\frac{\partial u_0}{\partial x}\frac{\partial \alpha}{\partial x}+u_0\frac{\partial^2 \alpha}{\partial x^2}\right)-\rho\frac{\partial^2 u_0}{\partial x^2}u_0\left(\frac{\beta^3-\alpha^3}{3}\right) \\ -\rho\frac{\partial u_0}{\partial x}\left(\alpha\frac{\partial u_0}{\partial x}+u_0\frac{\partial \alpha}{\partial x}\right)\left(\frac{\beta^2-\alpha^2}{2}\right)+\rho\left(\frac{\partial u_0}{\partial x}\right)^2\left(\frac{\beta^3-\alpha^3}{3}\right) \end{bmatrix}=-\hat{p}\beta+\overline{p}\alpha+{P_{1_z}}'-\rho g\left(\frac{\beta^2-\alpha^2}{2}\right). \tag{4.41b}$$

Differentiating Equation (4.41b) with respect to x and adding to Equation (4.40a) to eliminate the pressure term, leads to

$$\rho\begin{bmatrix} \frac{\partial u_0}{\partial t}\left(\beta-\alpha\right)+\frac{\partial u_0}{\partial x}u_0\left(\beta-\alpha\right)+\left(\beta\frac{\partial \beta}{\partial x}-\alpha\frac{\partial \alpha}{\partial x}\right)\left(\alpha\frac{\partial^2 u_0}{\partial x\partial t}+\frac{\partial u_0}{\partial t}\frac{\partial \alpha}{\partial x}\right)+\left(\frac{\beta^2-\alpha^2}{2}\right) \\ \left(\frac{\partial^2 \alpha}{\partial x^2}\frac{\partial u_0}{\partial t}+2\frac{\partial^2 u_0}{\partial x\partial t}\frac{\partial \alpha}{\partial x}+\alpha\frac{\partial^3 u_0}{\partial x^2\partial t}\right)-\left(\frac{\beta^3-\alpha^3}{3}\right)\frac{\partial^3 u_0}{\partial x^2\partial t}-\left(\beta^2\frac{\partial \beta}{\partial x}-\alpha^2\frac{\partial \alpha}{\partial x}\right)\frac{\partial^2 u_0}{\partial x\partial t}+ \\ \left(\begin{matrix} \frac{\partial u_0}{\partial x}\left(\frac{\beta^2-\alpha^2}{2}\right)+ \\ u_0\left(\beta\frac{\partial \beta}{\partial x}-\alpha\frac{\partial \alpha}{\partial x}\right) \end{matrix}\right)\left(\alpha\frac{\partial^2 u_0}{\partial x^2}+2\frac{\partial u_0}{\partial x}\frac{\partial \alpha}{\partial x}+u_0\frac{\partial^2 \alpha}{\partial x^2}\right)+u_0\left(\frac{\beta^2-\alpha^2}{2}\right) \\ \left(3\frac{\partial \alpha}{\partial x}\frac{\partial^2 u_0}{\partial x^2}+\alpha\frac{\partial^3 u_0}{\partial x^3}+3\frac{\partial u_0}{\partial x}\frac{\partial^2 \alpha}{\partial x^2}+u_0\frac{\partial^3 \alpha}{\partial x^3}\right)-\left(\frac{\beta^3-\alpha^3}{3}\right)\left(\frac{\partial^3 u_0}{\partial x^3}u_0+\frac{\partial^2 u_0}{\partial x^2}\frac{\partial u_0}{\partial x}\right) \\ -\left(\beta^2\frac{\partial \beta}{\partial x}-\alpha^2\frac{\partial \alpha}{\partial x}\right)\frac{\partial^2 u_0}{\partial x^2}u_0-\left(\beta\frac{\partial \beta}{\partial x}-\alpha\frac{\partial \alpha}{\partial x}\right)\left(\alpha\frac{\partial u_0}{\partial x}+u_0\frac{\partial \alpha}{\partial x}\right)\frac{\partial u_0}{\partial x}-\left(\frac{\beta^2-\alpha^2}{2}\right) \\ \left(\alpha\frac{\partial u_0}{\partial x}+u_0\frac{\partial \alpha}{\partial x}\right)\frac{\partial^2 u_0}{\partial x^2}-\left(\frac{\beta^2-\alpha^2}{2}\right)\left(2\frac{\partial \alpha}{\partial x}\frac{\partial u_0}{\partial x}+\alpha\frac{\partial^2 u_0}{\partial x^2}+u_0\frac{\partial^2 \alpha}{\partial x^2}\right)\frac{\partial u_0}{\partial x}+2\left(\frac{\beta^3-\alpha^3}{3}\right) \\ \frac{\partial u_0}{\partial x}\frac{\partial^2 u_0}{\partial x^2}+\left(\frac{\partial u_0}{\partial x}\right)^2\left(\beta^2\frac{\partial \beta}{\partial x}-\alpha^2\frac{\partial \alpha}{\partial x}\right) \end{bmatrix}=\begin{pmatrix} -\beta\frac{\partial \hat{p}}{\partial x}+\alpha\frac{\partial \overline{p}}{\partial x} \\ -\rho g\left(\beta\frac{\partial \beta}{\partial x}-\alpha\frac{\partial \alpha}{\partial x}\right) \end{pmatrix}. \tag{4.42}$$

Assuming the standard dynamic boundary condition on the free surface, then the pressure on the top surface is constant, so $\frac{\partial \hat{p}}{\partial x} = 0$. Rearranging and dividing Equation (4.42) by ρ gives

$$\begin{aligned}
&\left[\beta - \alpha + \left(\beta \frac{\partial \beta}{\partial x} - \alpha \frac{\partial \alpha}{\partial x}\right)\frac{\partial \alpha}{\partial x} + \left(\frac{\beta^2}{2} - \frac{\alpha^2}{2}\right)\frac{\partial^2 \alpha}{\partial x^2}\right]\frac{\partial u_0}{\partial t} + \\
&\left[\alpha\left(\beta \frac{\partial \beta}{\partial x} - \alpha \frac{\partial \alpha}{\partial x}\right) + \beta^2\left(\frac{\partial \alpha}{\partial x} - \frac{\partial \beta}{\partial x}\right)\right]\frac{\partial^2 u_0}{\partial x \partial t} + \\
&\left[\alpha\left(\frac{\beta^2}{2} - \frac{\alpha^2}{2}\right) - \left(\frac{\beta^3}{3} - \frac{\alpha^3}{3}\right)\right]\frac{\partial^3 u_0}{\partial x^2 \partial t} = \\
&\left[\alpha - \beta + 3\left(\frac{\alpha^2}{2} - \frac{\beta^2}{2}\right)\frac{\partial^2 \alpha}{\partial x^2} + \left(\alpha \frac{\partial \alpha}{\partial x} - \beta \frac{\partial \beta}{\partial x}\right)\frac{\partial \alpha}{\partial x}\right] u_0 \frac{\partial u_0}{\partial x} + \\
&\left[\left(\frac{\alpha^2}{2} - \frac{\beta^2}{2}\right)\frac{\partial^3 \alpha}{\partial x^3} + \left(\alpha \frac{\partial \alpha}{\partial x} - \beta \frac{\partial \beta}{\partial x}\right)\frac{\partial^2 \alpha}{\partial x^2}\right] {u_0}^2 + \\
&\left[\beta \frac{\partial \beta}{\partial x}(\alpha - \beta)\right]\left(\frac{\partial u_0}{\partial x}\right)^2 + \\
&\left[-\alpha\left(\frac{\alpha^2}{2} - \frac{\beta^2}{2}\right) + \left(\frac{\alpha^3}{3} - \frac{\beta^3}{3}\right)\right]\frac{\partial u_0}{\partial x}\frac{\partial^2 u_0}{\partial x^2} + \\
&\left[\alpha\left(\alpha \frac{\partial \alpha}{\partial x} - \beta \frac{\partial \beta}{\partial x}\right) + \beta^2\left(-\frac{\partial \alpha}{\partial x} + \frac{\partial \beta}{\partial x}\right)\right] u_0 \frac{\partial^2 u_0}{\partial x^2} + \\
&\left[\alpha\left(\frac{\alpha^2}{2} - \frac{\beta^2}{2}\right) - \left(\frac{\alpha^3}{3} - \frac{\beta^3}{3}\right)\right] u_0 \frac{\partial^3 u_0}{\partial x^3} + \frac{\alpha}{\rho}\frac{\partial \overline{p}}{\partial x} - g\left(\beta \frac{\partial \beta}{\partial x} - \alpha \frac{\partial \alpha}{\partial x}\right).
\end{aligned} \tag{4.43}$$

Pressure at the bottom surface in Equation (4.43) is eliminated using the *z*-direction momentum equation [Equation (4.41a)]. By differentiating Equation (4.41a) by *x*, and dividing by ρ, the following equation is obtained.

$$\frac{\partial\left[\begin{array}{l}\left(\beta-\alpha\right)\left(\alpha\frac{\partial^2 u_0}{\partial x\partial t}+\frac{\partial u_0}{\partial t}\frac{\partial\alpha}{\partial x}\right)-\frac{\partial^2 u_0}{\partial x\partial t}\left(\frac{\beta^2-\alpha^2}{2}\right)+\\ u_0\left(\beta-\alpha\right)\left(\alpha\frac{\partial^2 u_0}{\partial x^2}+2\frac{\partial u_0}{\partial x}\frac{\partial\alpha}{\partial x}+u_0\frac{\partial^2\alpha}{\partial x^2}\right)-\frac{\partial^2 u_0}{\partial x^2}u_0\left(\frac{\beta^2-\alpha^2}{2}\right)\\ -\frac{\partial u_0}{\partial x}\left(\beta-\alpha\right)\left(\alpha\frac{\partial u_0}{\partial x}+u_0\frac{\partial\alpha}{\partial x}\right)+\left(\frac{\partial u_0}{\partial x}\right)^2\left(\frac{\beta^2-\alpha^2}{2}\right)\end{array}\right]}{\partial x}=\frac{\partial\left(-\frac{\hat{p}}{\rho}+\frac{\overline{p}}{\rho}-g\left(\beta-\alpha\right)\right)}{\partial x}$$

$$\left(\begin{array}{l}\left[\begin{array}{l}\left(\beta-\alpha\right)\left(\frac{\partial\alpha}{\partial x}\frac{\partial^2 u_0}{\partial x\partial t}+\alpha\frac{\partial^3 u_0}{\partial x^2\partial t}+\frac{\partial^2 u_0}{\partial x\partial t}\frac{\partial\alpha}{\partial x}+\frac{\partial u_0}{\partial t}\frac{\partial^2\alpha}{\partial x^2}\right)\\ +\left(\frac{\partial\beta}{\partial x}-\frac{\partial\alpha}{\partial x}\right)\left(\alpha\frac{\partial^2 u_0}{\partial x\partial t}+\frac{\partial u_0}{\partial t}\frac{\partial\alpha}{\partial x}\right)\end{array}\right]\\ -\left[\frac{\partial^3 u_0}{\partial x^2\partial t}\left(\frac{\beta^2-\alpha^2}{2}\right)+\frac{\partial^2 u_0}{\partial x\partial t}\left(\beta\frac{\partial\beta}{\partial x}-\alpha\frac{\partial\alpha}{\partial x}\right)\right]+\\ \left[\begin{array}{l}u_0\left(\beta-\alpha\right)\left(3\frac{\partial\alpha}{\partial x}\frac{\partial^2 u_0}{\partial x^2}+\alpha\frac{\partial^3 u_0}{\partial x^3}+3\frac{\partial u_0}{\partial x}\frac{\partial^2\alpha}{\partial x^2}+u_0\frac{\partial^3\alpha}{\partial x^3}\right)\\ +\left(\frac{\partial u_0}{\partial x}\left(\beta-\alpha\right)+u_0\left(\frac{\partial\beta}{\partial x}-\frac{\partial\alpha}{\partial x}\right)\right)\left(\alpha\frac{\partial^2 u_0}{\partial x^2}+2\frac{\partial u_0}{\partial x}\frac{\partial\alpha}{\partial x}+u_0\frac{\partial^2\alpha}{\partial x^2}\right)\end{array}\right]\\ -\left[\left(\frac{\partial^2 u_0}{\partial x^2}\frac{\partial u_0}{\partial x}+\frac{\partial^3 u_0}{\partial x^3}u_0\right)\left(\frac{\beta^2-\alpha^2}{2}\right)+\frac{\partial^2 u_0}{\partial x^2}u_0\left(\beta\frac{\partial\beta}{\partial x}-\alpha\frac{\partial\alpha}{\partial x}\right)\right]\\ -\left[\begin{array}{l}\left(\frac{\partial u_0}{\partial x}\left(\frac{\partial\beta}{\partial x}-\frac{\partial\alpha}{\partial x}\right)+\frac{\partial^2 u_0}{\partial x^2}\left(\beta-\alpha\right)\right)\left(\alpha\frac{\partial u_0}{\partial x}+u_0\frac{\partial\alpha}{\partial x}\right)+\\ \frac{\partial u_0}{\partial x}\left(\beta-\alpha\right)\left(2\frac{\partial\alpha}{\partial x}\frac{\partial u_0}{\partial x}+\alpha\frac{\partial^2 u_0}{\partial x^2}+u_0\frac{\partial^2\alpha}{\partial x^2}\right)\end{array}\right]+\\ \left[\left(\frac{\partial u_0}{\partial x}\right)^2\left(\beta\frac{\partial\beta}{\partial x}-\alpha\frac{\partial\alpha}{\partial x}\right)+2\frac{\partial^2 u_0}{\partial x^2}\frac{\partial u_0}{\partial x}\left(\frac{\beta^2-\alpha^2}{2}\right)\right]\end{array}\right)=\frac{1}{\rho}\frac{\partial\overline{p}}{\partial x}-g\left(\frac{\partial\beta}{\partial x}-\frac{\partial\alpha}{\partial x}\right). \tag{4.44}$$

Rearranging Equation (4.44), the pressure at the bottom surface is given by,

$$
\begin{aligned}
\frac{1}{\rho}\frac{\partial \overline{p}}{\partial x} &= \frac{\partial u_0}{\partial t}\left(\left(\beta-\alpha\right)\frac{\partial^2 \alpha}{\partial x^2}+\frac{\partial \alpha}{\partial x}\left(\frac{\partial \beta}{\partial x}-\frac{\partial \alpha}{\partial x}\right)\right)+\frac{\partial^2 u_0}{\partial x \partial t}\left(2\left(\beta-\alpha\right)\frac{\partial \alpha}{\partial x}+\alpha\left(\frac{\partial \beta}{\partial x}-\frac{\partial \alpha}{\partial x}\right)-\left(\beta\frac{\partial \beta}{\partial x}-\alpha\frac{\partial \alpha}{\partial x}\right)\right)\\
&+\frac{\partial^3 u_0}{\partial x^2 \partial t}\left(\alpha\left(\beta-\alpha\right)-\left(\frac{\beta^2-\alpha^2}{2}\right)\right)+u_0\frac{\partial u_0}{\partial x}\left(3\frac{\partial^2 \alpha}{\partial x^2}\left(\beta-\alpha\right)+\frac{\partial \alpha}{\partial x}\left(\frac{\partial \beta}{\partial x}-\frac{\partial \alpha}{\partial x}\right)\right)\\
&+{u_0}^2\left(\frac{\partial^3 \alpha}{\partial x^3}\left(\beta-\alpha\right)+\left(\frac{\partial \beta}{\partial x}-\frac{\partial \alpha}{\partial x}\right)\frac{\partial^2 \alpha}{\partial x^2}\right)+\left(\frac{\partial u_0}{\partial x}\right)^2\left(-\alpha\left(\frac{\partial \beta}{\partial x}-\frac{\partial \alpha}{\partial x}\right)+\left(\beta\frac{\partial \beta}{\partial x}-\alpha\frac{\partial \alpha}{\partial x}\right)\right)\\
&+\frac{\partial^2 u_0}{\partial x^2}\frac{\partial u_0}{\partial x}\left(\left(\frac{\beta^2-\alpha^2}{2}\right)-\alpha\left(\beta-\alpha\right)\right)+u_0\frac{\partial^2 u_0}{\partial x^2}\left(2\frac{\partial \alpha}{\partial x}\left(\beta-\alpha\right)+\alpha\left(\frac{\partial \beta}{\partial x}-\frac{\partial \alpha}{\partial x}\right)-\left(\beta\frac{\partial \beta}{\partial x}-\alpha\frac{\partial \alpha}{\partial x}\right)\right)\\
&+u_0\frac{\partial^3 u_0}{\partial x^3}\left(\alpha\left(\beta-\alpha\right)-\left(\frac{\beta^2-\alpha^2}{2}\right)\right)+g\left(\frac{\partial \beta}{\partial x}-\frac{\partial \alpha}{\partial x}\right).
\end{aligned}
\tag{4.45}
$$

Inserting Equation (4.45) into Equation (4.43) and rearranging the terms will give the second GN equation,

$$
\left[\begin{array}{l}
\left[1+\frac{\partial \alpha}{\partial x}\frac{\partial \beta}{\partial x}+\frac{\left(\beta-\alpha\right)}{2}\frac{\partial^2 \alpha}{\partial x^2}\right]\frac{\partial u_0}{\partial t}+\\
\left[\left(\beta-\alpha\right)\left(\frac{\partial \alpha}{\partial x}-\frac{\partial \beta}{\partial x}\right)\right]\frac{\partial^2 u_0}{\partial x \partial t}+\\
\left[-\frac{\left(\beta-\alpha\right)^2}{3}\right]\frac{\partial^3 u_0}{\partial x^2 \partial t}
\end{array}\right]
=
\left[\begin{array}{l}
\left[-1-\frac{3\left(\beta-\alpha\right)}{2}\frac{\partial^2 \alpha}{\partial x^2}-\frac{\partial \alpha}{\partial x}\frac{\partial \beta}{\partial x}\right]u_0\frac{\partial u_0}{\partial x}+\\
\left[-\frac{\left(\beta-\alpha\right)}{2}\frac{\partial^3 \alpha}{\partial x^3}-\frac{\partial \beta}{\partial x}\frac{\partial^2 \alpha}{\partial x^2}\right]{u_0}^2+\\
\left[-\left(\beta-\alpha\right)\frac{\partial \beta}{\partial x}\right]\left(\frac{\partial u_0}{\partial x}\right)^2+\\
\left[-\frac{\left(\beta-\alpha\right)^2}{3}\right]\frac{\partial u_0}{\partial x}\frac{\partial^2 u_0}{\partial x^2}+\\
\left[-\frac{\partial \alpha}{\partial x}\left(\beta-\alpha\right)+\frac{\left(\alpha^2+\beta^2\right)}{\left(\beta-\alpha\right)}\frac{\partial \beta}{\partial x}\right]u_0\frac{\partial^2 u_0}{\partial x^2}+\\
\left[\frac{\left(\beta-\alpha\right)^2}{3}\right]u_0\frac{\partial^3 u_0}{\partial x^3}-g\frac{\partial \beta}{\partial x}
\end{array}\right].
\tag{4.46}
$$

Noting (and restating) the first GN equation,

$$
\frac{\partial \beta}{\partial t}=\frac{\partial\left(\left(\alpha-\beta\right)u_0\right)}{\partial x}.
\tag{4.34}
$$

The two GN equations can be written in terms of η and d as follows

$$\left[\begin{array}{l}\left[1-\frac{\partial d}{\partial x}\frac{\partial \eta}{\partial x}-\frac{(d+\eta)}{2}\frac{\partial^2 d}{\partial x^2}\right]\frac{\partial u_0}{\partial t}+\\ \left[(d+\eta)\left(-\frac{\partial d}{\partial x}-\frac{\partial \eta}{\partial x}\right)\right]\frac{\partial^2 u_0}{\partial x \partial t}+\\ \left[-\frac{(d+\eta)^2}{3}\right]\frac{\partial^3 u_0}{\partial x^2 \partial t}\end{array}\right]=\left[\begin{array}{l}\left[-1+\frac{3(d+\eta)}{2}\frac{\partial^2 d}{\partial x^2}+\frac{\partial d}{\partial x}\frac{\partial \eta}{\partial x}\right]u_0\frac{\partial u_0}{\partial x}+\\ \left[\frac{(d+\eta)}{2}\frac{\partial^3 d}{\partial x^3}+\frac{\partial \eta}{\partial x}\frac{\partial^2 d}{\partial x^2}\right]u_0{}^2+\\ \left[-(d+\eta)\frac{\partial \eta}{\partial x}\right]\left(\frac{\partial u_0}{\partial x}\right)^2+\\ \left[-\frac{(d+\eta)^2}{3}\right]\frac{\partial u_0}{\partial x}\frac{\partial^2 u_0}{\partial x^2}+\\ \left[\frac{\partial d}{\partial x}(d+\eta)+\frac{\left((h-d)^2+(h+\eta)^2\right)}{(d+\eta)}\frac{\partial \eta}{\partial x}\right]u_0\frac{\partial^2 u_0}{\partial x^2}+\\ \left[\frac{(d+\eta)^2}{3}\right]u_0\frac{\partial^3 u_0}{\partial x^3}-g\frac{\partial \eta}{\partial x}\end{array}\right], \tag{4.47}$$

$$\frac{\partial \eta}{\partial t}=-\frac{\partial\left((\eta+d)u_0\right)}{\partial x}. \tag{4.35}$$

4.6 Analytic Structure of Harmonic Solutions to GN Level 1 Equations

In order to understand the capabilities/limitations involved in the GN equations derived in the previous section, the dispersion relationship and the non-linearity properties of the GN equations are investigated. The former is compared with the wave dispersion of the full water wave equations while the latter are examined through perturbation analysis and compared with Stokes regular wave expansion.

4.6.1 GN Linear Wave Dispersion

The linearized GN Level 1 equations on constant water depth are

$$\frac{\partial u_0}{\partial t}-\frac{d^2}{3}\frac{\partial^3 u_0}{\partial x^2 \partial t}=-g\frac{\partial \eta}{\partial x}, \tag{4.48a}$$

and

$$\frac{\partial \eta}{\partial t}=-d\frac{\partial u_0}{\partial x}. \tag{4.48b}$$

Assume the solution for the surface elevation has a sinusoidal profile, such that

$$\eta = A\cos\left(\omega t - kx\right). \tag{4.49a}$$

Then, from Equation (4.48b), the horizontal velocity is given as

$$u_0 = \frac{A\omega}{kd}\cos\left(\omega t - kx\right). \tag{4.49b}$$

This expression for horizontal velocity satisfies the shallow water limit of the linear velocity (potential theory)

$$u = A\omega\frac{\cosh\left(k\left(z+d\right)\right)}{\sinh\left(kd\right)}\cos\left(\omega t - kx\right),$$

giving

$$\underset{kd\to 0}{u} = \frac{A\omega}{kd}\cos\left(\omega t - kx\right) \quad .$$

The above solutions for η and u_0 are inserted into Equation (4.48a) to obtain the following dispersion relationship for the Linearized GN Level 1 equations,

$$\omega^2 = \frac{gk^2d}{\left(1+\frac{\left(kd\right)^2}{3}\right)}. \tag{4.50}$$

To examine the relationship given by Equation (4.50), it is worth noting that the exact linear wave dispersion equation is given by

$$\omega^2 = kg\tanh\left(kd\right). \tag{4.51}$$

The 2nd order expansions of Equation (4.50) and Equation (4.51) both give,

$$\omega = k\sqrt{gd}\left(1 - \frac{1}{6}(kd)^2\right). \tag{4.52}$$

Figure 4.4 shows the relative wave speed against *kd* for the above three equations. It can be seen that the dispersion characteristics of the full water wave equations and GN Level 1 equations match well in shallow water ($kd < 1.4$). In contrast, the series expansion of both to O (k^2d^2) is much less satisfactory. Numerical simulations have been carried out by propagating single frequency regular waves over constant water depth, for a range of frequencies. The speed of the waves are measured and plotted in Figure 4.4. The numerical data matches very well with the GN analytical dispersion equation.

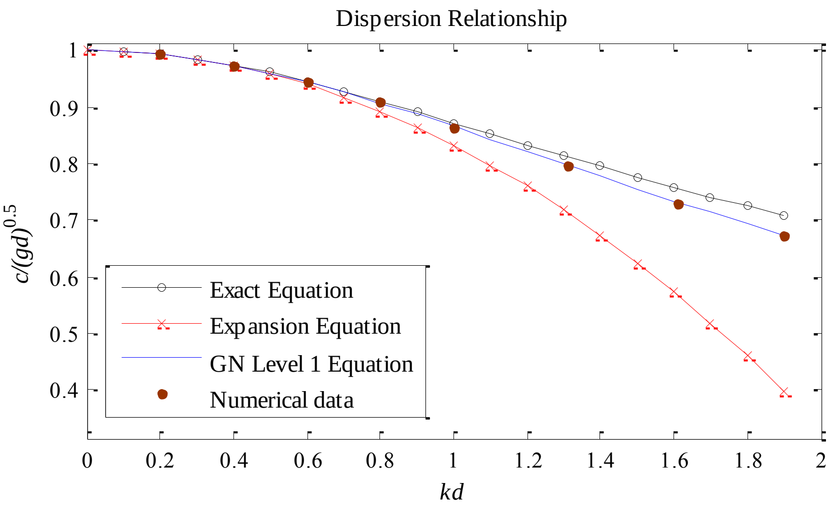

Figure 4.4: Dispersion relationships given by the exact linear wave dispersion equation [Equation (4.51)], the series expansion approximation [Equation (4.52)], the linearized GN level 1 dispersion equation [Equation (4.50)] and the numerical data

4.6.2 2nd Order Perturbation Analysis

The GN Level 1 Equations (retaining up to 2nd order terms) on constant water depth are

$$-\frac{\partial \eta}{\partial t} = \frac{\partial u_0}{\partial x}(\eta + d) + \frac{\partial \eta}{\partial x}u_0, \tag{4.53a}$$

and

$$\frac{\partial u_0}{\partial t}-d\frac{\partial \eta}{\partial x}\frac{\partial^2 u_0}{\partial x\partial t}-\frac{\left(d^2+2d\eta\right)}{3}\frac{\partial^3 u_0}{\partial x^2\partial t}=-u_0\frac{\partial u_0}{\partial x}-\frac{d^2}{3}\frac{\partial u_0}{\partial x}\frac{\partial^2 u_0}{\partial x^2}+\frac{d^2}{3}u_0\frac{\partial^3 u_0}{\partial x^3}-g\frac{\partial \eta}{\partial x}\,. \tag{4.53b}$$

Assume perturbation expansions for the solutions in the form of

$$\eta=A\left(\eta_1+\frac{A}{d}\eta_2\right), \tag{4.54a}$$

and

$$u_0=\frac{A\omega}{kd}\left(u_1+\frac{A}{d}u_2\right). \tag{4.54b}$$

Solving for the continuity equation, the perturbation expansions are inserted into Equation (4.53a) and the *A* terms collected together, giving

$$-A\left(\frac{\partial \eta_1}{\partial t}+\frac{A}{d}\frac{\partial \eta_2}{\partial t}\right)-\frac{A\omega}{kd}\left(\frac{\partial u_1}{\partial x}+\frac{A}{d}\frac{\partial u_2}{\partial x}\right)\left(A\left(\eta_1+\frac{A}{d}\eta_2\right)+d\right)-A\left(\frac{\partial \eta_1}{\partial x}+\frac{A}{d}\frac{\partial \eta_2}{\partial x}\right)\frac{A\omega}{kd}\left(u_1+\frac{A}{d}u_2\right)=0\,,$$

and

$$\begin{aligned}&A\left(-\frac{\partial \eta_1}{\partial t}-\frac{\omega}{k}\frac{\partial u_1}{\partial x}\right)+A^2\left(-\frac{1}{d}\frac{\partial \eta_2}{\partial t}-\frac{\omega}{kd}\eta_1\frac{\partial u_1}{\partial x}-\frac{\omega}{kd}\frac{\partial u_2}{\partial x}-\frac{\omega}{kd}u_1\frac{\partial \eta_1}{\partial x}\right)+A^3\left(\begin{aligned}&-\frac{\omega}{kd^2}\frac{\partial u_1}{\partial x}\eta_2-\frac{\omega}{kd^2}\frac{\partial u_2}{\partial x}\eta_1\\&-\frac{\omega}{kd^2}\frac{\partial \eta_1}{\partial x}u_2-\frac{\omega}{kd^2}\frac{\partial \eta_2}{\partial x}u_1\end{aligned}\right)\\&+A^4\left(-\frac{\omega}{kd^3}\eta_2\frac{\partial u_2}{\partial x}-\frac{\omega}{kd^3}\frac{\partial \eta_2}{\partial x}u_2\right)=0.\end{aligned} \tag{4.55}$$

From the linearized GN equations, the solution for the 1st order perturbation is given as,

$$\eta_1=u_1=\cos\left(\omega t-kx\right) \quad . \tag{4.56}$$

Solving Equation (4.55) for each order of *A* up to 2nd order using the linearized solution above,

$$\mathrm{O}(A) \quad : \qquad \left(-\frac{\partial \eta_1}{\partial t}-\frac{\omega}{k}\frac{\partial u_1}{\partial x}\right)=0\,,$$

which gives

$$\omega\sin\left(\omega t-kx\right)-\omega\sin\left(\omega t-kx\right)=0\,,$$

and

$$\mathrm{O}(A^2) \quad : \qquad \left(-\frac{1}{d}\frac{\partial \eta_2}{\partial t}-\frac{\omega}{kd}\eta_1\frac{\partial u_1}{\partial x}-\frac{\omega}{kd}\frac{\partial u_2}{\partial x}-\frac{\omega}{kd}u_1\frac{\partial \eta_1}{\partial x}\right)=0\,,$$

which gives

$$\frac{1}{d}\frac{\partial \eta_2}{\partial t}+\frac{\omega}{kd}\frac{\partial u_2}{\partial x}+\frac{\omega}{d}\sin\Big(2\left(\omega t-kx\right)\Big)=0\,. \tag{4.57}$$

Solving for momentum equation, the perturbation expansions are inserted into Equation (4.53b) and the A terms collected together, giving

$$\begin{aligned}
&\frac{A\omega}{kd}\left(\frac{\partial u_1}{\partial t}+\frac{A}{d}\frac{\partial u_2}{\partial t}\right)-dA\left(\frac{\partial \eta_1}{\partial x}+\frac{A}{d}\frac{\partial \eta_2}{\partial x}\right)\frac{A\omega}{kd}\left(\frac{\partial^2 u_1}{\partial x\partial t}+\frac{A}{d}\frac{\partial^2 u_2}{\partial x\partial t}\right)-\\
&\left(\frac{d^2+2dA\left(\eta_1+\frac{A}{d}\eta_2\right)}{3}\right)\frac{A\omega}{kd}\left(\frac{\partial^3 u_1}{\partial x^2\partial t}+\frac{A}{d}\frac{\partial^3 u_2}{\partial x^2\partial t}\right)+\frac{A\omega}{kd}\left(u_1+\frac{A}{d}u_2\right)\frac{A\omega}{kd}\left(\frac{\partial u_1}{\partial x}+\frac{A}{d}\frac{\partial u_2}{\partial x}\right)+\\
&\frac{d^2}{3}\frac{A\omega}{kd}\left(\frac{\partial u_1}{\partial x}+\frac{A}{d}\frac{\partial u_2}{\partial x}\right)\frac{A\omega}{kd}\left(\frac{\partial^2 u_1}{\partial x^2}+\frac{A}{d}\frac{\partial^2 u_2}{\partial x^2}\right)-\frac{d^2}{3}\frac{A\omega}{kd}\left(u_1+\frac{A}{d}u_2\right)\frac{A\omega}{kd}\left(\frac{\partial^3 u_1}{\partial x^3}+\frac{A}{d}\frac{\partial^3 u_2}{\partial x^3}\right)+\\
&gA\left(\frac{\partial \eta_1}{\partial x}+\frac{A}{d}\frac{\partial \eta_2}{\partial x}\right)=0,
\end{aligned}$$

and

$$A\left(\frac{\omega}{kd}\frac{\partial u_1}{\partial t}-\frac{d}{3}\frac{\omega}{k}\frac{\partial^3 u_1}{\partial x^2\partial t}+g\frac{\partial \eta_1}{\partial x}\right)+A^2\left(\begin{array}{l}
\frac{\omega}{kd^2}\frac{\partial u_2}{\partial t}-\frac{\omega}{k}\frac{\partial \eta_1}{\partial x}\frac{\partial^2 u_1}{\partial x\partial t}-\frac{1}{3}\frac{\omega}{k}\frac{\partial^3 u_2}{\partial x^2\partial t}-\\
\frac{2}{3}\frac{\omega}{k}\eta_1\frac{\partial^3 u_1}{\partial x^2\partial t}+\left(\frac{\omega}{kd}\right)^2 u_1\frac{\partial u_1}{\partial x}+\\
\frac{d^2}{3}\left(\frac{\omega}{kd}\right)^2\frac{\partial u_1}{\partial x}\frac{\partial^2 u_1}{\partial x^2}-\\
\frac{d^2}{3}\left(\frac{\omega}{kd}\right)^2 u_1\frac{\partial^3 u_1}{\partial x^3}+g\frac{1}{d}\frac{\partial \eta_2}{\partial x}
\end{array}\right)+A^3(\ldots)+A^4(\ldots)=0. \tag{4.58}$$

Solving Equation (4.58) for each order of A up to 2nd order using the linearized solution of Equation (4.56),

$$\mathrm{O}(A) \quad : \qquad \left(\frac{\omega}{kd}\frac{\partial u_1}{\partial t}-\frac{d}{3}\frac{\omega}{k}\frac{\partial^3 u_1}{\partial x^2 \partial t}+g\frac{\partial \eta_1}{\partial x}\right)=0\,,$$

which gives

$$-\frac{\omega^2}{kd}\sin\left(\omega t-kx\right)-\frac{\omega^2 kd}{3}\sin\left(\omega t-kx\right)+gk\sin\left(\omega t-kx\right)=0\,,$$

and rearranges to give

$$\omega^2=\frac{gk^2 d}{1+\frac{\left(kd\right)^2}{3}}\,,$$

and

$$\mathrm{O}(A^2) \quad : \qquad \left(\begin{matrix}\dfrac{\omega}{kd^2}\dfrac{\partial u_2}{\partial t}-\dfrac{\omega}{k}\dfrac{\partial \eta_1}{\partial x}\dfrac{\partial^2 u_1}{\partial x \partial t}-\dfrac{1}{3}\dfrac{\omega}{k}\dfrac{\partial^3 u_2}{\partial x^2 \partial t}-\dfrac{2}{3}\dfrac{\omega}{k}\eta_1\dfrac{\partial^3 u_1}{\partial x^2 \partial t}+ \\ \left(\dfrac{\omega}{kd}\right)^2 u_1\dfrac{\partial u_1}{\partial x}+\dfrac{d^2}{3}\left(\dfrac{\omega}{kd}\right)^2\dfrac{\partial u_1}{\partial x}\dfrac{\partial^2 u_1}{\partial x^2}-\dfrac{d^2}{3}\left(\dfrac{\omega}{kd}\right)^2 u_1\dfrac{\partial^3 u_1}{\partial x^3}+g\dfrac{1}{d}\dfrac{\partial \eta_2}{\partial x}\end{matrix}\right)=0\,,$$

which gives

$$\begin{aligned}&\frac{\omega}{kd^2}\frac{\partial u_2}{\partial t}-\omega^2 k\sin\left(\omega t-kx\right)\cos\left(\omega t-kx\right)-\frac{1}{3}\frac{\omega}{k}\frac{\partial^3 u_2}{\partial x^2 \partial t}- \\ &\frac{2\omega^2 k}{3}\sin\left(\omega t-kx\right)\cos\left(\omega t-kx\right)+\frac{\omega^2}{kd^2}\sin\left(\omega t-kx\right)\cos\left(\omega t-kx\right)- \\ &\frac{\omega^2 k}{3}\sin\left(\omega t-kx\right)\cos\left(\omega t-kx\right)+\frac{\omega^2 k}{3}\sin\left(\omega t-kx\right)\cos\left(\omega t-kx\right)+g\frac{1}{d}\frac{\partial \eta_2}{\partial x}=0,\end{aligned}$$

leading to

$$\frac{\omega}{kd^2}\frac{\partial u_2}{\partial t}-\frac{1}{3}\frac{\omega}{k}\frac{\partial^3 u_2}{\partial x^2 \partial t}+g\frac{1}{d}\frac{\partial \eta_2}{\partial x}+\left(-\frac{5}{6}\omega^2 k+\frac{\omega^2}{2kd^2}\right)\sin\left(2\left(\omega t-kx\right)\right)=0\,. \qquad (4.59)$$

It can be seen that from the 2nd order perturbation analysis, the resulting dispersion equation is the same as for the linearized GN equations shown earlier. This is in agreement with the Stokes expansion theory where the linear dispersion equation is still valid for second order solution.

Assuming a harmonic form, the solutions for the 2nd order perturbation can be expressed as,

$$\begin{aligned} \eta_2 &= e_2 \cos\left(2\left(\omega t - kx\right)\right), \\ u_2 &= v_2 \cos\left(2\left(\omega t - kx\right)\right), \end{aligned} \tag{4.60}$$

where e_2 and v_2 are non-dimensional constants. To find the value of these constants, insert Equation (4.60) into Equation (4.57) and Equation (4.59).

From Equation (4.57),

$$\frac{1}{d}\frac{\partial \eta_2}{\partial t} + \frac{\omega}{kd}\frac{\partial u_2}{\partial x} + \frac{\omega}{d}\sin\left(2\left(\omega t - kx\right)\right) = 0 \,,$$

or

$$\frac{-2\omega e_2}{d}\sin\left(2\left(\omega t - kx\right)\right) + 2v_2\frac{\omega}{d}\sin\left(2\left(\omega t - kx\right)\right) + \frac{\omega}{d}\sin\left(2\left(\omega t - kx\right)\right) = 0 \,,$$

giving

$$v_2 = e_2 - \frac{1}{2} \,. \tag{4.61}$$

From Equation (4.59),

$$\frac{\omega}{kd^2}\frac{\partial u_2}{\partial t} - \frac{1}{3}\frac{\omega}{k}\frac{\partial^3 u_2}{\partial x^2 \partial t} + g\frac{1}{d}\frac{\partial \eta_2}{\partial x} + \left(-\frac{5}{6}\omega^2 k + \frac{\omega^2}{2kd^2}\right)\sin\left(2\left(\omega t - kx\right)\right) = 0 \,,$$

or

$$\begin{aligned} &-\frac{2\omega^2 v_2}{kd^2}\sin\left(2\left(\omega t - kx\right)\right) - \frac{8}{3}k\omega^2 v_2 \sin\left(2\left(\omega t - kx\right)\right) + \frac{2gke_2}{d}\sin\left(2\left(\omega t - kx\right)\right) \\ &+ \left(-\frac{5}{6}k\omega^2 + \frac{\omega^2}{2kd^2}\right)\sin\left(2\left(\omega t - kx\right)\right) = 0, \end{aligned}$$

giving

$$-\frac{2\omega^2 v_2}{kd^2} - \frac{8}{3}k\omega^2 v_2 + \frac{2gke_2}{d} + \left(-\frac{5}{6}k\omega^2 + \frac{\omega^2}{2kd^2}\right) = 0 \,. \tag{4.62}$$

Insert Equation (4.61) into Equation (4.62) to solve for e_2, then,

$$-\frac{2\omega^2\left(e_2-\frac{1}{2}\right)}{kd^2}-\frac{8}{3}k\omega^2\left(e_2-\frac{1}{2}\right)+\frac{2gke_2}{d}+\left(-\frac{5}{6}k\omega^2+\frac{\omega^2}{2kd^2}\right)=0\ ,$$

or

$$e_2\left(-\frac{2\omega^2}{kd^2}-\frac{8}{3}k\omega^2+\frac{2gk}{d}\right)+\frac{3\omega^2}{2kd^2}+\frac{1}{2}k\omega^2=0\ ,$$

giving

$$e_2=\frac{\frac{3\omega^2}{2kd^2}+\frac{\omega^2k}{2}}{\frac{2\omega^2}{kd^2}+\frac{8\omega^2k}{3}-\frac{2gk}{d}}\ . \tag{4.63}$$

Replacing the ω term in Equation (4.63) with the dispersion relationship for linear GN equations,

$$e_2=\frac{\frac{3\left(\frac{gk^2d}{1+\frac{(kd)^2}{3}}\right)}{2kd^2}+\frac{\left(\frac{gk^2d}{1+\frac{(kd)^2}{3}}\right)k}{2}}{\frac{2\left(\frac{gk^2d}{1+\frac{(kd)^2}{3}}\right)}{kd^2}+\frac{8\left(\frac{gk^2d}{1+\frac{(kd)^2}{3}}\right)k}{3}-\frac{2gk}{d}}\ ,$$

or

$$e_2=\frac{\frac{\left(\frac{9gk}{3+(kd)^2}\right)}{2}+\frac{\left(\frac{3gk^3d^2}{3+(kd)^2}\right)}{2}}{\left(\frac{6gk}{3+(kd)^2}\right)+\left(\frac{8gk^3d^2}{3+(kd)^2}\right)-2gk}\ ,$$

giving

$$e_2=\frac{3+k^2d^2}{4k^2d^2}\ , \tag{4.64}$$

and

$$v_2=\frac{3-k^2d^2}{4k^2d^2}\ . \tag{4.65}$$

Both the values of e_2 and v_2 can be compared with the Stokes regular wave expansion. The first two terms of a Stokes regular wave expansion can be written

$$\eta = A\left(\cos\theta + S_{22}\frac{A}{d}\cos 2\theta\right),$$

where the Stokes 2nd order coefficient, S_{22} is given by

$$S_{22} = \frac{kd\left(1+2C\right)\coth\left(kd\right)}{2\left(1-C\right)},$$

and C = sech 2*kd.*

The Stokes coefficient S_{22} is equivalent to GN e_2. To compare the GN 2nd order coefficient given by Equation (4.64) with the Stokes coefficient, Figure 4.5 plots e_2 and S_{22} against *kd*. The coefficients match well for low values of *kd*. In fact, both have the same asymptotic form as *kd* reduces to zero, as shown here.

$$\underset{kd\to 0}{e_2} = \frac{3}{4k^2d^2}.$$

For S_{22}, with $\underset{kd\to 0}{\coth} kd = \frac{1}{kd}$, $\underset{kd\to 0}{\operatorname{sech}} 2kd = 1$,and

using a 2nd order Taylor Expansion for the denominator; $\operatorname{sech}\left(2kd\right) = 1 - \frac{\left(2kd\right)^2}{2} = 1 - 2\left(kd\right)^2$.

Hence,

$$\underset{kd\to 0}{S_{22}} = \frac{kd\left(1+2(1)\right)\frac{1}{kd}}{2\left(1-\left(1-2\left(kd\right)^2\right)\right)},$$

or

$$\underset{kd\to 0}{S_{22}} = \frac{3}{4\left(kd\right)^2}.$$

This prediction of 2nd order coefficient is more stringent (lower *kd* required) than for linear dispersion, as shown earlier.

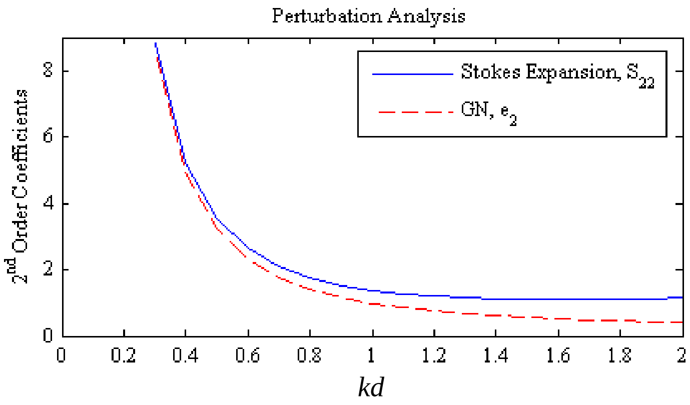

Figure 4.5: Perturbation Expansion for 2nd Order Coefficients e_2 and S_{22} plotted against *kd*

For the velocity, Fenton (1985) derived the Stokes regular wave expansion in terms of velocity potential. Differentiating the velocity potential expansion over *x* and using the exact linear wave dispersion to match the form of the above analysis, the velocity expansion can be written as,

$$u = -\bar{u} + \frac{2\omega}{k}\left((Ak)B_{11}\cos\theta + (Ak)^2 B_{21}\cos\theta + (Ak)^2 B_{22}\cos 2\theta + \ldots\right).$$

Taking the double frequency term, cos 2θ,

$$\frac{2\omega}{k}\left((Ak)^2 B_{22}\cos 2\theta\right) = \frac{A^2 w}{kd^2}\left(A_{22}\cos 2\theta\right),$$

where $A_{22} = 2(kd)^2 B_{22}$, and Stokes 2nd order coefficient, B_{22} is given by

$$B_{22} = \frac{3C^2}{2(1-C)^2},$$

and C = sech 2*kd*.

The Stokes coefficient A_{22} is equivalent to GN v_2 of Equation (4.65). To compare the GN 2nd order coefficient with the Stokes coefficient, Figure 4.6 plots v_2 and A_{22} against *kd*. The coefficients match well up to *kd* of 1.6. The non-linearity due to the surface elevation expansion (referring to e_2) limits the application of this theory, as compared to the linear dispersion equation and the velocity expansion.

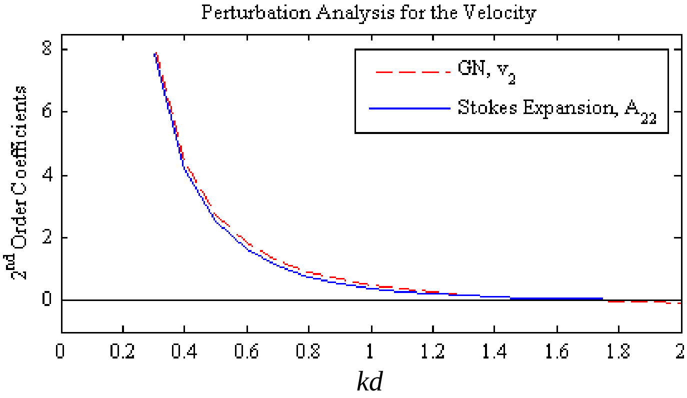

Figure 4.6: Perturbation Expansion for 2nd Order Coefficients v_2 and A_{22} plotted against *kd*

4.7 Numerical Solver

The GN equations for shallow water over a non-uniform bed are solved numerically using the finite difference method. Smooth solutions are obtained as long as the wave does not reach its breaking point (i.e. more than one water surface elevation value at a point in the spatial domain). The GN Level 1 equations for shallow water flow over a non-uniform bed are restated here.

$$\frac{\partial \beta}{\partial t} = \frac{\partial\left(\left(\alpha - \beta\right)u_0\right)}{\partial x}, \tag{4.34}$$

$$\left[\begin{array}{l}\left[1+\frac{\partial\alpha}{\partial x}\frac{\partial\beta}{\partial x}+\frac{(\beta-\alpha)}{2}\frac{\partial^2\alpha}{\partial x^2}\right]\frac{\partial u_0}{\partial t}+\\ \left[(\beta-\alpha)\left(\frac{\partial\alpha}{\partial x}-\frac{\partial\beta}{\partial x}\right)\right]\frac{\partial^2 u_0}{\partial x\partial t}+\\ \left[-\frac{(\beta-\alpha)^2}{3}\right]\frac{\partial^3 u_0}{\partial x^2\partial t}\end{array}\right]=\left[\begin{array}{l}\left[-1-\frac{3(\beta-\alpha)}{2}\frac{\partial^2\alpha}{\partial x^2}-\frac{\partial\alpha}{\partial x}\frac{\partial\beta}{\partial x}\right]u_0\frac{\partial u_0}{\partial x}+\\ \left[-\frac{(\beta-\alpha)}{2}\frac{\partial^3\alpha}{\partial x^3}-\frac{\partial\beta}{\partial x}\frac{\partial^2\alpha}{\partial x^2}\right]{u_0}^2+\\ \left[-(\beta-\alpha)\frac{\partial\beta}{\partial x}\right]\left(\frac{\partial u_0}{\partial x}\right)^2+\\ \left[-\frac{(\beta-\alpha)^2}{3}\right]\frac{\partial u_0}{\partial x}\frac{\partial^2 u_0}{\partial x^2}+\\ \left[-\frac{\partial\alpha}{\partial x}(\beta-\alpha)+\frac{(\alpha^2+\beta^2)}{(\beta-\alpha)}\frac{\partial\beta}{\partial x}\right]u_0\frac{\partial^2 u_0}{\partial x^2}+\\ \left[\frac{(\beta-\alpha)^2}{3}\right]u_0\frac{\partial^3 u_0}{\partial x^3}-g\frac{\partial\beta}{\partial x}\end{array}\right]. \qquad (4.46)$$

4.7.1 Finite Difference Scheme

A domain of length L with x as the spatial variable along the domain is discretised into N grid points. The spacing between any two adjacent points is given by

$$\Delta x = \frac{L}{N-1}.$$

The distance of the grid points from the origin at the left boundary is given by

$$x_i = (i-1)\Delta x \qquad \text{for } i = 1\ldots N.$$

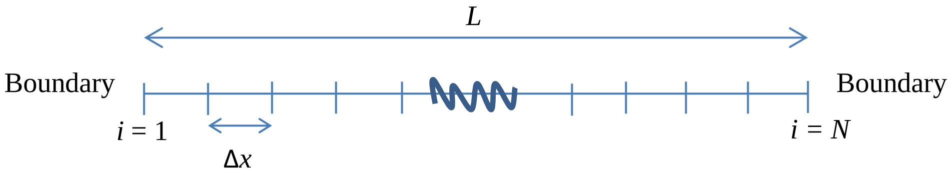

Figure 4.3: Definition sketch for the differencing domain

The spatial derivatives in the GN equations are approximated using fourth order central differences, which leads to 5-point centred stencils for the first and second order derivatives, and 7-point centred stencils for the third order derivatives. The choice of fourth order accuracy for the first order derivatives is due to the principle stated by Wei and Kirby (1995) where the truncation error for a second order accuracy could be large enough to affect the dispersive terms in the GN equations. Two extra grid points, named ghost points are included at both sides of the boundaries to deal with the near-boundary grid points (x_2, x_3, x_{N-2}, and x_{N-1}).

Given a function $f = f(x)$, the spatial derivatives are given as below;

$$\frac{df(x_i)}{dx} = \frac{-f_{i+2} + 8f_{i+1} - 8f_{i-1} + f_{i-2}}{12\Delta x},$$

$$\frac{d^2f(x_i)}{dx^2} = \frac{-f_{i+2} + 16f_{i+1} - 30f_i + 16f_{i-1} - f_{i-2}}{12\Delta x^2}, \tag{4.66}$$

$$\frac{d^3f(x_i)}{dx^3} = \frac{-f_{i+3} + 8f_{i+2} - 13f_{i+1} + 13f_{i-1} - 8f_{i-2} - f_{i-3}}{8\Delta x^3}.$$

4.7.2 Time Integration

The variables β and u are updated in time by

$$\beta^{n+1} = \beta^n + \Delta t \frac{d\beta^n}{dt},$$

$$u^{n+1} = u^n + \Delta t \frac{du^n}{dt}, \tag{4.67}$$

with the first order time derivative (the slope) solved using a fourth order Runge-Kutta method (RK4). RK 4 produces an effective slope which is derived from the weighted mean of slopes at four different points in the step interval, with the variables used at successive points being based on two different midpoint approximations. The algorithm for the time integration is as follows;

$$\frac{d\beta^n}{dt} = \frac{1}{6}\left(\frac{d\beta}{dt_1} + 2\frac{d\beta}{dt_2} + 2\frac{d\beta}{dt_3} + \frac{d\beta}{dt_4}\right) \qquad \frac{du^n}{dt} = \frac{1}{6}\left(\frac{du}{dt_1} + 2\frac{du}{dt_2} + 2\frac{du}{dt_3} + \frac{du}{dt_4}\right)$$

$$\frac{d\beta}{dt_1} = a(u^n, \beta^n) \qquad M\frac{du}{dt_1} = a(u^n, \beta^n)$$

$$\frac{d\beta}{dt_2} = a\left(u^n + \frac{1}{2}\Delta t\frac{du}{dt_1}, \beta^n + \frac{1}{2}\Delta t\frac{d\beta}{dt_1}\right) \qquad M\frac{du}{dt_2} = a\left(u^n + \frac{1}{2}\Delta t\frac{du}{dt_1}, \beta^n + \frac{1}{2}\Delta t\frac{d\beta}{dt_1}\right)$$

$$\frac{d\beta}{dt_3} = a\left(u^n + \frac{1}{2}\Delta t\frac{du}{dt_2}, \beta^n + \frac{1}{2}\Delta t\frac{d\beta}{dt_2}\right) \qquad M\frac{du}{dt_3} = a\left(u^n + \frac{1}{2}\Delta t\frac{du}{dt_2}, \beta^n + \frac{1}{2}\Delta t\frac{d\beta}{dt_2}\right)$$

$$\frac{d\beta}{dt_4} = a\left(u^n + \Delta t\frac{du}{dt_3}, \beta^n + \Delta t\frac{d\beta}{dt_3}\right), \qquad M\frac{du}{dt_4} = a\left(u^n + \Delta t\frac{du}{dt_3}, \beta^n + \Delta t\frac{d\beta}{dt_3}\right).$$

Equation (4.34) can be solved directly, given that the solution at the new time step involves only known solutions at previous time step. But Equation (4.46) involves mixed derivatives terms (i.e. both spatial and time derivatives), where the solution at the new time step for a grid point involves both known solutions at the previous time step and also solutions at the new time step of adjacent grid points, which are unknown. The mixed derivatives terms are treated by solving the variables for all grid points simultaneously. The spatially differenced Equation (4.46) can be rearranged to $[\boldsymbol{M}][\overrightarrow{\frac{du}{dt}}] = \boldsymbol{f}$, as shown in Equation (4.68) where $\boldsymbol{f}$ contains all the known solutions (right hand side of Equation 4.46) while $\boldsymbol{M}$ is called the coefficients matrix. This leads to a pentadiagonal matrix due to the 5-point stencil used for the highest order of the spatial discretisation in the mixed derivatives. Both the GN equations are solved for the inner grid points ($i = 2$ to $N - 1$) at each RK4 intermediate step and then updated using Equation (4.67). Note that the matrix in Equation (4.68) is yet to be completed. The matrix equations need to have the boundary conditions included before they can be solved. The final matrix with the required boundary conditions is shown in Equation (4.69). The notation $u_{t,i}$ is used to represent $\frac{du}{dt}$ at grid point i.

$$\begin{bmatrix} c_2 & d_2 & e_2 & & & & 0 \\ b_3 & c_3 & d_3 & e_3 & & & \\ a_4 & b_4 & c_4 & d_4 & e_4 & & \\ & a_5 & b_5 & c_5 & d_5 & . & \\ & & . & . & . & . & e_{N-3} \\ & & & . & . & . & d_{N-2} \\ 0 & & & & a_{N-1} & b_{N-1} & c_{N-1} \end{bmatrix} \begin{bmatrix} u_{t,2} \\ u_{t,3} \\ u_{t,4} \\ \\ \vdots \\ \\ u_{t,N-1} \end{bmatrix} = \begin{bmatrix} f_2 \\ f_3 \\ f_4 \\ \\ \vdots \\ \\ f_{N-1} \end{bmatrix}, \tag{4.68}$$

where *N* is the total grid points,

$$a_i = \frac{(P_{1i} + P_{2i})(\beta_i - \alpha_i)}{(144\Delta x^2)},\ b_i = \frac{-(P_{1i} + 2P_{2i})(\beta_i - \alpha_i)}{(18\Delta x^2)},\ c_i = P_{3i},$$

$$d_i = \frac{(P_{1i} - 2P_{2i})(\beta_i - \alpha_i)}{(18\Delta x^2)}, e_i = \frac{-(P_{1i} - P_{2i})(\beta_i - \alpha_i)}{(144\Delta x^2)},$$

$$P_{1i} = -\alpha_{i+2} + 8\alpha_{i+1} - 8\alpha_{i-1} + \alpha_{i-2} + \beta_{i+2} - 8\beta_{i+1} + 8\beta_{i-1} - \beta_{i-2},$$

$P_{2i} = 4(\beta_i - \alpha_i)$, and

$$P_{3i} = 1 + \left(\frac{(-\alpha_{i+2} + 8\alpha_{i+1} - 8\alpha_{i-1} + \alpha_{i-2})(-\beta_{i+2} + 8\beta_{i+1} - 8\beta_{i-1} + \beta_{i-2})}{144\Delta x^2}\right)$$
$$+ \frac{(\beta_i - \alpha_i)}{24\Delta x^2}\big(-\alpha_{i+2} + 16\alpha_{i+1} - 30\alpha_i + 16\alpha_{i-1} - \alpha_{i-2} + 20(\beta_i - \alpha_i)\big).$$

4.7.3 Boundary Conditions

Solid walls are implemented for both the left and right boundaries. There will be no flux at the boundaries, and the surface elevations at the boundaries are estimated by cubic Lagrange interpolation. For the ghost points, a symmetric option is used for the surface elevation, while an anti-symmetric option is used for the velocity; each boundary acting as the axis of symmetry. The conditions are as follows;

At the boundaries,

$$u_1 = u_N = 0,$$

$$\beta_1 = 4\beta_2 - 6\beta_3 + 4\beta_4 - \beta_5,$$

$$\beta_N = 4\beta_{N-1} - 6\beta_{N-2} + 4\beta_{N-3} - \beta_{N-4},$$

and at the ghost points,

$$\beta_0 = \beta_2, \beta_{N+1} = \beta_{N-1},$$

$$u_0 = -u_2, u_{N+1} = -u_{N-1},$$

$$u_{-1} = -u_3, u_{N+2} = -u_{N-2}$$

The matrix shown in Equation (4.68) is then updated following the boundary conditions.

$$u_{t,1} = 0, u_{t,N} = 0,$$

$$u_{t,0} = -u_{t,2}, u_{t,N+1} = -u_{t,N-1}.$$

Thus,

$$\begin{bmatrix} c_2 - a_2 & d_2 & e_2 & & & & 0 \\ b_3 & c_3 & d_3 & e_3 & & & \\ a_4 & b_4 & c_4 & d_4 & e_4 & & \\ & a_5 & b_5 & c_5 & d_5 & . & \\ & & . & . & . & . & e_{N-3} \\ & & & . & . & . & d_{N-2} \\ 0 & & & & a_{N-1} & b_{N-1} & c_{N-1} - e_{N-1} \end{bmatrix} \begin{bmatrix} u_{t,2} \\ u_{t,3} \\ u_{t,4} \\ \\ \vdots \\ \\ u_{t,N-1} \end{bmatrix} = \begin{bmatrix} f_2 - b_2\, u_{t,1} \\ f_3 - a_3\, u_{t,1} \\ f_4 \\ \\ \vdots \\ \\ f_{N-1} - d_{N-1}\, u_{t,N} \end{bmatrix}. \tag{4.69}$$

4.8 Conclusion

- A numerical solver for the GN equations in shallow water over a non-uniform bed has been developed, with capability of simulating waves in intermediate water depth.
- GN equations in shallow water are derived.
    - The GN equations are derived from the conservation of mass and momentum law together with the kinematic and dynamic boundary conditions for free

  surface flow of inviscid and incompressible liquid.
  - The equations are depth-integrated.
  - The velocity field is approximated by using a single sheet fluid model and assuming velocity profile over the water depth of the horizontal component to be uniform while the vertical component varies linearly from zero at bed to a maximum at the free surface, corresponding to shallow water flow.
- The velocity field is approximated by a finite sum of fundamental kinematic profiles, which leads to the approximation of the field equation but satisfies the boundary conditions exactly, which is in accordance with the research of simulating free surface flows.
  - Standard approach such as the Stokes-type perturbation method approximates the boundary condition.
- GN theory incorporates non-linear terms in its formulation, even at the lowest order, which is essential in the analysis of extreme waves.
- GN Level 1 equations developed here have dispersive characteristics which match well with the full water wave equations for $kd < 1.4$.
- 2nd order perturbation analysis shows that the non-linearity (2nd order coefficient of the perturbation expansions) is more stringent (lower kd required) than for linear dispersion.
- A finite difference scheme is applied to solve the derived GN equations numerically.
  - A fourth order accuracy is implemented for both space and time derivatives; using fourth order central differences in space and the time is integrated using a fourth order Runge-Kutta method (RK4).
- The mixed derivatives in the GN equations, together with the fourth order spatial discretisation applied for the finite difference scheme leads to a pentadiagonal matrix, which means that the variables at all grid points are solved simultaneously at each RK4 intermediate step.

5 GN Numerical Simulation of Solitary Waves

5.1 Introduction

Unlike oscillatory waves, solitary waves have no trough and are of infinite wave length in shallow water. These non-linear waves propagate without loss of form or amplitude over a frictionless horizontal bed in the absence of viscosity. Solitary waves have been modelled numerically using a variety of governing equations by many researchers, including Peregrine (1966), Synolakis (1987), Kim et al. (2003), Borthwick et al. (2006), Metayer et al. (2010), etc., who have investigated solitary wave interaction with beaches and walls. In practice, solitary waves can be used as a simplified model of an individual wave in a tsunami.

In order to validate that the GN equations can represent the behaviour of highly non-linear steep waves, the present numerical scheme is used to simulate solitary waves to check whether it is able to cope with the non-linearity. Furthermore, the results of this simulation will be compared against solutions of the Korteweg-de Vries (KdV) equation in order to improve our understanding of the nature of the GN equations when applied to solitary waves. In the governing mathematical equations, a solitary wave retains its shape and velocity by balancing the non-linear and dispersion terms. The KdV equation admits a solitary wave as one analytical solution (Drazin and Johnson, 1989). Craig (2006) has shown, using the full equations of motion for an inviscid and irrotational fluid, that the interaction between two solitary waves produces a small dispersive wave tail as part of the solution, and so is not a precisely clean process and reversible as predicted by the KdV equation. Other equations such as the Regularized Long Wave (RLW) equations show qualitatively the same behaviour as the KdV equation, but quantitatively there are small differences (Harland, 2010). This opens up the question as to which equation is more accurate, and also which one is more appropriate taking into account the accuracy of the solution, the complexity of the equation, or even in which domain (such as for small amplitude dispersive waves) the equations work best.

This chapter investigates solitary wave separation and solitary wave interactions using the GN equations. A solitary wave propagating in otherwise still water over a flat, horizontal, frictionless bed will retain its shape and speed as it moves, given the correct width and amplitude (i.e. a balance between non-linearity and dispersion). With an initial wave taller than the exact solitary wave but of the same width, the initial wave will evolve; splitting into two or more solitary waves and small dispersive waves. The overtaking of two solitary waves is another interesting case as it starts from two clean and well-separated individual waves which then interact, merge, and separate again; this is to be contrasted to the separation case above, in that the initial condition is forced to be a fully merged case. The results from the GN solver will then be compared with an analytical solution of the KdV equation based on the first three conserved quantities obtained by Curry (2008) and Harland (2010). The main section of this chapter involves solitary wave propagation over a sloping bed. During the simulation, the solitary wave is first generated in water of constant depth and then propagates up a slope. Due to the effect of the sloping bed, there is an increase in amplitude and decrease in wave speed compared to the initial solitary wave. This evolving profile then separates into at least two solitary waves once the single main input wave has reached the top of the shelf. The results are compared against experimental measurements obtained by Seabra-Santos et al. (1987) who examined the transformation of a solitary wave over a shelf.

5.1.1 Solitary Wave Profile

The assumed general form of the free surface elevation above still water level of a solitary wave propagating in water of constant depth is given by:

$$\eta = a \operatorname{sech}^2(b(x-ct)) \qquad (5.1)$$

where a = amplitude, $b = \frac{1}{2}\left(\frac{3a}{d^3}\right)^{\frac{1}{2}}$ is the inverse ‘width’, d = water depth, $c = \sqrt{gd}\left(1 + \frac{1}{2}\frac{a}{d}\right)$ is the solitary wave speed, x is horizontal distance, and t is time. Here it is assumed that the ratio of amplitude over water depth, a / d is small (Drazin and Johnson, 1989). From Equation (5.1), it can be seen that the wave speed increases linearly with amplitude above the linear shallow water speed whereas the 'width' of the solitary wave b^{-1} is inversely proportional to $a^{1/2}$. Taller solitary waves travel faster and are narrower than small-amplitude solitary waves. Equation (5.1) is the solution of the KdV equation.

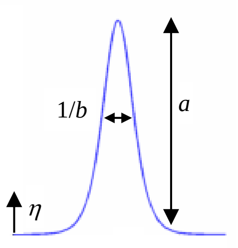

Figure 5.1: Solitary wave profile

5.2 Simulation Setup

From Metayer et al. (2010), the GN solitary wave form is slightly different to that for the KdV equation, having parameters

$b=\frac{1}{2}\left(\frac{3a}{d^2(d+a)}\right)^{\frac{1}{2}}$ and

$c=\sqrt{g(d+a)}$; $\frac{a}{d}$ valid for all ranges.

The spatial profile of Metayer et al. (2010) is taken as the initial condition for the numerical simulation, whereby the free surface is described by parameters as given above. Metayer et al. used a Godunov type scheme to solve the GN model describing dispersive shallow water waves numerically and also derived the analytical solitary wave solutions for their model. The horizontal fluid velocity term is given as $u=c\left(1-\frac{d}{\eta+d}\right)$. The difference in solitary wave profiles for both the KdV and GN equations can be seen clearly from Figure 5.2, where the GN solution is wider than that of the KdV equation.

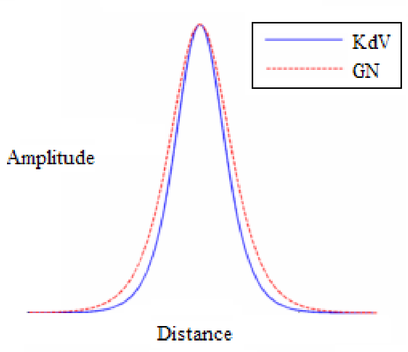

Figure 5.2: Solitary wave profile for KdV and GN solutions

A solitary wave propagating on a constant depth is first simulated to indicate that the GN numerical model is performing in a satisfactory manner. Figure 5.3 shows a distance-time (x,t) plot for solitary wave propagation with amplitude of 2 m on water depth of 10 m over time. It can be seen that the amplitude is constant in time and the shape of the wave is preserved. Figure 5.4 shows a zoom in on the same solitary wave after 480 s. There is a small dispersive wave of order 10^{-6} m produced behind the solitary wave. From an engineering point of view, this dispersive wave (which is from a numerical run of a 2 m solitary wave) is considered very small and will not affect the outcome. Therefore, this shows that the numerical scheme is able to produce solitary wave propagation with practically useful accuracy.

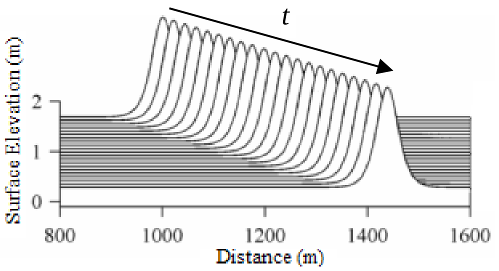

Figure 5.3: Solitary wave propagation

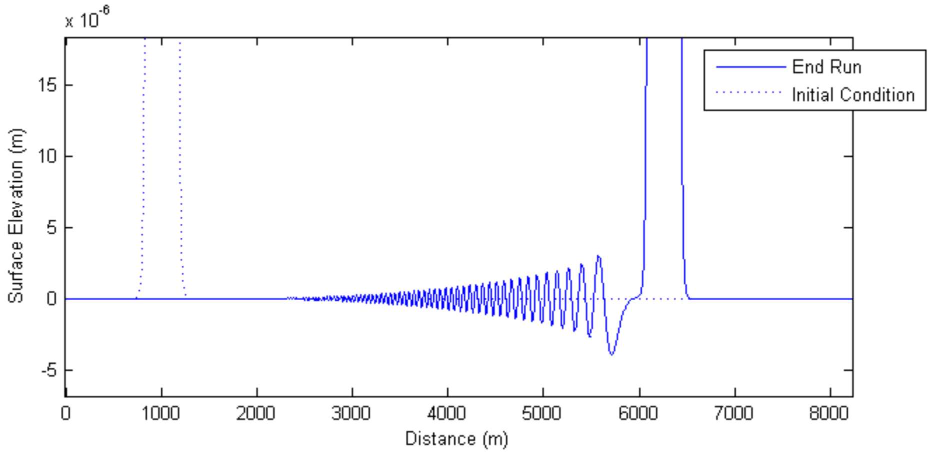

Figure 5.4: 2 m amplitude solitary wave propagation after 480 s

5.3 GN Simulation of Solitary Wave Separation

Solitary wave separation is interesting as a problem; a starting condition where a wave has higher amplitude compared to its width than a solitary wave. This initial condition will then evolve in time and separate into two or more solitary waves, most probably accompanied by small dispersive waves. The leading solitary wave will be higher than the initial wave, while the second and any subsequent waves will be much smaller.

A distance-time plot for an initial wave of amplitude 7 m on water of depth 10 m, with the initial width taken corresponding to that of a 2 m solitary wave, is shown in Figure 5.5. In this case, the initial wave splits into 3 solitary waves with a dispersive tail at the back. Both the third solitary wave and dispersive tails are not clearly visible in the figure but there is another small wave emitted, propagating in the opposite direction and being reflected back from the left wall boundary. The leading solitary wave is higher than the initial wave, while the third solitary wave is very small and yet to separate itself from the dispersive wave behind it. Much computational time is needed for the third solitary wave to be fully developed. Qualitatively the behaviour is very similar to that well-known for other weakly non-linear shallow water equations. The weak dispersive wave train emitted backwards does not occur for solutions to the one-direction KdV or RLW equations. In the simulation, the boundary conditions are periodic, so the backwards moving dispersive train then reflects off the end wall of the computational domain.

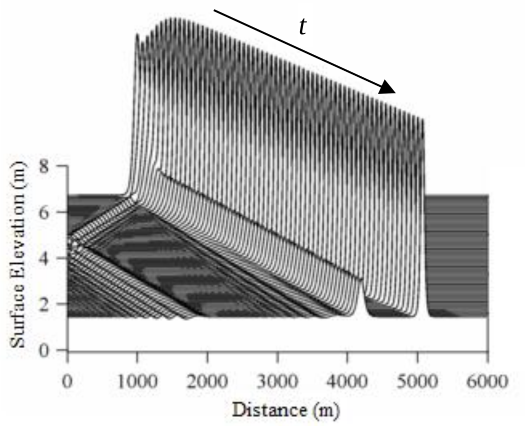

Figure 5.5: Wave separation with amplitude of 7 m on a 2 m solitary wave width

Wave initial amplitudes ranging from 2 m to 17 m and initial profile given by Equation (5.1), using the parameters stated in Section 5.2 have been simulated in 10 m water depth (obviously unphysical but a useful test case) with the initial wave widths corresponding to that of a solitary wave of amplitude of 2 m. This means that a wave of amplitude of 2 m will produce a solitary wave that propagates without any separation or change of amplitude, whereas a wave of amplitude higher than 2 m will result in at least two solitary waves with dispersive tails. Figure 5.6 plots the amplitude of the N-evolved solitary waves after separation against initial amplitude. Using Figure 5.5 as an example, a 7 m amplitude initial wave separates into 3 solitary waves and a dispersive tail (noting that the third-evolved solitary wave is not clearly visible). From Figure 5.6, this wave with initial amplitude of 7 m has separated into 3 solitary waves, with the leading solitary wave marked by squares indicating a height of about 9 m, followed by a 2 m and a smaller solitary wave, marked a_2 and a_3 respectively. Qualitatively, the GN equations have the same properties as the KdV equation, where in the region of the release of new solitary waves, the amplitudes of the leading solitary waves increase linearly while the new solitary waves increase quadratically from zero above an amplitude threshold for the initial condition (Curry, 2008).

It is to be expected that the splitting of an initial too-tall wave profile in the GN and KdV models would give similar results – given that both represent shallow water wave equations. But, the GN model will run without any failure even when the leading solitary wave, a_1 has reached an amplitude larger than the water depth. In reality the wave amplitude is limited by wave breaking about 0.7 times the water depth. GN Level 1 does not incorporate this limit in its formulation. A higher Level GN is needed to introduce realistic breaking limits (Shields and Webster, 1988 and Kim et al., 2003).

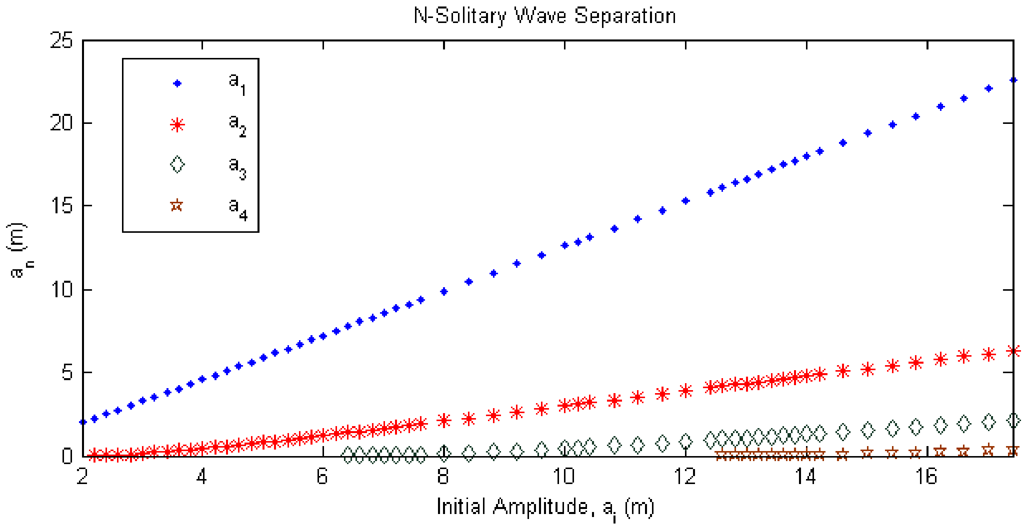

Figure 5.6: *N*-Solitary wave separation

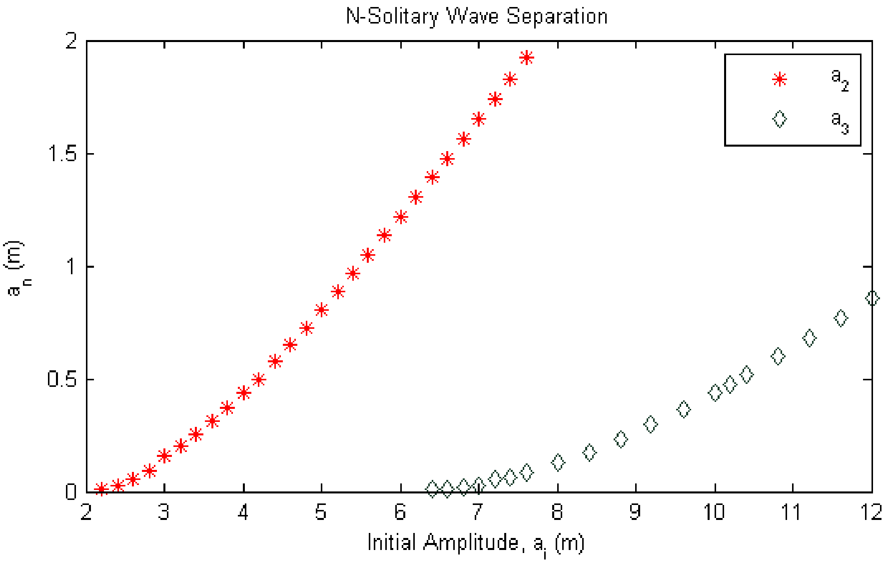

Figure 5.7: Zoomed in portion of Figure 5.6 - release of the 2nd and 3rd solitary waves

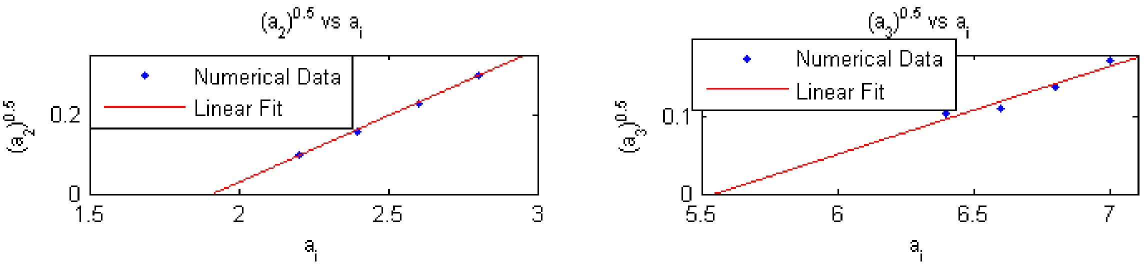

(a) (b)

Figure 5.8: a) The release of the 2nd solitary wave, b) The release of the 3rd solitary wave

To further investigate the GN model for solitary wave separation as compared to KdV, the region where the release occurs for new solitary waves is investigated. Figure 5.7 shows the parabolic growth in amplitude of the second and third solitary waves, while Figure 5.8 is plotted to demonstrate the behaviour in the vicinity of the release, by means of fits to $\sqrt{a_2}$ versus a_i and $\sqrt{a_3}$ versus a_i. It can be seen from Figure 5.8a that the resulting initial amplitude for the release of the second solitary wave i.e. at the point of intersection with the x axis is at a_i about 1.9 m, which is less than the KdV prediction of the release of a new solitary wave of 2 m amplitude (Johnson, 1997). Small solitary waves take time to distance themselves from the dispersive tails behind and reach an asymptotic form. The smaller the wave, the longer it takes for the wave to fully separate itself from the dispersive tail. This is clearly shown in Figure 5.8b where the amplitude for the third solitary wave for the case with initial wave amplitude, a_i of 6.4 m does not fit in with the other three amplitudes. A much longer simulation time is needed for the amplitude of this solitary wave to reach its plateau, at smaller amplitude and hence be in more reasonable agreement with the KdV prediction. For KdV, the release of the 3rd solitary wave occurs when the initial amplitude is 6 m. Therefore, it is not clear from the present analysis whether the GN approach gives exactly the same value as the KdV approach due to the limitation of numerical processing time. It takes weeks on a standard PC with Intel Core 2 Duo 2.93 GHz CPU of 4 GB RAM to achieve the result for the case with initial wave amplitude, a_i of 6.4 m plotted in Figure 6.4b. But as has been mentioned earlier, the numerical value is likely to differ slightly due to the different form of the equations.

Solitary wave separation is particularly interesting in terms of a different problem; a solitary wave propagating across a sharp change in the bed elevation (water depth). Mei (1983) used a linear scattering approximation for long waves approaching a step change (i.e. where there is large change in water depth in a relatively short horizontal distance). Curry (2008) then extended the analysis to solitary waves by estimating the critical depth ratios at which perfect solitary wave separation occurs in the shallower region. Given the critical ratios, the present case of the solitary wave separation in water of constant depth could provide a useful indication as to what are the amplitudes of the resulting separated solitary waves due to the presence of a step change in water depth.

5.3.1 Integrability of GN Equations

It is known that KdV equation is a completely integrable equation (Johnson, 1997); having an infinite number of conserved quantities. As has been shown previously, waves of higher initial amplitude for a given solitary wave width will separate, producing a discrete number of solitary waves. Interestingly for KdV, different solitary waves will give the same non-dimensional wave amplitude for the separated solitary waves, given the same scalar multiplier (κ) for the initial amplitudes. This section investigates the scalability of the GN equations using the scalar multiplier. Figure 5.9 shows the concept of the scalar multiplier, where κ = 1 corresponds to a solitary wave profile. The other two wave profiles correspond to the same solitary wave width of κ = 1 but with different amplitude, as expressed by Equation (5.2).

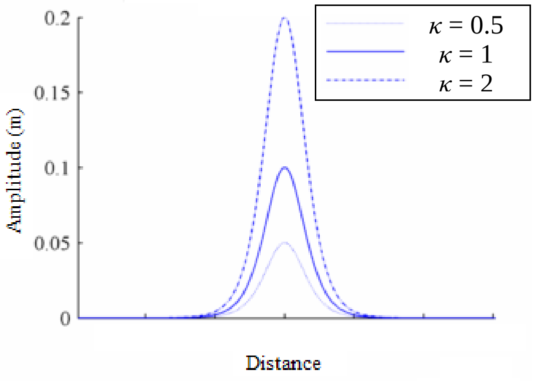

Figure 5.9: Scalar Multiplier for Wave Amplitude

$$\eta = \kappa a \operatorname{sech}^2(b(x-ct)) \qquad (5.2)$$

The KdV solitary wave depends only on the relative size of two input variables which are the input width, b^{-1} and amplitude, a over the water depth, d. But for the Regularized Long Wave (RLW) and GN equations, the absolute values of these variables are important. This is because the KdV equation is weakly non-linear, whereby the speed of the wave varies exactly linearly with the amplitude (see Section 5.1.1) whereas the wave speed for GN solution is slightly different (corrections beyond linear in amplitude) and is nominally valid for all range of a/d. Further analysis has been undertaken regarding solitary wave separation to investigate the scalability of the GN equations. Three series of solitary wave simulations have been undertaken with a solitary wave width corresponding to solitary wave amplitudes of 0.05 m, 0.1 m and 0.2 m each in water of 1 m depth. In each simulation, the initial amplitude is determined using a scalar multiplier, κ of value between 0.5 and 4. Table 5.1 below lists the scalar multiplier and the initial amplitude values for each series respectively.

Table 5.1: Scalar multiplier for the initial amplitudes with 3 different solitary wave widths

κ	Initial amplitude with solitary wave width corresponding to solitary waves of amplitude 0.05 m	Initial amplitude with solitary wave width corresponding to solitary waves of amplitude 0.1 m	Initial amplitude with solitary wave width corresponding to solitary waves of amplitude 0.2 m
0.5	0.025	0.05	0.1
0.75	0.0375	0.075	0.15
0.9	0.045	0.09	0.18
1	0.05	0.1	0.2
1.5	0.075	0.15	0.3
2	0.1	0.2	0.4
3	0.15	0.3	0.6
4	0.2	0.4	0.8

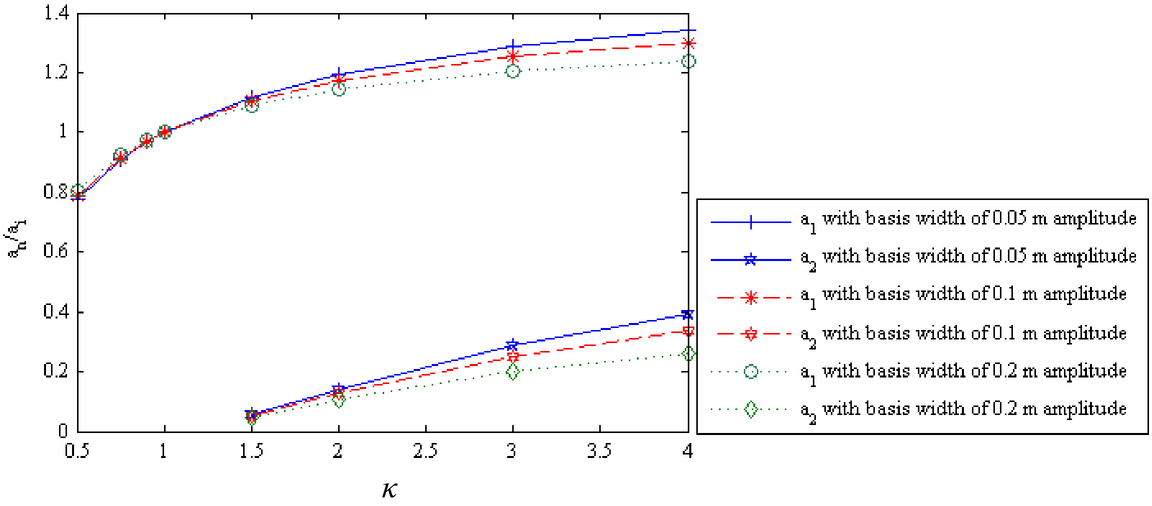

Figure 5.10: Non-dimensional wave amplitude for three different solitary wave widths

Figure 5.10 plots the superimposed non-dimensional solitary wave amplitudes of the leading and second solitary waves. It can be seen that again, qualitatively the behaviour of the GN equations is similar to that of the KdV equation where the resulting non-dimensional amplitudes of the separated waves are almost the same for the three different cases. At $\kappa = 1$, the leading solitary waves for all 3 series have the same non-dimensional amplitude of 1. For $\kappa < 1$, the initial wave will evolve into a single solitary wave with a relatively large dispersive tail.

A comparison is undertaken between the mass of the solitary waves after the separation with the initial waves. Figure 5.11 plots the ratio of the produced solitary wave mass at steady state (M_s) to the initial wave mass (M_i) against κ for $\kappa < 1$, where there is no separation of solitary waves. The mass of the resulting solitary wave is higher than that of the initial wave, indicating that each dispersive wave tail produced has a set-down; the average surface elevation of the tails is less than the mean water level of 1 m. As a result, the GN equations are not exactly scale-able, i.e. integrable unlike the KdV equation, in which the results for the different cases in each of the figures exactly overlap each other.

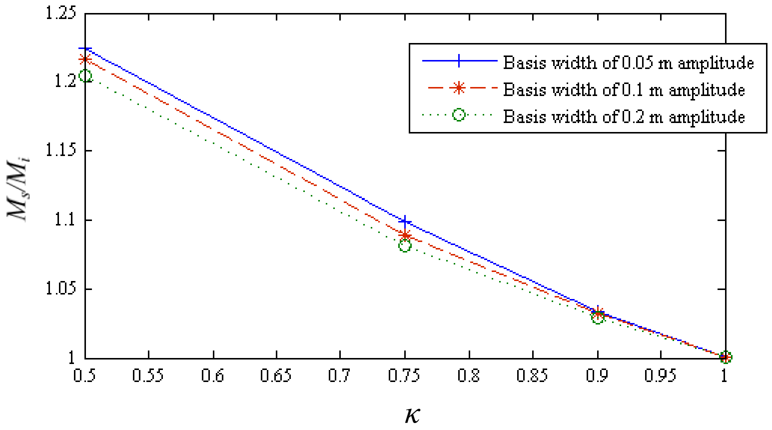

Figure 5.11: Ratio of the produced solitary wave mass at steady state (M_s) to the initial wave mass (M_i) for three different solitary widths

5.4 GN Simulation of Solitary Wave Interaction

Solitary waves can interact with each other at varying angle of incidence and amplitude, and are also not limited to only two solitary waves during an interaction. For a completely integrable equation such as the KdV equation, the interactions between solitary waves of different amplitude interact non-linearly and yet do not destroy each other (Johnson, 1997).

The present section investigates two solitary waves in the GN equations interacting as they advance in the same direction; a large amplitude solitary wave overtaking a small one. As the two waves interact, the fully merged wave has peak amplitude in between the two initial solitary wave amplitudes. There are three cases that could crudely characterise the shape of the merged waves; a double peak, a stretched solitary wave and a thin peak on a wide base. The merged shape depends on the difference in initial amplitude between the two solitary waves.

Figure 5.12 shows the profile-time plot for the interaction between two solitary waves of initial amplitude 6.5 m and 3.5 m, where the large solitary wave is released 500 m behind the lower amplitude solitary wave. The larger wave catches and interacts with the smaller solitary wave producing a double peak shape, whose amplitude is 4.7 m after which the waves change their identity; with the slower wave becoming taller and faster and accelerating ahead while the larger wave becomes smaller and is left behind.

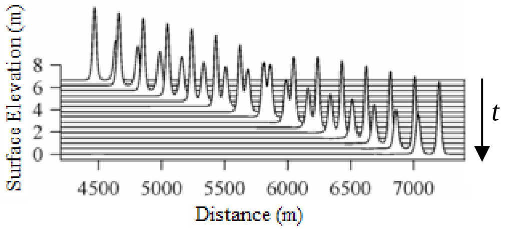

Figure 5.12: Two solitary waves interaction

Clearly to a first approximation the two non-linear waves simply pass through each other. It should be noted that they never completely merge; this issue will be investigated next.

Table 5.2 lists details of a parameter study considering different amplitudes of two solitary waves that have an average amplitude of 5 m in water of depth 10 m to produce the three fully merged wave shape considered above ('fully' corresponding to point of maximum interaction between the two solitary waves). Also listed are the corresponding inverse width, distance between peaks and the amplitude of the fully merged wave, as illustrated in the definition sketch of Figure 5.13. These values are obtained from a best-fit of the following equation to the numerical prediction of the profile of the merged pair of solitary waves at the point of maximum interaction:

$$\eta_f = a\left(\operatorname{sech}^2\left[b(x-L/2)\right]+\operatorname{sech}^2\left[b(x+L/2)\right]\right) \tag{5.3}$$

where η_f = surface elevation of the fitted function (m),

a = amplitude (m)

b = inverse width (m^{-1})

L = distance between the two peaks (m)

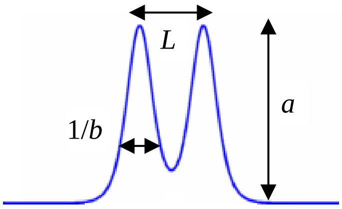

Figure 5.13: Definition sketch for the double peak profile

Table 5.2: Interaction of two solitary waves whose average amplitude is 5 m in water of depth 10 m

Initial condition		Sech^2 fit		
a_1(m)	a_2(m)	b (1/m)	L (m)	a (m)
5.05	4.95	0.04999	121.7	4.999
5.1	4.9	0.04997	107.90	4.996
5.2	4.8	0.04988	94.01	4.988
5.5	4.5	0.04944	75.57	4.944
5.7	4.3	0.04906	68.67	4.904
6	4	0.04842	61.14	4.834
6.5	3.5	0.04722	51.94	4.695
7	3	0.04584	44.49	4.527
7.3	2.7	0.04489	40.28	4.411
7.5	2.5	0.04419	37.43	4.326
7.7	2.3	0.04342	34.46	4.232
7.8	2.2	0.04300	32.90	4.181
7.9	2.1	0.04243	31.23	4.116
8	2	0.04208	29.49	4.071
8.1	1.9	0.04158	27.59	4.011
8.2	1.8	0.04102	25.49	3.947
8.5	1.5	0.03895	16.58	3.712
9	1	0.04168	0.00	3.821
9.5	0.5	0.05028	0.00	4.352

Figure 5.14 plots the fitted parameters in the double sech^2 function given in Equation (5.3) for the case where the amplitude of the larger wave is less than 8 m, giving a double peak merged shape. The assumed fitted sech^2 function gives a remarkably good approximation for the merged wave shapes, accurate to better than the thickness of the dashed lines on the plots.

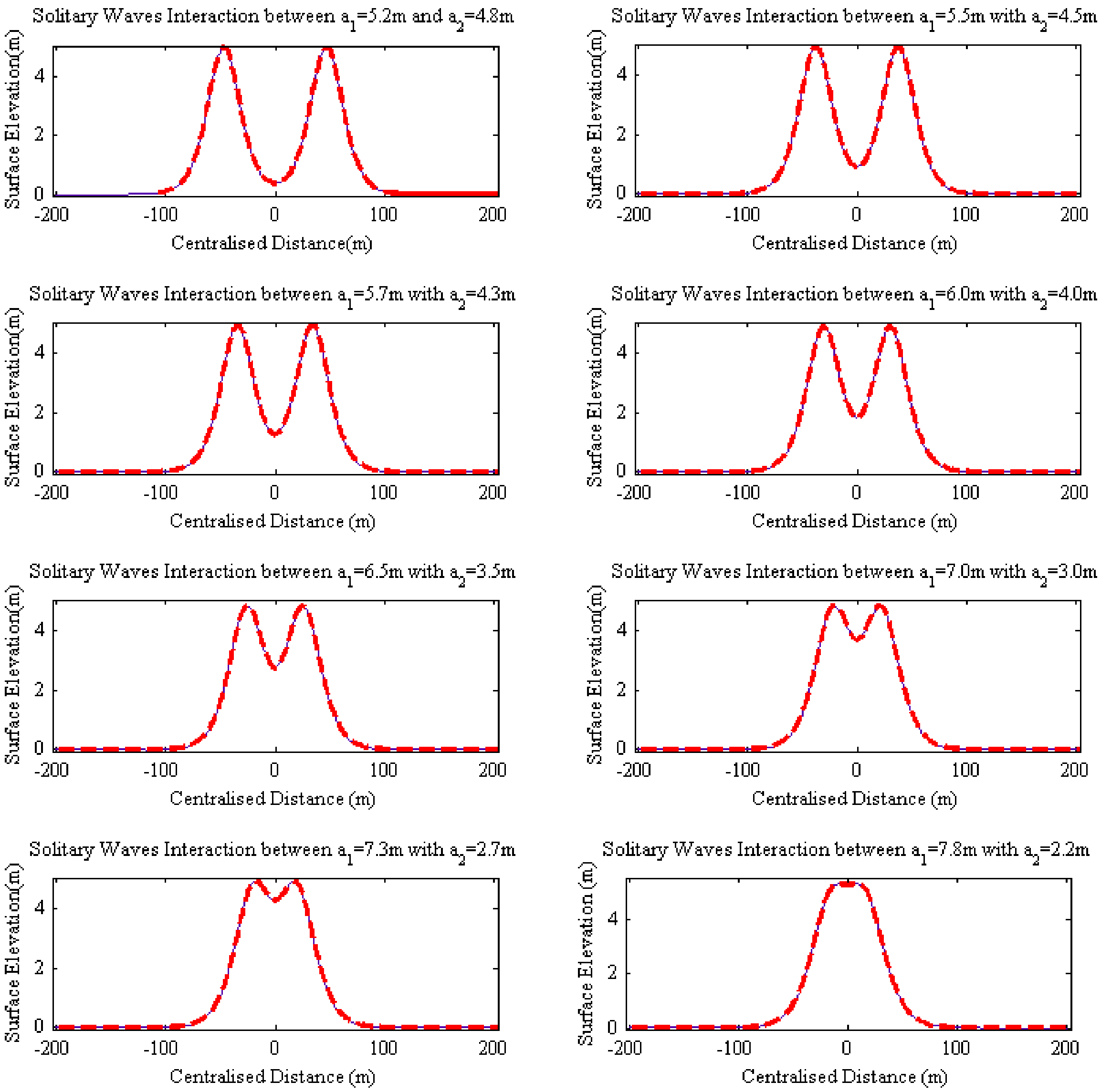

Figure 5.14: Double peak merged shape for two solitary wave interactions, solid line is the result from the numerical simulation and dashed line is the fitted function

Following Table 5.2, the simulated data are plotted systematically in Figure 5.15 to understand the behaviour of solitary wave-wave interactions. Figure 5.15a shows that as the difference in the initial amplitudes between the two solitary wave approaches zero, the inverse width of the fitted function for the resulting wave at maximum interaction between the two solitary waves approaches 0.05 m^{-1}. Interestingly, the inverse width of 0.05 m^{-1} corresponds to a solitary wave of amplitude of 5 m, equal to the averaged amplitude of the pair of solitary waves. This is backed up by Figure 5.15b in which the amplitude of the merged pair of solitary waves at maximum interaction approaches 5 m as the amplitude difference at initial condition decreases to zero. As the difference in amplitude between two initial solitary waves becomes small, the distance between the two peaks at maximum interaction becomes larger and would in principle approach infinity. Figure 5.15c shows the case where the distance between peaks at maximum interaction having an exponential increment as the difference between the initial amplitudes approaches zero. Simulations of two solitary waves with very small difference in amplitude are not worthwhile as it will take a very long time for the slightly larger wave to catch the smaller wave and produce the merged shape. This is obviously consistent with two solitary waves of same height 5 m not interacting with each other as they have the same speed, and thus the distance between them will stay arbitrarily large, i.e. 500 m apart for this simulation.

Whilst the exactly symmetric form of the assumed fully merged shape would suggest exact reversibility of the interaction, with precisely the same two solitary waves emerging from the interaction as those that entered. This is not quite the case. Figure 5.15d shows the difference in amplitude for the larger wave before and after the interaction. It can be seen that it is a locally parabolic curve in which the peak is at 8 m amplitude of the initial condition. This is the case at which the two solitary waves interact and give a shape which matches a single vertically stretched-like solitary wave, which is considered the perfect merged wave shape. Referring back to the scalar multiplier in Section 5.3.1, this stretched-like solitary wave is the same as a solitary wave but with $\kappa > 1$, which will then separate into an integer number of solitary waves. These previous simulations of waves with $\kappa > 1$ provide a forced initial condition for a merged shape. But for the current sets of simulations, more interestingly, the two solitary waves are free to interact with one another and produce the stretched-like solitary wave.

An initial amplitude for the larger solitary wave of higher than 8 m resulted in a wave with a thin peak on a wide-base. Referring back to Figure 5.15d, the occurrence of the maximum difference at 8 m initial amplitude of the larger wave is plausible because the most non-linear interaction occurs at a perfect merged wave shape, giving a higher difference in amplitude between the initial and end conditions of the larger wave. The inconsistency between the first two data points could be noise, as it is down to the level 10^{-5} of difference in value over a 5 m averaged amplitude height.

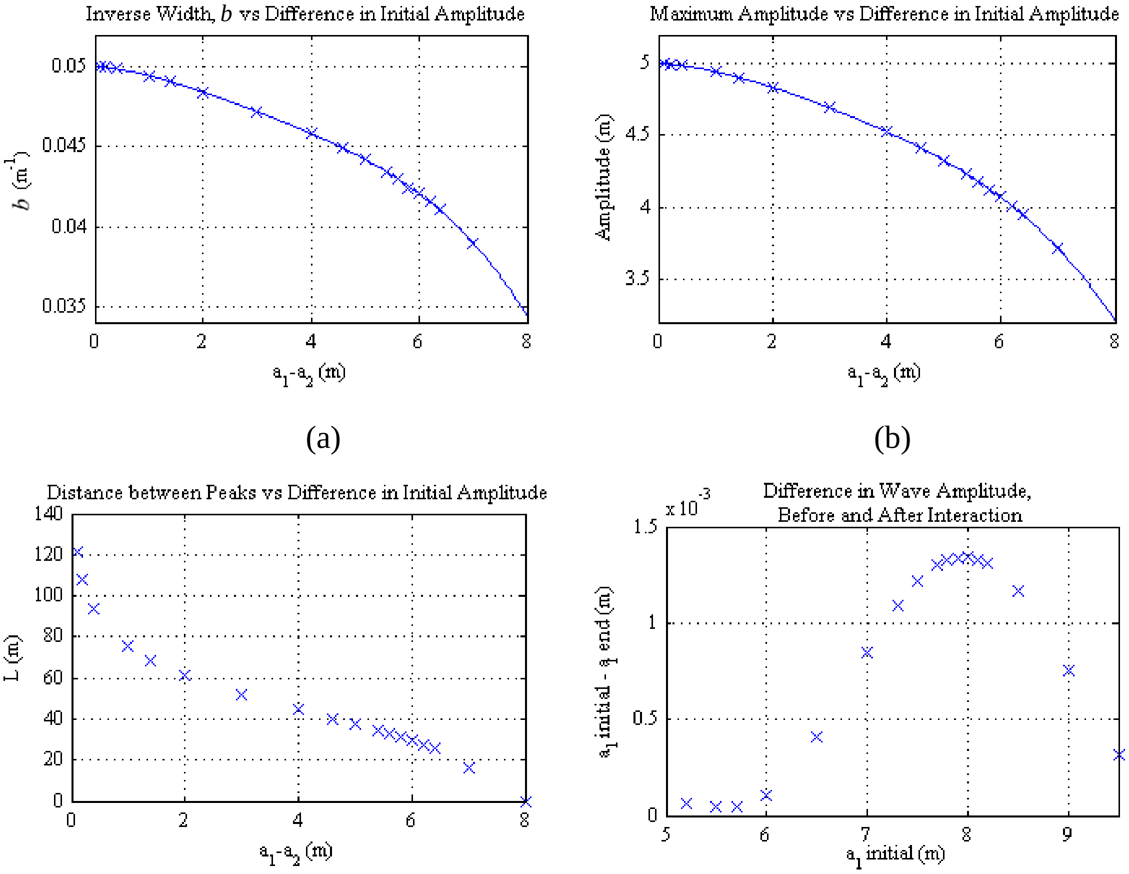

(a)

(b)

(c)

(d)

Figure 5.15: Sech^2 function fitted parameters for two solitary wave interactions

Overall, the interaction of two solitary waves in the GN model more closely matches those of the regularized long wave (or Peregrine) equation than those of the exactly integrable KdV equation.

5.5 GN Simulation of Solitary Wave on a Sloping Bed

Tsunami propagation from deep water to the coastal regions involves waves propagating on a decreasing water depth, a shelf. Although the seabed is irregular, and may include sudden drops and rises, a reasonable model has waves propagating on a uniformly decreasing water depth. The reduction in the water depth will result in reduced speed and increased amplitude. At the top of the shelf, these waves will have steeper fronts, which can separate into a number of solitary waves in the absence of wave breaking. This separation is a similar process as to what has been discussed in Section 5.3, in which a wave with higher amplitude than its equivalent solitary wave, given the same width, separates.

The problem setup is shown in Figure 5.16a, with a *cosh* function chosen for the slope of the bed bathymetry. This is to enable a smooth transition around the points of intersections between the two constant depth regions and the sloping bed. The depth function, α is given in Equation 5.4 where m is the bed slope, k_w controls the sharpness of the transition point at both ends of the sloping bed and x_o is the length of the slope in the horizontal direction. Equation 5.4 consists of two *cosh* functions summed to produce the bathymetry needed. Figure 5.16b shows both the function and also a zoomed-in of the transition point at x_o, where k_w ensures the smooth change between the two regions.

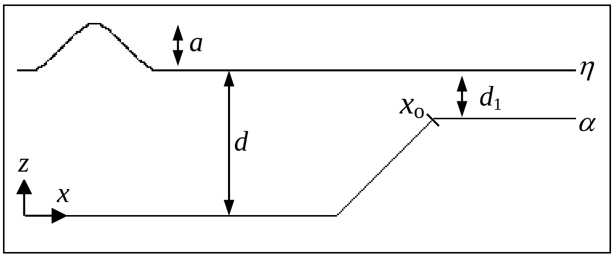

Figure 5.16a: Simulation domain with varying bathymetry

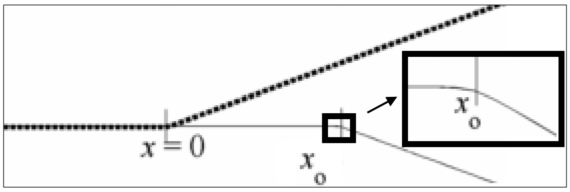

Figure 5.16b: The two *cosh* functions; dashed line is the $log[cosh[k_w x]]$ and, solid line is the $-log[cosh[k_w[x- x_o]]]$

$$\alpha = \frac{m}{2}\left(x_0 - x - \frac{1}{k_w}\log\left[\cosh\left[k_w\left(x - x_0\right)\right]\right]\right) + \frac{m}{2}\left(x + \frac{1}{k_w}\log\left[\cosh\left[k_w x\right]\right]\right) \tag{5.4}$$

A test of numerical accuracy has been carried out by propagating a solitary wave up a 1:30 slope and taking the result at a given time *t* = 130 s as an initial condition for a reverse run back to the original position. The end result after the reverse run is then compared with the initial solitary wave in the deeper water. Figure 5.17a shows the setup of the test while Figure 5.17b shows the result of the accuracy test. The numerical accuracy test involves a solitary wave of amplitude 0.097 m separating into 3 solitary waves on top of the shelf. Figure 5.17a also shows the separated two larger solitary waves at *t* = 130 s, while the third one is not visible due to the scale of the figure. Then, these 3 solitary waves were simulated back going down the slope and combined with each other to produce the initial solitary wave, with a slight numerical shift as seen in Figure 5.17b. There is a difference in amplitude of about 1 percent of the initial solitary wave amplitude after a total of 260 s run, with most of the error arising from this very slight positional shift. This shows that the numerical simulation is able to handle this highly non-linear wave propagation problem on water of varying depth in an adequate manner.

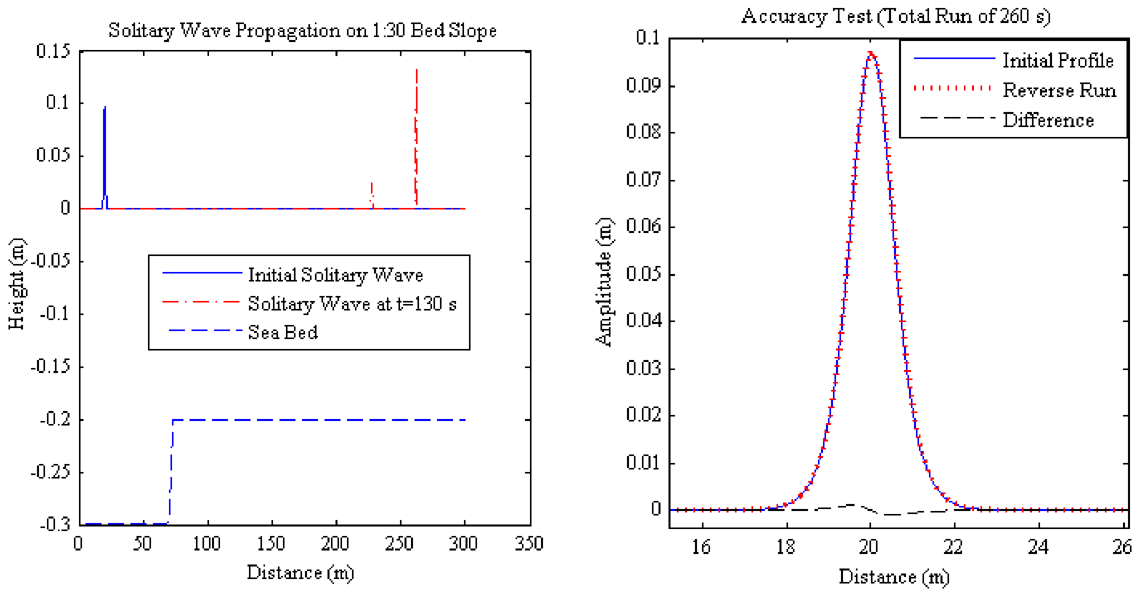

(a) (b)

Figure 5.17: Accuracy test for solitary wave propagating on a slope

The numerical model is now compared to the published experimental data of Seabra-Santos et al. (1987) who studied the transformation of a solitary wave over a shelf. The experiments were performed in a large channel 1.3 m deep, 36 m long and 0.55 m wide. A shelf of 18 m long and 10 cm high was inserted in the channel. Neither the length of the slope nor the steepness of the slope itself was specified in the paper. Thus, for the present numerical simulation, a slope of 1:30 is assumed so that a horizontal distance of 3 m will produce a depth change of 10 cm. The whole 18 m length of the shelf is required in the experimental condition for the waves to fully separate themselves from the others, produce the dispersive tail at the back and then to reach their asymptotic forms. This is clearly the case for the leading solitary wave. However, a much longer tank is in fact needed for the smaller solitary waves to reach their steady-state shape, as will be discussed later. Table 5.3 shows the configuration of the GN simulation in water depths of 0.3 m and 0.25 m with the amplitudes of the corresponding transmitted wave.

The length of the numerical shelf ranges between 100 m to 500 m, depending on the height of the initial amplitude. This is to enable the solitary waves produced at the top of the shelf to distinguish themselves from the solitary waves in front and the dispersive tails behind. Seabra-Santos et al. (1987) used probes with a precision of about 1×10^{-4} m to extract the values for the transmitted solitary waves, in which the length of the step is sufficient for each solitary wave to reach its plateau given the precision. But, 18 m of shelf is not enough for the smaller waves to separate properly. For the case of a solitary wave propagating from a 0.25 m to 0.15 m water depth, there should actually be a very small 3rd solitary wave also separating from the 2nd solitary wave, as shown in Table 5.3. This 3rd solitary wave was not detected in Seabra-Santos et al.'s experimental work. Although the 3rd solitary wave is very small, there is a significance difference in terms of the solitary wave's behaviour in different water depths. Figure 5.18 shows plots of non-dimensional transmitted wave amplitudes against non-dimensional initial amplitudes for two different water depths. They contain the results from the experimental wave channel, the GN numerical simulation and also a KdV equation based analytical approximation from Curry (2008). The analytical approach is undertaken by combining the linear scattering for a solitary wave over a step change followed by the KdV conserved quantity based analytical approach to constant depth splitting.

Table 5.3: Simulation configurations for solitary waves propagation on a slope. d is the water depth before the shelf, a_i is the initial amplitude and a_{tj} is the amplitude of the jth transmitted wave. All units are in m.

(Cases with *a*'s and *b*'s were not experimentally undertaken by Seabra Santos et al.)

Simulation	d	a_i	a_t1	a_t2	a_t3
1a	0.3	0.015	0.02085	0.00400	
1b	0.3	0.03	0.04126	0.00791	
1	0.3	0.0425	0.05814	0.01115	
2	0.3	0.068	0.09278	0.01767	
3	0.3	0.071	0.09689	0.01843	
4	0.3	0.075	0.10240	0.01945	
5	0.3	0.097	0.13313	0.02507	
5a	0.3	0.105	0.14455	0.02713	
5b	0.3	0.12	0.16635	0.03102	0.00015
7a	0.25	0.0075	0.01126	0.00295	0.00003
7b	0.25	0.0125	0.01864	0.00488	0.00004
7	0.25	0.0178	0.02642	0.00690	0.00007
8	0.25	0.0257	0.03798	0.00986	0.00011
9	0.25	0.0384	0.05667	0.01454	0.00028
10	0.25	0.0575	0.08568	0.02137	0.00090
11	0.25	0.0717	0.10838	0.02638	0.00160
12	0.25	0.074	0.11218	0.02720	0.00174
12a	0.25	0.0875	0.13530	0.03200	0.00280
12b	0.25	0.0925	0.14428	0.03380	0.00330

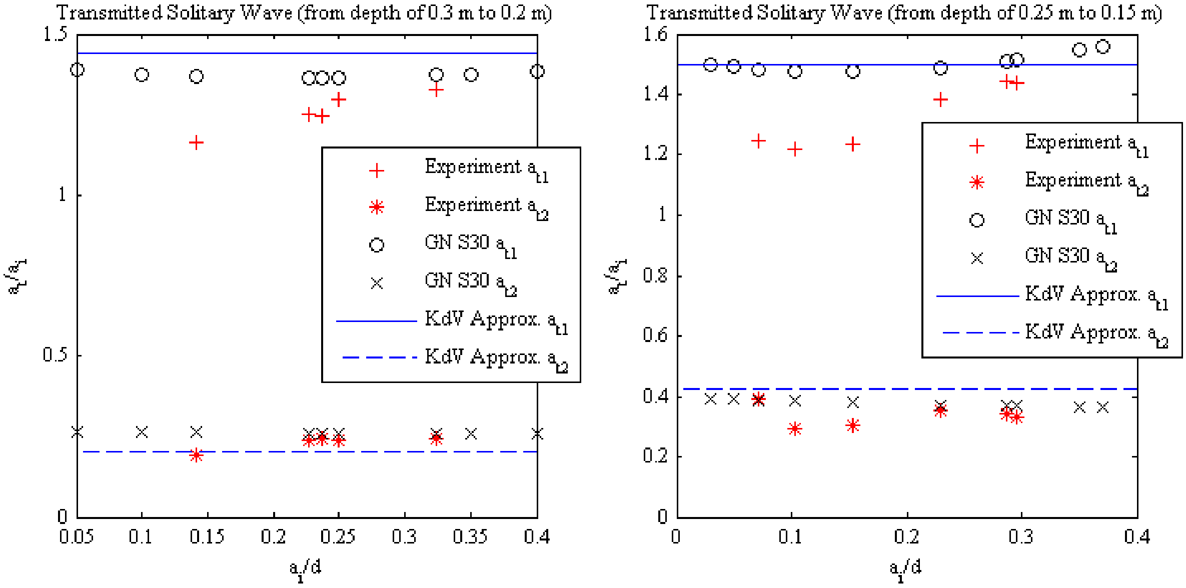

(a) (b)

Figure 5.18: Transmitted solitary waves over a step for initial water depths of a) 0.3 m and b) 0.25 m.

It can be seen from Figure 5.18 that generally, the numerical code is able to give good results. Although the transmitted amplitudes for the KdV analytical approximation do not depend on the non-dimensional amplitude of the incident wave, there is a slight dependence exhibited in the experimental and GN numerical results. In all cases, the experimental value is lower than the numerical prediction produced by the GN code. GN theory assumes that the water has no viscosity, so viscous damping is excluded. But experimentally, the waves experience energy dissipation due to the viscous damping effect. This reduces the height of its amplitude and is likely to broaden the wave width, and could be the reason for the discrepancies between the two. Due to the unknown nature of the length of the slope, numerical simulations have been carried out for slopes of 1:20 and 1:10 and are compared with one another to make sure that the discrepancies mentioned above are not due to the value of the slope. Figure 5.19 shows the transmitted wave amplitudes on three different slopes, with the water depth changing from 0.3 m to 0.2 m. The difference in value for the first transmitted wave is about 0.3 % compared to the averaged 14 % difference between the numerical and experimental results above. Clearly, the slope has little effect on the discrepancies mentioned above. This further strengthens the view that viscous damping plays an important role. For the 2nd transmitted wave, there is a rather larger separation in results for the higher amplitudes (more non-linear cases). It happens that the slope of 1:30 gives the closest value to the experimental results.

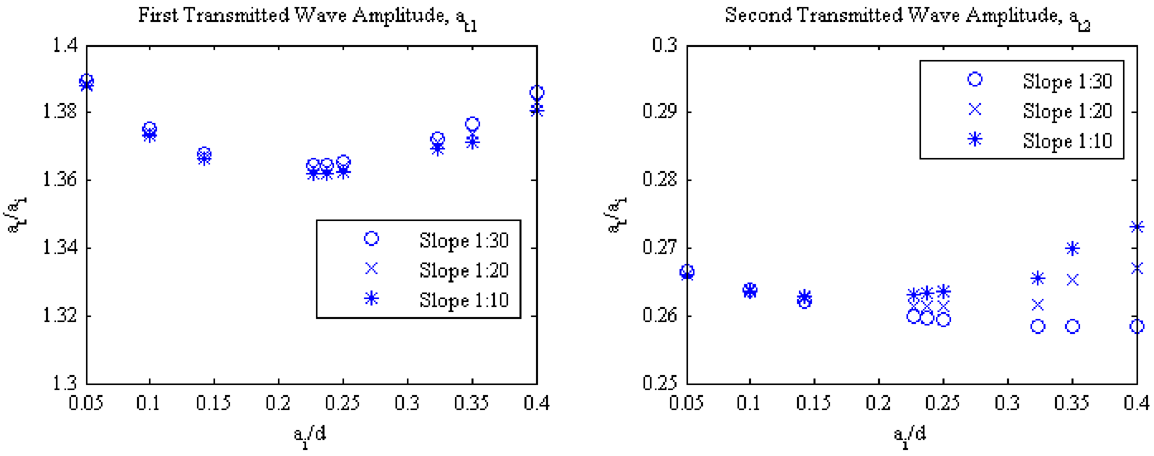

(a) (b)

Figure 5.19: Comparison of non-dimensional transmitted waves for 3 different bed slopes

The reflected waves are much smaller than the transmitted waves and are likely to propagate linearly without much change in their profile and velocity on water of constant depth. Figure 5.20a shows the reflected waves for 3 different initial water depths where the bed slope is 1:30. Clearly, it can be seen that all the results have the same trend, where the reflected wave amplitude relative to its initial amplitude decreases as the initial amplitude increases. A higher amplitude solitary wave has a narrower width, and when the wave interacts with the slope, the wave sees the slope as a more slowly varying depth then would a smaller amplitude solitary wave of broader width. Consequently, the reflected wave amplitude relative to the initial solitary wave is smaller, even though the reflected wave amplitude is actually larger. This is consistent with the observation in Figure 5.20a. Comparison with experimental results is shown in Figure 5.20b. Instead of using the bed slope of 1:30, a bed slope of 1:10 is used in the simulation. It is found that even with the steeper slope, the numerical values are less than half the values from the experiment.

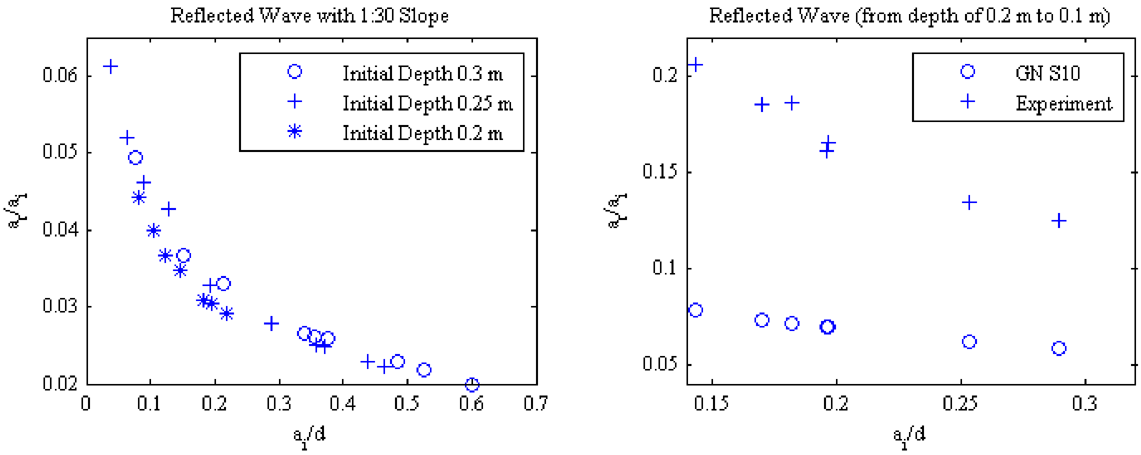

(a) (b)

Figure 5.20: Non-dimensional reflected waves, a) 1:30 slope with varying initial water depth, b) comparison with experimental results for 1:10 slope

The number of solitary waves produced depends on the depth ratio. Johnson (1997) gives estimates for the critical depth ratios at which perfect soliton separation occurs. These are listed in Table 5.4.

Table 5.4: Critical depth ratio for soliton separation

Number of solitary wave	d_1/d
1	1
2	0.6137
3	0.4510
4	0.3594

A solitary wave of amplitude of 0.0425 m (Simulation 1 of Table 5.3) on initial water depth of 0.3 m has been simulated propagating over a slope of 1:30 for four varying depth ratios. Table 5.5 summarises the observed results. It can be seen that the code is able to cope with the high depth changes and produce good solitary wave separation. Quantitatively, the critical depth ratio for GN equations is not exactly the same as for the Johnson’s KdV equation predictions. Using the KdV equation, the last depth ratio of 0.467 should produce only 3 solitary waves with dispersive tails.

Table 5.5: Observation of solitary wave separation using GN equations for varying water depth ratios

d_1/d	Observation
0.667	2 solitary waves with dispersive tails
0.6	3 solitary waves with dispersive tails
0.5333	3 solitary waves with dispersive tails
0.467	4 solitary waves with dispersive tails

5.6 Conclusion

- The numerical scheme is able to produce physically realistic solitary wave propagation; which shows the ability of the numerical model to cope with non-linearity. The solitary wave propagates in water of constant depth without loss of amplitude or velocity.
- In comparison with the KdV equation, qualitatively the GN equations have similar properties to the KdV equation.
  - For solitary wave separation;
    - A starting condition where a wave has higher amplitude compared to its width than a solitary wave has been simulated. This initial condition evolves in time and separate into two or more solitary waves, accompanied by small dispersive waves. The leading solitary wave is higher than the initial wave, while the second and any subsequent waves are much smaller.
    - In the region of the release of new solitary waves, the amplitude of the leading solitary wave increases linearly while the amplitude of the new

    solitary waves increasing in a quadratic manner above a critical threshold, the same behaviour shown by the KdV equation. This is expected as both approaches should adequately represent the same shallow water behaviour.

- It should however be noted that the solutions to the GN equations are not scalable in terms of *a*/*d*, unlike the KdV equation. The KdV equation is a weakly non-linear equation whereby the speed of the wave varies exactly linearly with the amplitude whereas the wave speed for GN solution is slightly different (corrections beyond linear in amplitude).
- The GN equations are able to simulate solitary wave interactions well.
    - Two solitary waves interacting as they advance in the same direction has been simulated; a large amplitude solitary wave overtaking a small one. As the two waves interact, the fully merged wave has peak amplitude in between the two initial solitary wave amplitudes. The waves change their identity; with the slower wave becoming taller and faster and accelerating ahead while the larger wave becomes smaller and is left behind.
    - The fitted sech^2 function gives a good approximation for the merged wave shapes.
- The GN equations are able to handle the highly non-linear wave propagation on a varying water depth.
    - Solitary waves propagation from deep water to shallow water on a rather steep slope (1:30) have been simulated. At the top of the shelf, these waves have steeper fronts, which separate into a number of solitary waves (transmitted solitary waves) in the absence of wave breaking. This separation is a similar process as to what has been discussed in the solitary wave separation, in which a wave with higher amplitude than its equivalent solitary wave, given the same width, separates.
    - There is a slight dependence to amplitude exhibited in the

    experimental (by Seabra-Santos et al., 1987) and GN numerical results for the transmitted solitary waves when compared to the analytical solution. The analytical approach is undertaken by combining the linear scattering for a solitary wave over a step change followed by the KdV conserved quantity based analytical approach to constant depth splitting.

    - Compared to the experimental results, the experimental value is lower than the numerical prediction produced by the GN model. GN theory assumes that the water has no viscosity, so viscous damping is excluded. But experimentally, the waves experience energy dissipation due to the viscous damping effect.

- In short, the numerical solver for the GN equations works well and the GN Level 1 gives quantitatively good results when compared to the corresponding solution of the KdV equation.

6 GN Numerical Simulation of Focussed Wave Groups

6.1 Introduction

A wave group consists of a number of individual waves travelling and interacting with each other. If all the individual waves within the wave group have the same phase (e.g. the peak crests or troughs elevations of all the individual waves are aligned in space and time), a focus wave group is produced. A focus wave group can be constructed to have the same profile as the average shape of extreme wave events in long random time series as shown by the laboratory data analysis in Chapter 2. Figure 6.1 depicts a typical focus wave group profile.

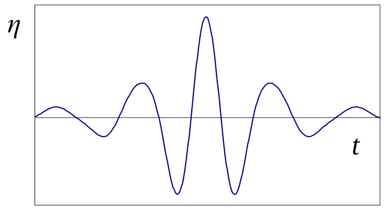

Figure 6.1: Focus wave group profile

The aim of this chapter is to understand the behaviour of focus wave groups representing extreme waves, in particular extreme wave's interaction with a mild sloping bed (slope of 1:100). Together with the data analysis in Chapter 2 and Chapter 3, the numerical result will hopefully give an insight on extreme wave's behaviour. In general, the current research should reproduce the observations by Hunt (2003). Experimental work by Hunt involved focus wave groups interacting with a plane beach with slope of 1:20 (which is relatively steep compared to the current research). Hunt showed that there is a gradual dispersion from focus at the toe of the beach to a rather less well-defined wave group; the higher frequency waves emerging from the main wave and also the presence of breaking for the main wave crest, which then developed into a saw-toothed shape. Numerical simulations of these experiments can also be seen in Orszaghova et al. (2012).

This chapter starts with investigation of the effect of water depth and wave steepness for wave groups propagating on constant water depth towards their focus profiles. The profile of the wave group will be affected by the balance between linear dispersion and non-linearity; examined through separation of harmonics using the Stokes water wave expansion. The next section investigates wave group propagation on a gentle slope. The sloping bed cases should reproduce the same behaviour of the constant depth cases; both the reduction in water depth and increment in wave steepness increase the contribution of the higher order harmonics in the wave group. But intriguingly, the numerical result shows that there is an extra wave set-up, a function of the sloping bed because there is no evidence of a wave set-up produced as the wave propagates on constant depth, apart from the free error wave. In order to gain a better understanding of the behaviour of focus wave groups on mild sloping beds, the numerical results are compared to the averaged large wave events constructed from the random wave propagation of the Lowish experimental data.

6.2 Simulation Setup

A NewWave-type wave group can be obtained from the JONSWAP spectrum (given in Equation (1.3) of Section 1.3) using Fourier series. The wave group is composed of the summation of all individual oscillating wave components consistent with the spectrum and can be written by,

$$\eta(x,t)=\sum_{i=1}^{N}a_i\cos(\omega_i t-k_i x) \tag{6.1}$$

where η is the free surface elevation, a_i is the amplitude of the ith component, ω_i is the wave frequency, k_i is the wave number, and N is the total number of spectral components.

By setting x = 0 m in Equation (6.1), a simple focus wave group in time is produced. However, the initial condition for the GN numerical simulation is taken to be a focus wave group in space, and thus the discretised wave number spectrum [$S(k)$] is used instead of the frequency spectrum (JONSWAP). The wave number spectrum can be obtained from the JONSWAP spectrum by;

$$S(k) = S(\omega) \tag{6.2}$$

where the GN linear dispersion equation [Equation (4.50) of Section 4.6.1] is utilized for the wave number step, Δk. This is necessary because the frequency step $\Delta\omega$ is uniform in the JONSWAP frequency spectrum, while Δk in the wavenumber spectrum will not be uniform.

6.3 Focussed Wave Groups on Water of Constant Depths

A series of focus wave groups, each propagating on constant water depth is simulated. The water depth (d) and amplitude of the focus wave groups (a) are varied to investigate their effect as the focus wave groups propagate. Thus, both the effects of linear dispersion and wave steepness are investigated.

From the GN linear dispersion equation, if the water depth, d changes for a given wavenumber, k, then the wave period, T changes. For these simulations, the peak wavenumber, k_p is set constant at 3.23 m and the peak wave period, T_p is varied during the interchange from the frequency spectrum to the wavenumber spectrum for different water depths. The input parameters for the spectra are as follows;

Table 6.1: Input parameters for the JONSWAP spectra

No.	d (m)	T_p (s)	$k_p d$
1	0.46	1.19	1.5 (deep water)
2	0.39	1.22	1.25
3	0.30	1.30	1
4	0.23	1.41	0.75
5	0.16	1.62	0.5 (shallow water)

The numerical scheme is setup as follows:

The grid spacing is $\Delta x = 0.04$ m and the time step is $\Delta t = 0.01$ s. The length of the tank (solid boundaries) is 250 m. At each water depth, the amplitude effects on the behaviour of the wave groups are also investigated. The wave groups start at $t = 0$ s (at focus) and are assumed to propagate linearly (using ak_p of 0.001) backwards until $t = -30$ s. Then, the surface elevation profile and velocity distribution along the tank are multiplied by a multiplication factor, M and propagated forward for 60 s until $t = +30$ s (this corresponds to 30 s beyond linear focus). The behaviour of these wave groups of different steepness will be directly compared with the linear wave group simulations, examining in particular the wave groups' structure at the linear focus time of $t = 0$ s. This wave steepness (ak_p) is based on the amplitude of the focus wave group, assuming perfect focussing, and the wavenumber corresponded to the peak period, T_p. Four different values of wave steepness for the wave groups at $t = -30$ s are investigated. These are listed in Table 6.2.

Table 6.2: Variation in wave steepness for wave groups at $t = -30$ s

No.	M	ak_p
a	1	0.001 (assumed linear)
b	100	0.1
c	200	0.2
d	400	0.4

Note that there will be free error waves evolving from the starting condition of the non-linear wave group at t = -30 s due to the linear structure of the wave group. But by simulating waves with a longer numerical tank (in order for the main wave packets to be further separated from the free error waves), the main results will not be affected.

Recall the modified Miche criterion introduced in Section 2.6. This is shown again in Equation (6.3). In deep water, the equation reduces to a maximum wave steepness $H_{max}k = 0.75$, and in shallow water, it reduces to a maximum height-to-depth ratio $H_{max}/d = 0.76$.

$$H_{\max} = \frac{0.24\pi}{k} \tanh\left(kd\right) \tag{6.3}$$

where

H = wave height,

k = wave number and,

d = water depth.

The most severe case (Case 5d, denoted by the shallow water group in Table 6.1, and the largest amplitude in Table 6.2) is at $k_pd = 0.5$ and $ak_p = 0.4$, where the amplitude to water depth ratio (a/d) is 0.77. This exceeds the modified Miche limiting criterion which is based on the limiting wave height, so actual water waves in a tank would be expected to have broken even if the numerical GN results show no indication of this.

6.3.1 Accuracy Test

Initially a linear focus wave group at $t = 0$ s is run backwards in time to $t = -30$ s. Then the amplitude and velocity are scaled up by a factor of 400. Next, the wave group at $t = -30$ s is propagated forwards for 60s. Figure 6.2a shows the initial and end profiles of the simulation for the most severe case (Case 5d). Next, the end result at $t = +30$ s is taken as the initial condition for a reversed run; the wave group propagating backwards for 60 s back to $t = -30$ s, performed by simply running the code with a negative time step. The end profile of the reversed run is then superimposed on the initial profile of the original run to compare both the profiles (both amplitude and phase).

Figure 6.2b shows the result for Case 5d, zoomed in onto the centre of the main wave packet so that the difference can be seen clearly. The original wave profile is very closely recovered from the reversed run. There is a very small shift in phase for the reversed run, but this phase lag is very small (< 0.1 s) compared to the total runs of 120 s (or 75 wave cycles with T_p = 1.62 s). This is acceptable considering the wave is very steep and in very shallow water depth, with associated complex interactions as demonstrated by the profile at t = +30 s in Figure 6.2a.

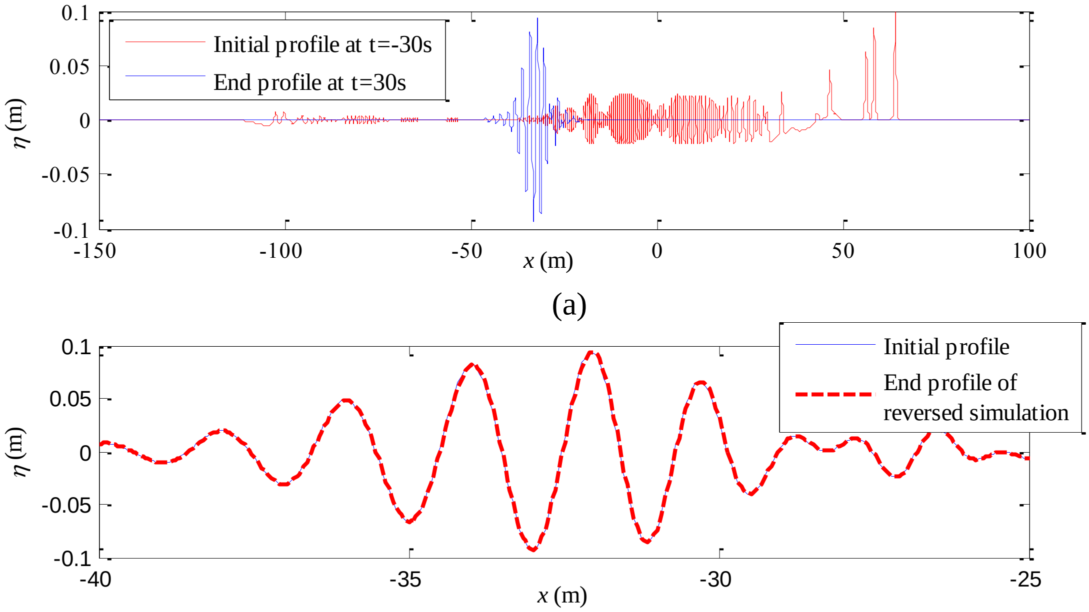

(a)

(b)

Figure 6.2: a) The initial and end profiles of the original simulation, b) Initial profile of the original simulation and the end profile of the reversed simulation for the most severe case (ak_p = 0.4, k_pd = 0.5)

The total energy (potential and kinetic energy) is often used as an estimate of the accuracy of potential flow simulations, for example Gibbs and Taylor (2005). In all conservative and non-dissipative wave problems, the total energy should be conserved. Potential energy is solely monitored here because it is well defined. For non-linear wave problems, potential energy may not be conserved in time as only the total, potential and kinetic, is a conserved quantity. In fact, variations in time between potential and kinetic energy for propagating wave trains are indicative of inherently non-linear interactions (Epilogue Part 2 of Lighthill, 2003). But, monitoring the potential energy only is useful in the context of a reversed run to assess the accuracy of the simulation.

The total potential energy over the wave tank is tracked over time for both the original and reversed run. This is plotted in Figure 6.3a. The reversed run recovers the potential energy at every time step. The plot shows the range from *t* = -30 s to *t* = -10 s, so that the oscillating potential energy at the initial stage of the simulation can be seen more clearly. Notice that the simulation starts from a dispersed condition, 30 s before the linear focus location. Because this is a very non-linear case (the surface elevation and velocity are scaled up 400 times from a linear condition at *t* = -30s), free error waves are introduced in the simulation from this starting condition. The error waves will interact with each other and also with the bound waves, resulting in the oscillation of potential energy at the early phase of the simulation. The potential energy after *t* = -20 s is close to constant. To explain this oscillation, Figure 6.3b shows the *x*-*t* plot for the surface elevation. The first 10 s is rather disorganised as the individual components of the wave group start to separate themselves from one another, followed by interactions of the individual components with each other at different space and time locations. It seems likely that the peaks in the potential energy correspond to wave crests combining where the reduction in potential energy relate to the diminishing magnitude of the surface elevation locally (the crests for a component wave package locally coinciding with the troughs of a second component packet). After 20 s, the wave group experiences less interaction between its individual wave components leading to a more constant value of potential energy. In all the simulations with different water depths and wave steepness, the potential energy check (end of the reversed run compared to the start of the original run) is accurate to 0.005 %, except for the most severe case which is accurate to 0.1 % (Case 5d).

Figure 6.3c plots the normalized mass of the wave group integrated over space at each time. The mass is integrated using the Simpson's rule and has been normalized by a mass-like quantity, $\sum_{space\ domain} \left|\eta\left(x, t=-30\right)\right|$ at the initial condition. The figure illustrates that mass is well conserved throughout the entire simulation. The step change at *t* = 0 s, albeit very small is probably caused by a combination of finite resolution in both space and time when the waves are most non-linear, arising because the lack of resolution of the high order harmonics and the movement of the error wave systems relative to the main wave packet.

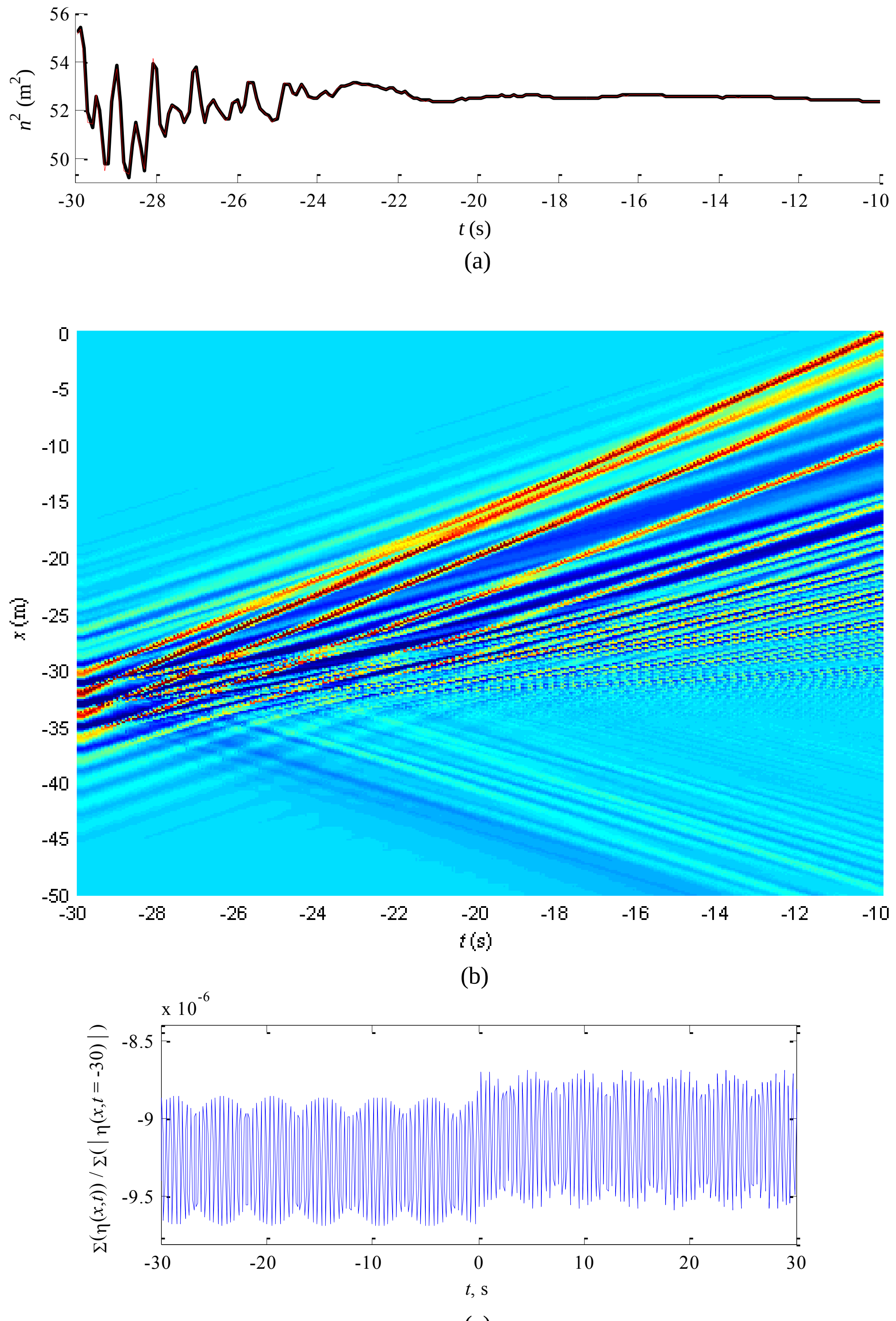

(a)

(b)

(c)

Figure 6.3: a) Potential energy over time for both the original (thick line) and reversed (thin line) simulations, b) *x*-*t* mesh plot, and, c) normalized mass of the wave group (in space) over time, for the most severe wave group case ($ak_p = 0.4$, $k_pd = 0.5$)

In addition, a comparison of focus wave group propagation has been made between simulations by the Madsen and Sørensen version of the Boussinesq equations and the GN equations. The former has been done by Orszaghova (2011), using a numerical wave paddle as a wave-maker. Extensive validations of the inbuilt wave paddle were undertaken by Orszaghova who simulated solitary waves and compact wave groups which were in good agreement with measured data (Orszaghova et al., 2012).

Figure 6.4 shows plots of the wave group propagations from focus at $x = 0$ m and $t = 0$ s at three different times using the Boussinesq equations driven by a first order paddle signal and the GN equations. The wave group was created using the Pierson-Moskowitz spectrum with peak frequency, ω_p of 2.91 Hz and focus wave group amplitude of 0.114 m, on water of constant depth of 0.5 m. As can be seen from the figure, the two sets of results have almost identical main wave group profiles. At $t = 5$ s, the peak amplitude and phase matches with slight differences in amplitude for crests and troughs before and after the peak crest. As the waves propagate away, double frequency and long free waves are produced. The profile and phase of the main wave packets and double frequency free waves are in agreement with each other but the agreement is less good for the long free waves. It has to be noted that for the Boussinesq simulation, the wave paddle is sent a displacement signal in time and correspondingly the wave paddle moves to create the focus wave group. There is a delay in time before the wave paddle achieves the peak displacement needed to produce the peak amplitude, and by this time the long free wave has been created and propagates ahead of the focus wave group. In contrast, using an initial condition in space for the GN simulation, a long free wave is created at the same time as the initial condition of the focus wave group. Thus, this might explain the faster long free wave separation from the main wave packet for the Boussinesq simulation. Overall, the degree of agreement between the solutions from the enhanced Boussinesq equations and the GN equations is satisfactory.

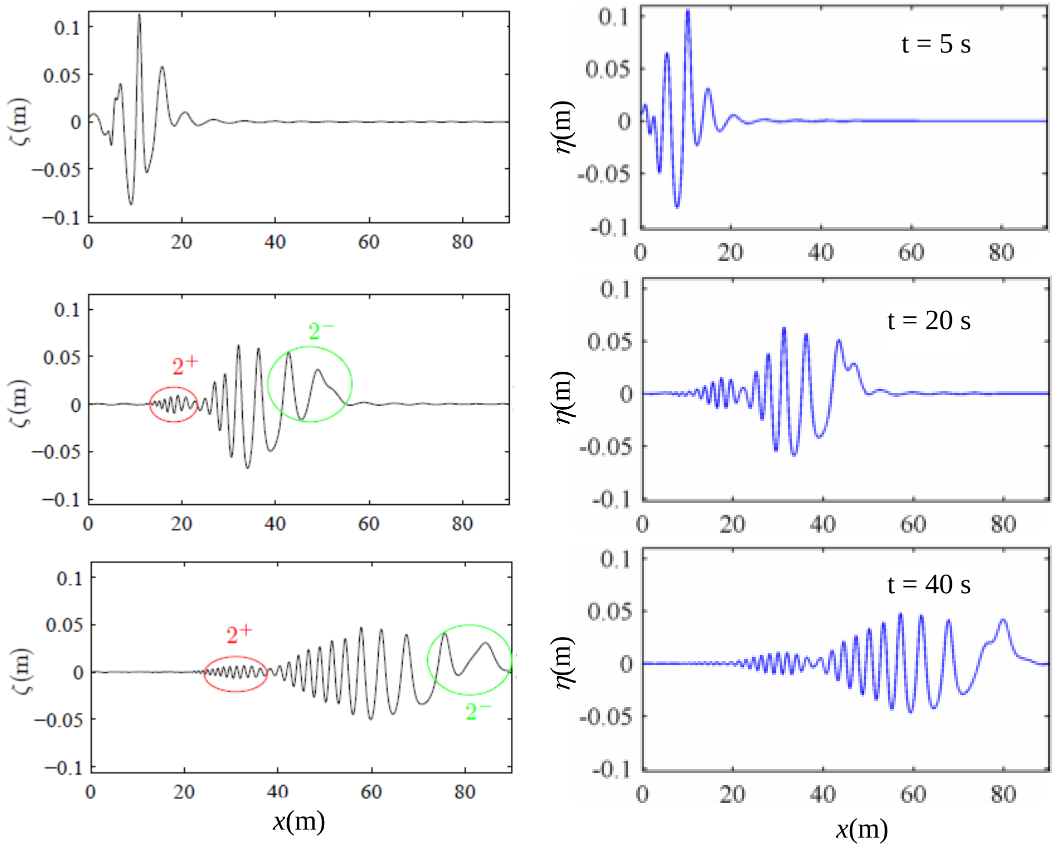

(a) (b)

Figure 6.4: Focus wave group simulation with $k_p \approx 1.42$ on constant depth of 0.5 m using, a) Boussinesq equations (Orszaghova, 2011) and, b) GN equations.

The convergence test has been undertaken in Section 6.4.1 which involves a more complicated case; a wave group propagating over a gentle slope. The result exhibits a fourth order accuracy, which is consistent with the RK4 time stepping and fourth order spatial discretisation. Regarding the dispersion property of the wave group, comparisons made in Figure 4.4 of Section 4.6.1 showed that the dispersion relationship for the numerical simulations matches very well with the GN analytical dispersion equation. Thus, this section, together with the validations against the solitary waves in Chapter 5 provides confidence that the numerical scheme is working as intended and is ready to be applied to other problems.

6.3.2 Effect of Water Depth on Linear Wave Groups

The behaviour of focus wave groups propagating on different water depths is investigated. Figure 6.5a shows *x*-*t* plots of the surface elevation for $ak_p = 0.001$ (linear wave group) from $t = -30$ s to $t = 30$ s for different water depths ($k_pd = 1.5$ to 0.5) while Figure 6.5b shows the envelope plot of the surface elevation. The top panel in Figure 6.5a is the initial condition i.e. the focus wave group at $t = 0$ s. Note that the *x*-axis is the spatial coordinate along the wave tank and the wave profiles at the front of each panels correspond to $t = 30$ s. Both the figures show that the linear dispersion is working well, with the wave groups widening and the amplitudes reducing with time in each plot either side of the focus point, especially for the deeper water cases where the phase speed of each linear component is a strong function of the wavelength. Also, the focussing of wave energy can be seen by following the highest peak in the middle of each plot (at $x = 0$ m). As the water depth decreases, the wave groups are less dispersive. In the shallowest water, the wave group almost maintains the same profile throughout the time period.

The wave groups are then decomposed to obtain the odd and even harmonics using the Stokes water wave expansion described in Section 3.3. Figure 6.6 presents *x*-*t* plots for the surface elevation together with its odd and even harmonics at $k_pd = 0.5$. The odd harmonics profiles are essentially identical to the crest elevation profiles and there are no free error waves visible. The even harmonics in Figure 6.6c do exist but are negligible as they are a factor of 100 smaller than the odd harmonics. This demonstrates that the wave group is behaving linearly even in the shallowest water depth. In deeper water, the contributions of the higher order harmonics are negligible.

Also from Figure 6.6c, as the wave group propagates away from the focus location, several small groups of waves can be seen propagating in the opposite direction. The same feature is observed during the solitary wave separation runs in Section 5.3; the solitary waves emit a small dispersive group in the other direction from the start of the simulation. Again, this is plausible as GN equations permit waves propagating in both directions, unlike the KdV equation.

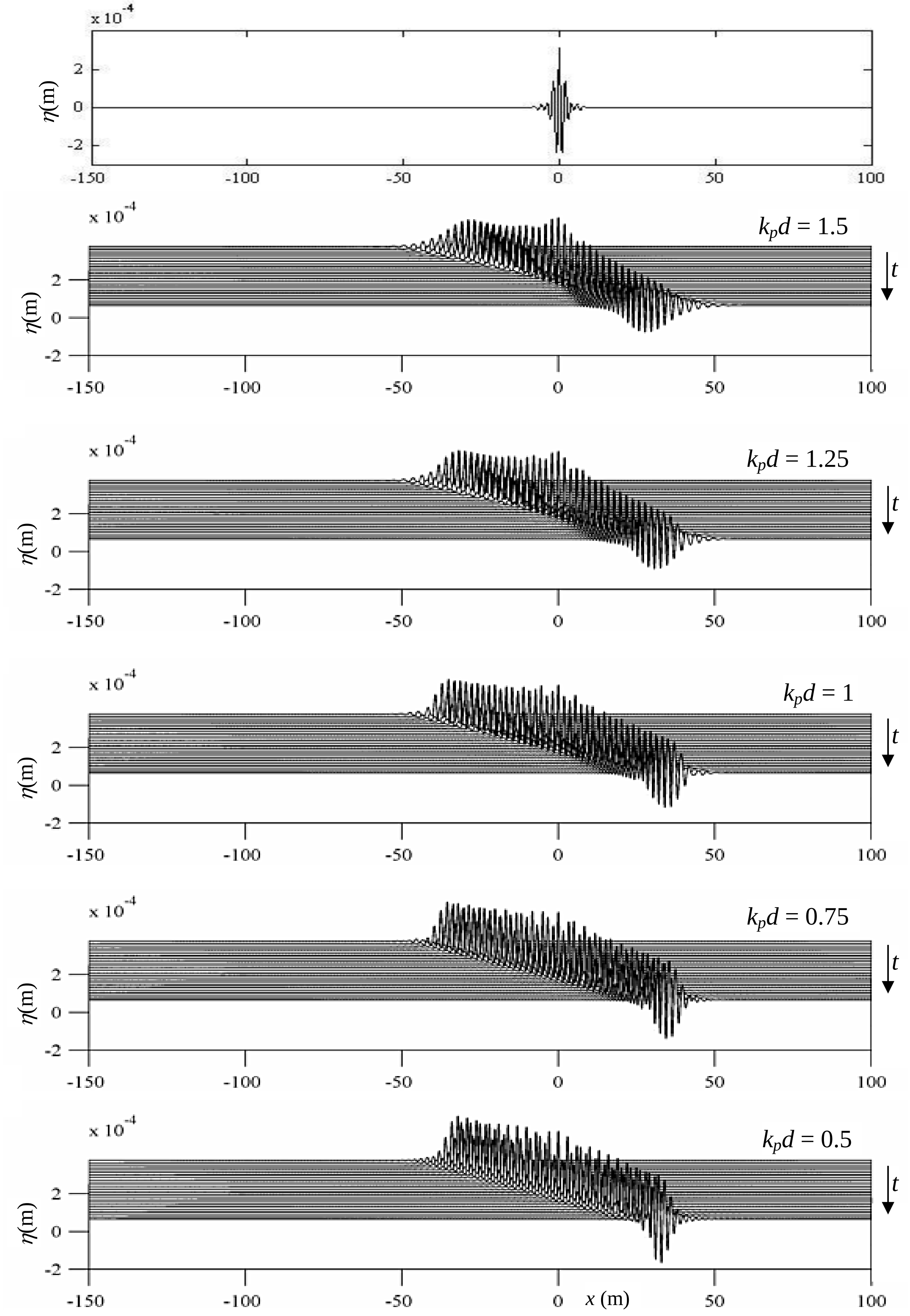

Figure 6.5a: x-t plot for linear wave group ($ak_p = 0.001$) propagation from $t = -30$ s to $t = 30$ s with decreasing water depth (linear wave focussing at $t = 0$ s, $x = 0$ m)

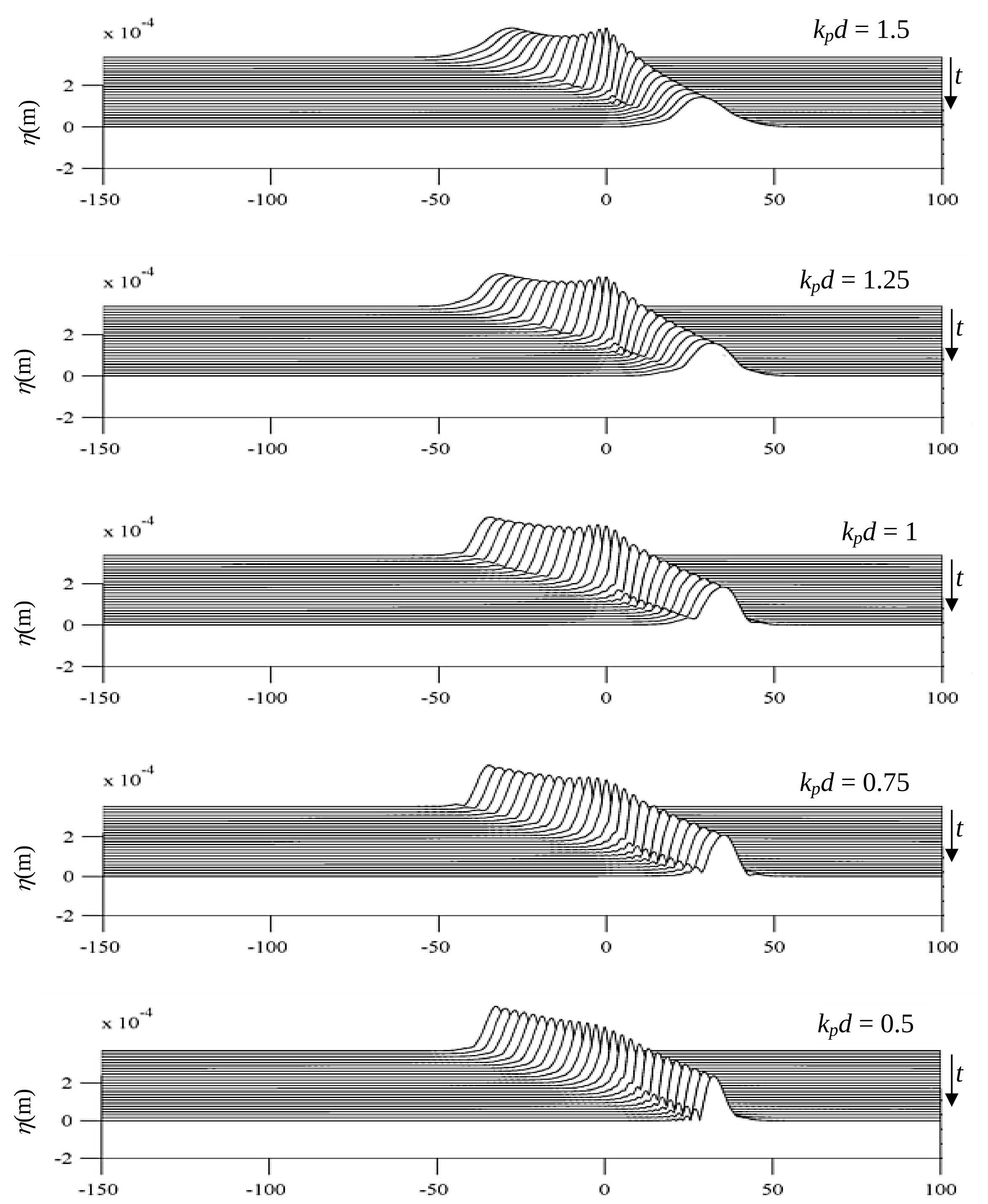

Figure 6.5b: x-t envelope plot for linear wave group (ak_p = 0.001) propagation from t = -30 s to t = 30 s with decreasing water depth (linear wave focussing at t = 0 s, x = 0 m)

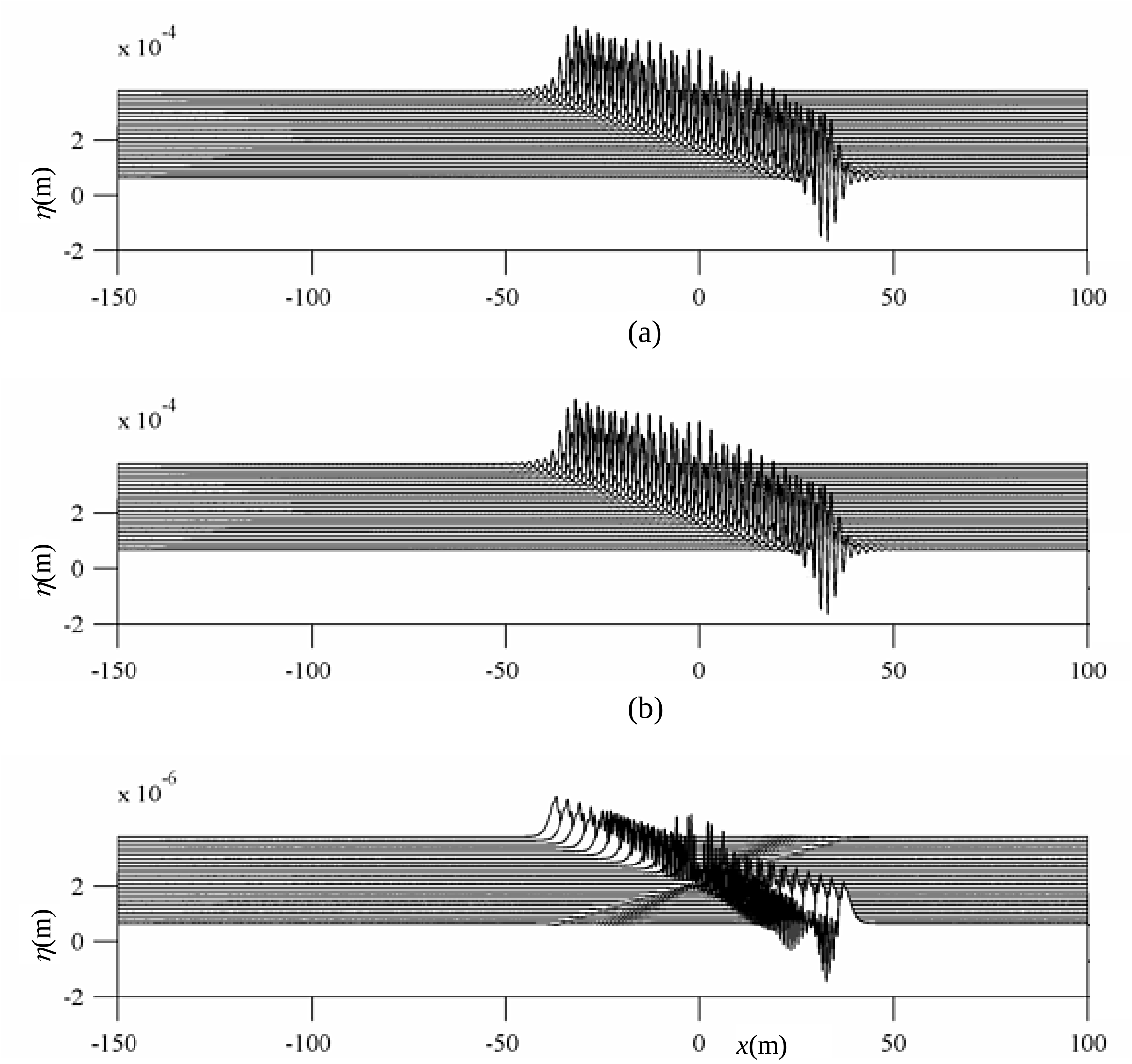

(a)

(b)

(c)

Figure 6.6: *x*-*t* plot for linear wave group ($ak_p = 0.001$) propagation at $k_p d = 0.5$; a) crest elevation, b) odd harmonics and, c) even harmonics from $t = -30$ s to $t = 30$ s (linear wave focussing at $t = 0$ s, $x = 0$ m)

6.3.3 Effect of Water Depth on Weakly Non-linear Wave Groups

Wave groups of $ak_p = 0.1$ are chosen to represent weakly non-linear wave groups. Figure 6.7 shows x-t plots of surface elevation for a focus wave group ($ak_p = 0.1$) at different water depths. Linear dispersion is strong when $k_pd > 0.75$. The wave groups gets wider, the amplitudes decrease over time, and wave focussing at $x = 0$ m can be observed. But, as the water depth is reduced, there is a small modulation instability opposing the dispersive focussing as the wave focusses at $x = 0$ m. This non-linear effect is discussed in Section 6.3.9. From the start condition at each water depth, a group of free error waves is produced behind the main wave group, and a wave hump produced in front, both are relatively larger as the depth is reduced. Also, the free waves and humps travel at speeds nearer to the main wave packets as the water depth is reduced. This shows that the dispersive characteristic of water waves still applies at all water depths. For the shallowest water depth, there appears to be several wave humps that are yet to separate themselves from the main wave packet. Furthermore, there are now two groups of free error waves behind the main wave group. In comparison with the linear case in Figure 6.5, the occurrences of wave humps and free error waves are due to the non-linearity, mostly at second order.

Separation of harmonics has been undertaken for all water depths for $ak_p = 0.1$. Figure 6.8 shows the odd harmonics of the wave group plotted at the same scale as Figure 6.7. Clearly the wave groups are dominated by the linear order harmonics, but the even harmonics contribution now is only about a factor of five smaller than the odd harmonics (contrasting the odd harmonics of Figure 6.8 with Figure 6.7). The odd harmonics are clean (without any free error waves), except for the shallowest water depth where there is a clear third order free error wave group propagating forwards behind the main wave. Figure 6.9 displays the even harmonics at a magnified vertical scale. As the same vertical scale is used for all the water depths, it can be seen that the contribution of even harmonics increases with decreasing water depths. It is interesting to note that the double frequency bound waves (which is the wave group behind the wave hump, and has the same phase as the linear wave packet shown in Figure 6.8) are riding in a hole, i.e. there is a long bound wave set-down which can be seen more clearly at shallow water depths.

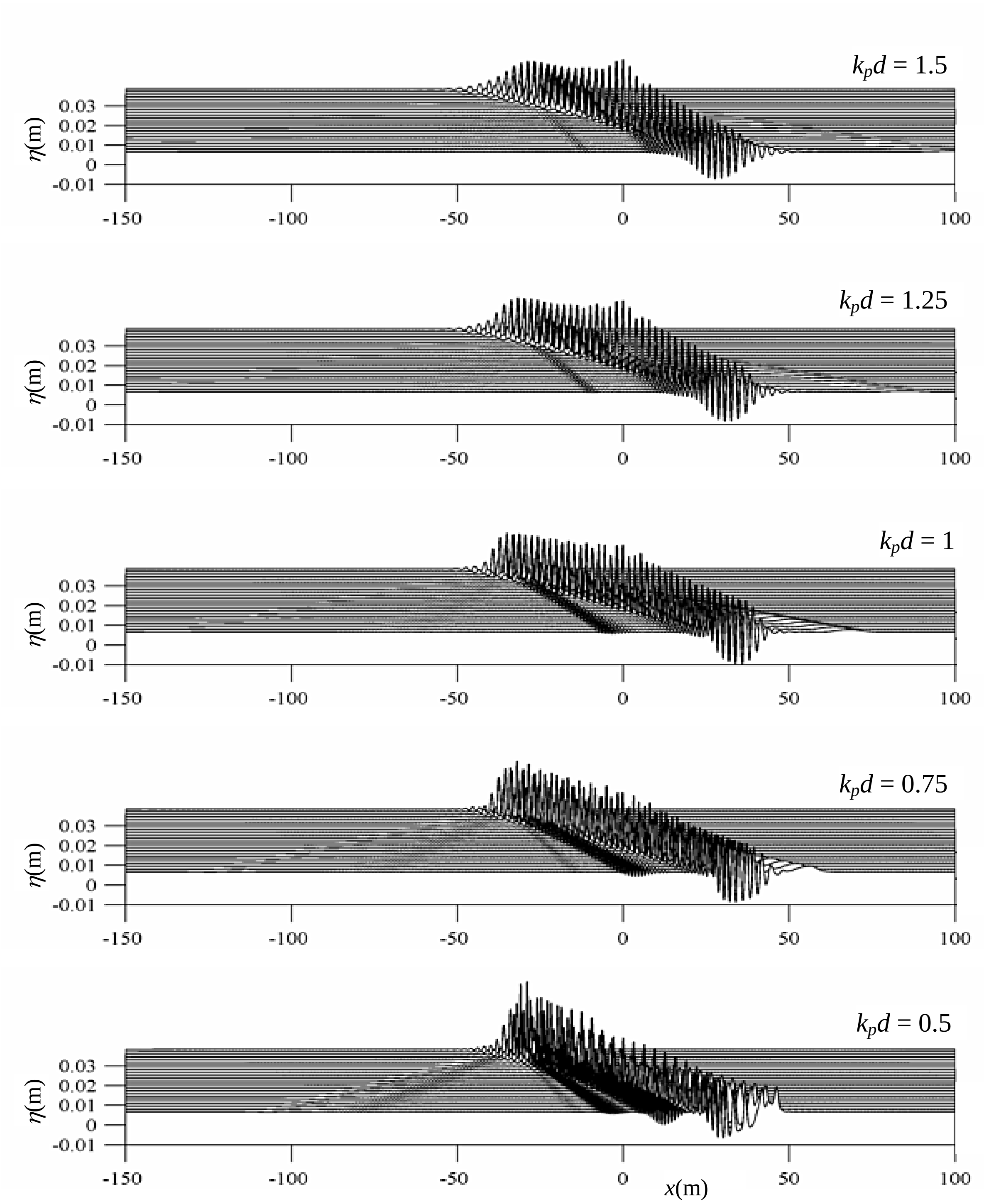

Figure 6.7: x-t plot for wave group ($ak_p = 0.1$) propagation from $t = -30$ s to $t = 30$ s with decreasing water depth (linear wave focussing at $t = 0$ s, $x = 0$ m)

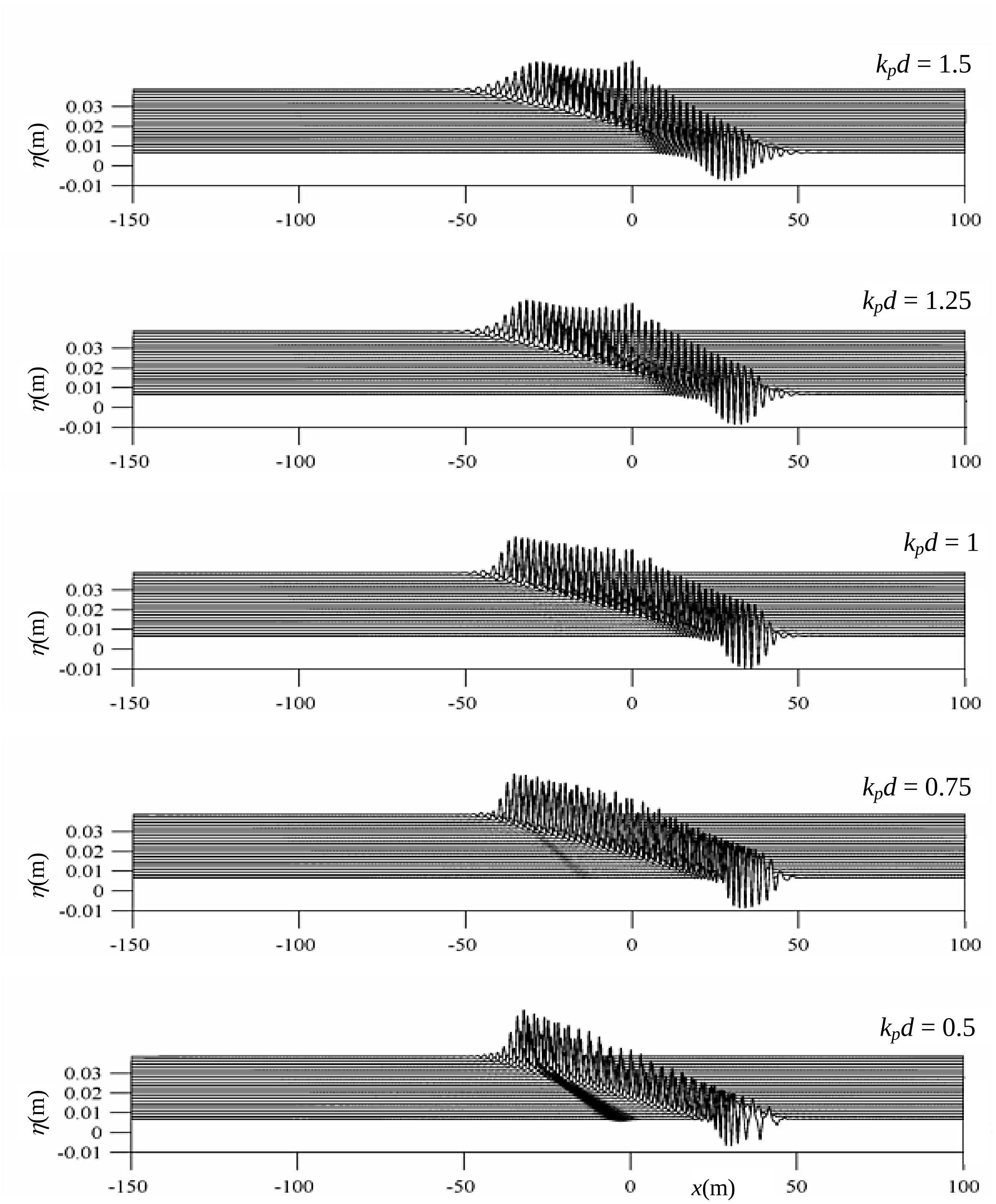

Figure 6.8: x-t plot for the odd harmonics wave group ($ak_p = 0.1$) propagation from $t = -30$ s to $t = 30$ s with decreasing water depth (linear wave focussing at $t = 0$ s, $x = 0$ m)

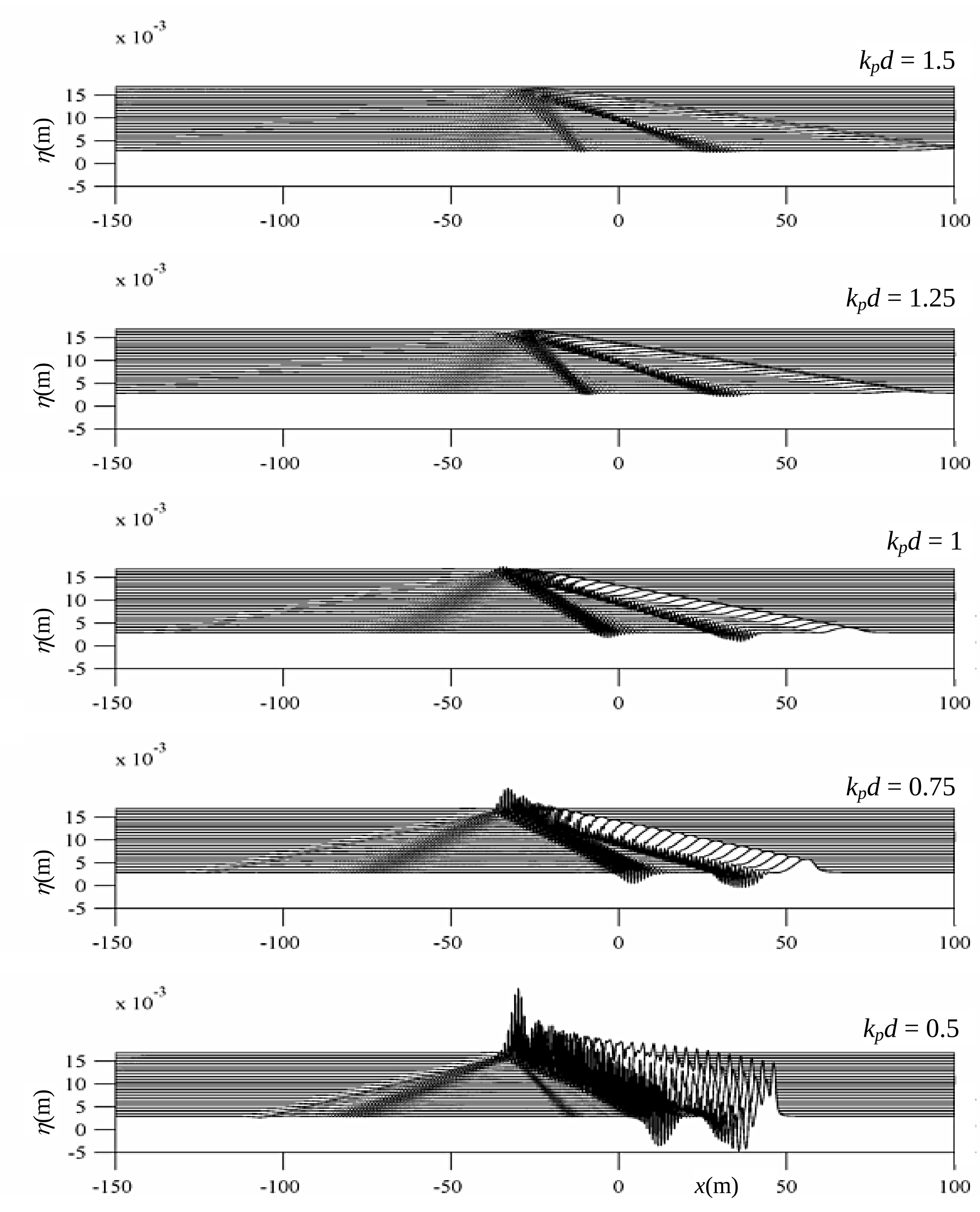

Figure 6.9: x-t plot for the even harmonics wave group ($ak_p = 0.1$) propagation from $t = -30$ s to $t = 30$ s with decreasing water depth (linear wave focussing at $t = 0$ s, $x = 0$ m)

6.3.4 Separation of Second Order Bound and Free Wave Components

In order to examine the bound wave set-down (the second order difference harmonics), the separation of even harmonics into second order sum harmonics and second order difference harmonics is achieved by spectral filtering according to the wavenumber using the spectral peak wavenumber k_p as the switch point between the low and high order filtering. Figure 6.10 shows the wave group harmonics for $ak_p = 0.1$ and $k_pd = 1$, where Figure 6.10d and Figure 6.10e plots the separation of even harmonics of Figure 6.10c. It can be seen that there is a wave set-down at the location of the double frequency bound waves. The magnitude of the wave set-down is almost the same as the amplitude of the double frequency bound waves. This occurrence of a significant wave set-down is in agreement with the observation in Section 3.3.2 for the random wave data measured in the laboratory.

To further examine the bound wave harmonics (i.e. the main wave packet), Figure 6.11 shows the linear harmonics, second order sum harmonics and the second order difference harmonics stacked vertically for different water depths with $ak_p = 0.1$. The even harmonics (second order sum and second order difference harmonics) have been scaled by a multiplication of [10, 10, 10, 5, 1] for each water depth, $k_pd = [1.5, 1.25, 1, 0.75, 0.5]$ for clear comparison with the linear harmonics. The phases of all the bound harmonics are aligned with the linear components at all water depths and at both times (t = 0 s, the linear focus time and $t = 40$ s, well after focus) showing that they are bound. At both times, there is obvious separation of harmonics in deeper water and down to k_pd of 0.75. The bound double frequency and long waves are clearly evident, as indicated by the smooth wave set-down. At k_pd of 0.75, the wave hump at $x > 5$ m for $t = 0$ s is actually the long free wave hump from the starting point at $t = -30$ s that is yet to completely separate from the main wave packet. The wave groups at the left hand side of $k_pd = 0.5$ and $k_pd = 0.75$ for $t = 40$ s are the second order free waves, which are yet to separate themselves from the main wave packet due to very weak dispersion in shallow water. At k_pd of 0.5, the separation of harmonics is not smooth. The wave set-down has small oscillations superimposed on it; the higher order harmonics are not aligned for the crest and trough focus runs, so the method of adding crest and trough cases does not work properly. Even so, the profile of the wave set-down is clear.

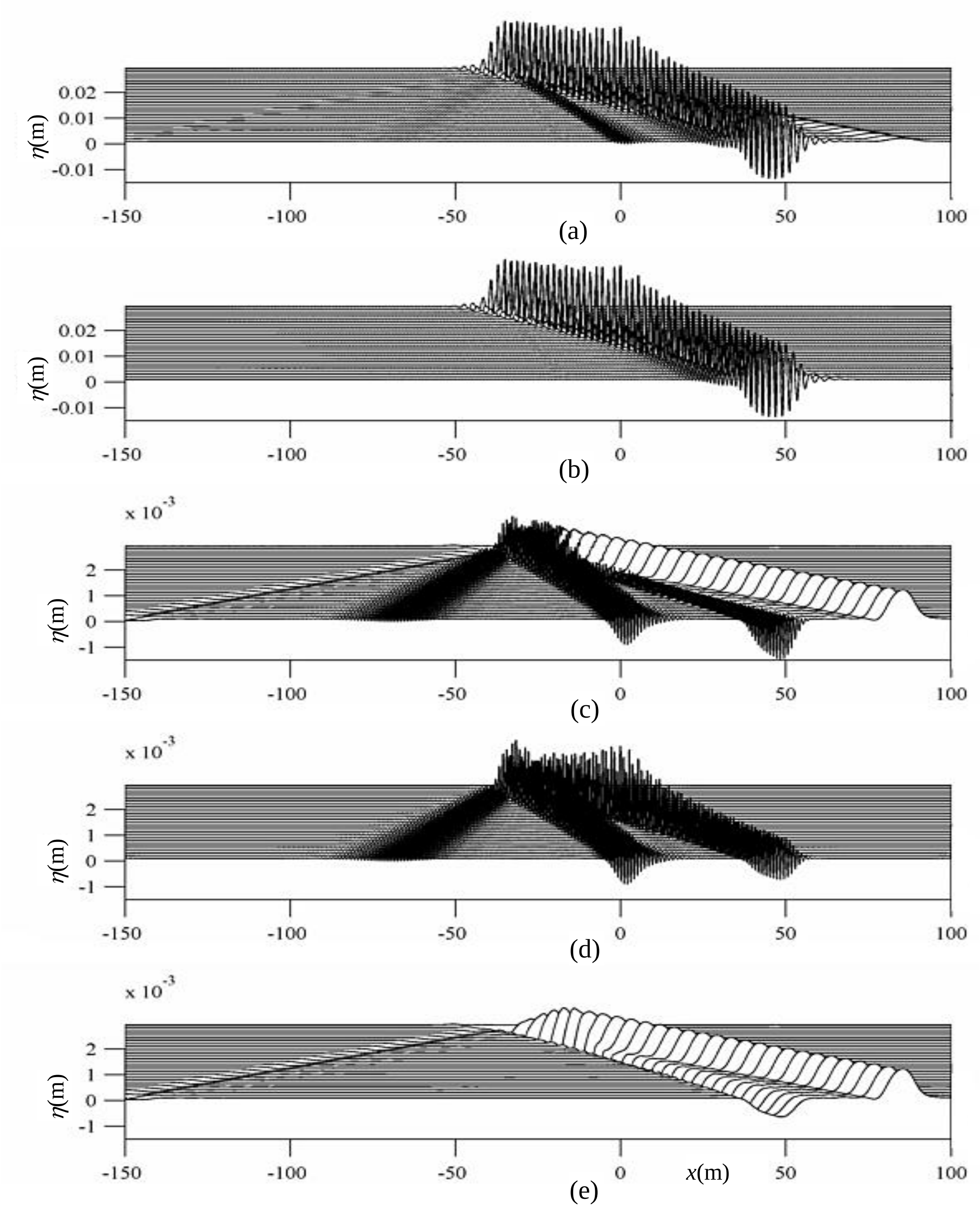

Figure 6.10: x-t plot for wave group ($ak_p = 0.1$) propagation at $k_pd = 1.0$; a) crest elevation, b) odd harmonics and, c) even harmonics, d) second order sum dominated harmonics and, e) second order difference harmonics from t = -30 s to t = 30 s (linear wave focussing at t = 0 s, x = 0 m)

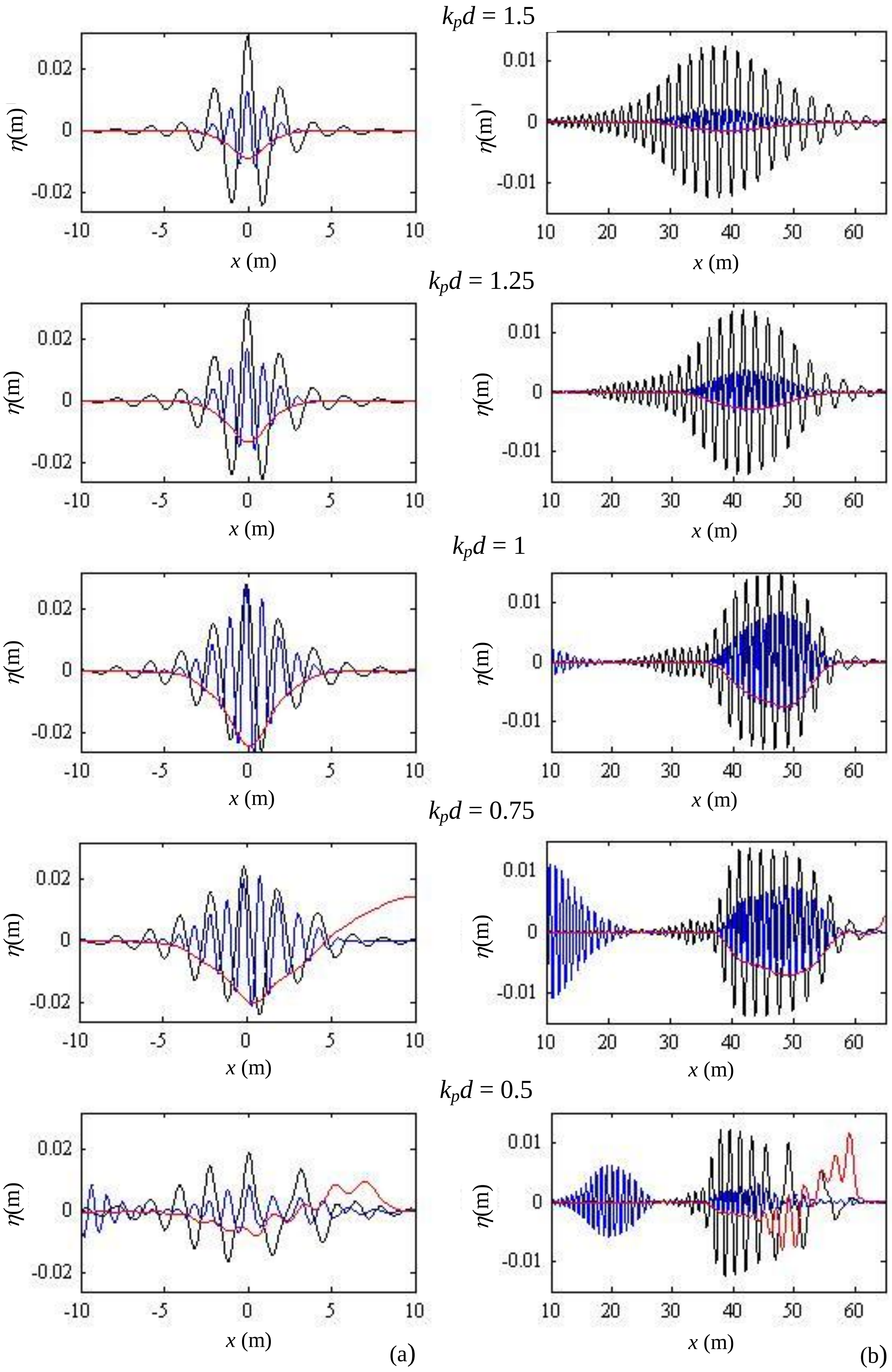

(a) (b)

Figure 6.11: Harmonics plot for wave group (ak_p = 0.1) at time a) t = 0 s and, b) t = 40 s with decreasing water depth; black lines for linear harmonics, blue lines for double frequency and, red lines for long wave. Even harmonics are not to scale in the vertical direction.

6.3.5 The Shape of the Second Order Sum and Difference Bound Waves Components

In order to approximate the second order sum and second order difference harmonics from the linear signal (linear harmonics), the Hilbert transform is applied. This NewWave (NW) based method through Hilbert transform is applied at the linear focus location (t = 0 s). The approximation for the shape of the second order contributions to NewWave is based on the identity;

For second order sum, the trigonometric identity

$$\cos(2\theta) = \cos^2\theta - \sin^2\theta \tag{6.4}$$

can be used to estimate the shape of the double frequency term

$$\mathrm{NW2} = \mathrm{NW}^2\text{-}\mathrm{NW_H}^2 \tag{6.5}$$

and likewise the second order difference,

$$\cos(2\Delta) \approx -\left(\cos^2\theta + \sin^2\theta\right) \tag{6.6}$$

giving

$$\mathrm{NW2\Delta} \approx \text{-}(\mathrm{NW}^2 + \mathrm{NW_H}^2) \tag{6.7}$$

where NW is the linear term and $\mathrm{NW_H}$ is the Hilbert transform of the NewWave signal (NW).

The amplitudes of the results are then scaled and the wave shapes are then compared with the harmonics obtained by spectral decomposition, as shown in Figure 6.12. For k_pd > 0.75, the NW estimated wave profiles are the same as the spectrally decomposed actual signals. There is weaker agreement at k_pd = 0.75 and no agreement at the shallowest water depth. Again, as has been demonstrated in Chapter 3, this NW-based method works acceptably well so long as the non-dimensional water depth, k_pd is larger than 0.5.

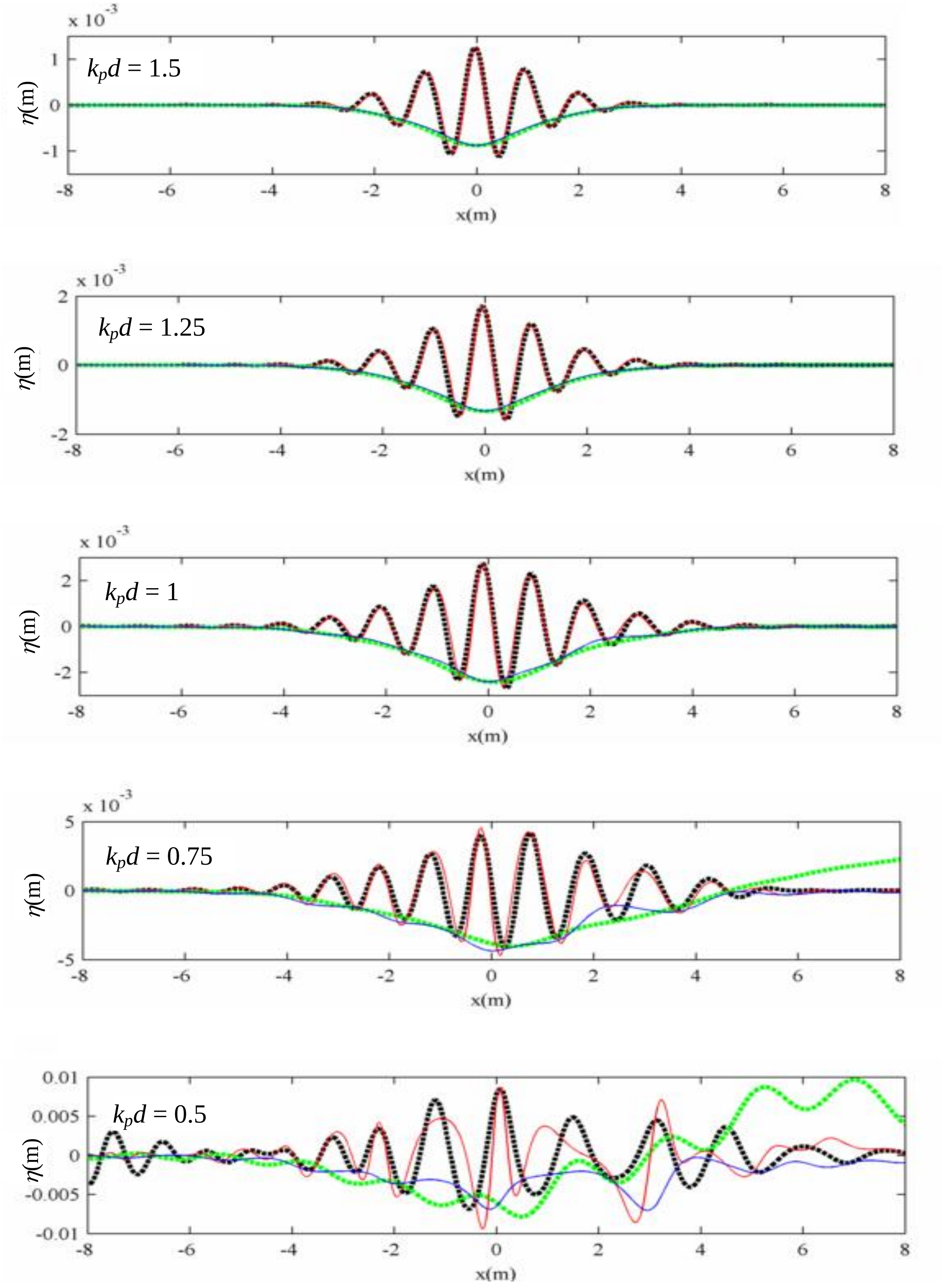

Figure 6.12: Comparing the profile of the normalized NewWave derived even harmonics (solid lines) with the even harmonics obtained by spectral decomposition (dashed lines) for wave group (ak_p = 0.1) at time t = 0s, against decreasing water depth.

6.3.6 Wave Steepness Effects for Intermediate Water Depth

Next, the behaviour is investigated of focus wave groups propagating on water of depth corresponding to $k_p d = 1$ with varying wave steepness. Figure 6.13 shows x-t plots for $k_p d = 1$ from $t = -30$ s to $t = 30$ s for four different wave steepness, ak_p. For the linear case, the wave group propagates smoothly. The wave group focuses at the middle of the top plot and at $t = 30$ s, the wave group is wider in width and lower in amplitude due to linear frequency dispersion. For a steeper wave group where $ak_p = 0.1$, the wave group is weakly non-linear and starts to shed free waves in the form of a wave hump in front of the main wave packet and a small dispersive wave group behind. At the most steep case of $ak_p = 0.4$, the wave group releases a substantial hump which then breaks up into several wave humps at the front followed by several wave groups at the back. There are also waves that propagate in the opposite direction. This is a very non-linear wave group and obviously the higher order harmonics components in the wave group are much more dominant compared to the linear harmonics.

The increase in the importance of even harmonics compared to the linear harmonics as the wave groups become steeper can be seen in Figure 6.14 which plots the envelopes of the various wave harmonics together against different wave steepness. Again, as in Figure 6.11, the even harmonics bound waves are perfectly in phase with the linear harmonics. The envelope of the linear wave becomes slightly distorted at $ak_p = 0.2$, and has a rather different shape for $ak_p = 0.4$.

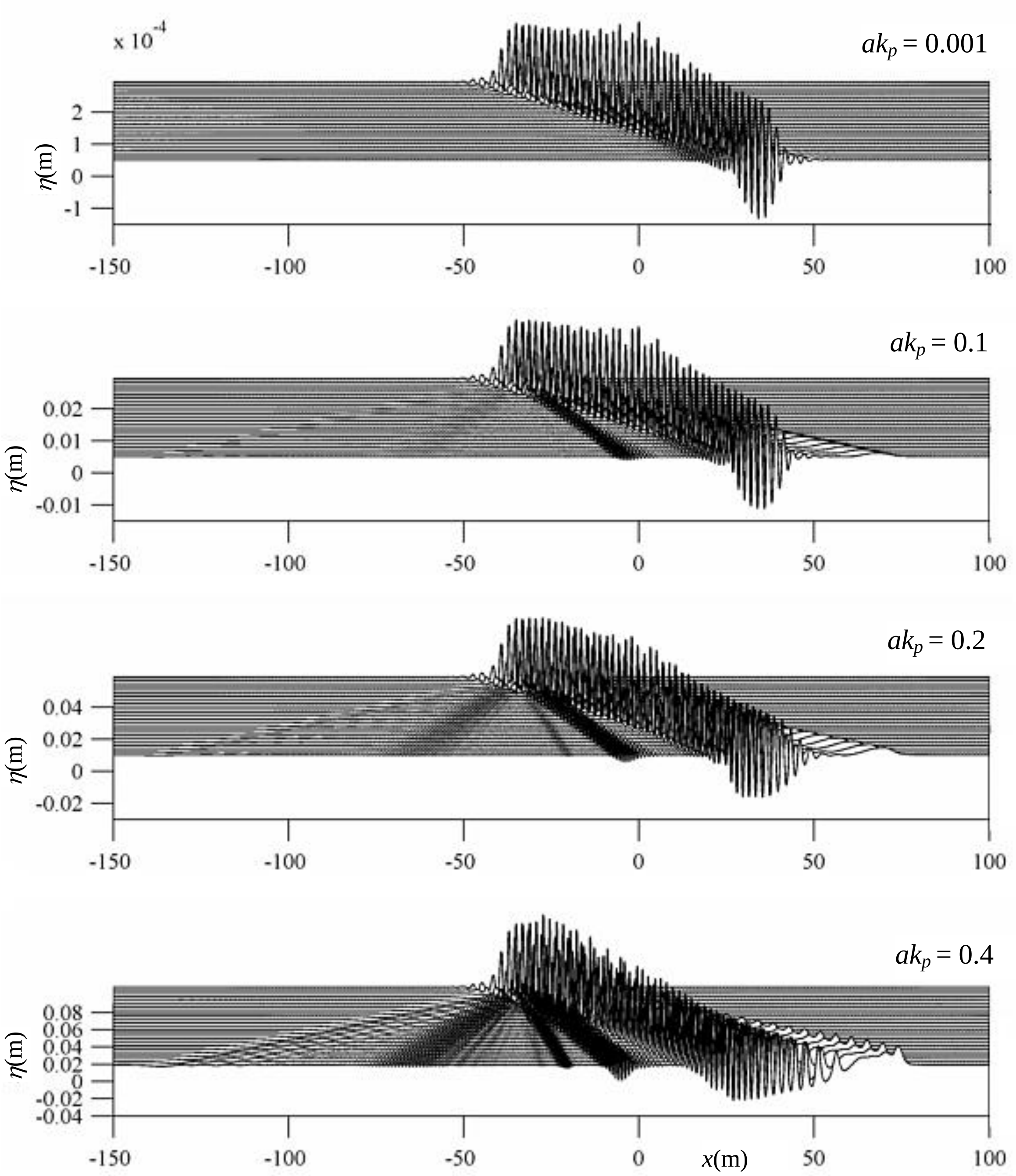

Figure 6.13: x-t plot for wave group at $k_pd = 1.0$ propagating from $t = -30$ s to $t = 30$ s with increasing steepness (ak_p) (linear wave focussing at $t = 0$ s, $x = 0$ m)

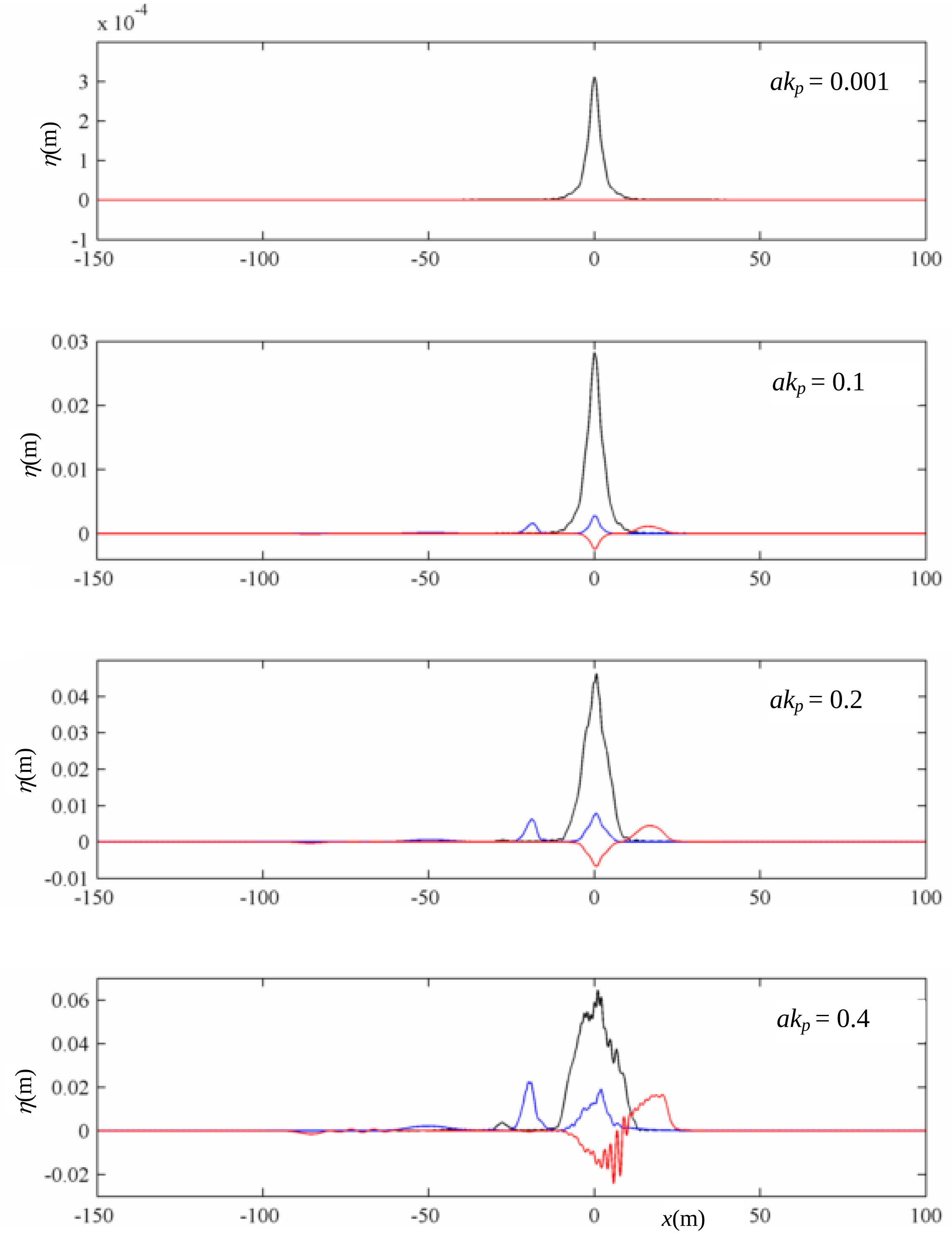

Figure 6.14: Harmonics plot for wave group with $k_pd = 1.0$ at $t = 0$ s against increasing steepness (ak_p); black lines for envelope of linear harmonics, blue lines for envelope of double frequency harmonics and, red lines for long wave (linear wave focussing at $t = 0$ s, $x = 0$ m)

6.3.7 Most Non-linear Case in Terms of Amplitude and Water Depth

Figure 6.15 shows the wave group propagation for the most severe case, at $k_pd = 0.5$ and $ak_p = 0.4$. The top panel shows three solitary waves leading the wave group followed by at least two more solitary waves which are yet to separate themselves from the group. The main wave packet and the free waves are very hard to distinguish from one another. Clearly the separation of harmonics does not work well. There are a lot of solitary waves and also wave set-down in the odd harmonics (Figure 6.15b) while the solitary waves in the even harmonics are apparently only half the height of the solitary waves in Figure 6.15a. This is not correct. The reason for these is because of the mis-alignment between waves in the crest elevation and trough elevation numerical runs. As shown in Figure 6.15d, the solitary waves from the trough elevations are not aligned with those for the crest elevation. The reason is due to the nature of the wave group, which is highly non-linear.

However, as has been stated before, the ratio a/d for this case is 0.77, which is physically implausible as the Miche limiting wave height criteria is being violated. However, it is still interesting that the GN code is able to cope without any stability issues. In a physical experiment, the wave breaking process is highly non-linear and the waves will have broken at this particular amplitude and water depth. However, overall, the physical trends of water waves are simulated correctly; solitary waves of higher amplitude travel faster regardless of how they are created for both the crest and trough elevations.

6.3.8 Most Non-Linear Case in Amplitude but in Deep Water

Figure 6.16 shows the separation of harmonics for wave group with $k_pd = 1.5$ and $ak_p = 0.4$, at the deepest water depth considered. Unlike the shallow water case, the harmonics are separated smoothly for this case. Linear, double frequency and long wave bound harmonics are present along with free double frequency and long waves. It should be stressed that the boundaries for this numerical code are solid boundaries located at $x = -150$ m and $x = +100$ m. So some reflection has started to occur on the right edge of Figure 6.16c and Figure 6.16e.

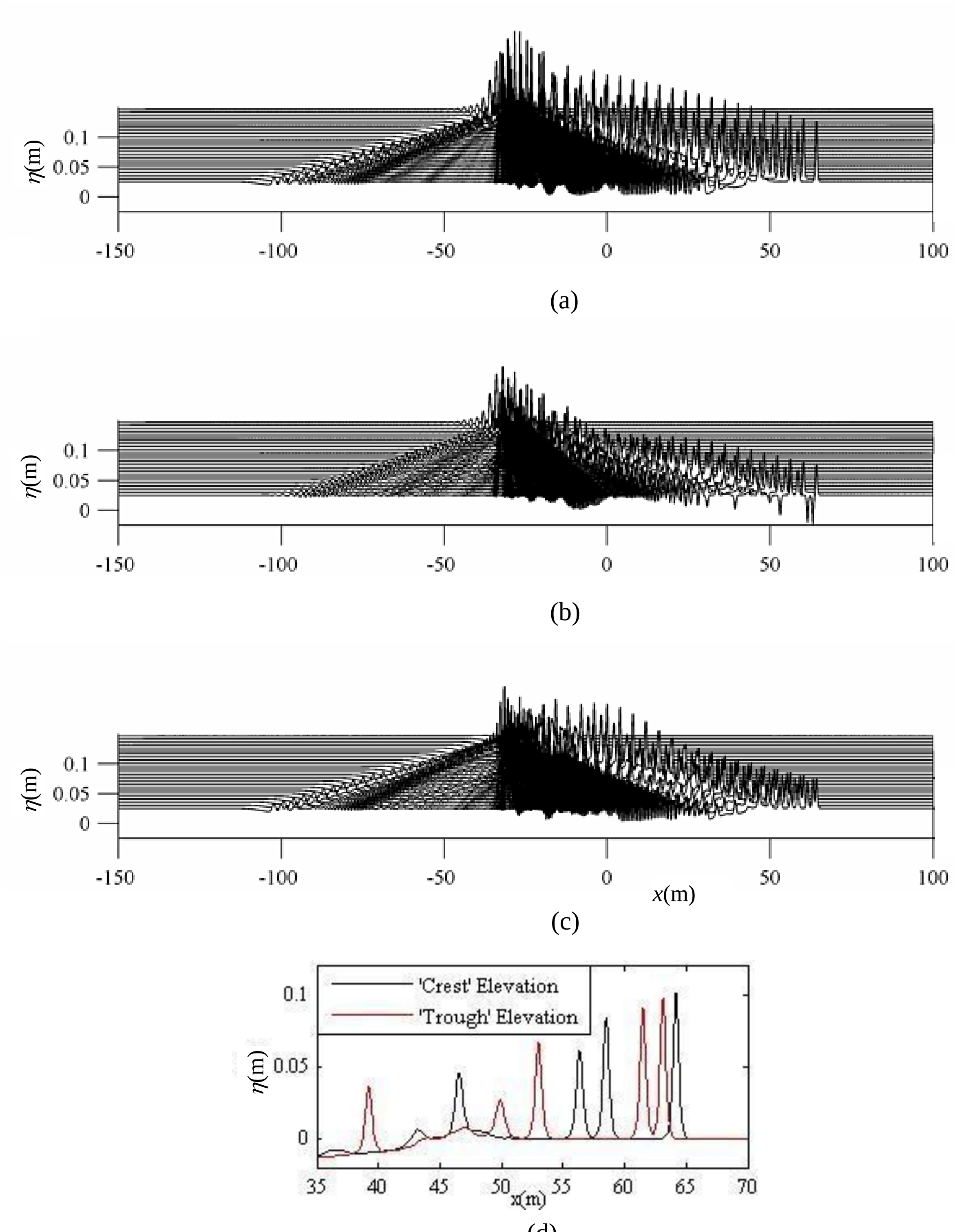

(a)

(b)

(c)

(d)

Figure 6.15: *x*-*t* plot for wave group ($ak_p = 0.4$) propagation at $k_pd = 0.5$; a) crest elevation, b) odd harmonics, c) even harmonics from $t = -30$ s to $t = 30$ s (linear wave focussing at $t = 0$ s, $x = 0$ m) and d) surface elevation plots at $t = 30$ s

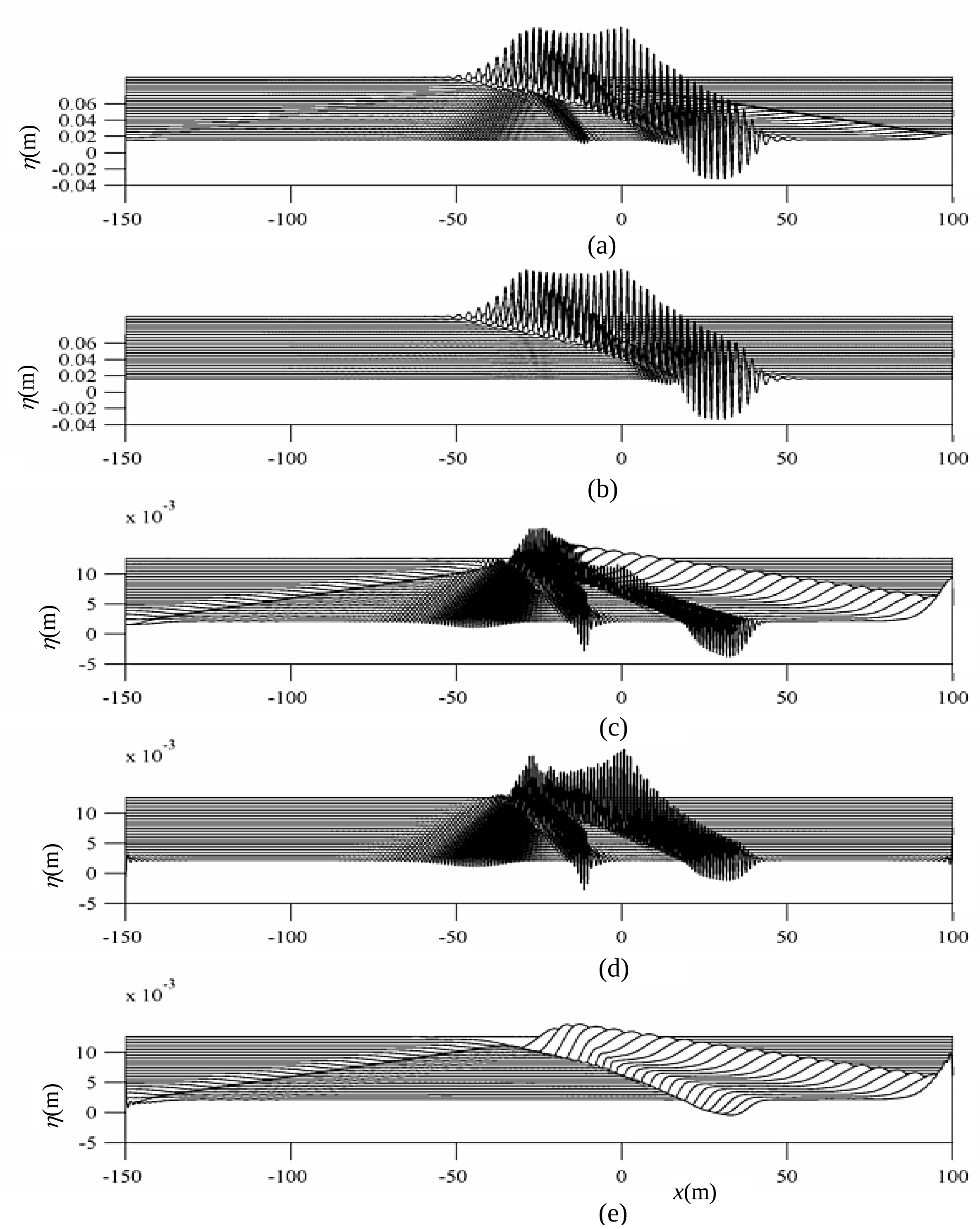

Figure 6.16: *x*-*t* plot for wave group ($ak_p = 0.4$) propagation at $k_pd = 1.5$; a) crest elevation, b) odd harmonics and, c) even harmonics, d) second order sum dominated harmonics and, e) second order difference harmonics from $t = -30$ s to $t = 40$ s

6.3.9 Non-linear Defocussing

Now consider the evolution of the envelope of the main wave packets through the focussing event. According to the linear dispersion equation, the wave speeds are functions of water depth, d and wave number, k. Thus in theory, the wave groups will travel at the same speed regardless of the amplitudes, given the same peak wavenumber and water depth.

Figure 6.17 shows the envelopes for different wave steepness (k_p is constant) at t = 0 s (Figure 6.17a) and t = 30 s (Figure 6.17b) for all the water depths with the envelope peak scaled to 1. For the deepest water depth (top panel) the envelopes overlap each other except for the highest amplitude case; showing that the dynamics of the weakly non-linear first order components are independent of amplitude. As the water depth is reduced, the similarity between the main wave packets slowly disappears. The main wave packets become wider (and less smooth due to modulation of the envelopes). The speeds of the main wave packets are still the same and the centre of the envelopes remain close to the origin in space, showing that focussing, although weaker than for a linear group, is still occurring. This behaviour is consistent with the switch in the non-linear changes in the focussing properties of the non-linear Schrödinger equation, from focussing of wave groups on deep water, to defocusing for groups on shallow water. It means that for waves in deep water, the non-linear dynamics enhance the focussing of a linear group resulting in a narrower, more compact and taller wave group than linear focussing would have produced. In contrast for shallower water (kd < 1.36), the non-linearity opposes the linear focussing leading to spatially broader and smaller amplitude wave groups at focus. The switch point is at kd = 1.36, so close to linear focussing for k_pd = 1.5 and k_pd = 1.25 is to be expected even for the finite amplitude groups, with defocusing being increasingly important as the water depth is reduced (Benjamin and Hasselmann, 1967 and Slunyaev et al., 2002). For k_pd = 0.5, broadening is clear but the idea of group dynamics rather than the dynamics of the individual waves is starting to fail.

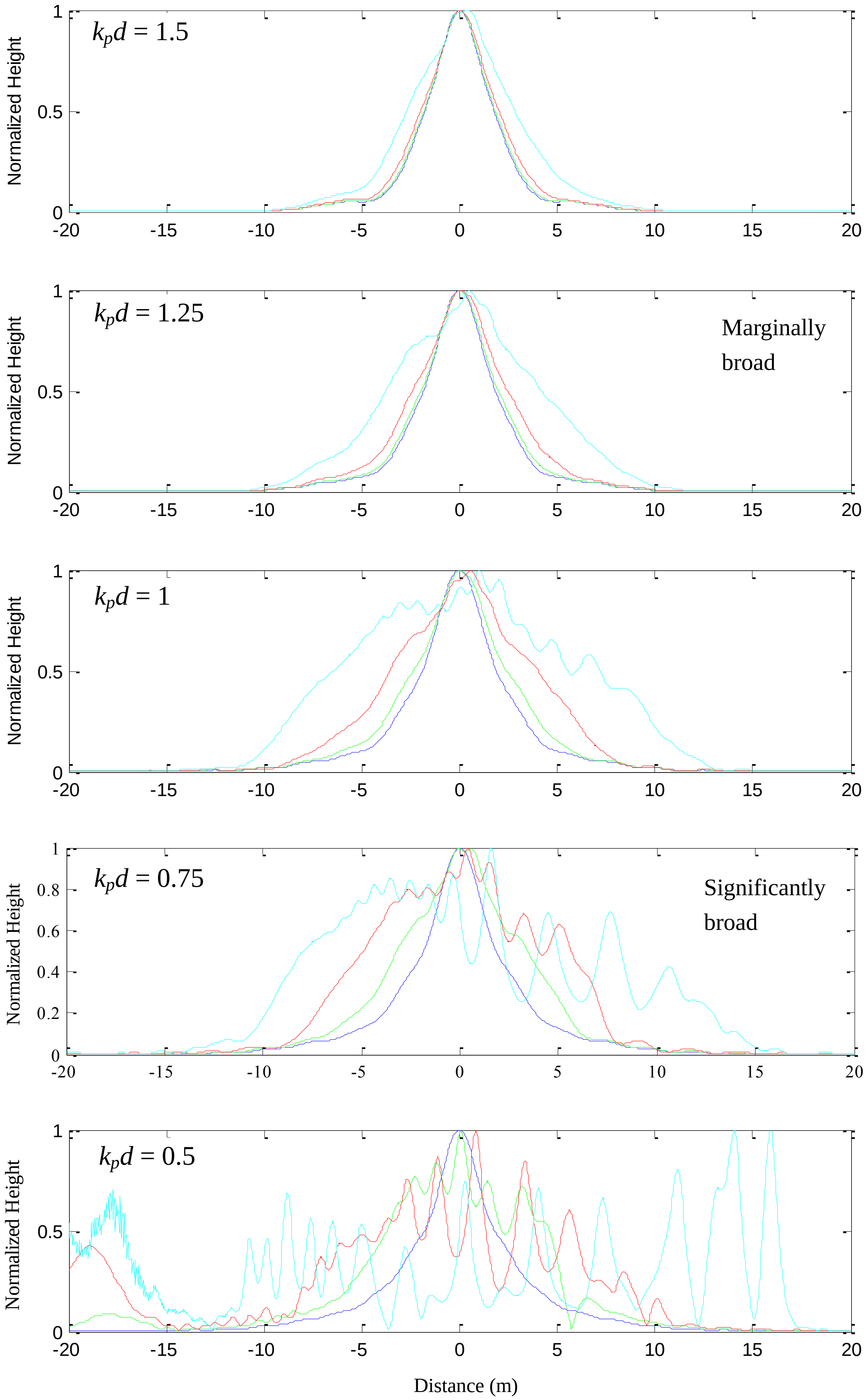

Figure 6.17a: Envelope of linear harmonics with normalized height at t = 0 s; blue line for ak_p = 0.001, green line for ak_p = 0. 1, red line for ak_p = 0.2 and, cyan line for ak_p = 0.4

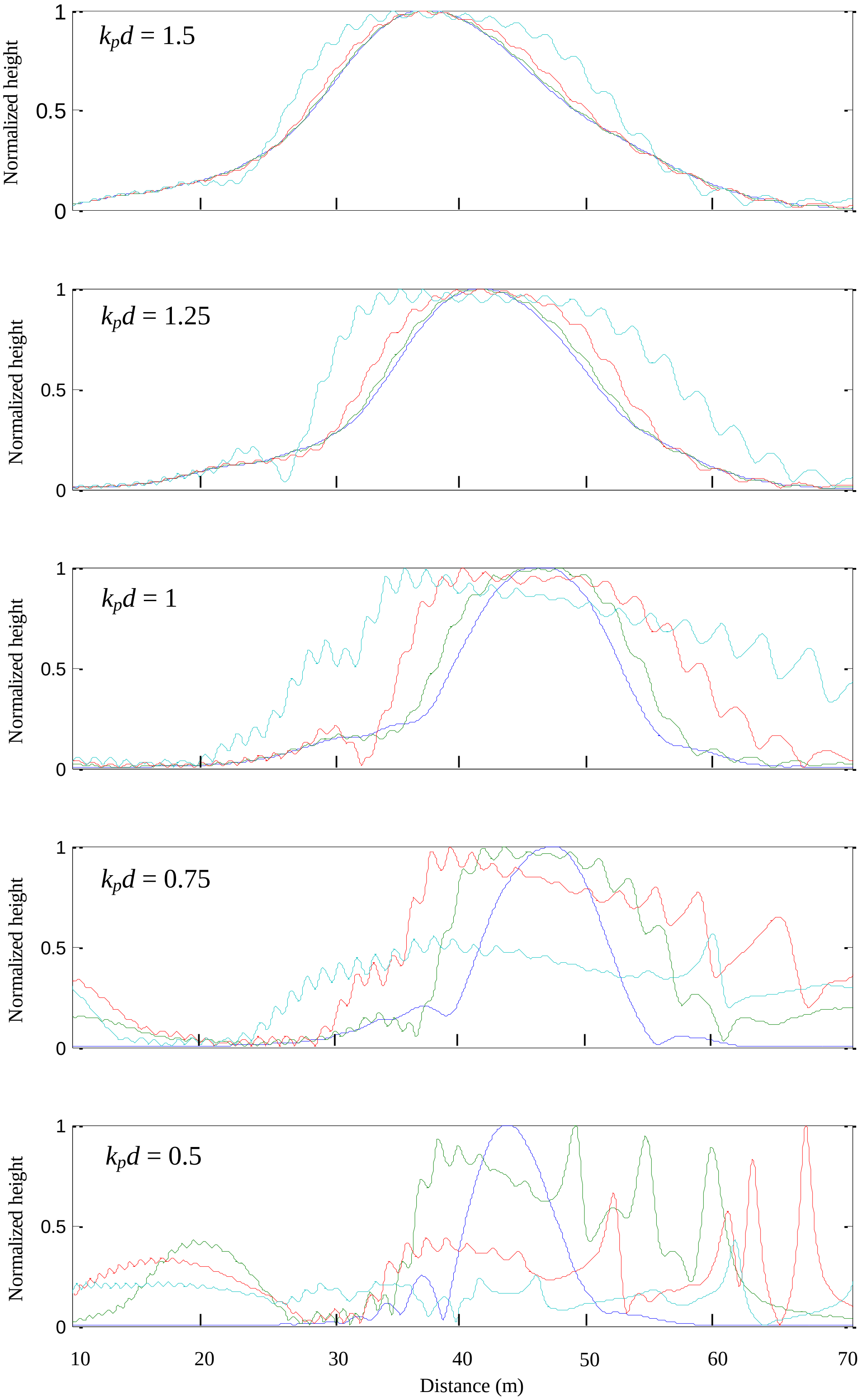

Figure 6.17b: Envelope of linear harmonics with normalized height at $t = 30$ s; blue line for $ak_p = 0.001$, green line for $ak_p = 0.1$, red line for $ak_p = 0.2$ and, cyan line for $ak_p = 0.4$

6.4 Focussed Wave Groups on Sloping Bed

A series of focussed wave groups, each propagating over a 1:100 sloping bed, is simulated. The numerical sea bed is configured to have the same dimensions as the experimental wave tank in Chapter 2, but with a few slight changes to prevent instability occurring in the numerical simulation. This is to allow direct comparison between the numerical and the experimental results and to understand further the nature of the wave groups. Instead of using the standard JONSWAP spectrum as applied in Section 6.3 for constant water depth, measured wave spectra at a few gauges from Case 1a1100 are taken as initial conditions for the present simulations (with input conditions for the Lowish experiment given in Table 2.1). As in Section 6.2, Equation (6.2) is implemented to transform the Lowish spectrum in the frequency domain to the wavenumber spectrum so that the initial condition for the GN numerical simulation is taken to be a focussed wave group in space.

Wave spectra at Gauges 1, 3, 5 and 6 of Case 1a1100 are evaluated for the numerical simulation, while data from the gauges at shallower water depths are ignored. Wave groups at Gauge 7 and Gauge 8 are not simulated because their wave spectra do not correspond to waves which are dominated by linear order. These waves are broken and highly non-linear. And furthermore, it has been shown that the NewWave method (which corresponds to the scaled linear order wave) applied in Section 3.2 does not work in these very shallow regions.

Table 6.3 lists the wave gauges with their corresponding water depths, d and peak wavenumber, k_p obtained from the peak period of the wave spectrum input for the Lowish experiment. Figure 6.18 shows the numerical wave tank setup, with the bed slope starting at $x = 122$ m and ending at $x = 170$ m. There are slight differences between the numerical wave setup and the experimental wave setup shown in Figure 2.2a. The constant water depth of 0.5 m for the numerical wave setup is appropriate because it is in relatively deep water, with k_pd of about 1.6. At this water depth, the dispersion properties are not governed by water depth and the contributions of higher order harmonics are very small, as has been shown in the second order coefficient plot against kd of Figure 4.5. The region of interest is from deep water where the depth is constant to the wave gauges along the slope. Thus, the right hand boundary will not affect the wave group propagation, as long as the free error long wave is not reflected back towards the main wave packet.

Table 6.3: Wave gauges and peak wavenumber from the Lowish experiment and their corresponding water depths and location in the numerical tank

Gauge	d (m)	k_p (m^{-1})	$k_p d$	Distance from left boundary (m)
1	0.40	3.24	1.3 (taken as deep water)	132
3	0.30	3.56	1.06	142
5	0.20	4.10	0.83	152
6	0.15	4.67	0.69	157

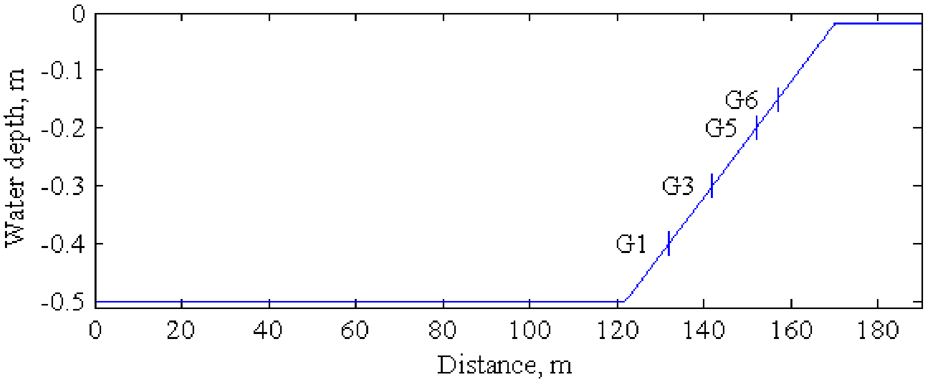

Figure 6.18: Numerical wave tank setup

The numerical scheme is setup as follows:

The grid spacing is $\Delta x = 0.04$ m and the time step is $\Delta t = 0.01$ s. The length of the tank (with solid boundaries) is 190 m. At each gauge, the influence of amplitude on the behaviour of the wave groups is also investigated. The wave groups start at $t = 0$ s (at focus) at their respective gauges and are assumed to propagate linearly (using ak_p of 0.001) backwards until $t = -80$ s. Then, the surface elevation profile and velocity distribution along the tank are multiplied by a multiplication factor, M and propagated forward for 85 s until $t = 5$ s (corresponding to 5 s after linear focussing). In order to separate the odd and even harmonics, a trough focussed wave propagation is also simulated, by using a negative signal for the initial condition at $t = 0$ s during the backwards linear wave group propagation. The wave groups are then decomposed to obtain the odd and even harmonics using the Stokes water wave expansion described in Section 3.3. The behaviour of these wave groups of different steepness is investigated for each gauge, examining in particular their structure at the linear focus time of $t = 0$ s. Four different values of wave steepness for the wave groups are investigated. These are listed in Table 6.4.

Table 6.4: Variation in wave steepness for wave groups at $t = -30$ s

No.	M	ak_p
a	1	0.001 (assumed linear)
b	100	0.1
c	200	0.2
d	250	0.25

6.4.1 Accuracy Test

The accuracy of the numerical model is assessed by comparing the surface elevations of the end result of a reverse simulation with the initial condition of a forward propagating simulation. The dispersed wave group at $t = -80$ s before linear focussing is propagated forward on a 1:100 slope to $t = 0$ s. Then, the end result of this original simulation is propagated backwards to $t = -80$ s to obtain the reversed simulation. Spatial resolutions, Δx, of between 0.2 m (course grid) to 0.02 m (fine grid) are considered with the corresponding time steps altered so that the Courant condition is constant at 0.5. The error contribution is determined using

$$||E|| = \sqrt{\ } (E_1^2+...+ E_N^2)$$

where $E_i = \eta_{end} - \eta_{initial}$ for the *i*th grid point and *N* is the total grid points. Gauge 5 has been chosen because it located in the shallow region of the domain, with a magnification factor, *M* of 200 so that it is a rather non-linear wave group. The results are shown in Table 6.5 and represented graphically in Figure 6.19. The numerical simulations exhibit fourth order accuracy, which is consistent with the RK4 time stepping and fourth order spatial discretisation.

Table 6.5: Convergence test result

Δx (m)	$\|\|E\|\|$
0.2	5.9E-3
0.08	2.5E-4
0.04	1.3E-5
0.02	5.7E-7

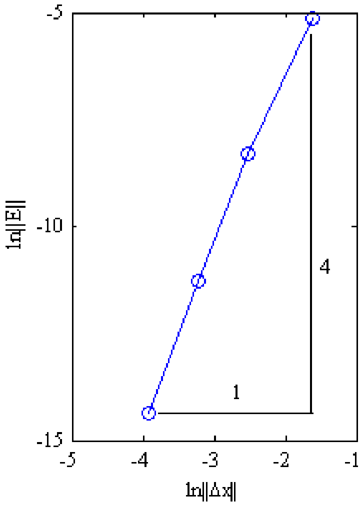

Figure 6.19: Convergence test result

6.4.2 Wave Steepness Effects

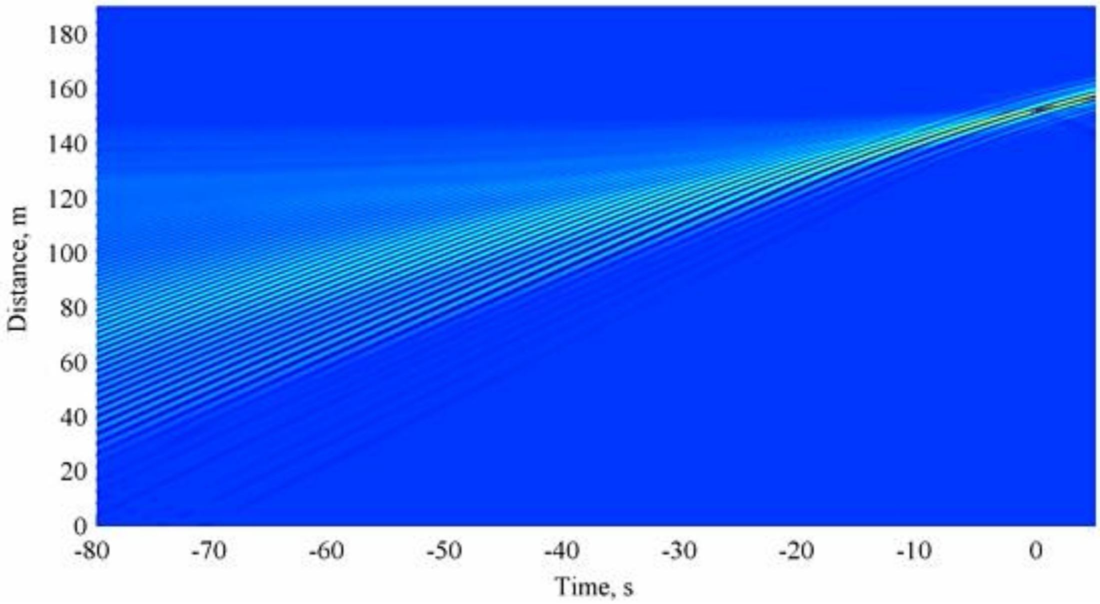

Figure 6.20: *x*-*t* contour plot for wave group propagation from t = -80 s to t = 5 s with linear wave group focussing at t = 0 s and x = 152 m (Gauge 5 with M = 200)

The general behaviour of the wave group propagations for each gauges and for all wave steepness, from their dispersed shape (at deep water) to their focus shape (on the slope) is captured in Figure 6.20, using Gauge 5 with M of 200 as an example. The dispersed wave group at t = -80 s propagates at deep water towards the sloping bed, which starts at x = 122 m and focuses at the gauge location (which is at x = 152 m for this case). This is shown by the brown colour which indicates the maximum surface elevation.

The shape and magnitude of the focus wave group at its linear focussing time, t = 0 s after a forward run from the dispersed location (t = -80 s) is investigated for each gauge. Figure 6.21 shows the odd and even harmonics time series at the linear focus locations for different wave steepness at each gauge (Notation G1 x M is used in the caption, where G represents gauge). As the wave steepness increases, the non-linearity increases at all gauges. This can be seen by the higher ratio of even harmonics to odd harmonics. Non-linearity also increases as the water depth is reduced, for a given wave steepness.

In order to obtain wave steepness, ak_p of about 0.001, the amplitudes at Gauge 1 and Gauge 2 are set to 3 x 10^{-4} m while the amplitudes at Gauge 5 and Gauge 6 are set to 2 x 10^{-4} m, due to the variability in the peak wave number, k_p. For each wave steepness, the peaks of the odd harmonics decrease slightly when the water depth is reduced, except for Gauge 6 where the peak seems to increase, which could be at the point of wave breaking. Also at Gauge 6, the peaks are narrower while the troughs are broader; displaying that there is a significant influence of higher order harmonics (mainly third order harmonics) at shallow water. Note that, as has been discussed in Section 3.2 of NewWave comparison with the odd harmonics, the combination of Stokes expansions for $[\eta_c-\eta_t]/2$, given in Section 3.3 shows that the odd harmonics contains the linear order, third order and higher order odd harmonics. Thus, as the water depth is reduced, the higher order harmonics will start to influence the signal.

Interestingly, the trough amplitudes experience relatively more reduction than the crest amplitudes as the water depth reduces. This effect is in qualitative agreement with the Lowish data discussed in Section 2.6, referring to Figures 2.10 and 2.11. This holds true as the wave group moves from deep water to shallow water, and non-linearity comes into action which makes the wave group asymmetric, with steeper crest and broader and smaller troughs.

For the even harmonics, it seems that a double frequency is superimposed on a long wave of almost the same magnitude, which can be clearly seen in the separation of even harmonics in Figure 6.22. Similar behaviour is observed for oscillatory wave propagation on constant depth, as discussed in Section 6.3.4. But, as the wave steepness increases, there is a wave set-up in front of the wave set-down, apart from the free error wave set-up which has travelled ahead. The wave set-up seems to be a function of the sloping bed because there is no evidence of a wave set-up produced as the wave propagates on constant depth, apart from the free error wave. This bed slope-induced wave set-up will be investigated further, later in the chapter.

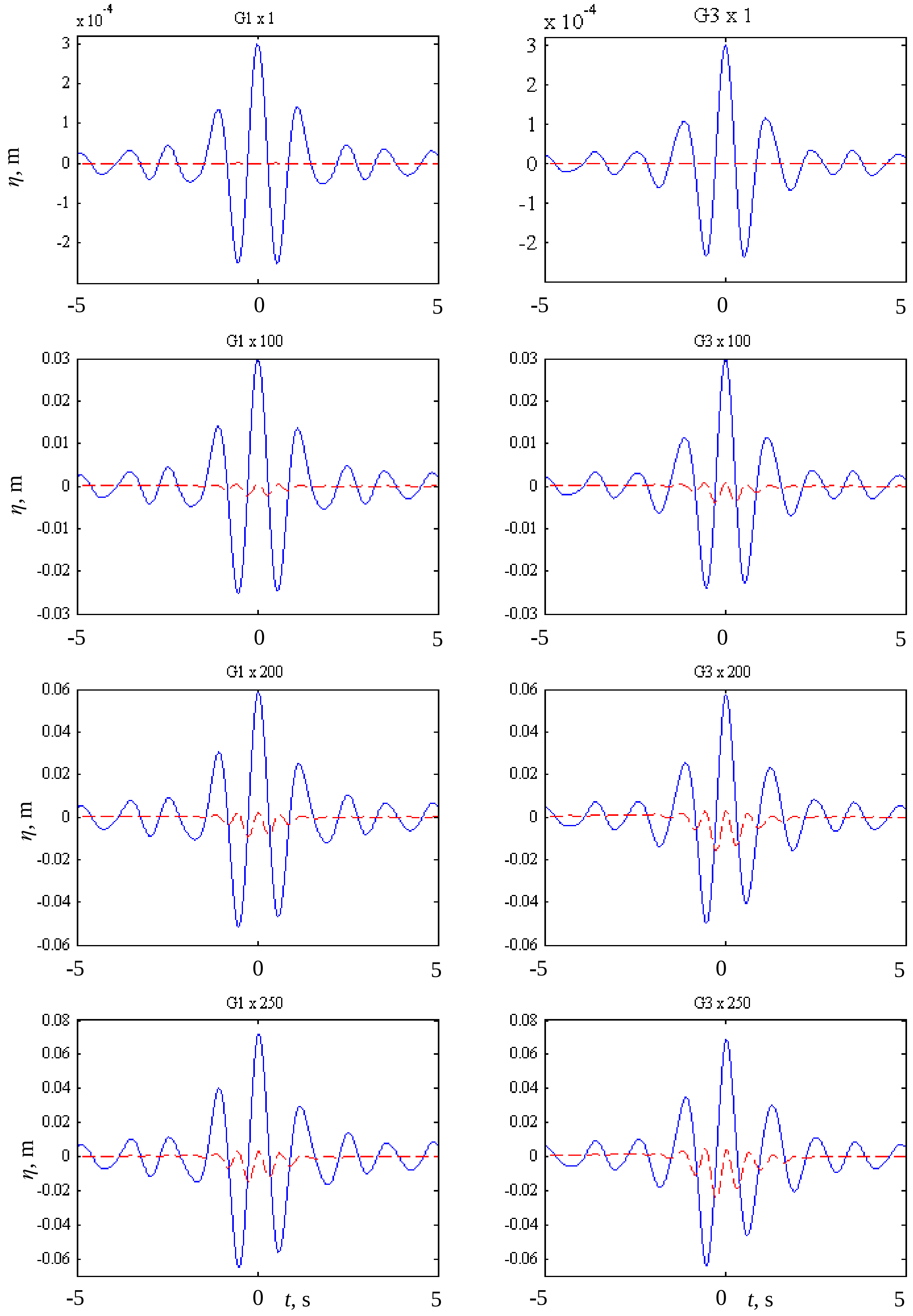

Figure 6.21a: Odd (solid) and even (dashed) harmonics for Gauges 1 and 3 with different wave steepness at the linear focus location.

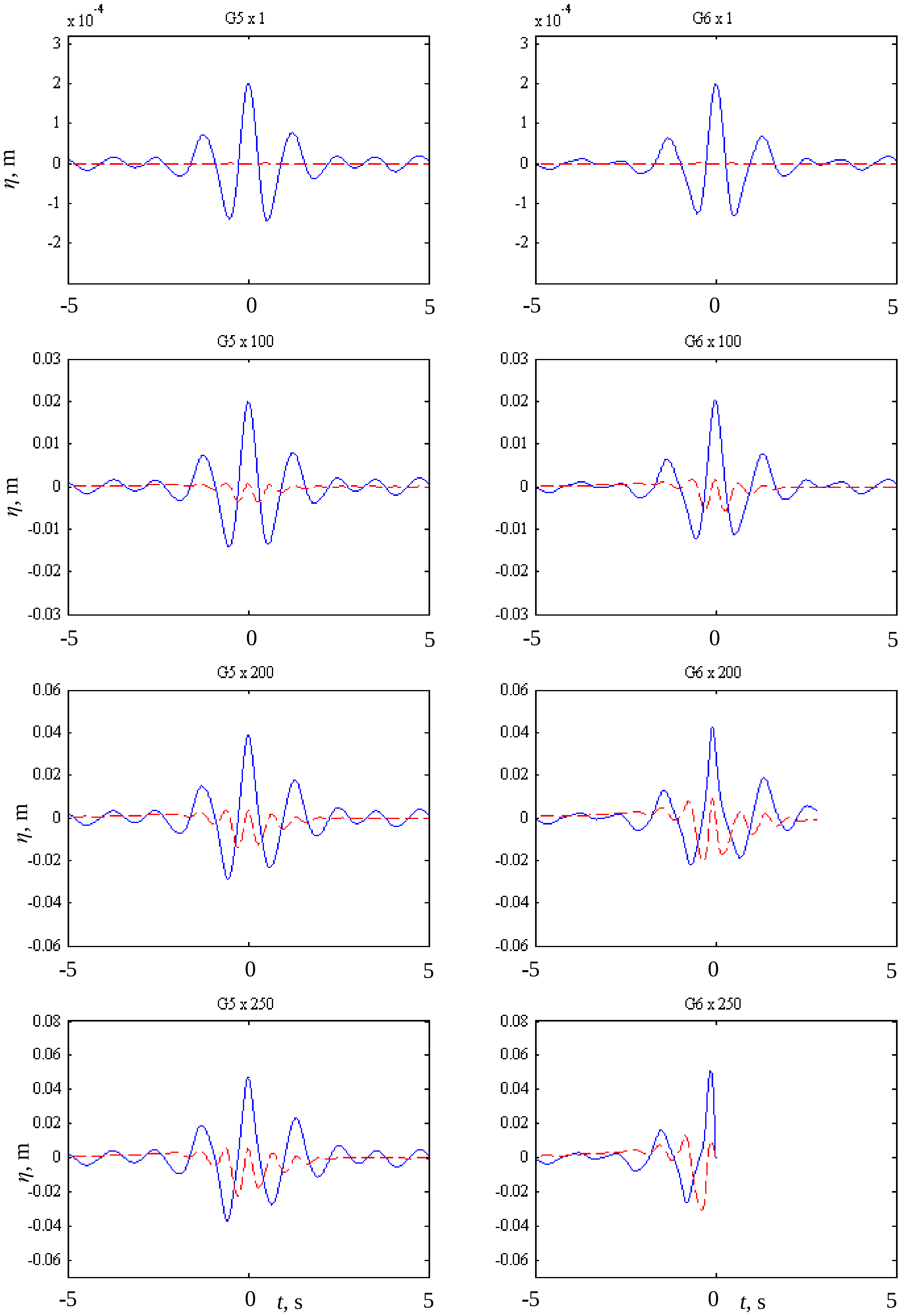

Figure 6.21b: Odd (solid) and even (dashed) harmonics for Gauges 5 and 6 with different wave steepness at the linear focus location.

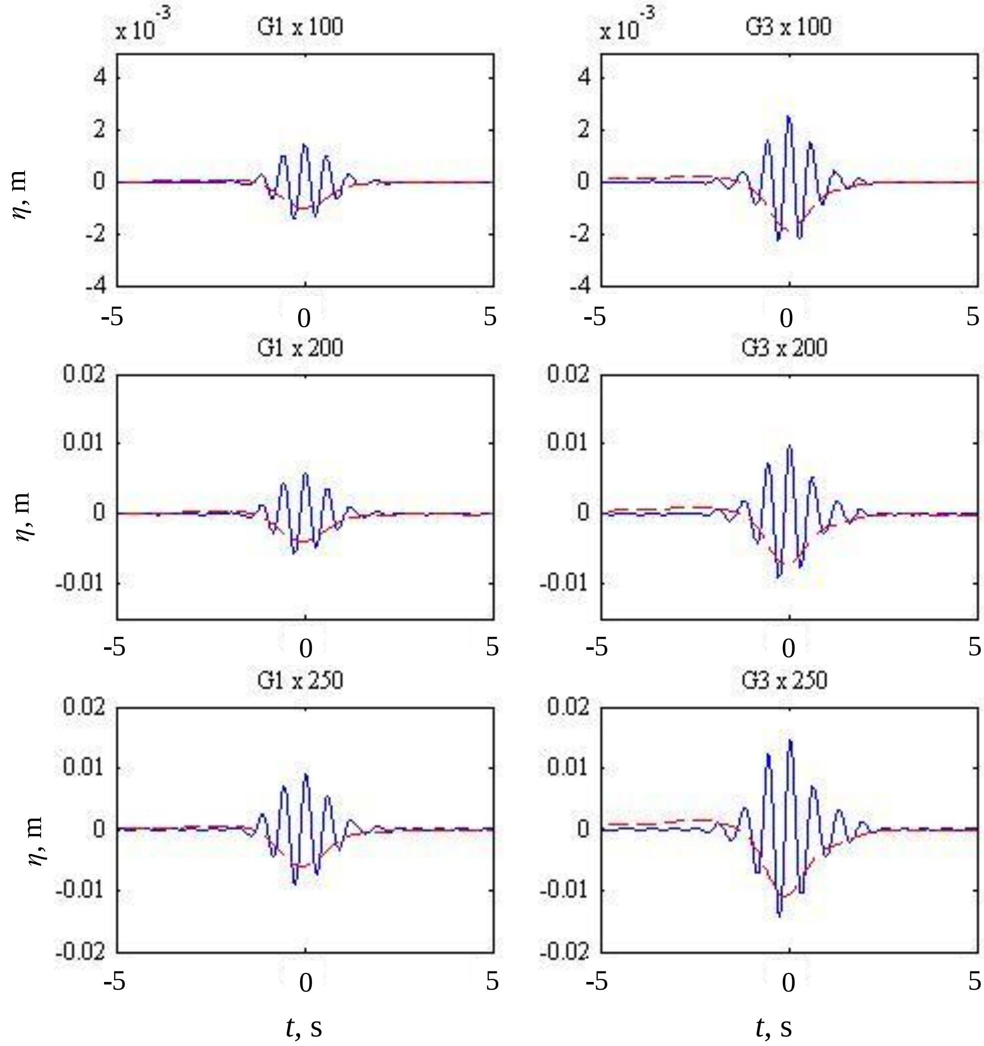

Figure 6.22a: Separation of even harmonics for Gauge 1 and Gauge 3. Solid lines are for the double frequency and dashed lines are for the long waves.

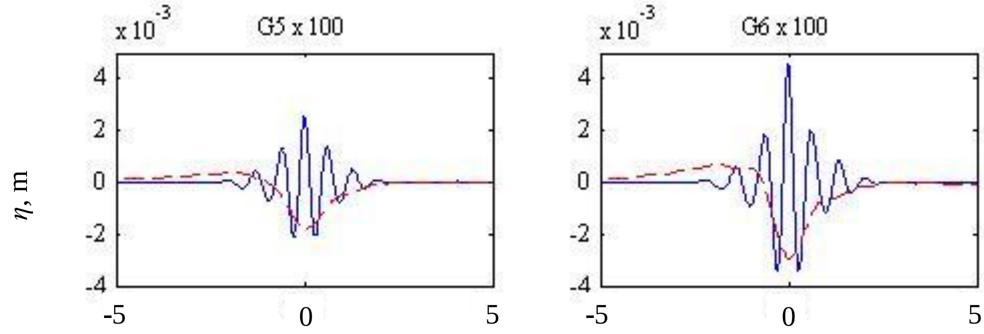

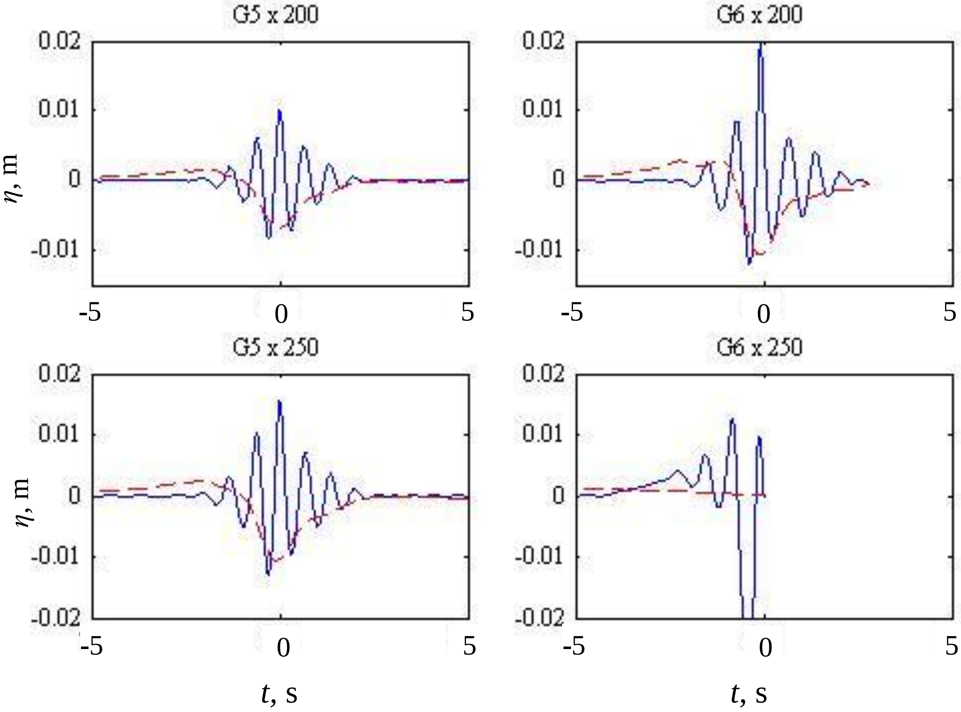

Figure 6.22b: Separation of even harmonics for Gauge 5 and Gauge 6. Solid lines are for the double frequency and dashed lines are for the long waves.

The lack of data in Figure 6.21b and Figure 6.22b (M = 200 and 250 of Gauge 6) is due to the very steep waves becoming unstable in the simulation. The combination of wave group focussing in shallow water and the transfer of energy by the reduction of horizontal velocity to the increment in crest amplitude due to the reduced water depth will increase the wave steepness dramatically. Given an already very steep wave group before wave focussing, the numerical code cannot cope with the high surface elevations and velocity differences between spatial points, and starts to give unreasonably high values, leading to failure of the simulation. Even after using a finer resolution of Δx = 0.02 m and smoothing of the solutions by means of a weighted average of the initially calculated solutions (for the free surface, η and velocity, u) at every time step does not resolve the instability. The five point stencil applied for the smoothing is as follows (Longuet-Higgins and Cokelet, 1976, Turnbull et al., 2003):

$$\eta_i = \frac{1}{16}\left(-\eta_{i-2} + 4\eta_{i-1} + 10\eta_i + 4\eta_{i+2} - \eta_{i+2}\right)$$

Figure 6.23 shows the very steep wave group ($M = 250$) spatial profiles at four different times before the rapid increase in surface elevation (at $t = 80.8$ s), at which the simulation fails. The linear wave focus is at $x = 157$ m (Gauge 6).

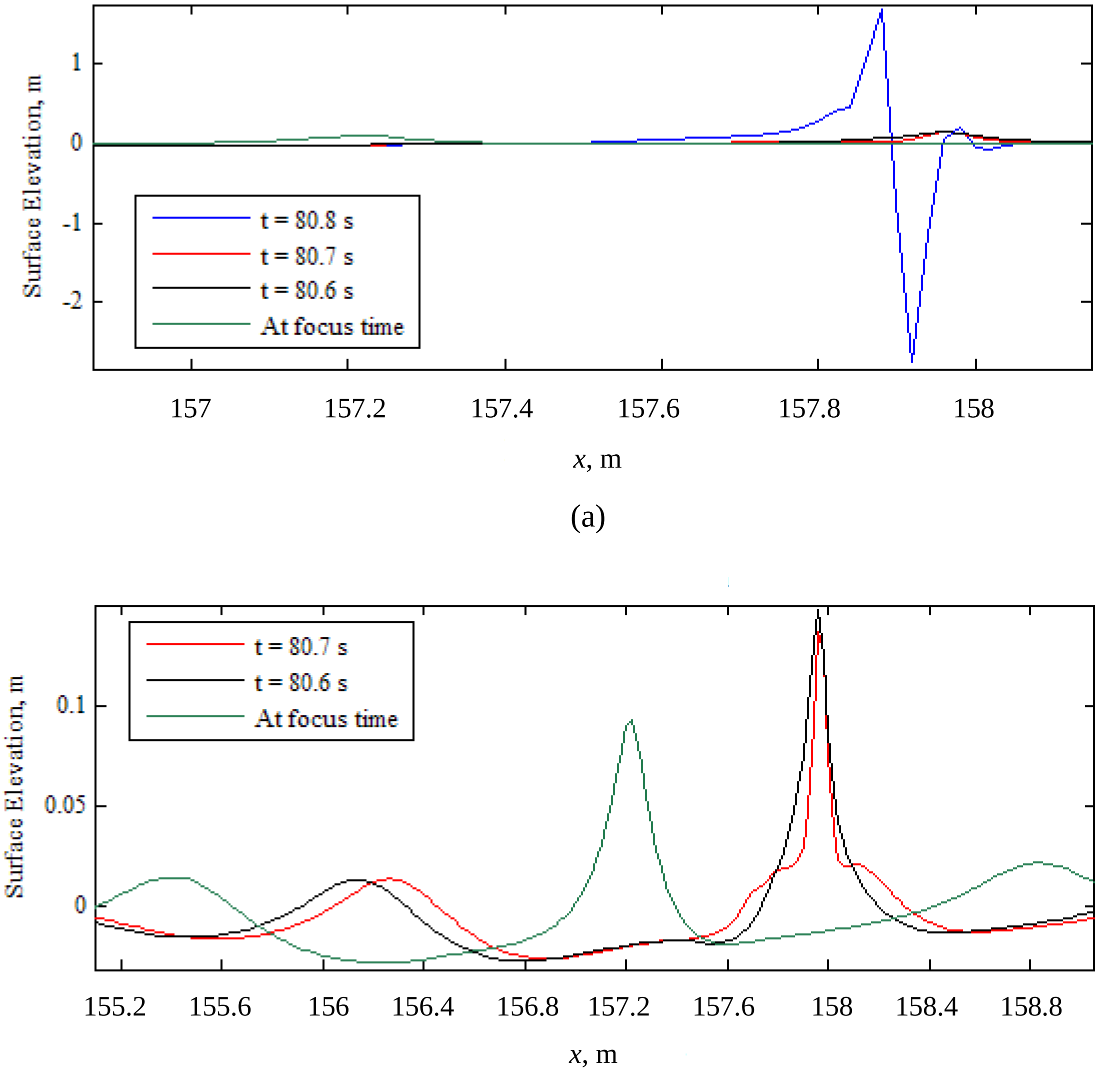

(a)

(b)

Figure 6.23: Local profiles of steep wave groups in shallow water with spatial resolution of 0.02 m a) development of instability and b) zoomed in portion of Figure 6.23a, with smoothed solutions at every 20 time steps.

Zooming in at the position of gauge 6 and ignoring the wave profile at t = 80.8 s, Figure 6.23b clearly shows the smooth increase in amplitude from linear focus at t = 80 s to t = 80.6 s, before the decrease of amplitude and the narrow peak on wide base wave profile at t = 80.7 s. At 0.1 s before the instability in Figure 6.23a, there is already a lack of correlation with the physical/real water wave in terms of the wave profile.

6.4.3 Comparison with Lowish data

As in the cases considered in the previous section, the wave group is propagated forward upon the 1:100 bed slope towards the linear focus location. But instead of varying the magnification factor M to investigate the effect of wave steepness, the corresponding M for the numerical simulation is chosen so that the linear peak matches the large wave event analysis of experimental Lowish data at each gauge. The average of the top 10 percent crests and troughs of Case 1a1100 is considered. Figure 6.24a compares the numerical and experimental odd harmonics time series, where the latter is the $[\eta_c - \eta_t]/2$ in Figure 3.2 from Section 3.2. It can be seen that the troughs and the crests either side of the main crest are much larger than the experimental data, suggesting that the numerical result is notably more narrow banded, and is shown in the amplitude spectrum plot of Figure 6.24b. The amplitude spectrum suggests that there is lack of non-linear interactions for the numerical data when compared to the experimental data. Increase in non-linear interactions would transfer the peak energy towards the higher frequencies and result in a better comparison with the experimental data. However, as the water depth is reduced, the peak spectra decreases and the third order harmonics (at about 2.5 Hz) increase (relative to the linear harmonics at about 0.8 Hz) for both the data. Furthermore, the wave period and the numbers of crests and troughs match each other. It should be noted that the experimental data consist of randomly propagating waves, whereas the numerical simulation consists of a single dispersed wave group propagating towards the focus wave profile.

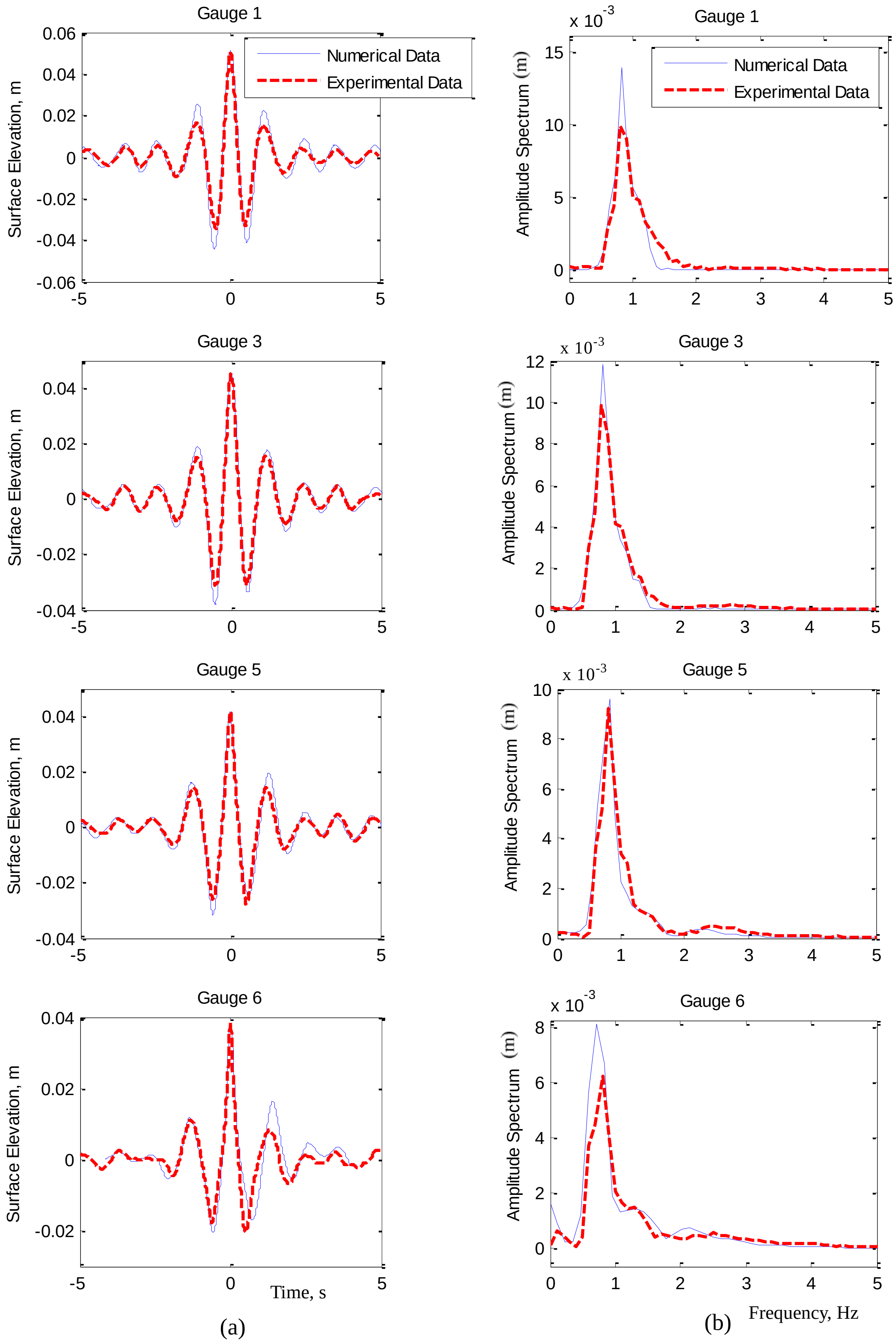

Figure 6.24: Comparison of the odd harmonics between numerical data and experimental data for; a) surface elevation and b) amplitude spectrum

Next, the second order sum is obtained by spectral filtering of the even harmonics signal. This numerical result is then compared with the analytical second order prediction for the magnitude of the second order sum, e_2 derived in Section 4.6.2. The analytical prediction is based on the linear signal in the numerical data and is given by

$$\frac{e_2}{d} EH2 ,$$

where $EH2 = OH^2 - OH_H{}^2$ and $e_2 = \frac{3+(kd)^2}{4(kd)^2}$, OH is the odd harmonics of the numerical data (which is dominated by the linear order terms) and subscript *H* corresponds to the Hilbert transform. The comparison between the numerical and analytical solution plotted in Figure 6.25a shows close agreement at all gauges, particularly regarding the crest. This shows that the numerical code is giving the desired second order sum contributions, in accord with the analytical solution. Comparing the analytical solution above (which is very close to the GN numerical solution) with the experimental data, Figure 6.25b shows that there is very good agreement in shallow water but less satisfactory agreement in deep water. The reason for plotting the analytical solution instead of the numerical solution against the experimental data for Figure 6.25b is to link them with the Stokes coefficient S_{22}. Using the Stokes coefficient S_{22} instead of e_2 for the same signal *EH2* gives a better result, but still does not give good agreement in deep water. The discrepancy with the experimental data could be due to the limitation of the GN Level 1 equation. A shallow water assumption of uniform horizontal velocity and linearly varied vertical velocity is not able to capture fully the energy of the second order sum component in deep water. This observation is based on the comparison between the Stokes coefficient S_{22} which is derived from the full water wave equation and e_2 which is from the GN equation. As shown in Figure 4.5 of Section 4.6.2, the coefficient e_2 matches S_{22} at shallow water but diverges at deep water.

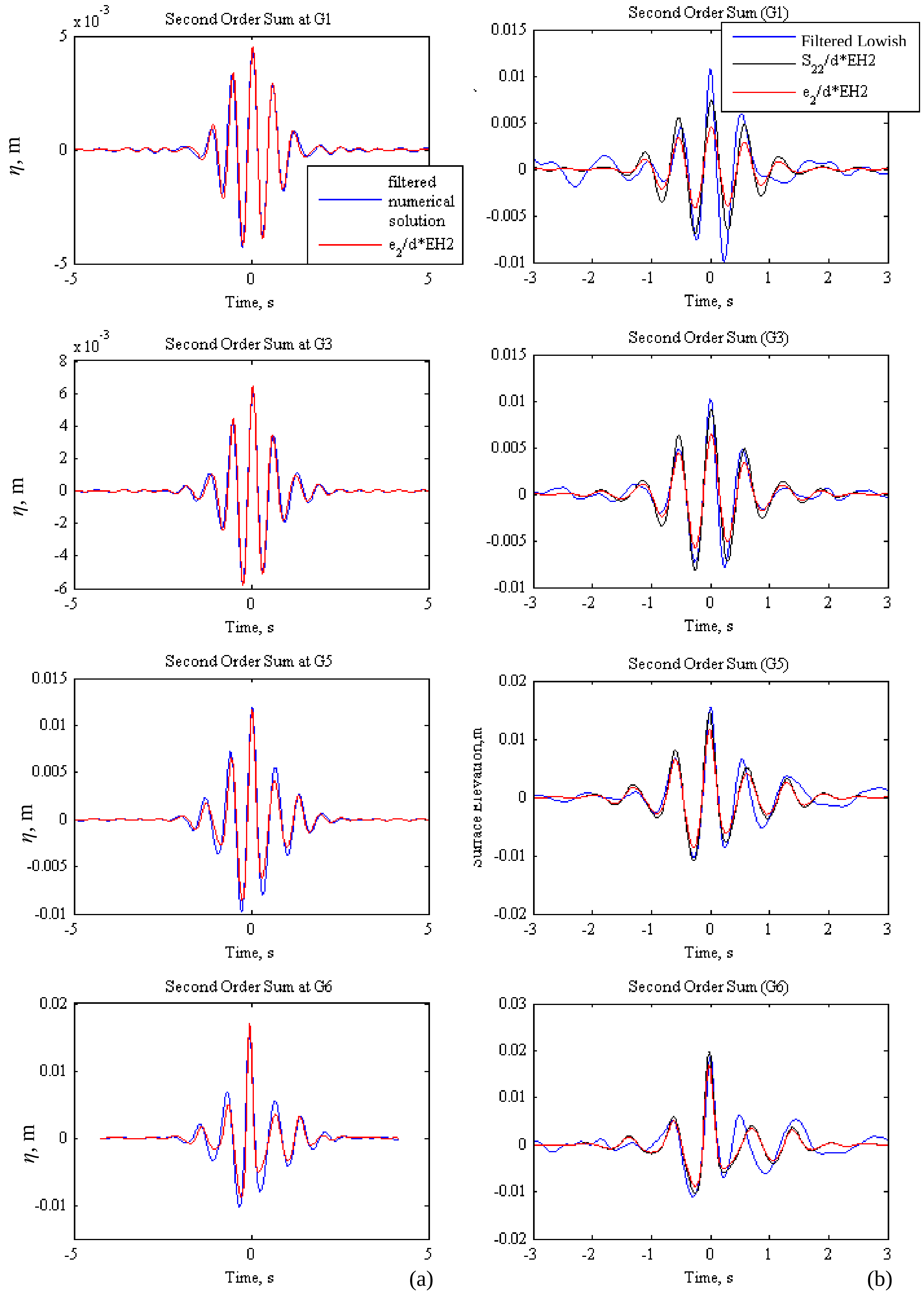

Figure 6.25: Comparison of second order sum terms between a) numerical solution and analytical solution and b) analytical solution with experimental data

The spatial profile instead of the time series is now examined at t = -5, 0 and 5 s. The linear, second order sum and second order difference terms spatial profiles are plotted in Figures 6.26a to 6.26d, for Gauges 1, 3, 5 and 6 respectively. At Gauge 1, Figure 6.26a shows the wave focusing from t = -5 s to t = 0 s and wave defocusing from t = 0 s to t = 5 s for all three harmonics. As the water depth reduces (different gauges), the wave dispersion weakens, and is overcome by non-linearity. This is shown by the increase in magnitude of the second order difference and sum terms at t = 5 s after the linear wave focus time, at the other gauges, especially Gauge 5 and Gauge 6 of Figure 6.26c and 6.26d.

Interestingly, the second order difference term produces a wave set-down, and two wave set-ups, the free error wave and the extra wave set-up, as has been mentioned in Section 6.4.2 (particularly Figure 6.22). Even more interesting is that the extra wave set-up is not bound to the main wave packet. In all water depths and at all times, the wave set-up keeps on increasing in amplitude as the wave group travels on the slope, little affected by the linear wave focus location. Obeying conservation of mass, this increasing mass of wave set-up through shoaling acts as a balance to the increment in magnitude of the wave set-down; pushing the mass of water ahead to produce the wave set-up. Unlike the free error wave set-up which is not affected much by the slope, this wave set-up continues to interact non-linearly with the main wave packet. Unfortunately, no physical validation can be made against the experimental data because there are no finely sampled spatial wave data throughout the wave tank at any time, only time series at gauges which are 5 m apart. Even the time series at the focus location will not pick up this increasing amplitude of wave set-up because this process happens downstream of the gauges. For example at Gauge 1, and at t = 5 s, the value of the wave set-up is about 0.5×10^{-3} m at x = 142 m, and not at the linear focus location. Figure 6.27 shows the second order difference for the numerical simulation at the focus location of each gauge and no evidence of the large wave set-up. Groesen and Westhuis (2002) produced the same extra wave set-up in their wave group propagation over a slope but not the continuous increment in amplitude seen here. The small length of the slope by Groesen and Westhuis means that the interaction between the wave set-up and the slope is limited; the wave set-up starts to travel ahead of the main wave packet on constant depth.

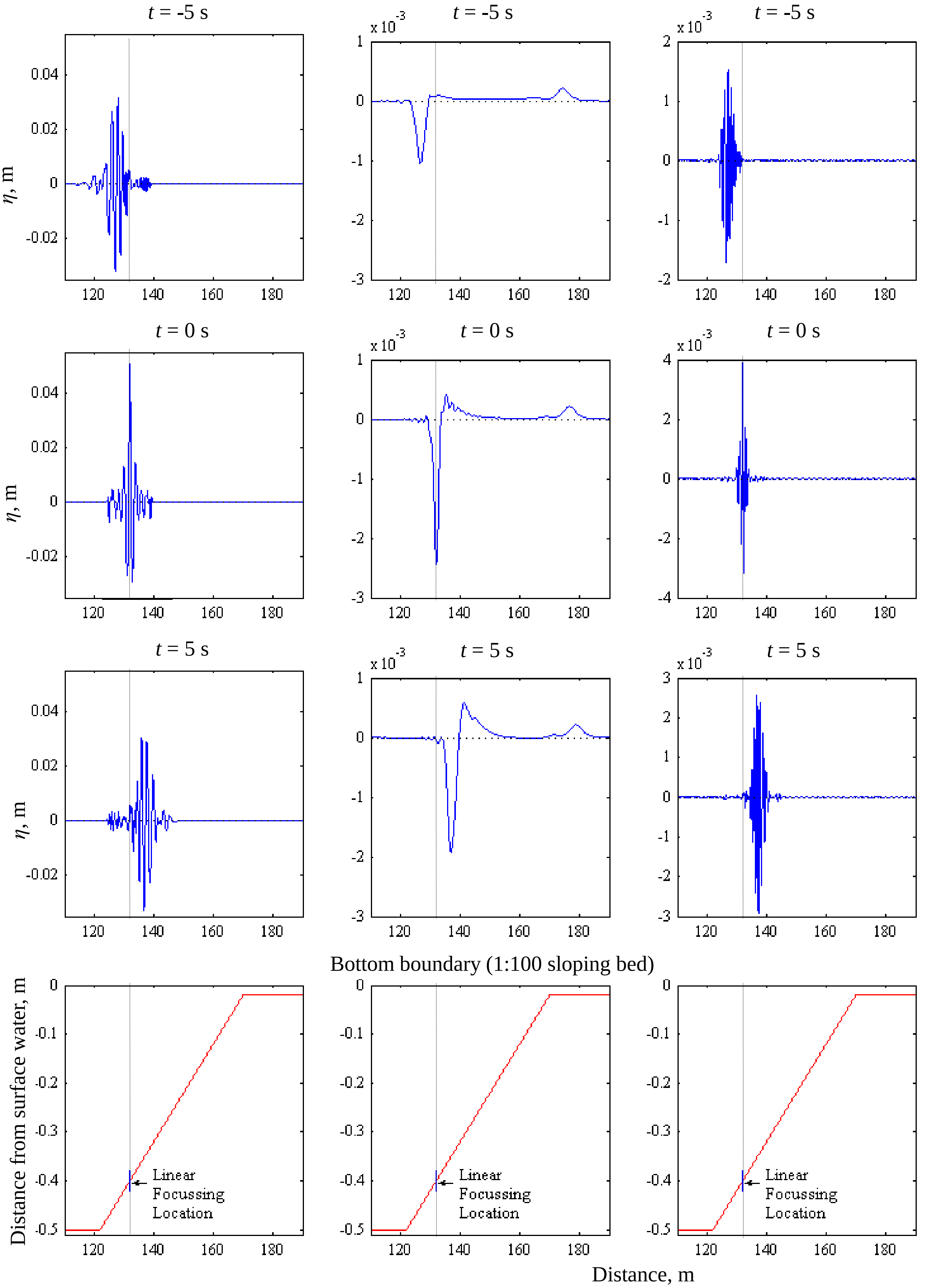

Figure 6.26a: Spatial profiles of numerical results at Gauge 1 for *t* = -5, 0 and 5s (left panels: odd harmonics, centre panels: second order difference, right panels: second order sum).

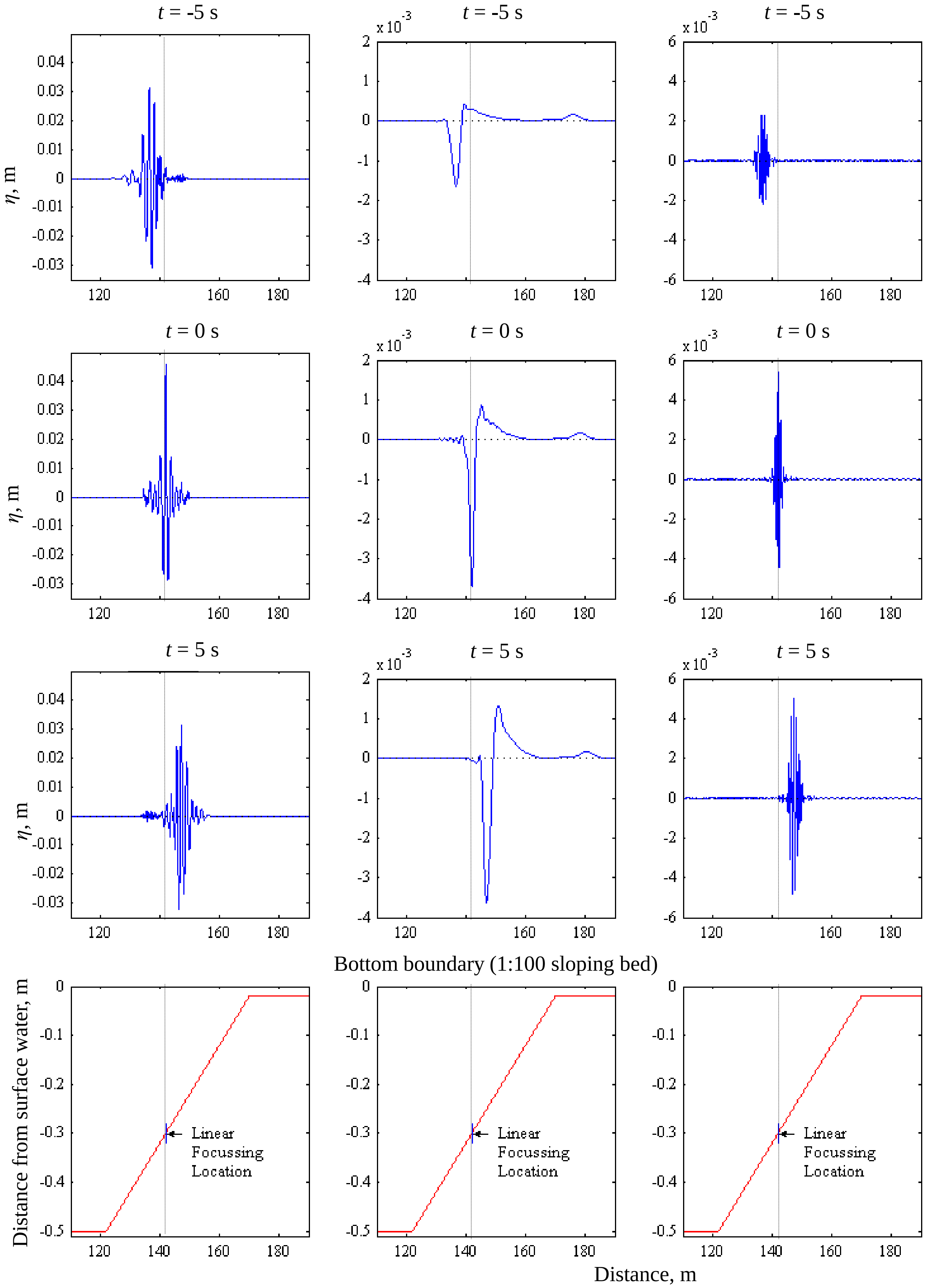

Figure 6.26b: Spatial profiles of numerical results at Gauge 3 for *t* = -5, 0 and 5s (left panels: odd harmonics, centre panels: second order difference, right panels: second order sum).

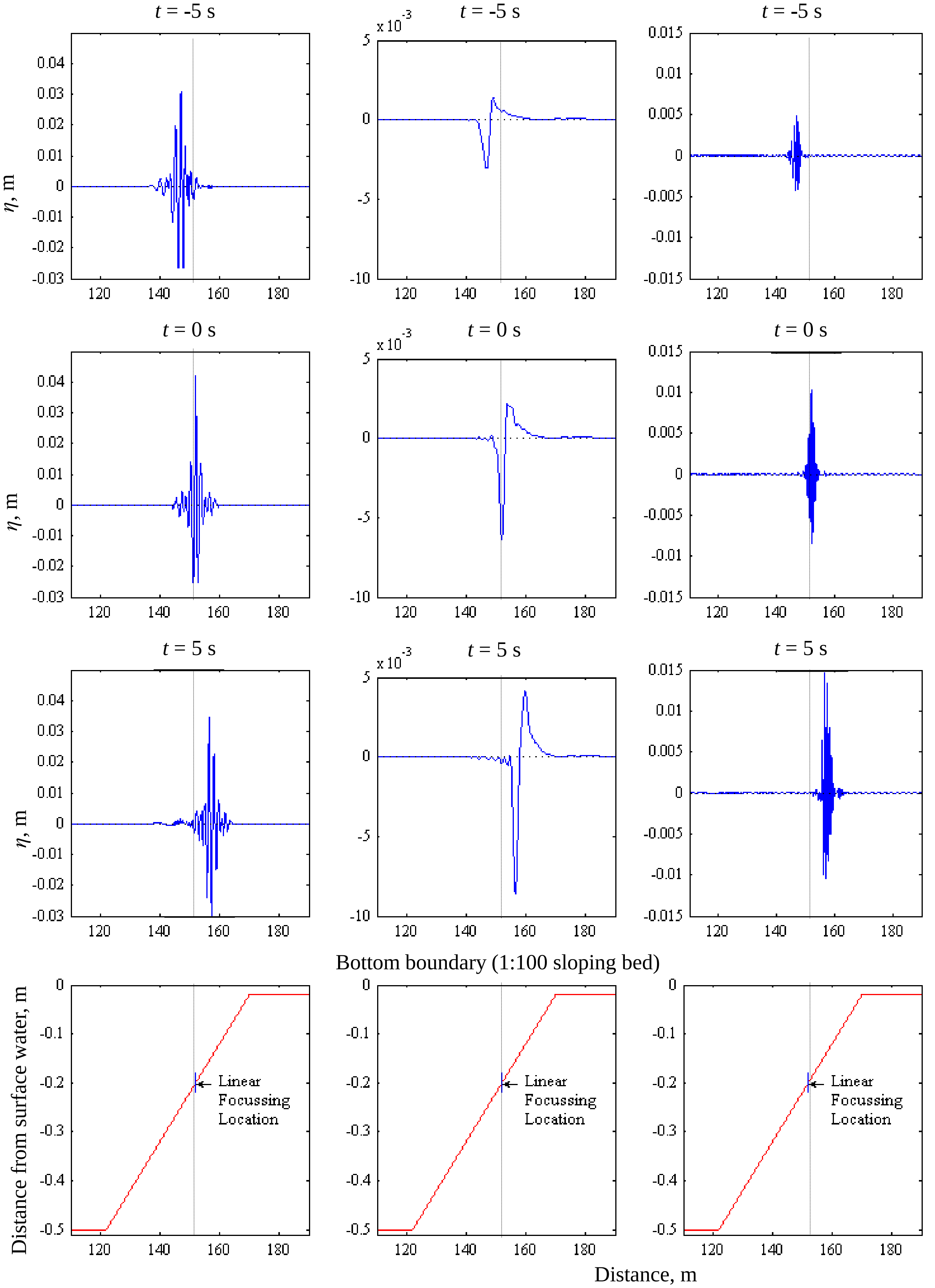

Figure 6.26c: Spatial profiles of numerical results at Gauge 5 for *t* = -5, 0 and 5s (left panels: odd harmonics, centre panels: second order difference, right panels: second order sum).

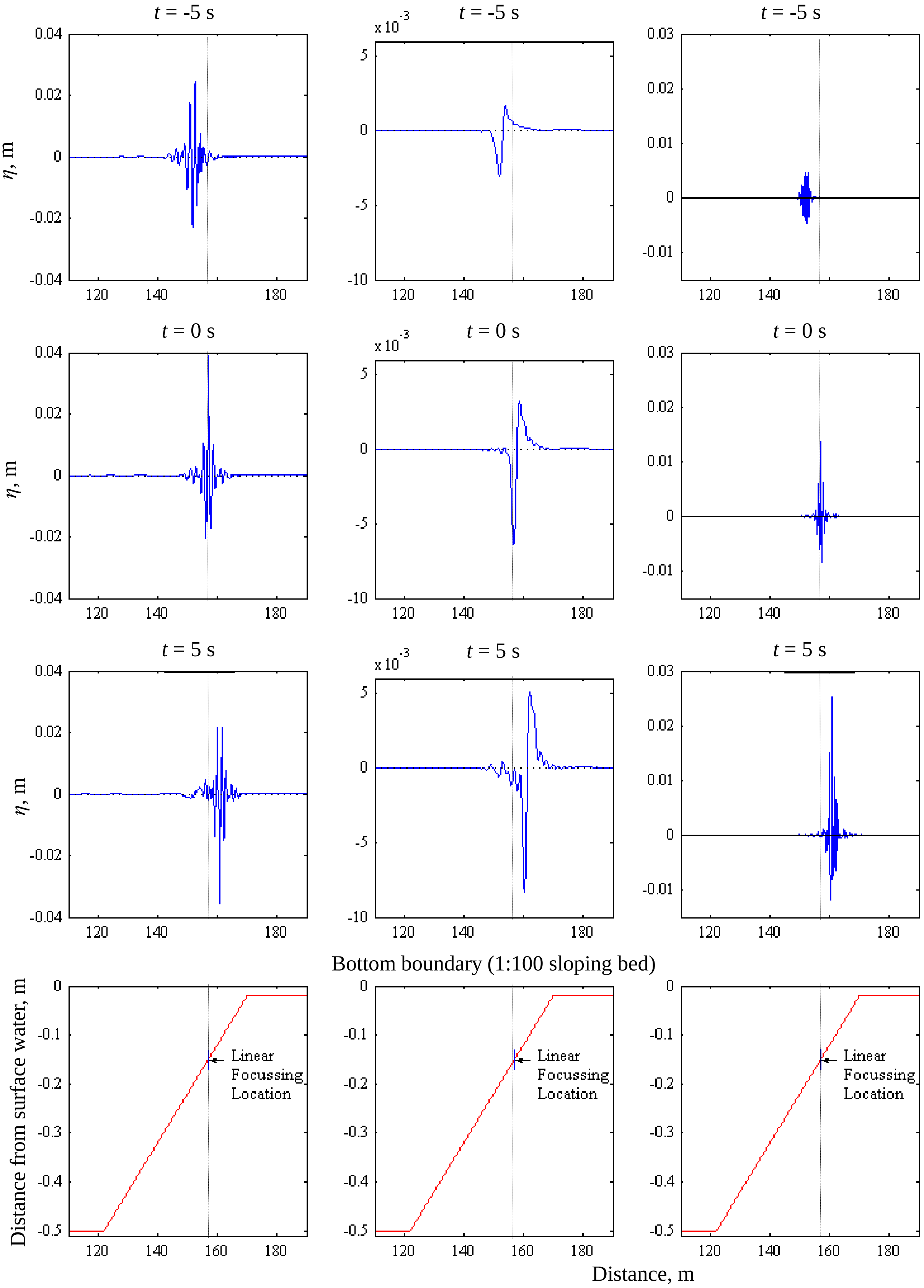

Figure 6.26d: Spatial profiles of numerical results at Gauge 6 for *t* = -5, 0 and 5s (left panels: odd harmonics, centre panels: second order difference, right panels: second order sum).

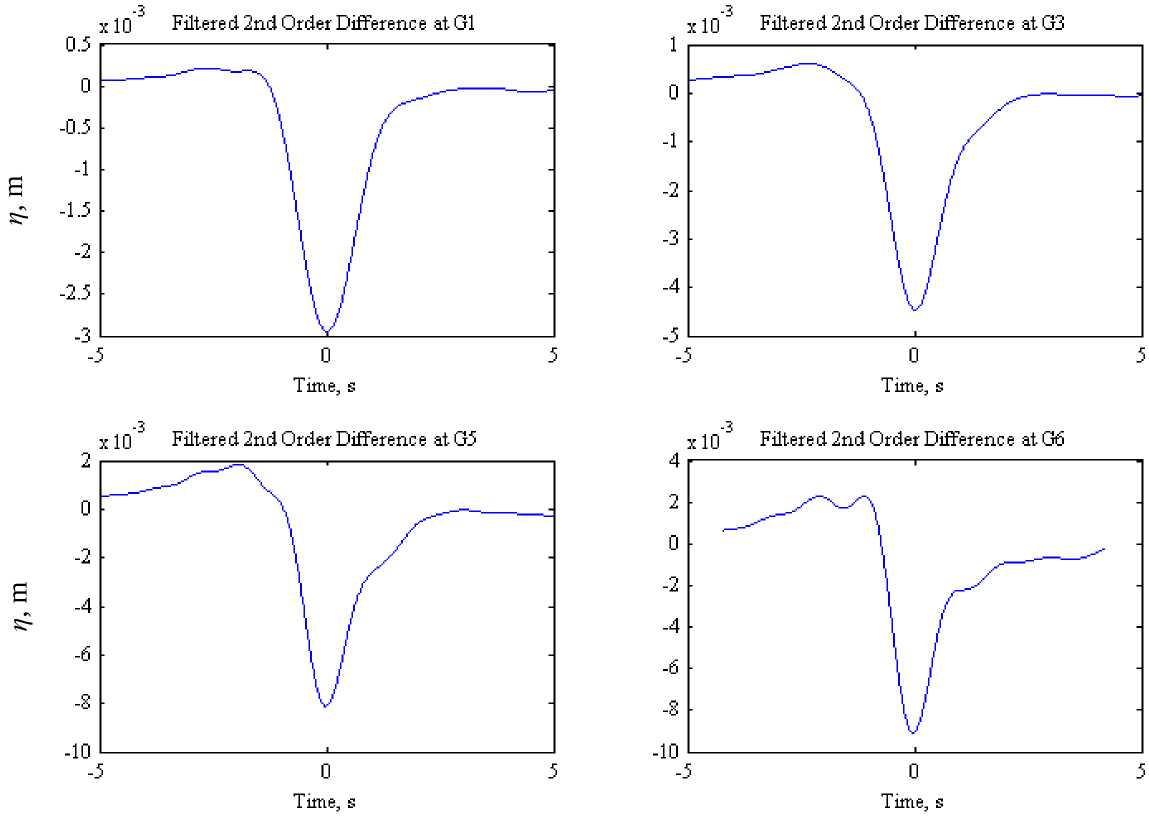

Figure 6.27: Second order difference at four different gauges

Figure 6.28 compares the numerical solution against the analytical solution of e_2 for the second order sum term at Gauge 3, now for the spatial profile instead of the time series in Figure 6.25. The numerical solution slightly under predicts the peak at the linear focus location, but otherwise gives good agreement at all three different times.

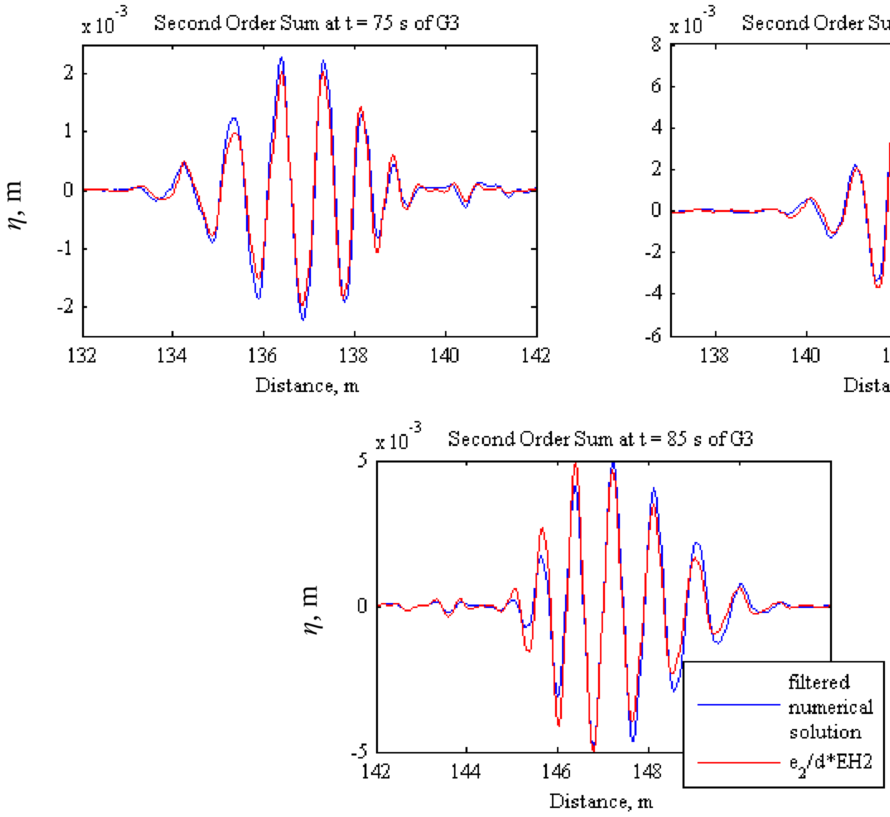

Figure 6.28: Comparison of the second order sum terms with analytical solution (in space)

6.5 Conclusion

- The general behaviour of wave groups is simulated correctly by the GN code;
  - The simulations are reversible and potential energy is properly conserved,
  - Linear dispersion works well; the wave groups get wider and amplitudes are smaller as they propagate away from the focus location,
  - Free error waves are produced from linear-based initial conditions. Their magnitudes increase as the water depth is reduced.

  Both the reduction in water depths and increase in wave steepness increase the contribution of higher order harmonics in the wave group. They also lead to free waves in the form of a wave hump at the front of the main wave packet and a small dispersive wave group behind.
- Smooth and clean decomposition of odd and even harmonics is achieved using the Stokes water wave expansion, except for waves in very shallow water for the constant depth case.

  - Weakly non-linear wave groups ($ak_p = 0.1$), are dominated by the linear harmonic but the even harmonics' contribution are significant. Also, the bound double frequency waves are riding in a depression (there is a bound wave set-down).
  - The phases of the double frequency and long waves set-down are aligned with the linear components, showing that they are bound.
  - For the most severe case with $k_pd = 0.5$ and $ak_p = 0.4$, the separation of harmonics breaks down. In real water waves, the waves are most probably broken at this particular amplitude and depth. However, it is still interesting that the GN code is able to cope without any stability issues. The produced solitary waves with higher amplitudes travel faster showing that, overall, the physics of water waves are simulated correctly.
- NewWave-based method through the Hilbert transform is able to estimate the shape of the bound double frequency and long wave set-down profiles for k_pd larger than 0.5. The results and the limitation of this method have been demonstrated before for the NewWave analysis applied to random data in Chapter 3, and works as long as the non-dimensional water depth k_pd is larger than 0.5.
- In addition, defocussing of wave groups in shallow water is observed. This is consistent with the non-linear defocussing properties of the non-linear Schrödinger equation (NLSE) in shallow water.

  The switch point for the NLSE is at kd 1.36, so linear focussing here for $k_pd = 1.5$ and $k_pd = 1.25$ is to be expected with defocusing being increasingly important as the water depth is reduced. At $k_pd = 0.5$ the broadening is clear but the idea of group dynamics rather than the dynamics of the individual waves is starting to fail.
- Qualitatively, the numerical wave groups on a gentle slope produce the same behaviour as the experimental data; the trough amplitudes experience relatively more reduction than the crest amplitudes as the water depth reduces.
- Evident of an extra wave set-up as the wave group propagates on a slope. It appears to be a function of the sloping bed.

  This bed slope-induced wave set-up continues to increase in amplitude and interacts non-linearly with the main wave packet as it travels up the slope, which can be seen clearly along the length of the domain. A time series plot at the focus location will not show this rather large wave set-up because the process occurs downstream of the location. By conservation of mass, the increasing magnitude of wave set-down pushes the mass of water ahead, producing the wave set-up.

7 Conclusions and Recommendations

Introduction

There are two main contributions in this thesis. First, a detailed wave-by-wave statistical analysis of the shoaling of steep waves on gentle slopes, based on experimental data from Imperial College (Lowish, 2007 and Katsardi et al., 2013). Second, a Green-Naghdi (GN) numerical model, which is able to simulate non-linear and steep waves, has been developed and validated. Coupled with statistical analysis, mainly through a method called NewWave implemented as an initial condition for the GN numerical simulations and also using experimental data of random waves propagating on gentle slopes, the general behaviour and detailed physics of waves on gentle slopes have been examined and conclusions are made. The developed GN numerical model for shallow water (which is also applicable for intermediate water depth) has been validated thoroughly with solitary wave simulations; solitary wave separations and solitary wave interactions on constant depth and solitary wave propagation over varying water depth. This is then applied to simulate NewWave-type focussed wave group propagation on a gentle slope, representing the behaviour of extreme waves.

A deeper understanding of the nature of both the GN predicted and experimentally measured extreme waves, which can be highly non-linear, is obtained through the combination of the statistical analysis of the experimental data and the numerical simulation. In particular, Stokes' water wave expansion is applied extensively to separate the higher order harmonics and often to quantify them through the NewWave-based approach. This thesis is by no means a conclusive research in terms of understanding the behaviour of steep waves, and thus recommendations will be made for future work.

Statistical Analysis of Experimental Data

Propagation of random waves from deep into shallow water obtained through experimental data from a wave flume has been analysed by examining the changing shape, crest, trough and wave heights as the waves shoal. This is done by averaging the large wave events at each water depth along the wave flume and applying the NewWave analysis. In previous work, NewWave has solely been tested for waves on relatively deep water (*kd* ~ 1.2 – 1.6 and *kd* ~ 3). Now, it has been shown that NewWave can also be applied to waves on relatively shallow water with *kd* as low as 0.5. So, it is appropriate for a much wider range of *kd* than previously tested. Basically, NewWave is valid so long as the global wave behaviour is dominated by frequency dispersion.

The principal observations are as follows:

- Sharpening of crest and broadening of troughs can be seen as the waves propagate into shallow water.
- The shapes of all the large waves considered are very similar during the time from 1 s before to 1 s after the maximum crest occurs, where the peak period T_p is 1.2 s. Further from the crests conditioning points, the individual shapes are distributed randomly. In shallow water, there is a definite crest height limitation criterion and also a loss of symmetry in the horizontal direction.
- Applying a simple separation of wave harmonics works well for extracting the linear term up to the gauge where the asymmetry in shape starts to become apparent and then increases rapidly in shallow water. The NewWave methodologies give very satisfactory representations of average large wave events for non-breaking waves. Once large-scale breaking occurs, NewWave fails to match the measured data. NewWave appears to be a reasonable model for waves in deep and intermediate water depth (*kd* > 0.5).
- For the even bound harmonics; dominated by double frequency second order terms, the period taken from trough to trough along the crest is halved compared to the odd harmonics.

- Also seen is a set-down term in deeper water (the troughs either side of the crest are larger than the crest itself); a wave group rides in a depression of its own making. In the shallow regions, this local set-down is as large as the double frequency sum term.
- Attempts have been made to model waves after the main breaker line, which appears to be at around $kd \approx 0.5$ for sufficiently energetic wave fields. Two models have been used; a simple solitary wave form riding on an unknown local current, and a hydraulic jump. In both cases, the wave crests move faster than the assumed wave forms on shallow water, requiring that they ride on a significant and highly variable onshore current. Given the limited data available for the shallowest depths, the analysis cannot be taken further.
- In terms of the modified Miche criterion produced in the first phase of Lowish study, use of either the wavenumber ($k = k_p$) based on deep water wave spectral peak or a local NewWave type model with a local zero-crossing based wavenumber ($k = k_{NW}$) is appropriate, with the NewWave based model appearing to be a closer bounding limit to the data.

The basic NewWave analysis has been extended from being a model of the main linear part of the average large wave event only to being able to estimate the shape and magnitude of second and third order sum contributions with reasonably good results by using a Hilbert Transformation-based method. Combined with NewWave, the height of extreme waves can be estimated.

- The contribution of both second and third order sum harmonics increases in magnitude as the waves shoal, which is essential in the build-up of extreme waves.

Green-Naghdi (GN) Numerical Model

A numerical solver for the GN equations in shallow water over a non-uniform bed has been developed, with the capability of simulating steep waves on varying water depth. The GN equations are derived using a different (and simpler) notation than is used by Demirbilek and Webster (1992). A brief investigation shows that the one sheet GN equation set permits solitary wave behaviour similar to that well known for the Korteweg-de Vries equation.

Mathematical Formulation of the Green-Naghdi Equations

The GN equations are a depth-integrated equations, derived from conservation of mass and momentum laws together with the kinematic and dynamic boundary conditions for free surface flow of inviscid and incompressible liquid.

- The velocity field is approximated by using a single sheet fluid (GN Level 1) model and assuming the velocity profile of the horizontal component to be uniform while the vertical component varies linearly from zero to a maximum at the free surface, corresponding to shallow water flow.
- GN equations satisfy the boundary conditions exactly, which is in accordance with the research of simulating free surface flows, and incorporates non-linear terms in its formulation even at the lowest order, which is essential in the analysis of steep waves.

A finite difference scheme is applied to solve the derived GN Level 1 for shallow water equations numerically. Fourth order accuracy is implemented for both the space and time derivatives; using fourth order central differences in space and the time is integrated using a fourth order Runge-Kutta method (RK4). The mixed derivatives in the GN equations, together with the fourth order spatial discretisation, leads to a pentadiagonal matrix, which means that the variables at all grid points are solved simultaneously at each RK4 intermediate step. Solid walls are implemented at both left and right boundaries.

Validation of the GN Numerical Model through Simulation of Solitary Waves

The numerical scheme is able to produce physically realistic solitary wave propagation; which shows the ability of the numerical model to cope with non-linearity. In comparison with the KdV equation, qualitatively the GN equations have similar properties to the KdV equation.

- Unlike KdV, the GN equations are not completely integrable. The KdV equation is a weakly non-linear equation whereby the speed of the wave varies exactly linearly with the amplitude. For GN equations, there are corrections beyond linear in amplitude for the wave speed.

- The GN equations are able to simulate the solitary wave separation and also solitary wave interactions well. The fitted sech^2 function gives a good approximation for the merged wave shapes for the overtaking interaction of two solitary waves.
- The GN equations are able to handle the highly non-linear solitary wave propagation on gentle slopes. Solitary wave propagation from deep water to shallow water on a rather steep slope (1:30) has been simulated. At the top of the shelf, a solitary wave has a steep front, which separates into a number of solitary waves in the absence of wave breaking. The GN numerical model gives good results for the transmitted solitary waves when compared to the analytical solution. The analytical approach is undertaken by combining the linear scattering for a solitary wave over a step change followed by the KdV conserved-quantity-based analytical approach to constant depth splitting.

Compared to the experimental results by Seabra-Santos et al. (1987) for solitary waves propagating up a change in depth on a slope (1:30), the experimental value of the transmitted solitary waves is lower than the numerical prediction produced by the GN code. GN theory assumes that the water has no viscosity, so viscous damping is excluded. But experimentally, the waves experience energy dissipation due to the viscous damping effect. Thus, both the GN numerical and experimental results are in reasonable agreement, considering the inviscid assumption of the GN equations.

In short, the numerical solver of the GN equations works well and the GN Level 1 gives quantitatively good results when compared to the corresponding solution of the KdV equation.

GN Numerical Solution of Focussed Wave Groups

The developed and validated numerical model is used to simulate focussed wave groups on both constant depth and gentle slope. For the latter, the initial data were taken from the experiments in the Lowish project so that both the results from the numerical and experimental analysis could be compared. In general, the behaviour of waves simulated by the numerical simulation is very similar to that observed in the experimental data. The NewWave approach and also the Hilbert transformation-based extensions for the shape of the second order sum contributions work well at intermediate and deep water depth ($kd > 0.5$).

Both the reduction in water depth and increase in wave steepness increase the contribution of higher order harmonics in the wave group, narrowing the crests and broadening the troughs. The increase in wave steepness from a linearised condition in deep water propagating towards the linear focus location at shallow water does not change significantly the non-linear focus location. This suggests that the focussing wave event is mainly a contribution of the linear dispersive focussing. The GN equations also shows the property of the NLSE, non-linear defocussing for $kd < 1.36$. This suggests that the Benjamin-Feir instability is not an important factor for the occurrence of extreme waves in intermediate water depth compared to deeper water.

Non-linearity does play an important part in the structure of waves. As has been shown for the experimental data analysis, there is evidence of vertical asymmetry also for the numerical simulation as the water depth is reduced (different gauges); the trough amplitudes experience relatively more reduction than the crest amplitudes as the water depth reduces. Thus the higher order harmonics are becoming increasingly important for shoaling wave groups. The shapes and magnitudes of the higher order harmonics can be estimated through the Hilbert transformation of the NewWave. Given random waves in a sea-state and also the bathymetry of the seabed (assuming uniform change), the height of an extreme waves can be estimated at points up the slope by using NewWave and applying its non-linear second and higher order harmonics correction.

Interestingly, the second order difference term produces an extra wave set-up on gentle slopes, and is not bound to the main wave packet. In all water depths and at all times, the bed slope-induced wave set-up keeps on increasing in amplitude as the wave group travels on the slope, little affected to the linear wave focus location. Obeying conservation of mass, this increasing mass of wave set-up due to shoaling acts as a balance to the increment in magnitude of the wave set-down; pushing the mass of water ahead to produce the wave set-up. This wave set-up can continue to interact non-linearly with the main wave packet. Unfortunately, no physical validation can be made against the experimental data because there are no finely sampled spatial wave data along the wave tank at any time, only time series at gauges which are 5 m apart. Even the time series at the focus location will not pick up this increasing amplitude of wave set-up because this process happens upstream of the gauges as the main wave event passes. Groesen and Westhuis (2002) observed the same bed slope-induced wave set-up in their simulations of wave group propagation over a slope but not the continuous increment in amplitude seen here. However, the small length of the slope by Groesen and Westhuis means that the interaction between the wave set-up and the slope is limited; the wave set-up starts to travel ahead of the main wave packet on constant depth. The physics of the response of the second order difference term to varying water depth is not fully understood.

Recommendations

Most important recommendation concerns the comparison which has been made between the random waves of experimental data with the focussed wave group modelling from GN equations. To allow a direct and better comparison between them, either experimental model tests with initial waves that will focus in time at particular points on the slope should be performed or else paddle-type wave generation be included in the numerical simulation, which would allow modelling of random wave propagation. Then, the same statistical analysis executed in the experimental data could be applied to the numerical simulations of random waves. The latter is more appropriate given the code that has been developed.

From the literature review, NewWave has been applied to field measurement data for waves on relatively deep water ($kd \sim 1.2 – 1.6$ and $kd \sim 3$). It would be interesting to apply the same statistical analysis through the NewWave methodology to field measurements closer inshore for kd as low as 0.5, so that the change in shape of the NewWave and the TMA spectrum can be observed as the waves propagate in a line of wave gauges towards shallow water.

Regarding the overshoot of surface elevation from the experimental data shown for cases with 1 in 250 sloping bed (Figure 2.15 from Section 2.6), the internal examiner has pointed out other research that gives a higher surface elevation than predicted by the Gaussian distribution for random waves associated with bed slope changes for non-uniform bathymetry. Trulsen et al. (2012), through statistical analysis using skewness and kurtosis on laboratory data showed that there is a local maximum of the surface elevation at the top of a slope where a flat shelf starts, which is well beyond the Gaussian statistics. This is at the point of the intersection between the sloping bed with the constant depth at the shallow water region. Numerically, Sergeeva et al. (2011) also presented the same behaviour using KdV equation. It could be the cause of some freak waves. Demonstrating this behaviour through GN modelling using the same bed condition used in the Lowish experiment should reproduce the same overshoot seen in the experimental data. Sergeeva et al. (2011) showed that the length of the sloping bed does not influence this behaviour. But, further analysis can be done by investigating the smoothness of the transition point, by varying the parameter k_w from Equation (5.4) of Section 5.5.

The GN Level 1 equations developed here have dispersive characteristics which match well with the full water wave equation for $kd < 1.4$ but 2nd order perturbation analysis shows that the depth requirement for accurately matching the second order non-linearity is more stringent than for linear dispersion. A better shape function for the approximation of the vertical variation of the velocity field in Green-Naghdi theory would be sufficient to address the required problem, enabling the GN equations to model waves in deeper water relatively accurately. Also, GN Level 1 does not have an upper bound in terms of the physically realistic modelling of waves. At least a Level 2 GN model would be needed to inherently allow wave breaking properties (Kim et al., 2003). Clearly, a high level GN theory ought to be capable of solving both shallow and deep water problems. The high complexity of the formulation could be tackled by using powerful symbolic mathematical software such as *Mathematica*, and the solution of the resulting equations could be done with relatively modest computational effort.

It seems that the second order difference term plays a part in the behaviour of wave groups, especially with the set-down effect interacting with the decrease of water depth. A better model of the second order difference term than the NewWave-based approximation would help in establishing the shape and magnitude correctly and explaining the occurrence of the bed slope-induced wave set-up during wave groups shoaling. Experimentally, a finely-sampled spatial data set would help to validate the bed slope-induced wave set-up shown numerically by the wave group propagation on the gentle slope.

Although the free error waves have not affected the main results; by simulating waves with a longer numerical tank (in order for the main wave packets to be further separated from the free error waves), it would be interesting to see if any difference results from using a second order correct solution for the initial conditions of the numerical simulations. This will avoid free error waves.

Lastly, the incorporation of waves and current action into a GN approach ought to be possible. The action of waves with currents travelling in opposite direction has been one of the reasons of the occurrence of extreme waves e.g. in the Agulhas current which travels down the east coast of Africa (Lavrenov and Porubov, 2006).

References

Adcock T.A.A., Taylor P.H., Yan S., Ma Q.W. and Janssen P.A.E.M., 2011, Did the Draupner Wave occur in a Crossing Sea?, *Proceedings of the Royal Society A*; Vol. 467: 3004-3021.

Baldock T.E., Swan C. and Taylor P.H., 1996, A Laboratory Study of Nonlinear Surface Waves on Water, *Philosophical Transactions of the Royal Society of London. Series A*; Vol. 354: 649-676.

Bateman W.J.D., Swan C. and Taylor P.H., 2001, On the Efficient Numerical Simulation of Directionally Spread Surface Water Waves, *Journal of Computational Physics*; Vol. 174: 277-305.

Bateman W.J.D., Swan C. and Taylor P.H., 2003, On the Calculation of the Water Particle Kinematics Arising in a Directionally Spread Wavefield, *Journal of Computational Physics*; Vol. 186: 70-92.

Beji S. and Battjes J.A., 1993, Experimental Investigation of Wave Propagation over a Bar, *Coastal Engineering*; Vol. 19: 151-162.

Benjamin T.B. and Hasselmann K., 1967, Instability of Periodic Wavetrains in Nonlinear Dispersive Systems [and Discussion], *Proceedings of the Royal Society A*; Vol. 299: 59-76.

Billingham J. and King A.C., 2000, Wave Motion, *Cambridge Texts in Applied Mechanics, Cambridge University Press*.

Boccotti P., 1983, Some New Results on Statistical Properties of Wind Waves, *Applied Ocean Research*; Vol. 5: 134-140.

Booij N., Ris R.C. and Holthuijsen L.H., 1999, A Third-Generation Wave Model for Coastal Regions. Part 1. Model Description and Validation, *Journal of Geophysical Research*; Vol. 104: 7649-7666.

Borthwick A.G.L., Ford M., Weston B.P., Taylor P.H. and Stansby P.K., 2006, Solitary Wave Transformation, Breaking and Run-up at a Beach, *Proceedings of the Institution of Civil Engineers, Maritime Engineering*; Vol. 159: 97-105.

Bouws E., Gunther H., Rosenthal W. and Vincent C.L., 1985, Similarity of the Wind Wave Spectrum in Finite Depth Water 1. Spectral Form, *Journal of Geophysical Research.*; Vol. 90: 975–986.

Chan C.T., Swan C., 2003, Modelling Surface Water Waves using a High-Level GLN Theory, *International Conference on Estuaries and Coasts*; 735-741.

Craig W., 2006, Surface Water Waves and Tsunamis, *Journal of Dynamics and Differential Equations*; Vol. 18: 525-549.

Craig W. and Sulem C., 1993, Numerical Simulation of Gravity Waves, *Journal of Computational Physics*; Vol. 108: 73-83.

Curry J., 2008, Tsunami Approaching the Coast: Solitary Waves Hitting a Shallow Water Shelf, *4th Year Project, Department of Engineering Science, University of Oxford*.

Dean R.G. and Dalrymple R.A., 1984, Water Wave Mechanics for Engineers and Scientists, *World Scientific Advanced Series on Ocean Engineering*; Vol. 2.

Demirbilek Z. and Webster W.C., 1992, Application of the Green-Naghdi Theory of Fluid Sheets to Shallow-Water Wave Problems, *Report 1. Model Development. US Army Engineers Waterways Experiment Station, Coastal Engineering Research Center. Technical Report CERC-92-11*.

Dingemans M.W., 1997, Water Wave Propagation Over Uneven Bottom- Part 1: Linear Wave Propagation, *World Scientific Advanced Series on Ocean Engineering*; Vol. 13.

Dingemans M.W., 1997, Water Wave Propagation Over Uneven Bottom- Part 2: Non-linear Wave Propagation, *World Scientific Advanced Series on Ocean Engineering*; Vol. 13.

Drazin P.G. and Johnson R.S., 1989, Solitons: An Introduction, *Cambridge Texts in Applied Mechanics, Cambridge University Press*.

Ertekin R.C. et al., 1986, Waves Caused By a Moving Disturbance in a Shallow Channel of Finite Width, *Journal of Fluid Mechanics*; Vol. 169: 275-292.

Fenton J.D., 1985, A Fifth-Order Stokes Theory for Steady Waves, *Journal of Waterway, Port, Coastal, and Ocean Engineering*; Vol. 111:216-234.

Fenton J.D. and Rienecker M.M., 1982, A Fourier Method for Solving Nonlinear Water-Wave Problems: Application to Solitary-Wave Interactions, *Journal of Fluid Mechanics*; Vol. 118: 411-443.

Gibbs R.H. and Taylor P.H., 2005, Formation of Walls of Water in 'Fully' Nonlinear Simulations, *Applied Ocean Research*; Vol. 27: 142-157.

Gibson R.S. and Swan C., 2007, The Evolution of Large Ocean Waves: The Role of Local and Rapid Spectral Changes, *Proceedings of the Royal Society A*; Vol. 463: 21-48.

Green A.E., Laws N. and Naghdi P.M., 1974, On the Theory of Water Waves, *Proceedings of the Royal Society A*; Vol. 338: 43-55.

Green A.E., Laws N. and Naghdi P.M., 1986, A Nonlinear Theory of Water Waves for Finite and Infinite Depths, *Philosophical Transactions of the Royal Society of London. Series A*; Vol. 320: 37-70.

Groesen, E.van and Westhuis J.H., 2002, Modelling and Simulation of Surface Water Waves, *Mathematics and Computers in Simulation*; Vol. 59: 341-360.

Harland B., 2010, Solitary Wave Merging, *4th Year Project, Department of Engineering Science, University of Oxford*.

Holthuijsen L.H., 2006, Waves in Oceanic and Coastal Waters, *Cambridge University Press*.

Hughes S.A., 1993, Physical Models and Laboratory Techniques in Coastal Engineering, *World Scientific Advanced Series on Ocean Engineering*; Vol. 7.

Hunt A., 2003, Extreme Waves, Overtopping and Flooding at Sea Defences, *DPhil Thesis, University of Oxford.*

Johnson R.S., 1997, A Modern Introduction to the Mathematical Theory of Water Waves, *Cambridge Texts in Applied Mathematics, Cambridge University Press*.

Jonathan P. and Taylor P.H., 1997, On Irregular, Nonlinear Waves in a Spread Sea, *Journal of Offshore Mechanics and Arctic Engineering*; Vol. 119: 37-41.

Katsardi V., Lutio L.de and Swan C., 2013, An Experimental Study of Large Waves in Intermediate and Shallow Water Depths. Part I: Wave Height and Crest Height Statistics, *Coastal Engineering*; Vol. 73: 43-57.

Kim, J.W., Bai K.J., Ertekin R.C. and Webster W.C., 2001, A Derivation of the Green-Naghdi Equations for Irrotational Flows, *Journal of Engineering Mathematics*; Vol. 40: 17-42.

Kim J. W., Bai K. J., Ertekin R.C. and Webster W.C., 2003, A Strongly-Nonlinear Model for Water Waves in Water of Variable Depth-The Irrotational Green-Naghdi Model, *Journal of Offshore Mechanics and Arctic Engineering*; Vol. 125: 25-32.

Kim J. and Ertekin R., 2002, Hydroelasticity of an Infinitely Long Plate in Oblique Waves: Linear Green-Naghdi Theory, *Proceedings of the Institution of Mechanical Engineers, Part M: Journal of Engineering for the Maritime Environment*; Vol. 216: 179-197.

Lavrenov I.V. and Porubov A.V., 2006, Three Reasons for Freak Wave Generation in the Non-uniform Current, *European Journal of Mechanics B/Fluids*; Vol. 25: 574-585.

Li W.H. and Lam S.H., 1964, Principles of Fluid Mechanics, *Addison-Wesley Publishing Company, Inc*.

Lighthill J., 2003, Waves in Fluids, *Cambridge University Press*.

Limits on Waves in Shallow Water (Lowish) Report, 2007, *Shell International Exploration and Production B.V., Rijswick*. Contributions from Imperial College, Oxford University, Forristall Ocean Engineering and Shell International Exploration and Production (Private Communication).

Lindgren G., 1970, Some Properties of a Normal Process Near a Local Maximum, *The Annals of Mathematical Statistics;* Vol. 41: 1870-1883.

Longuet-Higgins M.S. and Cokelet E.D., 1976, The Deformation of Steep Surface Waves on Water. I. A Numerical Method of Computation, *Proceedings of the Royal Society A*; Vol. 350: 1-26.

Ma Q.W. and Yan S., 2006, Quasi ALE Finite Element Method for Nonlinear Water Waves, *Journal of Computational Physics*; Vol. 212: 52-72.

Mei C.C., 1983, The Applied Dynamics of Ocean Surface Waves, *John Wiley & Sons, Inc*.

Métayer O.Le, Gavrilyuk S. and Hank S., 2010, A Numerical Scheme for the Green-Naghdi Model, *Journal of Computational Physics*; Vol. 229: 2034-2045.

Miche M., 1944, Mouvements ondulatoires de la mer en profondeur constante ou decroissante, *Annales des pontes et chaussees*; Vol. 114: 25-78, 131-164, 270-292, 369-406.

Munson B.R., Young D.F. and Okiishi T.H., 2006, Fundamentals of Fluid Mechanics, *John Wiley & Sons (Asia) Pte Ltd*.

Nelson R.C., 1994, Depth Limited Design Wave Heights in very Flat Regions, *Coastal Engineering*; Vol. 23: 43-59.

Orszaghova J., 2011, Solitary Waves and Wave Groups at the Shore, *Dphil thesis, Department of Engineering Science, University of Oxford*.

Orszaghova J., Borthwick A.G.L. and Taylor P.H., 2012, From the Paddle to the Beach – A Boussinesq Shallow Water Numerical Wave Tank based on Madsen and Sørensen's Equations, *Journal of Computational Physics*; Vol. 231: 328-344.

Peregrine D.H., 1966, Long Waves on a Beach, *Journal of Fluid Mechanics*; Vol. 27: 815-827.

Sarpkaya T. and Isaacson M., 1981, Mechanics of Wave Forces on Offshore Structures, *Van Nostrand Reinhold Company*.

Seabra-Santos F.J., Renouard D.P. and Temperville A.M., 1987, Numerical and Experimental Study of the Transformation of a Solitary Wave over a Shelf or Isolated Obstacle, *Journal of Fluid Mechanics*; Vol. 176: 117-134.

Sergeeva A., Pelinovsky E. and Talipova T., 2011, Nonlinear Random Wave Field in Shallow Water: Variable Korteweg-de Vries Framework, *Nat. Hazards Earth Syst. Sci.*; Vol. 11: 323-330.

Shields J.J. and Webster W.C., 1988, On Direct Methods in Water-Wave Theory, *Journal of Fluid Mechanics*; Vol. 197: 171-199.

Slunyaev A., Kharif C., Pelinovsky E. and Talipova T., 2002, Nonlinear Wave Focusing on Water of Finite Depth, *Physica D: Nonlinear Phenomena*; Vol. 173: 77-96.

Smith J.M., 1999, Wave Breaking on an Opposite Current, *Coastal Engineering Technical Note IV-17, US Army Corps of Engineers.*

Smith R., 1979, Giant Waves, *Journal of Fluid Mechanics*; Vol. 77: 417-431.

Synolakis C.E., 1987, The Runup of Solitary Waves, *Journal of Fluid Mechanics*; Vol. 185: 523-545.

Stewart R.H., 1997, Introduction to Physical Oceanography, *Department of Oceanography, Texas A&M University; Open Source Textbook:http://oceanworld.tamu.edu/resources/ ocng_textbook/contents.html.*

Taylor P.H. and Williams B.A., 2004, Wave Statistics for Intermediate Depth Water – NewWaves and Symmetry, *Journal of Offshore Mechanics and Arctic Engineering*; Vol. 126: 54-59.

Tromans P.S., Anaturk A.R. and Hagemeijer P., 1991, A New Model for the Kinematics of Large Ocean Waves –Application as a Design Wave, *Proceeding of the First International Offshore and Polar Engineering Conference*; Vol. 3: 64-71.

Trulsen K., Zeng H., and Gramstad O., 2012, Laboratory Evidence of Freak Waves Provoked by Non-uniform Bathymetry, *Physics of Fluids*; Vol. 24: 097101.

Tucker M.J. and Pitt E.G., 2001, Waves in Ocean Engineering, *Elsevier Ocean Engineering Book Series*; Vol. 5.

Turnbull M.S., Borthwick A.G.L. and Taylor R. Eatock, 2003, Numerical Wave Tank based on a σ-transformed Finite Element Inviscid Flow Solver, *International Journal for Numerical Methods in Fluids*; Vol. 42: 641-663.

Walker D.A.G., Taylor P.H. and Taylor R.E., 2004, The Shape of Large Surface Waves on the Open Sea and the Draupner New Year Wave, *Applied Ocean Research*; Vol. 26: 73-83.

Wei G. and Kirby J.T., 1995, Time-Dependent Numerical Code for Extended Boussinesq Equations, *Journal of Waterway, Port, Coastal, and Ocean Engineering*; Vol. 121:251-261.

Xu Q., Pawlowski J.S. and Baddour R.E., 1997, Development of Green-Naghdi Models with a Wave-Absorbing Beach for Nonlinear, Irregular Wave Propagation, *Journal of Marine Science and Technology*; Vol. 2: 21-34.

Yan S. and Ma Q.W., 2007, Numerical Simulation of Fully Nonlinear Interaction between Steep Waves and 2D Floating Bodies using the QALE-FEM method, *Journal of Computational Physics*; Vol. 221: 666-692.

Zhao B.B. et al., 2009, Tsunamis Simulation by using Green-Naghdi Theory, *24th International Workshop on Water Waves and Floating Bodies*.

Zhao B.B., Duan W.Y. and Webster W.C., 2010, A Note on 3-Dimensional Green-Naghdi Theory, *25th International Workshop on Water Waves and Floating Bodies*.